

Dissertation

**Optical tweezers for DNA translocation
and cell elasticity experiments**

Sebastian Knust

Experimental Biophysics and Applied Nanoscience
Faculty of Physics
Bielefeld University

sknust@physik.uni-bielefeld.de

May 2020

Academic Advisor: Prof. Dr. Dario Anselmetti

Explanations exist; they have
existed for all time; there is
always a well-known solution to
every human problem – neat,
plausible, and wrong.

Henry Louis Mencken

Diese Arbeit ist auf alterungsbeständigem Papier gemäß DIN EN ISO 9706 gedruckt.

Erklärung

Ich erkläre hiermit,

- dass mir die geltende Promotionsordnung der Fakultät für Physik bekannt ist.
- dass ich die vorliegende Dissertation selbst angefertigt, keine Textabschnitte von Dritten oder eigenen Prüfungsarbeiten ohne Kennzeichnung übernommen und alle von mir benutzten Hilfsmittel und Quellen in der Arbeit angegeben habe.
- dass Dritte weder unmittelbar noch mittelbar geldwerte Leistungen von mir für Vermittlungstätigkeiten oder für Arbeiten erhalten haben, die im Zusammenhang mit dem Zustandekommen oder dem Inhalt der Dissertation stehen.
- dass ich diese Dissertation oder wesentliche Teile davon nicht als Prüfungsarbeit für eine staatliche oder andere wissenschaftliche Prüfung eingereicht habe.
- dass ich die gleiche, eine in wesentlichen Teilen ähnliche oder eine andere Abhandlung nicht bei einer anderen Hochschule als Dissertation eingereicht habe.

Bünde, den 25. Mai 2020

Sebastian Knust

Gutachter:

- Prof. Dr. Dario Anselmetti
- Prof. Dr. Thomas Huser

Contents

I. General Introduction and Theory	11
1. Introduction and Motivation	13
2. Microfluidics	17
2.1. Hydrodynamics	17
2.1.1. Navier-Stokes equation	17
2.1.2. Hagen-Poiseuille flow	18
2.1.3. Reynolds number	19
2.1.4. Stokes friction	21
2.1.5. Surface potential and the electrical double layer	23
2.2. Electrokinetics	24
2.2.1. Electrophoresis and electroosmosis	25
2.2.2. Dielectrophoresis	25
2.3. Brownian motion and diffusion	26
3. Optical Tweezers	29
3.1. History	29
3.2. Gaussian and laser optics	30
3.2.1. Free space Gaussian optics	30
3.2.2. Focused Gaussian optics	32
3.2.3. Real Gaussian beams	34
3.2.4. Laser	36
3.2.5. Fibre laser	39
3.2.6. Polarisation	39
3.3. Theory of optical trapping	41
3.3.1. 2D optical traps	41
3.3.2. 3D optical traps	43
3.3.3. Non-Gaussian beam profiles	44
3.3.4. Hooke's Law	45

3.3.5.	Langevin equation	46
3.4.	Force analysis	46
3.4.1.	Scattered light analysis	47
3.4.2.	Video-based analysis	48
3.5.	Interference effects in the vicinity of surfaces	50
3.6.	Force calibration	51
3.6.1.	Stokes' Law	51
3.6.2.	Power Spectral Density (PSD) analysis	52
4.	Theory of Nanopore translocation	59
4.1.	DNA	59
4.1.1.	Structure and role	59
4.1.2.	Entropic behaviour	61
4.2.	Electrical resistance of nanopores	62
5.	Theory of Cell Elasticity	63
5.1.	Setup of a cell	63
5.2.	Viscoelasticity	65
5.2.1.	Stress and Strain	65
5.3.	Viscoelastic models	65
5.3.1.	Purely elastic behaviour (spring)	66
5.3.2.	Purely viscous behaviour (dashpot)	66
5.3.3.	Series and parallel behaviour	66
5.3.4.	Multi-element models	68
5.4.	Experimental determination of viscoelastic parameters	71
5.4.1.	Creep recovery test	71
5.4.2.	Stress relaxation test	72
5.4.3.	Oscillatory analysis	72
5.4.4.	General method	73
II.	DNA translocation through nanopores in boron nitride and molybdenum disulfide	75
6.	Experimental setup	77
6.1.	Optical setup	77
6.2.	Microfluidic setup	79

6.3. Software	83
7. Monolayer membrane and nanopore preparation	85
7.1. Boron nitride	86
7.1.1. Material properties	86
7.1.2. Exfoliation	86
7.1.3. Transfer to substrate	89
7.1.4. Monolayer identification	89
7.1.5. Transfer to membrane	90
7.2. Molybdenum disulphide	91
7.2.1. Material properties	92
7.2.2. Exfoliation	93
7.2.3. Transfer to substrate	93
7.2.4. Monolayer identification	93
7.2.5. Transfer to membrane	93
7.2.6. Nanopore milling	94
8. Results	97
8.1. High-speed force detection	97
8.2. Boron nitride	100
8.2.1. Silicon wafer substrate	100
8.2.2. PDMS substrate	102
8.2.3. PMMA substrate	102
8.3. Molybdenum disulphide	102
8.3.1. Identification of monolayer flakes on PDMS	104
8.3.2. Wedging transfer	105
8.3.3. Transfer by viscoelastic stamping	106
8.3.4. Nanopore milling	106
8.3.5. DNA translocation with optical tweezers	113
8.3.6. Free DNA translocation	122
9. Conclusions and Outlook	125
III. Cell elasticity investigation with Elasto-Tweezers	127
10. Experimental setup	129
10.1. Optical tweezers setup	129

10.2. Microfluidics setup	131
10.2.1. General setup	132
10.2.2. Microfluidic chip	132
10.2.3. Temperature control	142
10.3. Software	142
11. Experimental protocols	145
11.1. Cell culture	145
11.2. Manufacture of microfluidic chips	145
11.2.1. PDMS chips	145
11.2.2. COC chips	146
11.3. Bead surface modifications	146
11.4. Declogging of microfluidic switches	147
11.5. Preparation of solutions	147
11.6. Installation and preparation of microfluidic chip	147
11.7. Cell viability verification	149
12. Results	151
12.1. Temperature control	151
12.2. Polarisation	152
12.3. Bead surface modifications	156
12.3.1. Carboxylated beads	156
12.3.2. Amino coated beads	156
12.3.3. Uncoated beads	156
12.4. Microfluidic design performance	157
12.4.1. Design 1: Corridors with adjacent trapping chambers	157
12.4.2. Design 2: Linear design	158
12.4.3. Design 3: Cross design with integrated experimental areas	159
12.5. Cell elasticity measurements	160
12.5.1. Cluster of HEK-293 cells and PDMS residue	160
12.5.2. Single HEK-293 cell with one static bead	161
12.5.3. Single HEK-293 cell with two optically trapped beads	163
12.5.4. Very stiff single HEK-293 cell	166
12.6. Cell viability verification	168
13. Conclusions and Outlook	169

IV. Conclusions, Outlook and Appendix	171
14. Summary and Outlook	173
A. User manual for the nanopore setup	175
A.1. Safety information	175
A.2. System overview	175
A.2.1. Hardware overview	175
A.2.2. Software overview	176
A.3. Performing experiments	178
A.3.1. Turning the system on	178
A.3.2. Controlling andor.vi	180
A.3.3. Controlling tweezer2.vi	181
A.4. Packing data	191
A.5. Analysing data	192
A.5.1. Measurement selection	192
A.5.2. Frame Selection & Edge Detection Settings	193
A.5.3. Autofocus calibration	194
A.5.4. Force Analysis	195
A.5.5. Results	197
B. User manual for the Elasto-Tweezers setup	199
B.1. Safety information	199
B.2. System overview	199
B.2.1. Hardware overview	199
B.2.2. Software overview	200
B.3. Performing experiments	201
B.3.1. Turning the system on	201
B.3.2. Controlling ET.vi	202
B.3.3. Controlling overview.vi	209
B.3.4. Resolving common issues	213
B.4. Packing data	215
B.5. Force analysis	215
B.5.1. Measurement selection	216
B.5.2. Frame Selection & Edge Detection Settings	216
B.5.3. Force Analysis	218
B.5.4. Results	220

Contents

B.6. Stress / strain analysis	221
C. Fitting numerical solutions of first-order differential equations with Gnuplot	225
D. List of figures	227
E. List of publications and conference contributions	233
F. Bibliography	235
G. Danksagung	249

Part I.

General Introduction and Theory

1. Introduction and Motivation

Since the first description by Arthur Ashkin in 1970¹ optical tweezers have become a widespread tool in biophysical laboratories. With optical tweezers a tightly focused laser beam can be used to three-dimensionally trap and move small particles like cells or polystyrene beads. Not only do optical tweezers enable the micromanipulation of these particles, they can also be used to measure the forces acting on them in the very small regime of just a few piconewtons. Thus optical tweezers have also become a standard tool in single molecule force spectroscopy, which seeks to study the motions and forces of biological molecules and other biological activity².

This fundamental role of optical tweezers in modern biophysical research was ultimately recognised in 2018: Half of the 2018 Physics Nobel Prize “for groundbreaking inventions in the field of laser physics” was awarded to Arthur Ashkin “for the optical tweezers and their application to biological systems”³.

Deoxyribonucleic acid (DNA) is the macromolecule carrying the genetic information of the vast majority of known organisms. As such, it is a highly interesting subject of single molecule force spectroscopy. In conjunction with optical tweezers, one can either attach a DNA molecule to one bead on either end to stretch it, or one can attach only one end of a DNA molecule to a bead and thread the other end into a small nanopore, e.g. by applying an electrical potential.

By attaching ligands to the DNA during either experiment, the force behaviour will change. This can be used to analyse the binding energy and kinetics of the ligand, which is a base for further investigation of the role or potential harm of specific ligands.

Previously, I introduced video-based force detection for optical tweezers as my Bachelor thesis^{4,5}. For my Master thesis, I evaluated the viability of ultra thin solid state membranes for DNA translocation experiments⁶. The first part of this dissertation is a continuation of these two previous works. As a first step, I introduce a new camera into the optical tweezers setup to allow for high-speed force detection. This is then used to analyse the translocation of DNA through extremely small nanopores in atomically thin solid state membranes in a variety of conditions.

On the other side of the spectrum of interesting biological entities for force spectroscopy

1. Introduction and Motivation

are whole cells. The correct mechano-elastic properties of cells are essential for both their health and their function. This is perhaps best illustrated by the cells forming the heart muscle.

The study of cell elasticity of cells suffering certain diseases, foremost cardiovascular diseases, or genetic mutations has therefore direct applications in the field of medicine and drug development. With optical tweezers, it is possible to attach beads on opposite sides of cells and stretch or squeeze them. By observing the response of the cell both during and immediately after external stimuli, it is possible to derive both elastic and viscous properties of the cell. These can then be compared to known healthy cells to get further insights into the pathomechanisms of diseases.

The second part of this work describes the cell elasticity investigation with Elasto-Tweezers. Elasto-Tweezers is a ROCKET* joint project between Ionovation GmbH (hardware setup), Bielefeld University (software and experiments), HDZ NRW (cell supplier and know-how), University of Twente (microfluidic design and prototyping), and Micronit Microtechnologies (microfluidic fabrication).

In this thesis, I present the optical tweezers setup developed in this project as well as microfluidic designs to facilitate cell elasticity experiments. I demonstrate this setup's capability to perform cell elasticity measurements on cell from the HEK293 cell line^{7,8}, which is a well known reference cell line widely used in cell biology.

This dissertation is therefore structured in multiple parts. The first part consists of this introduction and an introduction into microfluidics, optical tweezers, the theory of nanopore translocation and the theory of cell elasticity in chapters 2–5, respectively.

The second part describes the DNA translocation experiments. First, I explain the experimental setup and the changes introduced in this work. Then, I show the preparation of monolayer membranes of both boron nitride and molybdenum disulphide and the milling of nanopores in the latter material. Finally, I present the results obtained from various DNA translocation experiments through molybdenum disulphide nanopores.

The third part focusses on the cell elasticity investigations with Elasto-Tweezers. First, I describe the setup of the optical tweezers, the microfluidics and the software. Then, I present experimental protocols, followed by the results.

The two main parts each close with conclusions and an outlook. I summarise these findings in chapter 14, presenting an overall conclusion and an outlook on future experiments and setup.

*ROCKET (RegiOnal Collaboration on Key Enabling Technologies) is supported by the European Union, the Dutch Ministry of Economics, the Dutch provinces Gelderland and Overijssel, the State Chancellery of Lower Saxony and the Ministry of Economics of North Rhine-Westphalia within the scope of INTERREG Deutschland-Nederland

The appendix contains the user manuals for the software I wrote during the dissertation as well as supplementary material and a list of publications and conference contributions.

2. Microfluidics

Microfluidic systems are structures for manipulating fluids (mostly liquids) at the microrange. Typical dimensions of structures are in the range of tens to hundreds of micrometers, and the total liquid volume is in the range of microlitres or less⁹⁻¹¹. As surfaces scale with d^2 and volumes scale with d^3 ,¹² surface effects play a dominant role in microfluidic designs^{13,14}. This gives rise to unique and novel methods for flow control¹⁵ and accentuates the importance of proper surface preparation and coating¹⁶.

In this chapter, I will introduce the relevant phenomena in the fields of hydrodynamics and electrokinetics. I will also emphasize Brownian motion and diffusion which not only play an antagonistic role in trapping objects but also can serve as an important calibration tool for optical tweezers.

2.1. Hydrodynamics

2.1.1. Navier-Stokes equation

Except for the rare and exotic superfluids¹⁷, every fluid exhibits viscosity¹⁸, which is essentially internal resistance to flow – a form of energy dissipation. Therefore, a theoretical description of fluid flow must account for viscosity. This description is performed by the Navier-Stokes equation[†]:

$$\rho \left(\frac{\partial \vec{v}}{\partial t} + (\vec{v} \cdot \nabla) \vec{v} \right) = -\nabla p + \eta \Delta \vec{v} + \left(\xi + \frac{\eta}{3} \right) \nabla (\nabla \cdot \vec{v}) + F_{\text{ext}}^{\vec{v}} \quad (2.1)$$

This already assumes constant (dynamic) viscosity η as well as constant second / volume viscosity ξ throughout the fluid. For aqueous solutions, we can additionally assume incompressibility. This gives $\nabla \cdot \vec{v} = 0$ and therefore simplifies the Navier-Stokes solution even further to¹⁸⁻²⁰

$$\rho \left(\frac{\partial \vec{v}}{\partial t} + (\vec{v} \cdot \nabla) \vec{v} \right) = -\nabla p + \eta \Delta \vec{v} + F_{\text{ext}}^{\vec{v}} \quad (2.2)$$

[†]A derivation of the Navier-Stokes equation falls outside the scope of this thesis. For a brief description, see e. g. §15 of Landau and Lifschitz [18]

2. Microfluidics

The questions of existence of smooth and globally defined solutions for the Navier-Stokes equation is one of the Millenium Prize Problems and remains unproven to date. For all but the most trivial problems, numerical solutions to the Navier-Stokes equation are sought. Especially considering the multitude of possible external forces acting on the liquid, especially electrical fields, this is quite sensible.

2.1.2. Hagen-Poiseuille flow

From the Navier-Stokes equation, we can derive the flow profile and rate of a steady flow ($\partial\vec{v}/\partial t = 0$) through channels with constant cross-section.

2.1.2.1. Channels with circular cross-section

For a circular cross-section (e. g. a pipe with radius R) working in a cylindrical coordinate system, we have $v_r = v_\theta = 0$ as well as $\partial\vec{v}/\partial\theta = \partial v_z/\partial z = 0$. This greatly reduces the complexity of the Navier-Stokes equation as the left side becomes 0. Assuming no external forces, this gives

$$\frac{1}{r} \frac{\partial}{\partial r} \left(r \frac{\partial v_z}{\partial r} \right) = \frac{1}{\eta} \frac{\partial p}{\partial z} \quad (2.3)$$

With boundary conditions $v_z(r = R) = 0$ (no slip at the pipe wall) and $v_z(r = 0) < \infty$ (finite flow velocity in the centre of the pipe), the flow profile can be obtained as

$$v_z(r) = -\frac{1}{4\eta} \frac{\partial p}{\partial z} (R^2 - r^2) \quad (2.4)$$

which is a parabolic flow profile.

Integrating over the cross-section gives a volumetric flow rate of

$$Q = -\frac{\pi R^4}{8\eta} \frac{\partial p}{\partial z} \quad (2.5)$$

or, in the more common relation describing the pressure drop along a pipe with length L ,

$$\Delta P = \frac{8\eta L Q}{\pi R^4} \quad (2.6)$$

Such a flow is called a *Hagen-Poiseuille flow* with eq. 2.6 being the Hagen-Poiseuille equation²¹, named after the seminal independent papers describing it by Gotthilf Hagen²² and Jean Poiseuille^{23,24}.

2.1.2.2. Channels with rectangular cross-section

Whilst circular cross-section is important in everyday life, in microfluidics rectangular or approximately rectangular cross-sections are most often encountered. For a rectangular cross-section with flow along the x -axis, height h (with $0 \leq y \leq h$) and width l (similarly with $0 \leq z \leq l$), Joseph Boussinesq derived^{25,26}:

$$v(y, z) = -\frac{1}{2} \frac{y}{\eta} \frac{\partial p}{\partial x} (h - y) + 4 \frac{h^2}{\eta \pi^3} \frac{\partial p}{\partial x} \sum_{n=0}^{\infty} \frac{\sinh\left(\frac{(2n+1)\pi z}{h}\right) + \sinh\left(\frac{(2n+1)\pi(l-z)}{h}\right)}{(2n+1)^3 \sinh\left(\frac{(2n+1)\pi l}{h}\right)} \sin\left(\frac{(2n+1)\pi y}{h}\right) \quad (2.7)$$

$$Q = -\frac{h^3 l}{12\eta} \frac{\partial p}{\partial x} + \frac{16h^4}{\pi^5 \eta} \frac{\partial p}{\partial x} \sum_{n=0}^{\infty} \frac{\cosh\left(\frac{(2n+1)\pi l}{h}\right) - 1}{(2n+1)^5 \sinh\left(\frac{(2n+1)\pi l}{h}\right)} \quad (2.8)$$

These equations exemplify the analytical difficulties that the Navier-Stokes equation poses. In this specific case, a very good approximation is available as²⁷

$$Q = \frac{12h^3 l}{\eta} \frac{\partial p}{\partial x} \left(1 - \frac{192}{\pi^5} \frac{h}{l} \tanh\left(\frac{\pi l}{2h}\right)\right) \quad \text{for } l \geq h \quad (2.9)$$

$$\frac{\partial p}{\partial x} = \frac{\Delta P}{L} = \frac{12\eta Q}{lh^3} \frac{1}{1 - \frac{192}{\pi^5} \frac{h}{l} \tanh\left(\frac{\pi l}{2h}\right)} \quad \text{for } l \geq h \quad (2.10)$$

For $l < h$ we can simply rotate the system by 90° , effectively swapping l and h as well as y and z .

For larger aspect ratios ($l \gg h$) the last factor ($1 - \dots$) becomes 1, further simplifying the equation:

$$Q \approx \frac{12h^3 l}{\eta} \frac{\partial p}{\partial x} \quad \frac{\Delta P}{L} \approx \frac{12\eta Q}{lh^3} \quad \text{for } l \gg h \quad (2.11)$$

2.1.3. Reynolds number

For most problems in hydrodynamics, an interesting question is that of scalability. Ideally, we should be able to analyse problems with dimensionless numbers to facilitate scaling. The Navier-Stokes equation eq. 2.2 obviously consists of the inertial terms on the left side (containing density ρ) and the viscous part and forces on the right side.

We can introduce some typical scales for the system²⁸⁻³¹, namely the typical velocity v_0 and the typical length L_0 , giving the dimensionless:

$$\vec{v}' := \frac{\vec{v}}{v_0} \quad \vec{\nabla}' := \vec{\nabla} L_0 \quad \Delta' := \Delta L_0^2 \quad t' := \frac{t}{t_0} = \frac{v_0}{L_0} t \quad p' := \frac{p}{p_0} = p \frac{L_0}{\eta v_0} \quad (2.12)$$

2. Microfluidics

which corresponds to these inverse relations:

$$\vec{v} = \vec{v}'v_0 \quad \vec{\nabla} = \frac{\vec{\nabla}'}{L_0} \quad \Delta = \frac{\Delta'}{L_0^2} \quad t = t' \frac{L_0}{v_0} \quad p = p' \frac{\eta v_0}{L_0} \quad (2.13)$$

They can be used to transform the Navier-Stokes equation (with $F_{\text{ext}}^{\vec{v}} = 0$) to

$$\rho \left(\frac{v_0^2}{L_0} \frac{\partial \vec{v}'}{\partial t'} + \frac{v_0^2}{L_0} (\vec{v}' \vec{\nabla}') \vec{v}' \right) = - \frac{\eta v_0}{L_0^2} \vec{\nabla}' p' + \frac{\eta v_0}{L_0^2} \Delta' \vec{v}' \quad (2.14)$$

which produces the dimensionless Navier-Stokes equation

$$\text{Re} \left(\frac{\partial \vec{v}'}{\partial t'} + (\vec{v}' \vec{\nabla}') \vec{v}' \right) = - \vec{\nabla}' p' + \Delta' \vec{v}' \quad (2.15)$$

Here, Re is the *Reynolds number* (coined by Arnold Sommerfeld³¹ after the important experimental work by Osborne Reynolds^{29,30}). It is defined according to the above equations as

$$\text{Re} := \frac{\rho v_0 L_0}{\eta} \quad (2.16)$$

with fluid density ρ , typical / average velocity v_0 , fluid viscosity η and typical size l_0 . The typical size can be either the diameter of a circular or spherical obstruction or the diameter of a circular tube / fluid channel. For rectangular channels, the hydraulic diameter D_h is used, which is³²

$$D_h = \frac{4A}{C} = \frac{2hl}{h+l} \quad (2.17)$$

with cross-section surface A and circumference C .

The Reynolds number describes the ratio between inertial forces and viscous forces. It therefore also defines whether flow is laminar (i. e. streams flow parallel to each other and velocity at any point in the stream is time-invariant for constant boundary conditions) or turbulent (i. e. quasi-random flow motion in both space and time). A direct consequence of laminar flow is that mixing only occurs in the direction of flow or by diffusion (see section 2.3).

The ranges of the regimes vary in the literature and depend in detail on the specifics of the particular system of interest^{31,32}. However, the consensus is that for values $\text{Re} \ll 100$, especially $\text{Re} < 1$ we have laminar flow. For $\text{Re} \gg 1000$ on the other hand, we have turbulent flow

Typically in microfluidics and also in this thesis, we have $\rho \approx 1000 \text{ kg m}^{-3}$, $v_0 < 10 \text{ mm s}^{-1}$, $L_0 < 100 \text{ }\mu\text{m}$ and $\eta \leq 1 \text{ mPa s}$. This gives us $\text{Re} < 1$, placing microfluidics firmly into the laminar regime.

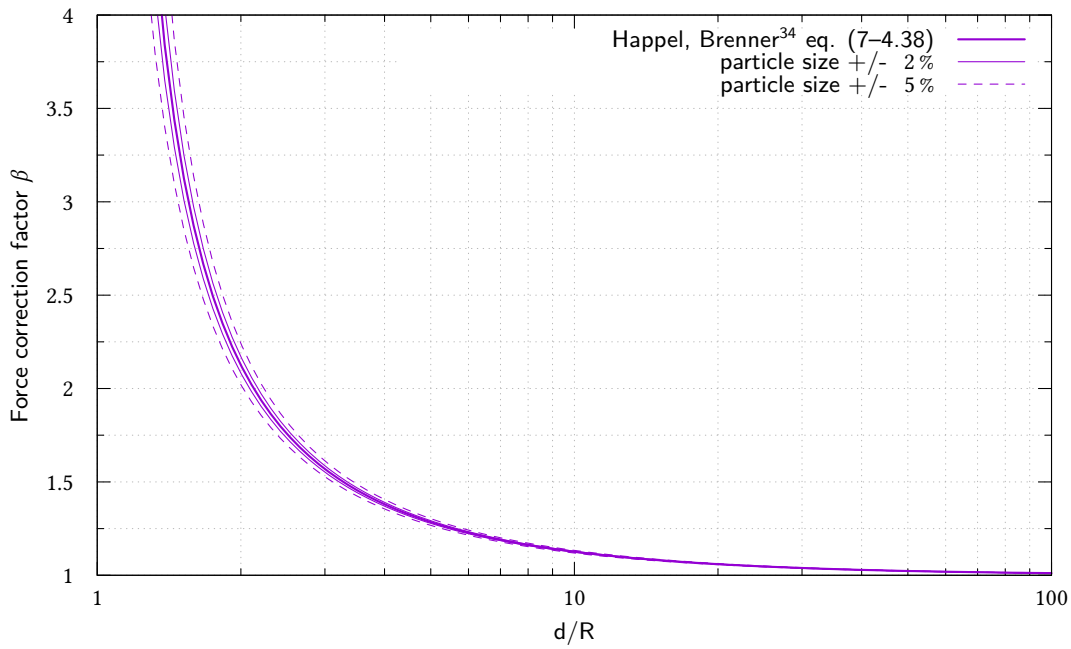


Fig. 2.1.: Correction factor for a particle moving perpendicular to a single plane wall according to Happel & Brenner³⁴

2.1.4. Stokes friction

Rewriting the Navier-Stokes equation eq. 2.2 for $Re \rightarrow 0$, we get the simple relation

$$\vec{\nabla} p = \eta \Delta \vec{v} \quad (2.18)$$

Stokes showed that this can be used to derive the friction force acting on a spherical particle (with radius R) in such a flow (at velocity \vec{v}) at low Reynolds numbers as^{28,33}

$$\vec{F} = -6\pi\eta R\vec{v} \quad (2.19)$$

However, this is only the case if the liquid reservoir is large enough. Once walls are less than ten to twenty times the particle size away from the particle, correction terms need to be considered. We will consider the two different cases relevant to the two experimental parts of this thesis.

Moving a particle perpendicular (i. e. towards or away from) a single plane surface, Happel

2. Microfluidics

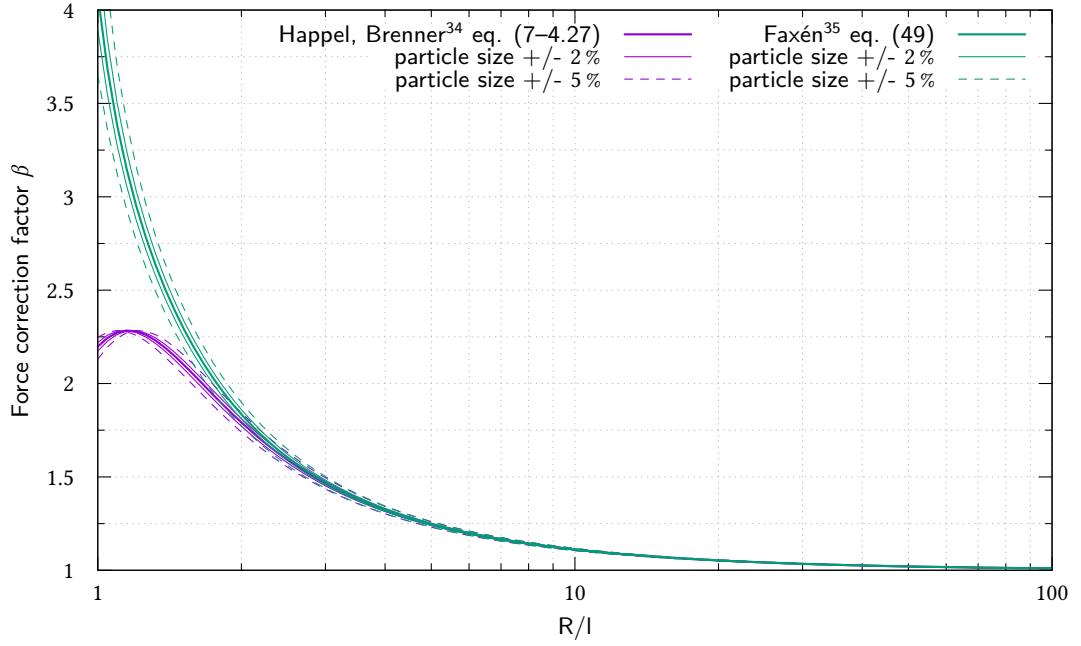


Fig. 2.2.: Correction factor for a particle moving parallel to and centred between two plane walls according to Happel & Brenner³⁴ and Faxén³⁵

and Brenner³⁴ give a correction term β for $F = -6\pi\eta Rv \cdot \beta$ as:

$$\beta = \frac{4}{3} \sinh \alpha \sum_{n=1}^{\infty} \frac{n(n+1)}{(2n-1)(2n+3)} \left(\frac{2 \sinh(2n+1)\alpha + (2n+1) \sinh 2\alpha}{4 \sinh^2(n+\frac{1}{2})\alpha - (2n+1)^2 \sinh^2 \alpha} - 1 \right) \quad (2.20)$$

where $\alpha = \cosh^{-1} d/R$ with distance d between the *particle centre* and the wall.

For the motion of a sphere parallel to and centred between two plane walls distanced $2l$ apart (i. e. the centre of the particle is l from both walls), Faxén found, in part by numerical integration, the value³⁵

$$\beta = \left(1 - 1.004 \frac{R}{l} + 0.418 \frac{R^3}{l^3} - 0.169 \frac{R^5}{l^5} \right)^{-1} \quad (2.21)$$

In their newer publication³⁴, Happel and Brenner add the fourth-order summand $0.21 \frac{R^4}{l^4}$, citing Faxén and stating the source of this additional summand as private communication. Unfortunately, for small channels the two equations diverge significantly, as illustrated in fig. 2.2.

Thomas Töws of the Condensed Matter Theory Group at Bielefeld University kindly per-

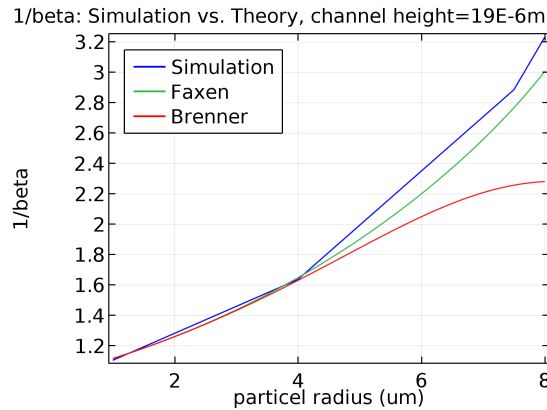


Fig. 2.3.: Simulation (blue) of the correction factor for a particle moving parallel to and centred between two plane walls compared with the results of Faxén (green) and Happel & Brenner (red). Graph and simulation provided by Thomas Töws, Condensed Matter Theory, Bielefeld University

formed a simulation with linear discretisation for the channel size relevant in this work. The result is shown in fig 2.3. Clearly, the simulation agrees with Faxén’s original description, which I will use henceforth.

In addition to the need for consideration of these correction factors, calibration based on Stokes’ Law has a few other disadvantages. The most significant is simply the need to move the particle at all. This requires large enough moving space so that the movement time and therefore the amount of data is sufficient (for $3\ \mu\text{m}$ particles and $10\ \text{pN}$ force, the speed is already $397\ \mu\text{m s}^{-1}$). Also, each movement of the particle induces a risk to trap dirt or another particle.

2.1.5. Surface potential and the electrical double layer

Surfaces in contact with aqueous ionic solutions often exhibit a surface potential, which depends on the pH value of the solution. In this thesis, we are typically working with buffered solutions and can assume pH 7.

Charged surfaces attract counter ions from the solution and therefore appear electrically neutral from a distance. Of course, surface effects play a major role in microfluidics and we therefore cannot simply discard the behaviour at the interface. The assembly of counter ion directly at the surface forms the *Stern layer*³⁶. Here, we can assume the counter ions to be immobilised at the surface. The layer is of molecular thickness. At its boundary, the remaining potential difference to the bulk solution is the ζ potential, which is a material property.

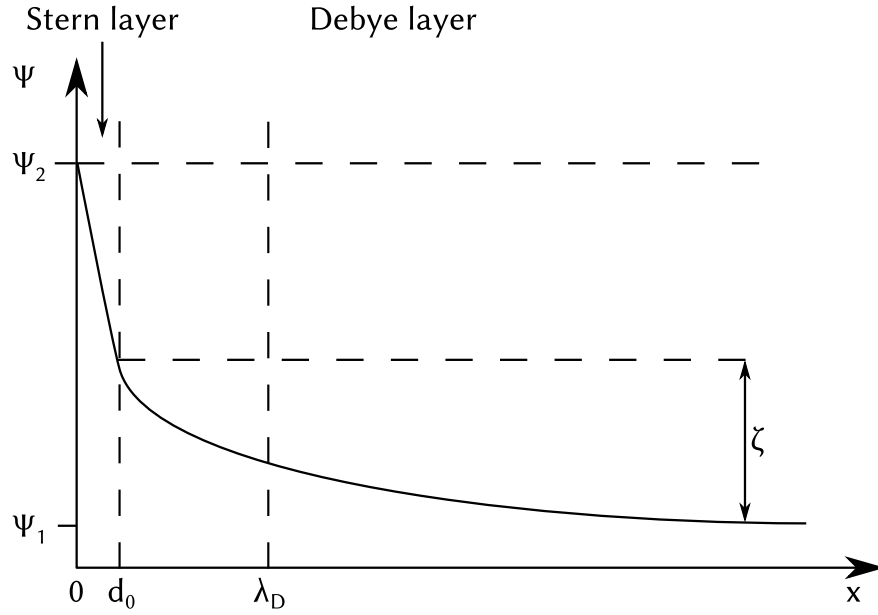


Fig. 2.4.: Sketch of the potential near a charged surface (at $x = 0$). Adapted from Kuhn et al.³⁶

The immobile Stern layer is followed by a layer of mobile counter ions, the *Debye layer*. Here the potential follows an exponential decay with the *Debye length* λ_D as the critical length. It can be calculated as

$$\lambda_D = \sqrt{\frac{\epsilon k_B T}{2 N_A e^2 I}} \quad \text{width } I = \frac{1}{2} \sum_i c_i z_i^2 \quad (2.22)$$

where ϵ is the permittivity of the solution ($\epsilon = \epsilon_0 \epsilon_r$) and I is the ionic strength, calculated from the charge numbers z_i and concentrations c_i of each ion in solution.

The resulting potential landscape is illustrated in fig. 2.4. The Stern layer and Debye layer together are commonly referred to as the *electrical double layer*.

Taking potassium chloride solutions as an example, we have $I = c$ where c is the potassium chloride concentration. For a high concentration of 1 M, this gives a Debye length of $\lambda_D = 0.3$ nm, whereas a low concentration of 1 mM gives $\lambda_D = 9.7$ nm. We can therefore assume that the width of the electrical double layer is typically less than 10 nm.

2.2. Electrokinetics

Combining microfluidic with electrical fields offers a new toolbox for introducing movement. Here, I will briefly describe both electrophoresis and electroosmosis, as well as di-

electrophoresis.

2.2.1. Electrophoresis and electroosmosis

Applying a DC voltage along a flow channel creates an electric field, which we will assume to be homogeneous. In microfluidic channels the electrical double layer is formed at the channel boundaries, creating areas of non-zero net charge. These areas, the Debye layers at the walls, are subject to field induced movement of velocity $v = \mu_{EO}E$. This phenomenon is called *electroosmosis*.

Assuming the no-slip condition, i. e. the flow at the surface is zero, and a channel that is large compared to λ_D , the *electroosmotic mobility* μ_{EO} can be derived from the Navier-Stokes-equation as³⁷

$$\mu_{EO} = -\frac{\varepsilon_0 \varepsilon_r \zeta}{\eta} \quad (2.23)$$

We can of course apply this phenomenon not only on a fluid moving relative to a wall. Let us instead consider a particle moving within a solution. This particle also exhibits an electrical double layer and we can obtain similarly a velocity due to *electrophoresis*, which is $v = \mu_{EP}E$ with

$$\mu_{EP} = +\frac{\varepsilon_0 \varepsilon_r \zeta}{\eta} \quad (2.24)$$

Electrophoresis and electroosmosis can therefore be considered as the same effect only with a different frame of reference. This also means that it is not possible to move a particle whose ζ potential (and therefore surface properties) are identical to the wall with electrophoresis, as the simultaneously occurring electroosmosis will negate the movement.

2.2.2. Dielectrophoresis

For the above discussion of electrophoresis and electroosmosis, we have considered a homogeneous electrical field. However, whenever we encounter changes of width of a microfluidic channel or e. g. a nanopore, the field becomes inhomogeneous.

For a dipole (with dipole moment \vec{p} in an inhomogeneous electric field, we get the potential energy $W = -\vec{p} \cdot \vec{E}$, resulting in a non-zero force $\vec{F} = \vec{p} \nabla \vec{E}$. However, we can also induce a dipole moment with the electric field, which is $\vec{p} = \alpha \vec{E}$ with polarisability α . This gives rise to the *dielectrophoretic* force $F_{DEP}^{\vec{}} = \alpha \nabla \vec{E}^2$.

If we now apply a AC voltage instead of a DC voltage, dielectrophoresis will still occur, with

$$F_{DEP}^{\vec{}} = \alpha \nabla \int_0^{2\pi/\omega} \vec{E}^2 = \frac{1}{2} \alpha \nabla \vec{E}^2 \quad (2.25)$$

2. Microfluidics

However, electrophoresis will not occur as the time-averaged electric field is zero. This allows for dielectrophoretic trapping of polarisable particles such as biological molecules and cells.

2.3. Brownian motion and diffusion

Small particles in a fluid medium are never truly at rest. One of the first and the most prominent description of such movement was made by Robert Brown in 1828³⁸ on pollen grains. A first thorough theoretical description of this *Brownian motion* was performed by Albert Einstein in 1905³⁹. In this explanation, the Brownian motion is described based on molecular kinetic thermodynamics due to the molecular motion of the surrounding particles. He uses the Fokker-Planck equation to calculate the time evolution of the probability density of a Brownian particle.

Three years later, Paul Langevin published his alternative derivation of Einstein's result^{40,41}. It is effectively a simple application of Newton's second law to a particle under a stochastic force, given by the equipartition theorem. The resulting equation for a particle with position x , mass m , and drag coefficient γ in an external potential Φ is the so-called *Langevin equation*:

$$m\frac{dx}{dt^2} + \gamma\frac{dx}{dt} + \Phi' = \xi(t) \quad (2.26)$$

The Brownian noise is $\xi(t)$. It is a Gaussian white noise which follows the fluctuation-dissipation theorem

$$\langle \xi(t) \rangle = 0 \quad \forall t \quad \langle \xi(s)\xi(t) \rangle = 2\gamma k_B T \delta(t-s) \quad \forall s, t \quad (2.27)$$

For spherical particles at laminar flow (low Reynolds numbers), the drag coefficient γ is described by the Stokes' law²⁸ as

$$\gamma = 6\pi\eta R \quad (2.28)$$

where R is the radius of the particle and η is the dynamic viscosity of the surrounding liquid.

Let us now consider the case of no or constant external potential, that is $\Phi' = 0$. We also multiply eq. 2.26 with x , giving

$$mx\frac{d^2x}{dt^2} + \gamma x\frac{dx}{dt} = x\xi \quad (2.29)$$

We can use these two identities to incorporate the extra factors x into the differentials:

$$x\frac{dx}{dt} = \frac{1}{2}\frac{dx^2}{dt} \quad x\frac{d^2x}{dt^2} = \frac{1}{2}\frac{d^2x^2}{dt^2} - \left(\frac{dx}{dt}\right)^2 \quad (2.30)$$

This gives

$$\frac{m}{2} \frac{d^2 x^2}{dt^2} - m \left(\frac{dx}{dt} \right) + \frac{\gamma}{2} \frac{dx^2}{dt} = x\xi \quad (2.31)$$

Let us now take the time-average of this equation, considering both the relation $\langle \xi \rangle = 0$ from the fluctuation-dissipation theorem as well as the equipartition theorem $m \left(\frac{dx}{dt} \right)^2 = k_B T$:

$$\frac{m}{2} \frac{\langle d^2 x^2 \rangle}{dt^2} - k_B T + \frac{\gamma}{2} \frac{\langle dx^2 \rangle}{dt} = 0 \quad (2.32)$$

$$\frac{\langle d^2 x^2 \rangle}{dt} + \frac{\gamma}{m} \frac{\langle dx^2 \rangle}{dt} = \frac{2k_B T}{m} \quad (2.33)$$

Introducing $\alpha := \frac{\langle dx^2 \rangle}{dt}$ gives us a first-order differential equation

$$\dot{\alpha} + \frac{\gamma}{m} \alpha = \frac{2k_B T}{m} \quad (2.34)$$

The general solution to this is

$$\alpha = \frac{2k_B T}{\gamma} + C \exp\left(-\frac{\gamma}{m} t\right) \quad (2.35)$$

For large times $t \gg \frac{m}{\gamma}$, we can easily use this result to obtain a value for $\langle x^2 \rangle$ by integration:

$$\langle x^2 \rangle = \frac{2k_B T}{\gamma} t = 2Dt \quad (2.36)$$

with $D = \frac{k_B T}{\gamma}$ the coefficient of diffusion.

Specifically, for spherical particles the coefficient of diffusion is given by the Stokes-Einstein equation^{39,42,43}

$$D = \frac{k_B T}{6\pi\eta R} \quad (2.37)$$

This treatment so far has been for the one-dimensional case. For multi-dimensional cases, we can easily see that the mean-square displacements in all dimensions are identical ($\langle x^2 \rangle = \langle y^2 \rangle = \langle z^2 \rangle$). This gives for the multi-dimensional displacement the general relation $\langle r^2 \rangle = n\langle x^2 \rangle$ with the dimensionality n , leading to the general diffusion relationship

$$\langle r^2 \rangle = 2nDt \quad (2.38)$$

*Considering polystyrene particles in water at room temperature, for a 15 μm particle we require $t \gg 12.5 \mu\text{s}$.

For a 3 μm particle, this value is further reduced to 0.5 μs . We can therefore safely assume that the limit is satisfied throughout this thesis

3. Optical Tweezers

Optical Tweezers are a fundamental tool in modern biophysics. Its chief developer, Arthur Ashkin, was awarded half of the 2018 Physics Nobel Prize for this groundbreaking invention. I start this chapter with a brief historical introduction, followed by the required laser theory. Then, I explain the theory of optical trapping with the relevant laws and effects describing both the trapping and the behaviour of trapped particles. Afterwards, I discuss the different methods to perform force analysis in the experimental setup. I also quickly describe some interference effects that are observed near weakly reflecting surfaces. Finally, I discuss the various methods to perform force calibration for optical tweezers with an emphasis on issues relevant to this work.

3.1. History

The first basis for what we call *optical tweezers* nowadays was laid by Arthur Ashkin in his 1970 paper¹ “Acceleration and Trapping of Particles by Radiation Pressure”, which describes that when a bead approaches a TEM₀₀-mode laser beam, it is both “accelerated in the direction of the light” and “drawn in to the beam axis”. This effect, the 2D or radial optical trapping, is the fundamental effect on which every optical tweezers is based.

There are multiple possibilities to use this effect to create a 3D optical trap. On the one hand, a 2D optical trap can be coupled with another force countering the acceleration along the optical axis. For example, another optical trap¹ or a setup using gravitation (leading to the term *Optical Levitation*⁴⁴) can be used. On the other hand, a single beam can be focused tightly, creating a 3D single beam optical trap without the need for any external forces, as first demonstrated 1986 by Ashkin et al.⁴⁵ Such a 3D single beam optical trap is commonly called *optical tweezers*.

Optical tweezers soon became a standard tool for single molecule force spectroscopy (next to atomic force microscopy and, more recently, magnetic tweezers)². Here, the studied molecules are attached to a trapped bead. Famous works depending on optical tweezers include the characterisation of the kinesin molecular motor system by Steven Block et al. in 1990⁴⁶ and the description of the entropic elasticity of λ phage DNA (according to the worm-like

3. Optical Tweezers

chain model) by Carlos Bustamante et al. in 1994⁴⁷.

At the experimental biophysics group in Bielefeld, optical tweezers have been introduced by Andy Sischka in 2001⁴⁸. They were first used for DNA stretching experiments between an optically trapped bead and a bead trapped by a micropipette^{49,50}. A second optical tweezers system was introduced by Andy Sischka in 2006. In 2007, one of the systems was reconfigured and is now dedicated to investigating the translocation of DNA through nanopores and featured force analysis based on backscattered light detection⁵¹. In 2012, I added a video-based force analysis method to that system⁴.

3.2. Gaussian and laser optics

Optical trapping is based on the distinct properties of laser beams. Strictly speaking, using a laser is not necessary but rather stems from convenience and practicability. Therefore, in this section I briefly introduce and review the theory of Gaussian optics with a focus on the required theory for optical trapping as well as the practical realisation and differences to an ideal Gaussian beam. I also briefly explain the theory of lasers with a focus on fibre lasers as used in this thesis. Finally, I describe the polarisation of light and how it can be utilised and manipulated for dual-beam optical tweezers.

3.2.1. Free space Gaussian optics

Light as an electromagnetic wave is subject to the Maxwell equations. For the light field strength E in an euclidian coordinate system, the wave equation can be derived as*:

$$\left(\frac{\partial^2}{\partial x^2} + \frac{\partial^2}{\partial y^2} + \frac{\partial^2}{\partial z^2} - \frac{1}{c^2} \frac{\partial^2}{\partial t^2} \right) E = 0 \quad (3.1)$$

Apart from the rather simple plane wave solution to this partial differential equation, spherical waves form another common group of solutions. Their general form is

$$E(r, t) = \frac{A}{r} \exp(-i(kr - \omega t)) \quad (3.2)$$

with r being the distance to the wave origin point. As usual, k denotes the angular wave number, for which the relation $k = 2\pi/\lambda$ holds.

Obviously, we could centre the wave at the origin of the coordinate system. However, it is also possible to assume the center to be at the complex location $(0, 0, -iz_R)$ with $z_R \in \mathbb{R}$

*The derivations in this subsection are covered in most textbooks on optics and lasers. Here, I perform the derivations following the texts of Eichler and Eichler⁵², Svelto⁵³, and Silfvast⁵⁴.

the so-called *Rayleigh length*. We can then furthermore introduce $q := z + iz_R$ and use the cylindrical notation with $r = \sqrt{x^2 + y^2}$ to get

$$E(r, z, t) = \frac{A}{\sqrt{q^2 + r^2}} \exp\left(-i(k\sqrt{q^2 + r^2} - \omega t)\right) \quad (3.3)$$

Since we are only interested in the far-field behaviour near the optical axis, the paraxial approximation $r \ll |q|$ can be used to simplify this to

$$E(r, z, t) \approx \frac{B}{q} \exp\left(-i\frac{kr^2}{2q}\right) \exp(i(\omega t - kz)) \quad (3.4)$$

with $B = A \exp(kz_R)$ just like A before a constant of amplitude.

This equation is the fundamental description of a Gaussian beam, which is also the primary mode of most lasers, the TEM_{00} mode. It is therefore of essential importance in the field of optical tweezers.

For better understanding, the complex value $1/q$ (which also depends on z) is often separated into real and imaginary parts:

$$\frac{1}{q(z)} = \frac{z - iz_R}{z^2 + z_R^2} = \frac{1}{R(z)} - i\frac{2}{kw^2(z)} \quad (3.5)$$

$$\text{with } R(z) = z + \frac{z_R^2}{z} \quad \text{and} \quad w(z) = \sqrt{\frac{2}{kz_R}} \sqrt{z^2 + z_R^2} \quad (3.6)$$

We introduced two new values, $R(z)$ and $w(z)$. $R(z)$ is the wave front radius of curvature at distance z along the axis. As can easily be seen, we have the two behaviours $R(z) \approx z$ for $|z| \gg z_R$ and $R(z) \rightarrow \infty$ for $z \rightarrow 0$. This can be interpreted as a Gaussian beam being a mixture between spherical and plane wave due to the complex origin.

The parameter $w(z)$ denotes the beam waist. If we look at the intensity distribution (with $I = |E|^2$) perpendicular to the optical axis, we get the beam profile

$$\frac{I}{I_{\max}} = \exp\left(-\frac{2r^2}{w^2(z)}\right) \quad (3.7)$$

This profile is obviously a Gaussian, thus the name *Gaussian beam*. At the beam waist $r = w$, the intensity is reduced to $1/e^2 = 0.135$ of the maximum intensity.

As we can see, the beam waist is minimal at $z = 0$. In datasheets, one commonly finds the minimum beam waist $2w_0 = 2w(0) = 2\sqrt{2z_R/k} = 2\sqrt{\frac{\lambda z_R}{\pi}}$ as a parameter to describe a Gaussian beam. In fact, this parameter together with the position of minimum beam waist

3. Optical Tweezers

(i.e. the position of $z = 0$), the wavelength λ , and the laser power completely specifies a Gaussian beam.

Alternatively the divergence angle is often used in laser characterisation. It is defined as

$$\theta = \lim_{z \gg z_R} \frac{w(z)}{z} = \frac{w_0}{z_R} = \frac{\lambda}{\pi w_0} \quad (3.8)$$

3.2.2. Focused Gaussian optics

For calculating the form of a Gaussian beam after optical components, ray transfer matrix analysis, also known as ABCD matrix analysis, can be used. In general, ray transfer matrix analysis is valid for paraxial systems and gives a relation between the parameters (r_1, θ_1) of an input beam (that is, the distance from the optical axis and the angle with the optical axis) and (r_2, θ_2) of an output beam as⁵⁵:

$$\begin{bmatrix} r_2 \\ \theta_2 \end{bmatrix} = \begin{bmatrix} A & B \\ C & D \end{bmatrix} \begin{bmatrix} r_1 \\ \theta_1 \end{bmatrix} \quad (3.9)$$

Using this method, the calculation of field propagation in a paraxial system only depends on knowledge of the ABCD matrices for the relevant optical components. In our case, two matrices are important: The free space propagation matrix M_f (with distance z) and the matrix for a thin lens M_l (with focal length f). They are:

$$M_f = \begin{bmatrix} 1 & z \\ 0 & 1 \end{bmatrix} \quad M_l = \begin{bmatrix} 1 & 0 \\ -\frac{1}{f} & 1 \end{bmatrix} \quad (3.10)$$

For Gaussian beams, the complex beam parameter q is changed by the ABCD matrix as follows^{54,56}:

$$q_2 = \frac{Aq_1 + B}{Cq_1 + D} \quad (3.11)$$

As can be seen trivially, for free space propagation along the axis for length z , we get $q_2 = q_1 + z$, which is exactly the definition of q .

Let us now take a look at a focused Gaussian beam, illustrated in fig. 3.1. If the beam waist is a distance a in front of a thin lens with focal length f , we have immediately before and after the lens:

$$q_1 = a + iz_R \quad q_2 = -a' + iz'_R \quad (3.12)$$

With eqs. 3.10 and 3.11, we also get

$$\frac{1}{q_2} = \frac{1}{q_1} - \frac{1}{f} \quad (3.13)$$

This finally leads to the relations⁵²

$$a' = f + \frac{f^2(a-f)}{(a-f)^2 + z_R^2} \quad (3.14)$$

$$z'_R = z_R \frac{f^2}{(a-f)^2 + z_R^2} \quad (3.15)$$

$$w'_0 = \frac{w_0 f}{\sqrt{(a-f)^2 + \left(\frac{\pi w_0^2}{\lambda}\right)^2}} \quad (3.16)$$

Typical non-divergent laser beams have a Rayleigh length in the range of $z_R \sim 1$ m. Therefore, we can assume $z_R \gg f$. Also, typically we have either $a \approx f$ or $a = 0$. Thus, we get the approximations

$$a' \approx f \quad (3.17)$$

$$w'_0 \approx \frac{\lambda f}{\pi w_0} \quad (3.18)$$

Notably, the focus is at the focal length of the lens and a smaller focus spot is obtained by using a wide beam before the lens. This can be obtained with a beam expander. In practise, the limit is the size of the lens. Typically the focal length is similar to the radius of the lens

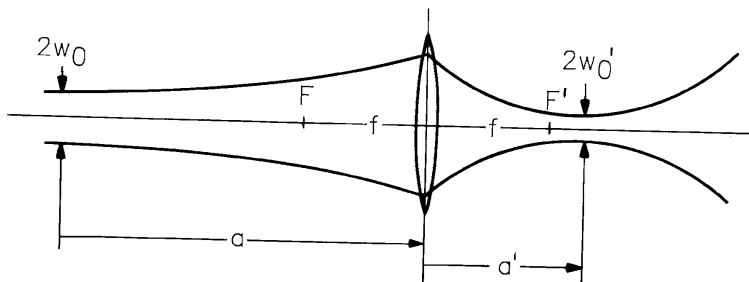


Fig. 3.1.: Focussing of a Gaussian beam by a thin lens with focal length f with initial beam waist w_0 a distance a in front of the lens. The resulting beam waist w'_0 is distanced a' from the lens. Image adapted from Eichler and Eichler [52]

3. Optical Tweezers

and thus the beam waist. Therefore the practical limit of spot size is

$$w_{\min} \approx \frac{\lambda}{\pi} \quad (3.19)$$

3.2.3. Real Gaussian beams

Until now, we have only described the properties of an ideal Gaussian beam. This however holds only true for a single-mode TEM₀₀ laser without any optical aberrations.

For a quantitative description of the laser beam quality, let us consider the beam parameter product, which is the product of beam divergence and beam waist⁵⁴. It corresponds to the étendue in classical optics. If we now look at the minimum value this parameter can obtain, we get

$$w_0 \theta = \frac{\lambda}{\pi} \quad (3.20)$$

A real laser beam can now be described as an ideal beam with a wider divergence and larger beam waist. Let us take the divergence and minimum waist of a real beam as

$$\Theta = M\theta \quad W_0 = Mw_0 \quad (3.21)$$

We then get

$$W_0 \Theta = M^2 \frac{\lambda}{\pi} \quad (3.22)$$

This M^2 is the beam quality factor. It can be measured with commercially available instruments and is part of the specification of most high-quality lasers.

Let us now have a look at the propagation of a 1064 nm laser with a starting $2w_{01}$ of 1.5 mm after a 60× Zeiss objective (tube length for Zeiss microscopes is $t = 165$ mm, therefore $f = 2.75$ mm). In this case, we have $z_R = 1.66$ m $\gg f$ and therefore the minimum beam waist is at the focal length. The resulting spot size is $2w_{02} = 2.48$ μm , which is well above the wavelength. This behaviour is illustrated in the top graph of fig. 3.2

Let us now introduce a beam expander, which expands the beam to $2w_{01} = 5.7$ mm, the back aperture size of the objective. We have $z_R = 24.0$ m, so again $z_R \gg f$. The resulting spot size is now $2w_{02} = 0.654$ μm . This is illustrated in the bottom graph of fig. 3.2. From eq. 3.19, we would expect $2w_{\min} \approx 0.677$ μm , so we are in very good agreement.

Also shown in the two graphs is the beam waistline for non-ideal beams with M^2 of 1.1, 1.2, and 1.3. Whilst the beam quality factor has an effect on the beam profile, it is negligible compared to the effect of proper beam expansion. Of course, if beam expansion is already used as far as practically possible, M^2 still plays an important role. For the shown quality factors here, the beam expands by 4.9 %, 9.5 %, and 14.0 %, respectively.

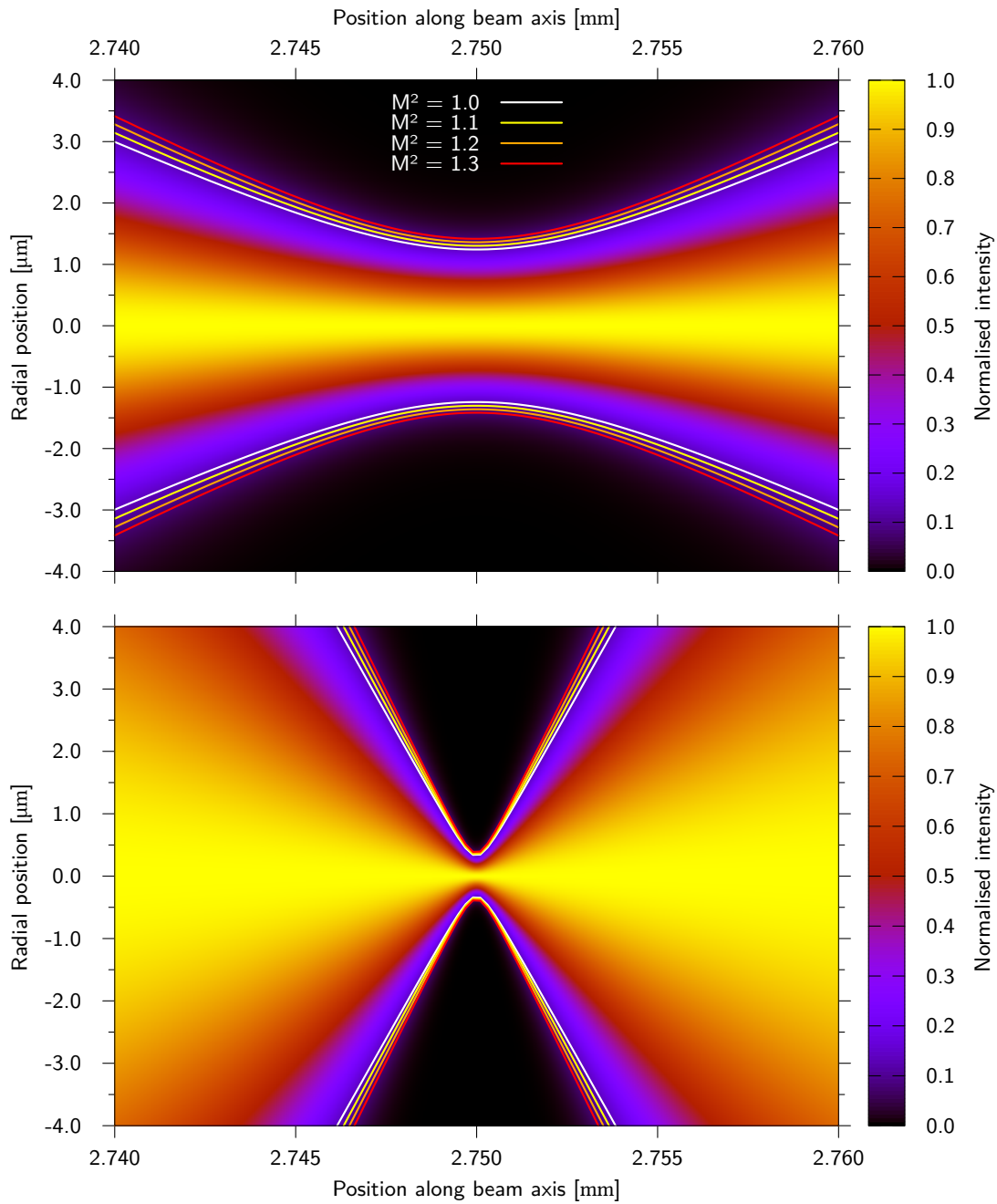


Fig. 3.2.: Intensity Profile of an ideal Gaussian beam and beam waists for an ideal beam as well as three real beams with M^2 of 1.1, 1.2, and 1.3. The beam is focused by a 60× Zeiss objective ($f = 2.75$ mm). (top): incident beam waist $2w_0 = 1.5$ mm (bottom): $2w_0 = 5.7$ mm

3. Optical Tweezers

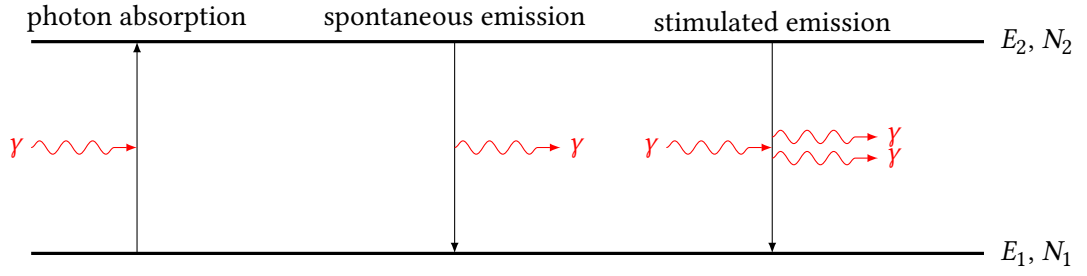


Fig. 3.3.: Illustration of the mechanisms of photon absorption, spontaneous emission and stimulated emission

3.2.4. Laser

Until now, we have seen how Gaussian beams propagate and how real Gaussian beams, which are emitted by lasers, differ from this idealisation. We will now explain what exactly a *laser* is and how it works.

The laser (*light amplification by stimulated emission of radiation*) is an oscillator that amplifies light by creating a population inversion in the laser medium (which gives a specific laser its name). This amplification takes place in an optical cavity, which forms the oscillator and allows only a fraction of the light to escape on one side, creating the laser beam.

Briefly, let us consider atoms with two energy levels E_1 and E_2 with $E_2 > E_1$ and the corresponding number of atoms in each state N_1 and N_2 . If we now apply an electromagnetic field, it can couple to the atom which absorbs a photon to move into an excited state (*photon absorption*). That excited state can now either decay spontaneously into a photon with a specific half-life (*spontaneous emission*), or it can again couple to the electromagnetic field and emit a photon in phase with the field (*stimulated emission*). These three mechanisms are illustrated in fig. 3.3.

If we take a look at the rate equations for these three processes, we get the simple relations

$$\frac{dN_1}{dt} = -B_{12} N_1 \rho(\nu) \quad (\text{photon absorption}) \quad (3.23)$$

$$\frac{dN_1}{dt} = A_{21} N_2 \quad (\text{spontaneous emission}) \quad (3.24)$$

$$\frac{dN_1}{dt} = B_{21} N_2 \rho(\nu) \quad (\text{stimulated emission}) \quad (3.25)$$

Here, A_{21} , B_{12} and B_{21} are the Einstein coefficients and $\rho(\nu)$ is the spectral energy density of the electromagnetic field at the frequency ν corresponding to the transition energy $\Delta E = E_2 - E_1$. In thermodynamic equilibrium, we require the sum of those three processes to be

nought. Since the energy distribution is known by the Maxwell-Boltzmann distribution and the background radiation is known by Planck's law, we can derive the following universal relations between the three coefficients:

$$\frac{A_{21}}{B_{21}} = \frac{8\pi h\nu^3}{c^3} \quad (3.26)$$

$$B_{21} = B_{12} \quad (3.27)$$

assuming that the two states are not degenerated.

We can see that spontaneous emission is of course not dependent on the electromagnetic field, but only on the number of atoms in the excited state. Also, spontaneous and stimulated emission are competing processes. For a strong stimulated emission, we need a long lifetime of the excited state (so that A_{21} is low), a high spectral density at the correct frequency, and a high number of atoms in the excited state.

An electromagnetic wave passing a medium is of course changing its intensity due to absorption according to Beer's law as

$$I(z) = I_0 \exp(-\alpha z) \quad (3.28)$$

with the absorbance α , which is dependent on the frequency of the wave. It can be calculated as⁵⁷

$$\alpha = (N_1 - N_2) \sigma(\nu) \quad (3.29)$$

with the frequency-specific absorption cross section $\sigma(\nu)$. As we can see, α becomes negative for $N_2 > N_1$, which would lead to an exponential *increase* of the intensity.

Obviously, that cannot be true in thermal equilibrium. In fact, from Maxwell-Boltzmann statistics we can calculate that in thermal equilibrium, the ratio between the two populations is

$$\frac{N_2}{N_1} = \exp\left(-\frac{\Delta E}{k_B T}\right) \quad (3.30)$$

which is less than unity for positive temperatures.

Therefore, we need a way to artificially create this *population inversion*. In a strict two-state system with non-degenerate states, this is not possible, since photon absorption and stimulated emission are coupled. Ideally, we should completely decouple the laser process from the pumping process, which is done in the four-state system illustrated in fig. 3.4.

Here, we take the ground state E_1 and pump it optically to a short-lived intermediate-state E_4 . The atom then transitions fast and radiationless into the relatively long-lived upper laser state E_3 , from which it radiates to the lower laser level E_2 . This state is again short-lived and

3. Optical Tweezers

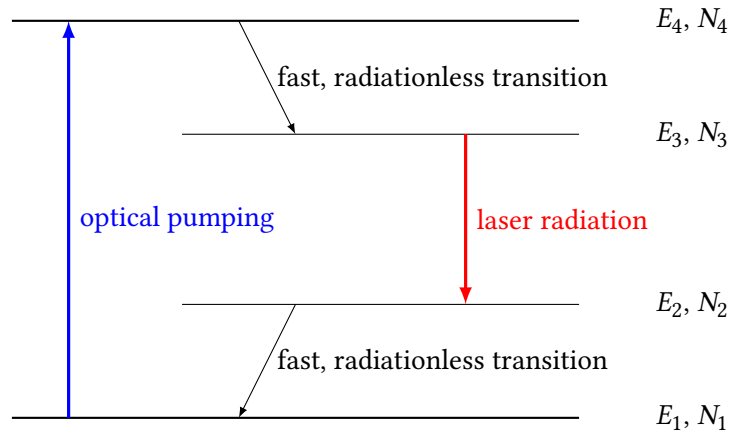


Fig. 3.4.: Four level energy diagram for a laser

a radiationless transition to the ground state occurs. Due to this last transition, the lower laser level is very sparsely populated, enabling an easy and efficient population inversion and therefore lasing.

As a laser medium, a wide variety of different materials are suitable. In solid state lasers, the active laser material are ions that are doped in a crystalline or glass medium. A typical solid state laser is the Nd:YAG laser, which consists of an yttrium aluminium garnet ($Y_3Al_5O_{12}$) doped with neodymium ions. In a gas laser, discharges from gasses such as a helium neon mixture (where the helium is pumped and transfers the energy to the neon, which performs the laser transition) or carbon dioxide are used. Lasers using fluorescent dyes are also used, both in liquid solution and embedded in a solid-state matrix. Diode lasers operate at a p-n junction in semiconductors. Most notably, laser diodes can be pumped electronically. As they are also available in a wide range of wavelengths, they are mostly used to provide the optical pumping for other laser types.

Independent of the type of laser medium, an optical cavity has to be formed around it to create a laser. This cavity allows the laser to oscillate, which enables a high amplification. If the amplification is greater than the losses of the resonator, an (initially) exponential rise in power is observed. However, the higher intensity also means that the excited laser state is depleted faster, which ultimately leads to an equilibrium state. The output power can now only be increased by increasing the pump power, which has practical limits. As we can see however, a modulation and regulation of the pump power allows the laser power to be modulated and regulated as well.

The way the cavity is formed depends on the specific type of laser. For solid state lasers, the edges are typically polished and coated with a mirror. Usually, mode selecting elements

are introduced as well to limit unwanted laser modes from being activated. These selectors are generally based on interference effects. It should be noted that every laser mode always has a non-zero width due to line broadening effects. Most notably are broadening by the uncertainty of the energy states due to their short lifetime and the Stark effect, which shifts and splits the energy levels in the presence of an electric field, like that of ions of the laser medium in a surrounding matrix in solid-state lasers.

3.2.5. Fibre laser

Optical fibres are thin threads of glass with a higher index of refraction at the core. Due to total internal reflection, the fibre acts as a waveguide. Proper doping of the fibre creates a special type of solid state laser, the fibre laser. Compared with other laser types, fibre lasers offer very high optical quality due to the self-focussing properties of a fibre. Since they can easily form a cavity several kilometres long, high output power are also achievable. Finally, the laser light is inherently coupled into the fibre. This allows for easy delivery to the required destination without having to deal with long beam paths.

Depending on the size of the fibre core, multiple different light modes can exist. However, reducing the core size to the order of magnitude of the wavelength limits the modes until only a single (ground) mode is exhibited. Such fibres are called *single-mode optical fibre*⁵⁸. This mode is not the TEM_{00} mode of a Gaussian beam, but instead the so-called LP_{01} mode. The form of this mode strongly depends on the geometry and especially on the radial distribution of the refraction indices. An analytical solution is impossible in most cases⁵⁵. A Gaussian beam is mostly a sufficient approximation of the ground mode, with typical fibre lasers having $M^2 \approx 1.1$.

By using multiple layers in the fibre, it is possible to keep the laser light in the fibre core whilst having an outer cylindrical layer with the pumping light. This pumps the laser along the whole length of the fibre, further increasing power output. Such a fibre is called a double-clad fibre⁵⁹.

3.2.6. Polarisation

Since light is an electromagnetic wave, it has both an electric and a magnetic field component. These components are perpendicular to each other and to the direction of travel (i. e. z). The direction of the field component oscillations can vary within the xy plane perpendicular to the propagation. For simplicity, let us only consider the electric field.

3. Optical Tweezers

The temporal field distribution at a specific point within the wave can be described as

$$\hat{E}(t) = \hat{E}_x(t) + \hat{E}_y(t) = \varepsilon_x \sin(\omega t + \phi_x) \hat{x} + \varepsilon_y \sin(\omega t + \phi_y) \hat{y} \quad (3.31)$$

with unit vectors \hat{x} and \hat{y} .

If we have either ε_x or ε_y zero, or $\phi_x = \phi_y$, we get a purely linear polarised wave. For $\varepsilon_x = \varepsilon_y$ and $\phi_y = \phi_x \pm \pi/2$ the wave is circular polarised. For the general case $\varepsilon_x \neq \varepsilon_y \neq 0$, the wave is elliptical polarised.

Of course, ε_x and ε_y themselves do not have to be constant over time. In this case, the wave is said to be unpolarised.

Some special optical components are selective to the polarisation of the light passing through. For example, birefringent materials have a refractive index that depends on the direction and polarisation of the light passing through. This can be used to both split light depending on the polarisation and to introduce a selective phase shift in one of the two field directions, due to the changed local speed of light. The former allows the creation of a polarising beam splitter, whilst the latter generates a waveplate. If the phase shift is 180° , corresponding to half the wavelength, this is called a half-wave plate. If the phase shift is 90° , we get a quarter-wave plate. Whilst a half-wave plate rotates the polarisation of linear polarised light, a quarter-wave plate can be used to transform linear polarised light into circular polarised light.

The combination of waveplates and beam splitters allows a wave to be split in two halves and rejoined without (noticeable) losses. To this end, the polarisation is first transformed to a circular one, if necessary. Since a circular polarised wave can be described as two perpendicularly linear polarised waves of equal intensity, the polarising beam splitter will split that wave into two halves of linear polarised light with orthogonal polarisation direction. Another beam splitter (used in reverse) can then rejoin them again. Whilst this is possible with a classical beam splitter (a half-mirror) as well, the joining beam splitter loses 50 % of both beams, which the polarising variant does not.

Another possible combination is to pass linear polarised light through a beam splitter and afterwards through a quarter-wave plate. If that light is reflected, the circular polarisation direction switches from right-handed to left-handed (or vice-versa). Therefore, it is linear polarised perpendicular to the incoming light after the quarter-wave plate and can thus be split with the beam splitter, for example towards a detector.

Polarised light can be created with polarisers at a loss of power. Alternatively, most lasers directly generate polarised light. For fibre lasers, special polarisation maintaining fibres (PM fibres) have to be used to create light in a reliable polarisation state. The core of these fi-

bres is intentionally distorted in an elliptic fashion to prevent unintended coherent crosstalk between different polarisation modes⁵⁶.

3.3. Theory of optical trapping

Optical trapping can be performed in two different regimes: In the Mie regime, particles larger than the wavelength of the trapping light are used. Such particles are typically spherical beads of glass or polystyrene with a functionalised surface. In the Rayleigh regime, particles smaller than the wavelength of the light are analysed. Typical particles here are single atoms and molecules in the context of laser cooling.

In this thesis, I am attaching the studied molecules and cells to polystyrene particles. Therefore, I will only explain optical trapping in the Mie regime. First, I describe the mechanics of optical trapping in two dimensions. Then, I show how this can be modified to enable optical trapping in three dimensions with just a single trapping beam. I also investigate the effects of non-Gaussian beam profiles on the trapping. Finally, I explain Hooke's Law for optical tweezers and I describe the Langevin equation for optical trapping.

3.3.1. 2D optical traps

We will now use the properties of a Gaussian beam to explain the effect of optical trapping. Since we are working in the Mie regime $r \gg \lambda$ (with r the particle radius), we will use geometric ray optics to easily explain trapping first in 2D and then in 3D. For much smaller particles in the Rayleigh regime $r \ll \lambda$, we could describe trapping as a form of dielectrophoresis, which is covered extensively in literature^{45,60}.

Using ray optics, the two important phenomena are refraction and reflection. For typical systems used in optical tweezers, like glass/water and polystyrene/water, the reflectivity of the particles is very small. Therefore, the main effect is refraction.

In both refraction and reflection, the direction of the light changes. However, photons carry a momentum $p = h/\lambda$. Since the momentum is conserved, there has to be an induced momentum on the particle surface.

The reflection and refraction of a beam by a spherical polystyrene particle is illustrated in fig. 3.5. If the bead is centred within the symmetrical (Gaussian) beam profile, the radial forces acting on the bead are symmetric to the optical axis. Thus, only forces in axial direction contribute to the total force. The bead is pushed along the beam direction by radiation pressure.

Assuming the bead is now radially deflected, the beam profile is no longer symmetrical to the axis of the bead. Therefore, radial forces now also contribute to the total force. This is

3. Optical Tweezers

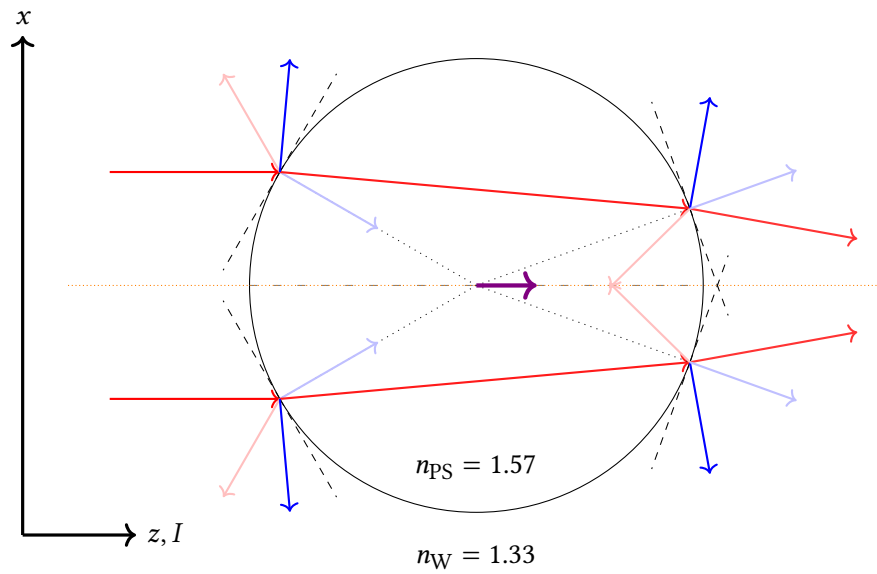


Fig. 3.5.: Light paths (red, intensity distribution in orange) and resulting forces (blue) for refraction (saturated) and reflection (pale) at a polystyrene bead suspended in water. The resulting total force is shown in violet.

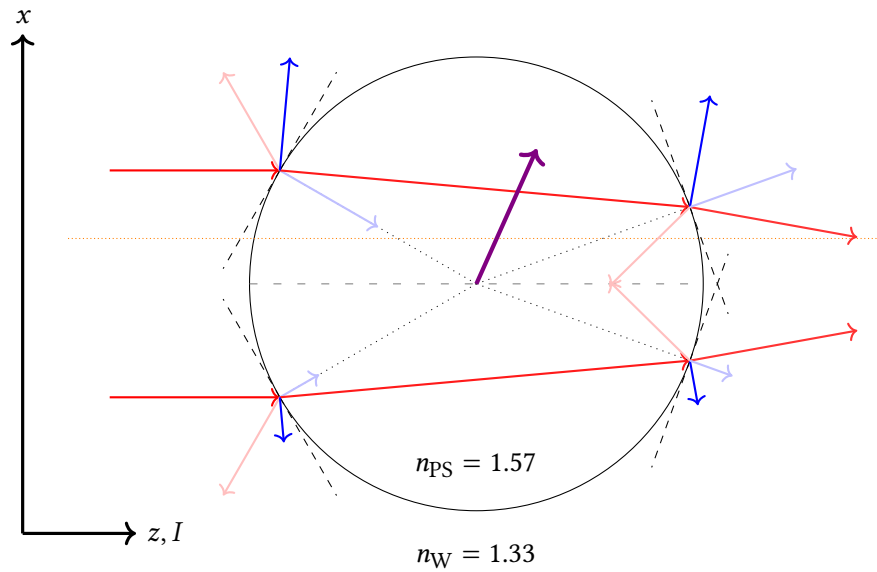


Fig. 3.6.: Light paths (red, intensity distribution in orange) and resulting forces (blue) for refraction (saturated) and reflection (pale) at a displaced polystyrene bead suspended in water. The resulting total force is shown in violet.

illustrated in fig. 3.6. Since the beam is more intense near the optical axis, the forces acting on the bead there are also stronger. Those forces pull the bead back towards the optical axis. Since the radiation pressure is still acting as well, a 2D optical trap can be achieved.

Obviously, this requires a suitable beam profile with the intensity decreasing with distance to the beam centre, at least on the scale of the particle size. Conveniently, Gaussian beams fulfil that requirement.

3.3.2. 3D optical traps

For a 3D optical trap, we could now either use an opposing force (like gravitation or a second beam), or form the beam in such a way that the radiation pressure is cancelled. Focusing the beam is one such way.

Fig. 3.7 illustrates the forces acting on a bead which is radially centred in a focused beam. In fig. 3.7a, the bead is placed behind the focal point. The – at this point divergent – laser beam induces forces on the bead which pull it towards the source of the laser beam and thus towards the focus. In fig. 3.7b, the bead is placed in front of the focal point. Here, the convergent beam enhances the radiation pressure and induces forces away from the laser source.

We therefore can trap a particle in the axial direction by focussing a laser beam. It should be noted that the particle is not trapped at the exact focal position, but a bit behind it, due to radiation pressure. Combining this axial trapping by a focussed beam with the 2D trapping by a suitable beam profile, such as a Gaussian, creates a single-beam 3D optical trap, called

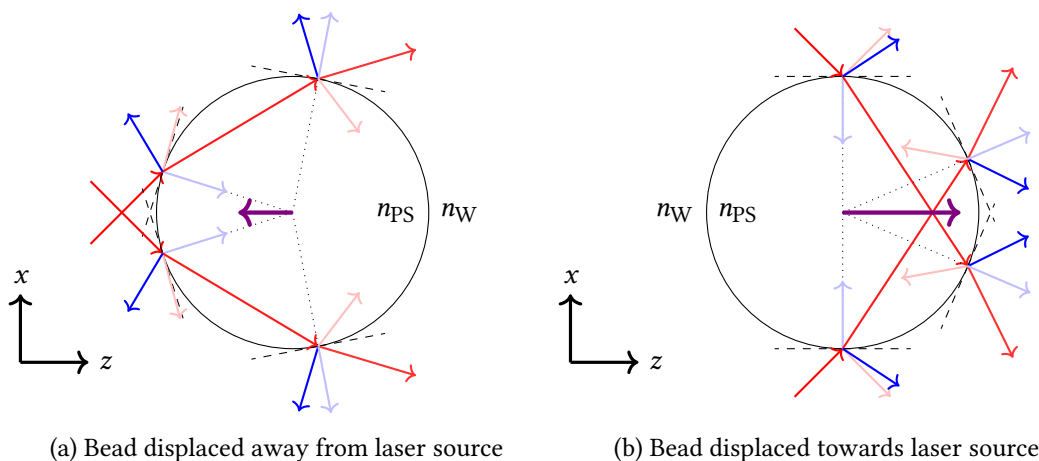


Fig. 3.7.: Light paths (red) and resulting forces (blue) for refraction (saturated) and reflection (pale) at a polystyrene bead suspended in water. The resulting total force is shown in violet.

optical tweezers.

3.3.3. Non-Gaussian beam profiles

Especially for axial optical trapping, we have seen that high angles of incidence of the light on the particle are the most relevant for strong trapping. It might therefore be beneficial to use a beam profile that provides ample power at the edge of the beam whilst still being suitable for 2D trapping.

One such beam profile is the special TEM_{01}^* mode, the so-called *doughnut profile*, which is illustrated in fig. 3.8. It is created by superimposing two Gaussian beams with TEM_{01} and TEM_{10} mode. Alternatively, it can be approximated by blocking the center part of a Gaussian beam with an obstruction filter. The resulting beam has a rotation invariant beam profile of

$$I = I_0 \left(\frac{r}{w(z)} \right)^2 \exp \left(-\frac{2r^2}{w^2(z)} \right) \quad (3.32)$$

Numerical integration of the forces acting on a displaced particle by each individual beam ray was performed by A. Ashkin⁶¹ to quantify the total trapping forces. For a TEM_{01}^* beam, he found that compared to a TEM_{00} beam (both with the size of the lens aperture equal to w_0) maximum trapping forces of an axially displaced bead are increased by 33.3 % and 28.9 %

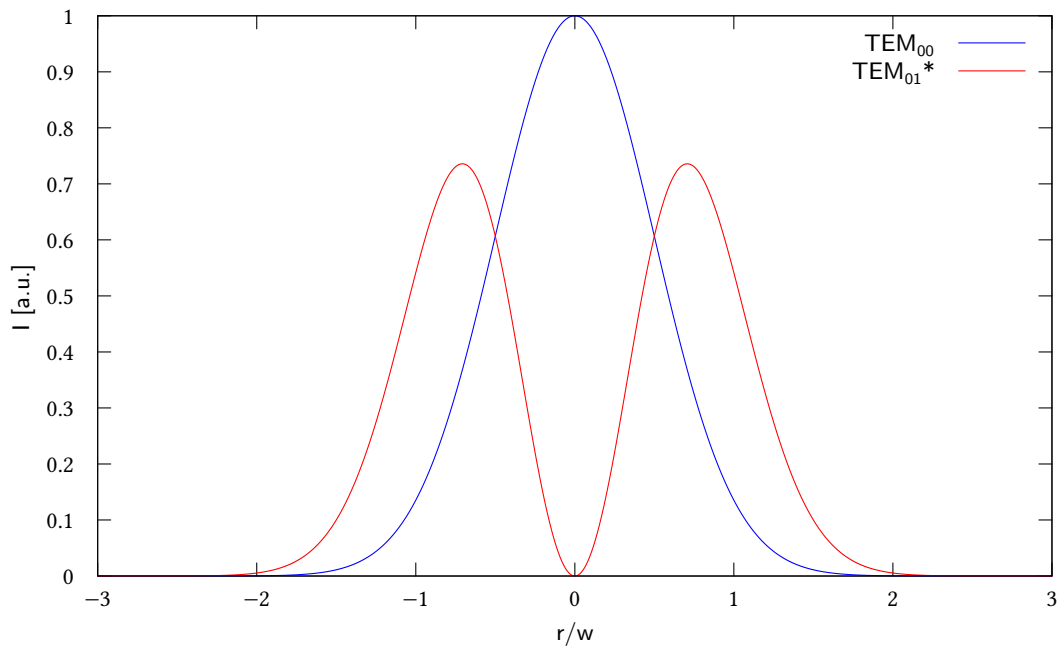


Fig. 3.8.: Beam profiles of TEM_{00} and TEM_{01}^* modes

for a backwards and forwards displaced particle, respectively. For a radially displaced bead however, the maximum trapping force is decreased by 15.2 %.

This shows that the use of a non-Gaussian beam profile can enhance the axial trapping capabilities of optical tweezers at the cost of decreased radial trap stability. Therefore, a suitable beam profile for each individual use-case should be employed.

3.3.4. Hooke's Law

For quantitative optical tweezers experiments, we are not only interested in trapping (and moving) particles, but primarily in the forces acting on them. Unfortunately, direct measurement of the forces is not possible. However, the deflection of the bead from the rest position can usually be determined quite easily. Therefore, we only need a way to convert these deflections into forces.

For small displacements of the trapped particle x , y , and z (using the same coordinate system as previously, so that x and y are radial deflections and z is the axial deflection), the assumption of a harmonic potential seems reasonable:

$$\Phi(x, y, z) = \frac{1}{2} (k_x x^2 + k_y y^2 + k_z z^2) \quad (3.33)$$

As shown before, the system is typically radially symmetrical, so we can set $k_x = k_y = k_r$. For the forces, we then get Hooke's Law:

$$\vec{F} = -\vec{\nabla}\Phi(x, y, z) = - \begin{pmatrix} k_r x \\ k_r y \\ k_z z \end{pmatrix} \quad (3.34)$$

Of course, this relation is only valid if the initial assumption of a harmonic potential holds true. By numerically integrating the forces acting on the bead, we can verify that. Arthur Ashkin performed such calculations⁶¹. The results are shown in fig. 3.9 together with linear approximations.

As can be seen in fig. 3.9a, for axial displacements a linear force response can be reasonably assumed for displacements smaller than $0.3R$ towards the laser and smaller than $0.5R$ away from the laser. For radial displacements, we can see in fig. 3.9b that a displacement of less than $0.5R$ is required for a linear force response.

3. Optical Tweezers

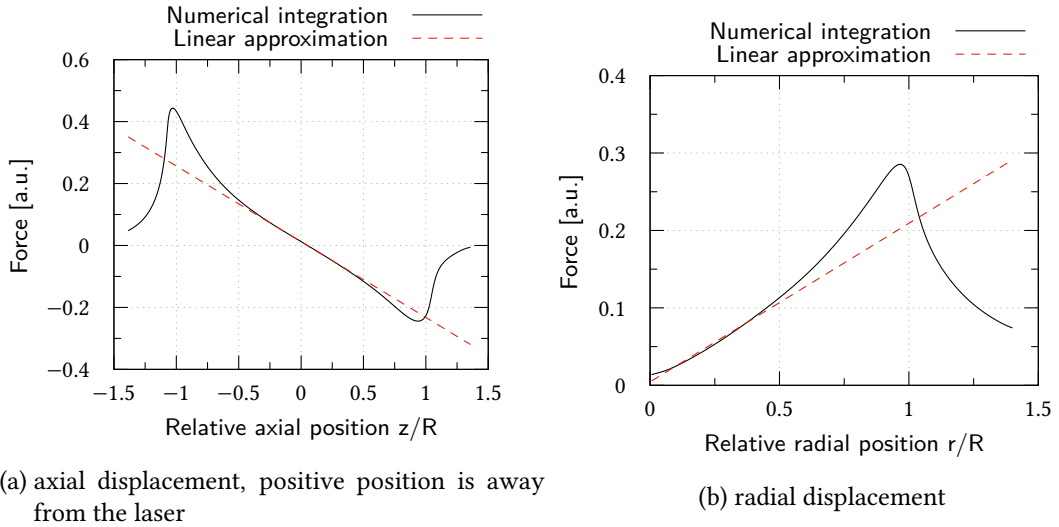


Fig. 3.9.: Numerical integration and linear approximation of the trapping forces for axial and radial displacement. Numerical integrations by A. Ashkin⁶¹.

3.3.5. Langevin equation

As we have seen before in section 2.3 particles in fluid medium are subject to Brownian motion, which can be described by the Langevin equation 2.26:

$$m\ddot{x} + \gamma\dot{x} + \Phi' = \xi(t)$$

In an optical tweezers system, the external potential is harmonic, as shown in the last subsection. Therefore, $\Phi' = kx$.

As we have also seen earlier, the dampening time in the systems used in this thesis are in the microsecond range. As we are only observing in the millisecond range and above, we can consider the system overdamped and ignore the mass inertia term.

Therefore, the final Langevin equation for optical tweezers is

$$\gamma\dot{x} + kx = \xi(t) \tag{3.35}$$

We will utilise this result later in section 3.6 to perform force calibration on the system.

3.4. Force analysis

As mentioned before, force analysis for optical tweezers is based on measuring the deflection of the particle from rest position. Forces can then be calculated using Hooke's law as

discussed earlier. It is even conceivable to use the non-linear relationship between force and displacement instead of the linear approximation. Especially if dealing with large forces / displacements, this should be considered.

For measuring the displacement of the trapped particle, scattered light analysis has been used for a long time. I will discuss it briefly below. However, in this work we are only using a newer, video-based detection method. Since I introduced it in my Bachelor thesis⁵, an interested reader might refer to it for a more detailed, in-depth discussion. However, this method is explained here as well, with a few updates.

3.4.1. Scattered light analysis

The analysis of the scattered trapping light is the straightforward method for deflection detection in optical tweezers. In the easiest setup, a second objective is used to capture the forward-scattered light. A four-quadrant photodiode is then used for detection⁶². Radial displacement of the beads also leads to radial shift in laser intensity on the photodiode in the same direction. Axial displacement leads to a change in total intensity.

The advantage of this method is directly obvious: Since a photodiode is used, the measured quantities are analogue. This allows for inherently high data rate acquisition. However, the disadvantages are equally obvious: Other particles in the immediate vicinity of the trapped particle also contribute to the scattered light, thus distorting the measurement. Also, a second objective is required. Since we now have one objective on either side of the sample, thickness quickly becomes an issue. With typical working distances of 250 μm , thin microfluidics have to be used and incorporation of other instruments is rather difficult.

Of course, the backscattered trapping light can be used as well⁶³. Good signals can be obtained by exploiting polarisation. To that end, a linear polarised laser is used. It first passes a polarising beam splitter and then a quarter-wave plate. The now circularly polarised laser changes the polarisation direction on backscattering and is converted back into orthogonal linearly polarised light, which can be filtered out with the beam splitter.^{51,64}

Detection of the displacement is then performed just as in the forward-scattered case. The disadvantage of requiring a second objective is overcome. However, we now require a polarised trapping laser and a – at least partially – reflective trapped particle. A higher reflectivity of the particle directly corresponds with less detector noise. This is an issue both for trapping biological particles, where the reflectivity cannot be tuned, as well as for experiments near weakly reflecting membranes, as explained in the next section.

3.4.2. Video-based analysis

Considering the issues with scattered light analysis, video-based analysis offers a simple and highly versatile method to detect the displacement of trapped particles at the cost of decreased temporal resolution. Here, we simply take a video of the particle and automatically detect its position and size with suitable algorithms on a PC. Obviously, the position corresponds to radial displacement. For axial displacement, typically the apparent size of the particle changes, mostly due to diffraction. The latter however is highly dependent on the experimental setup, especially on the lighting.

To achieve reasonable temporal resolution high-speed video cameras should be used. For immediate user feedback, the detection should be performed in real-time. Nevertheless, it is often advisable to also record the raw video for improved offline detection. This demands a great amount of processing power and data storage capability from the used PC. Fortunately, processing power and storage capacity has increased exponentially in the last few decades^{65,66}. There is also the requirement of sufficient lighting for noise-free high frame rate images, which must be taken into account when designing the setup.

For improved spatial resolution the image is typically passed through a telescopic post-magnification after the objective. It should be configured in such a way that the image of the trapped particle is half as large as the camera chip. This way, if the particle at rest is centered in the camera image, then the particle is still fully visible at maximum radial displacement.

In this work, I use the principal particle detection algorithm that I developed in my Bachelor thesis⁵. The polystyrene particles that are used in this work can be characterised as a dark ring. After manual selection of an annular region of interest, up to 360 radial spokes are considered. Using a built-in LabView function, we analyse the brightness gradients along the spokes. From inside to outside, the image first gets darker (from bead centre to bead edge) and then lighter again (from bead edge to background). The two extreme values of the gradient of each spoke therefore correspond to an edge from bright to dark and from dark to bright. Taking the point centred between those then gives us the position of the bead edge along that specific spoke. We then fit a circle through all edge position points to get the final position and size of the particle. This process is illustrated in fig. 3.10.

All camera images are subject to noise. Furthermore, minute dirt grains can adversely effect the edge detection. Therefore, we do not simply take the intensities exactly along each spoke as the basis for the edge detection. Instead, along each spoke neighbouring pixels are averaged along a width specified by the user. Also, the gradient is determined using a convolution with a gradient kernel. The larger this kernel, the more robust the system is to noise and disturbances. The kernel size can also be specified by the user.

The region of interest only has to be selected once for an optical trap. However, it has

to be adjusted for larger radial forces. To this end, the result of the last frame can be used as the new position. Furthermore, for sudden increases in force a two-pass method can be used: First, using the previous result as a starting value the edge-detection is performed with reduced parameters (i. e. width, kernel size and spoke spacing). Then, that result is taken as the basis for a second pass with higher fidelity.

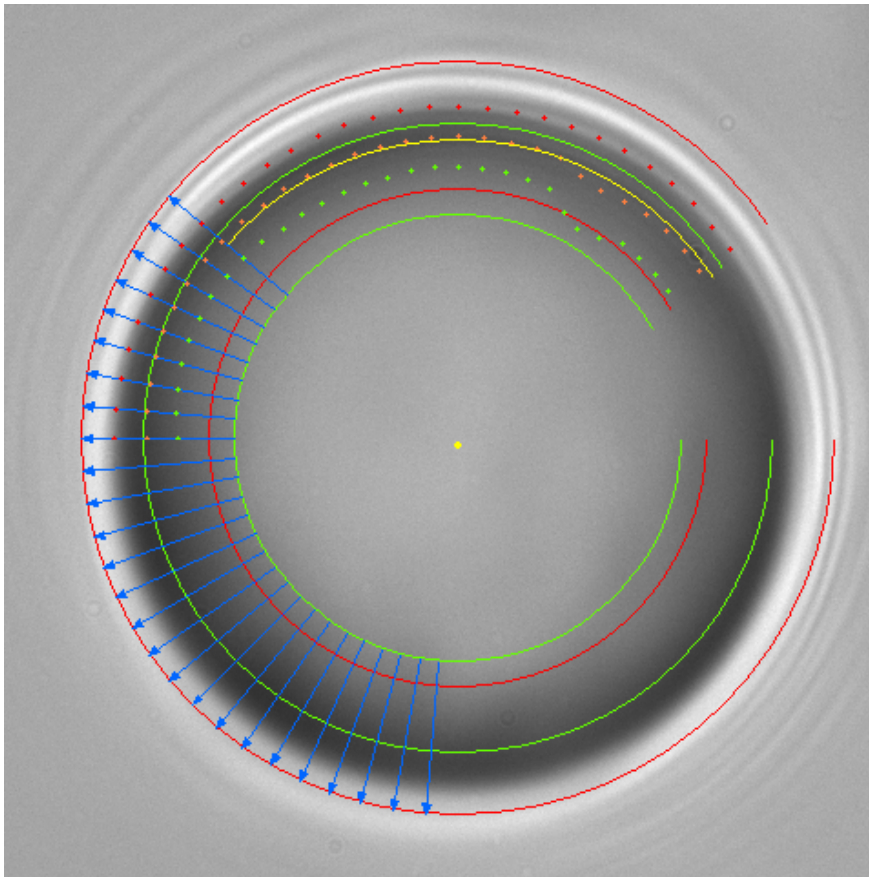


Fig. 3.10.: Still frame of the measurement camera with a trapped polystyrene particle. The annular regions of interest for the falling (bright to dark) and rising (dark to bright) edges are illustrated by two circles in green and red, respectively. Within these circles, spokes are added (blue arrows). For clarity, here we only show one spoke every 5° , instead of every 1° . The edge points are found along the spokes (green and red, for falling and rising, respectively) and the centre point (orange) is calculated. Finally, a circle (yellow) is fitted through those (orange) points, giving a centre position (yellow dot) and a radius.

3.4.2.1. Online versus offline analysis

Video-based force detection can generally be performed online, that is in real-time, or offline. For online analysis, the video does not need to be saved. However, average performance needs to be real-time. In contrast, for offline analysis performance the video is recorded to (temporary) storage and analysed later. This allows the user to review the detection, fine-tune parameters and perform the analysis with higher fidelity than possible online.

With currently available computer systems, parallelisation must be exploited to achieve high frame rates. A typical workstation computer nowadays is capable of running between 8 and 64 threads in parallel. For the video-based analysis, this typically means that multiple frames are analysed in parallel. As a direct consequence, the results of an immediately preceding frame are not (yet) available. This is a severe limit for the two-pass strategy for rapidly changing radial forces.

As stated before, in this thesis we use a hybrid approach exclusively: For user feedback, online analysis is performed, albeit with reduced fidelity and, in the case of the DNA translocation setup, with reduced time resolution. Considering the prototypical nature of the setups used in this work, this seems appropriate.

In our setups, data rates are in the range of 200 MB s^{-1} to 250 MB s^{-1} , which equates to 720 GB h^{-1} to 900 GB h^{-1} . With typical hard disk capacities of 8000 GB, long-term storage of the raw video data is not sustainable. Instead, offline analysis needs to be performed and verified regularly, allowing old raw video data to be deleted.

3.5. Interference effects in the vicinity of surfaces

Optical trapping is typically performed in microfluidic structures of some kind. In closed fluidic systems, there is always a surface perpendicular to the laser beam beyond the trapped particle. This surface, just as the trapped particle, reflects the trapping laser light, creating a standing wave. Even though the laser is divergent at this place and the reflectivity is typically in the range of 1%^{51,67}, it nevertheless cannot be neglected^{4,5}.

The result of this standing wave is a displacement of the axial zero force position of the bead when approaching, or moving away from, a surface. For experiments where axial forces are measured, such as DNA translocation experiments, this is an undesired artefact. Fortunately, the magnitude depends on both the reflectivity of the surface as well as the reflectivity of the trapped particle. Whilst the surface cannot be modified in most cases, the reflectivity of the trapped particle for a specific wavelength can be changed by using internal destructive interference⁶⁸.

Quite intuitively, for larger particles (diameter D , refractive index n ; $n D \gtrsim 2\lambda$) the optimal

particle size for minimal reflectivity is found as slightly less than⁶⁸

$$n D = \left(l + \frac{1}{2} \right) \lambda \quad l \in \mathbb{N} \quad (3.36)$$

3.6. Force calibration

Until now, force values have been acquired in arbitrary units, which we shall call \check{x} with zero-force value \check{x}_0 . Sometimes (e. g. for radial forces with video-based detection), but not always, the conversion factor ζ of these units into a physical displacement is known, i. e. $x = \zeta(\check{x} - \check{x}_0)$. Whilst in these cases a direct conversion might theoretically be possible by calculating the trap spring constant, it would require exact knowledge of trap geometry, laser power, and particle geometry. These values might fluctuate and are not readily available. Therefore, empirical calibration protocols are employed. They commonly fall into two categories: drag force based analysis and analysis of the Power Spectral Density (PSD).

3.6.1. Stokes' Law

As we have seen before, a sphere with radius R moving in a laminar flow of speed v (i. e. at low Reynolds numbers $Re = vR\rho/\eta \ll 1$ with particle density ρ) through a fluid with dynamic viscosity η is subject to Stokes' drag force.

$$F = -6\pi\eta Rv\beta \quad (3.37)$$

where β is the correction term for moving close to the vicinity of a surface, according to eq. 2.20 or 2.21.

Measuring the arbitrary unit value \check{x} , we get a force value as

$$F = k\zeta(\check{x} - \check{x}_0) \quad (3.38)$$

Calibration now seems to be quite simple at first glance: We simply determine \check{x}_0 at rest and move the particle with constant velocity through the surrounding liquid to calibrate the factor $k\zeta = \frac{-6\pi\eta Rv\beta}{\check{x} - \check{x}_0}$. However, due to the surface correction β , this is not straightforward. We require precise knowledge of the distance from any close walls to perform correct calibration. Furthermore, for calibration perpendicular to the plane, we need to take into consideration that β depends on the distance to the wall (via $\alpha = \cosh^{-1} d/R$ with distance d) and is thus not a constant.

In addition to the need for consideration of these correction factors, calibration based on Stokes' Law has a few other disadvantages. These are simply based on the need to move

3. Optical Tweezers

the particle at all. This requires large enough moving space so that the movement time and therefore the amount of data is sufficient (for $3\ \mu\text{m}$ particles and $10\ \text{pN}$ force, the speed is already $397\ \mu\text{m s}^{-1}$). Also, each movement of the particle induces a risk to trap dirt or another particle.

3.6.2. Power Spectral Density (PSD) analysis

Due to these disadvantages, a calibration method that does not require the bead to be moved is desired. Fortunately, every trapped particle is subject to Brownian motion (in a harmonic potential) as described earlier in section 3.3.5. We can use the distinct power spectrum of this noise to perform a calibration without moving the particle.

3.6.2.1. Fourier transform

The Fourier transform converts a signal from the time domain into the angular frequency domain (with the angular frequency $\omega = 2\pi f$). It is defined as

$$\mathcal{F}(f(t)) = \hat{f}(\omega) = \int_{-\infty}^{\infty} f(t) \exp(-i\omega t) dt \quad (3.39)$$

Of course this definition is only valid for integrable functions over \mathbb{R} . For measured signals, discrete formulations are used – typically the algorithm by Cooley and Tukey⁶⁹, which is simply called a fast Fourier transform algorithm, or FFT.

Care must be taken regarding pre-factors. In typical analysis software, Fourier conversion is carried out with frequencies instead of angular frequencies, leading to an additional factor of 2π for Fourier transforms and $4\pi^2$ for power spectra. Some conventions also split this pre-factor into $\sqrt{2\pi}$ for both the Fourier transform and the inverse Fourier transform. I will not use that in this work and stick to the definition as stated above, occasionally switching from angular frequencies to frequencies depending on the context.

As can be seen quite easily from the definition, Fourier transforms offer linearity, that is for numbers a and b and functions f and g , we have $\mathcal{F}(af(t) + bg(t)) = a\hat{f}(\omega) + b\hat{g}(\omega)$. Also, the Fourier transform of $f(t) = 1$ is $\hat{f}(\omega) = 2\pi\delta(\omega)$ with the Dirac delta function $\delta(\omega)$. We also have $\mathcal{F}(\dot{f}(t)) = i\omega\hat{f}(\omega)$.

The power spectral density (PSD) of a signal $x(t)$ is

$$S_{xx} = \langle |\hat{x}(t)|^2 \rangle \quad (3.40)$$

Additionally, the Wiener–Khinchine theorem states that the PSD of a stationary random

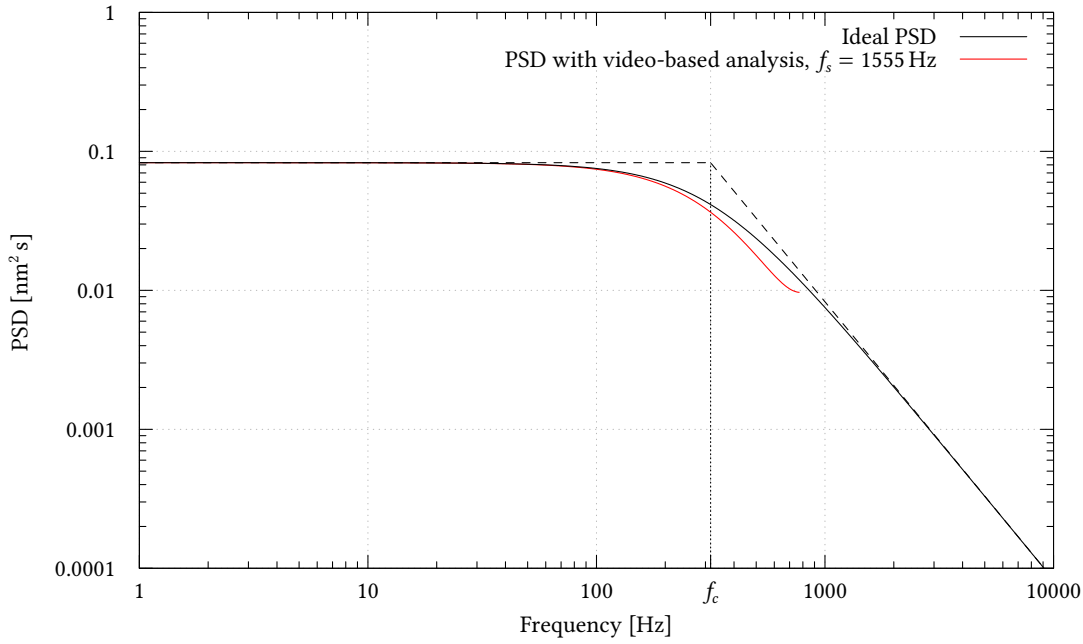


Fig. 3.11.: PSD of a $3\ \mu\text{m}$ particle in water at $25\ ^\circ\text{C}$ in an optical trap with $k = 50\ \text{pN}\ \mu\text{m}^{-1}$. The corner frequency is $f_c = k/2\pi\gamma = 316\ \text{Hz}$.

process is related to its autocorrelation function by^{70,71}

$$S_{\xi\xi} = \langle |\hat{\xi}|^2 \rangle = \int_{-\infty}^{\infty} e^{i\omega t_0} \langle \xi(t)^* \xi(t - t_0) \rangle dt \quad (3.41)$$

We can now apply these formulas to our specific problem. Our random process follows the fluctuation-dissipation theorem (eq. 2.27). Taking the Langevin equation eq. 3.35, performing a Fourier transform and squaring the absolute gives us

$$\gamma\dot{x} + kx = \xi \quad (3.42)$$

$$\gamma i\omega\hat{x} + k\hat{x} = \hat{\xi} \quad (3.43)$$

$$\hat{x} = \frac{\hat{\xi}}{\gamma i\omega + k} \quad (3.44)$$

$$S_{xx}(\omega) = |\hat{x}|^2 = \frac{S_{\xi\xi}}{\gamma^2\omega^2 + k^2} = \frac{k_B T}{\frac{1}{2}\gamma\left(\omega^2 + \frac{k^2}{\gamma^2}\right)} \quad (3.45)$$

$$S_{xx}(f) = \frac{k_B T}{2\pi^2\gamma(f^2 + f_c^2)} \quad \text{with} \quad f_c = \frac{k}{2\pi\gamma} \quad (3.46)$$

3. Optical Tweezers

For calibration, we now once more take a look at the force as given by eq. 3.38:

$$F = k\zeta(\ddot{x} - \ddot{x}_0)$$

First, we again determine \ddot{x}_0 at rest. For simplicity, let us assume $\ddot{x}_0 = 0$. We then have $F = k\zeta\ddot{x}$ and, more importantly

$$\ddot{x} = \frac{x}{\zeta} \quad (3.47)$$

We then perform a FFT and square the absolute, giving the power spectrum as:

$$S_{\ddot{x}\ddot{x}} = |\text{FFT}(\ddot{x})|^2 = \left| \mathcal{F}\left(\frac{x}{\zeta}\right) \right|^2 = \left| \frac{\hat{x}}{\zeta} \right|^2 = \frac{k_B T}{\frac{1}{2}\zeta^2\gamma\left(\omega^2 + \frac{k^2}{\gamma^2}\right)} = \frac{k_B T}{2\pi^2\zeta^2\gamma(f^2 + f_c^2)} \quad (3.48)$$

A PSD for a 3 μm particle in water at 25 $^\circ\text{C}$ in an optical trap with $k = 50 \text{ pN}\mu\text{m}^{-1}$ – all typical values – is shown in fig. 3.11. As can be seen, the PSD can be split into two parts:

$$S_{\ddot{x}\ddot{x}} = \frac{k_B T}{\frac{k^2\zeta^2}{2\gamma}} \quad \text{for } f \ll f_c \quad (3.49)$$

$$S_{\ddot{x}\ddot{x}} = \frac{k_B T}{2\pi^2\gamma\zeta^2 f^2} \quad \text{for } f \gg f_c \quad (3.50)$$

We can therefore use the behaviour for low frequencies to easily determine the factor $k\zeta$, giving us the required parameter for force conversion. To get separate values for k and ζ , we have to look at the behaviour for high frequencies.

For scattered light analysis, this method works very well and should be the preferred calibration method. However, video-based analysis has the disadvantage of a low data rate. For a data rate f_{aq} , with FFT we can only get the PSD up to $f_{aq}/2$. For our setups, this is at most 778 Hz, which does not fulfil $f \gg f_c$ in typical cases. Unfortunately, the quality of FFT is better the larger the frequency. A measured PSD is shown in fig. 3.12.

Another issue with video-based analysis is the inherent averaging caused by video cameras. Until now, we have assumed that every data point \ddot{x} is a momentarily recording of the particle position. However, a video-camera exposes every single frame. This corresponds to an averaging as long as the shutter is opened. In our case, we can assume that for a frame rate f_s , every frame / data point is an average over the duration $\tau_s = 1/f_s$. Mathematically,

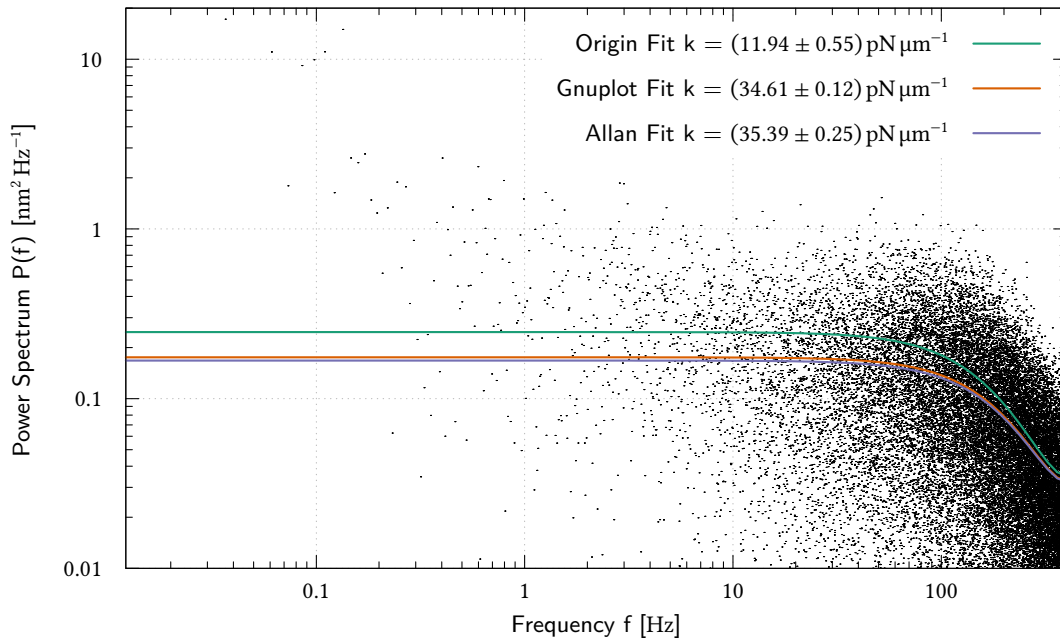


Fig. 3.12.: Measured PSD of a $3.05 \mu\text{m}$ polystyrene particle on a glass slide trapped with approx. 750 mW laser power. FFT performed by Matlab on a 82 s long data set recorded with 800 fps . Data fitted to the aliasing-corrected eq. 3.53 with both Origin and Gnuplot. Also shown is the result of Allan variance analysis on the same data set as fitted with Gnuplot

3. Optical Tweezers

this corresponds to a convolution of the signal with a boxcar function Π :

$$x_i = [x * \Pi_{\tau_s}](t_i) \quad \Pi_{\tau_s}(t) = \begin{cases} 1/\tau_s & \text{if } |t| < \tau_s/2 \\ 0 & \text{otherwise} \end{cases} \quad (3.51)$$

This convolution can be handled rather easily, since the Fourier transform of a convolution is the product of the Fourier transform of the convolution components – in this case, this simply adds a factor

$$\frac{\sin^2(\pi f \tau_s)}{(\pi f \tau_s)^2} \quad (3.52)$$

to the PSD.

However, this correction only accounts for the low-pass filtering due to the averaging. Additionally, there is an aliasing effect, which causes the PSD at frequency f to also contain contributions from the frequencies $f + n f_s$ with $n \in \mathbb{Z}^{72}$. The effects of this aliasing were calculated by Lansdorp and Saleh⁷², giving the final low-pass and aliasing corrected PSD as

$$P^*(f) = \frac{2k_B T \gamma}{k^3} \left(k + \frac{2\gamma f_s \sin^2\left(\frac{\pi f}{f_s}\right) \sinh\left(\frac{k}{\gamma f_s}\right)}{\cos\left(\frac{2\pi f}{f_s}\right) - \cosh\left(\frac{k}{\gamma f_s}\right)} \right) \quad (3.53)$$

Overall, these corrections are shown in fig. 3.11 in comparison to the uncorrected PSD. The low-frequency behaviour is still unchanged and could be used for calibration.

3.6.2.2. Allan variance

Allan variance (AV or σ_A^2) however offers an improved calibration protocol specifically for video-based analysis with optical tweezers. Originally developed by David Allan for use in atomic frequency standards, it is defined as half of the averaged squared difference between consecutive, locally averaged samples. In contrast to PSD analysis, it takes place in the time-domain, with the length of the local averaging as the independent variable:

$$\sigma_A^2(\tau) = \frac{1}{2} \left\langle (\bar{x}_{\tau,j+1} - \bar{x}_{\tau,j})^2 \right\rangle \quad \bar{x}_{\tau,j} = [x * \Pi_{\tau}](j\tau) \quad (3.54)$$

Since every frame is already a local average over time τ_s , the AV can be estimated from the measured data quite easily for averaging times $\tau = n\tau_s$ with $n \in \mathbb{N}$. For calibration, we of course need to know how the AV should look like in theory. Fortunately, Barnes et al.⁷³ have

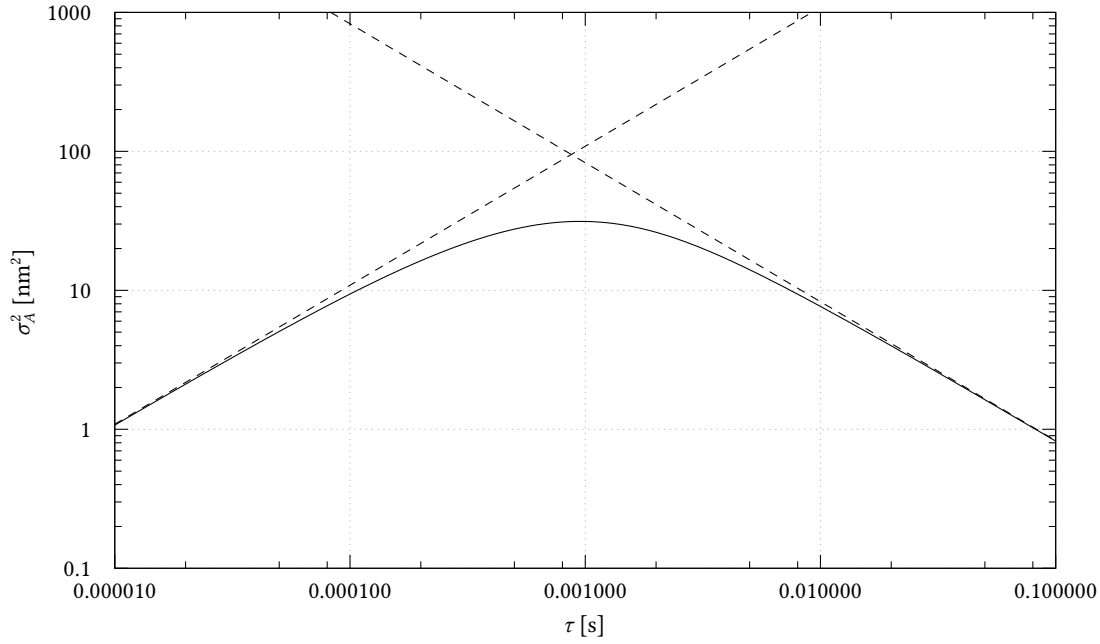


Fig. 3.13.: AV of a 3 μm particle in water at 25 $^{\circ}\text{C}$ in an optical trap with $k = 50 \text{ pN } \mu\text{m}^{-1}$.

derived the relationship between AV and PSD as: *

$$\sigma_A^2(\tau) = 2 \int_{-\infty}^{\infty} P(f) \frac{\sin^4 \pi f \tau}{(\pi f \tau)^2} df \quad (3.55)$$

This integral can be solved analytically and yields

$$\sigma_A^2(\tau) = \frac{2k_B T \gamma}{k^2 \tau} \left(1 + \frac{2\gamma}{k\tau} e^{-\frac{k\tau}{\gamma}} - \frac{\gamma}{2k\tau} e^{-\frac{2k\tau}{\gamma}} - \frac{3\gamma}{2k\tau} \right) \quad (3.56)$$

This result is illustrated in fig. 3.13. As can be seen, we again have two distinct parts for low

*We use eq (23), with $\sigma_A^2(\tau) = \langle \sigma_y^2(2, \tau, \tau) \rangle$ and thus $r = 1$ (as stated leading up to eq. (11)). The derivation of eq (23) can be found in Appendix I of the paper. Since we use the two-sided definition of the PSD (the integral goes from $-\infty$ to $+\infty$ instead of from 0 to $+\infty$) in contrast to Barnes et al.⁷³, we need to expand the integration bounds accordingly.

Comparing this equation with eq. (16) in the Lansdorp and Saleh paper⁷², they have an additional factor 2 in the integral. This factor seems to be erroneous, since it does not give their (otherwise correct) result of eq. (17).

3. Optical Tweezers

and high times, corresponding to high and low frequencies in the PSD:

$$\sigma_A^2(\tau) = \frac{2k_B T \tau}{3\gamma} \quad \text{for } \tau \ll \frac{\gamma}{k} \quad (3.57)$$

$$\sigma_A^2(\tau) = \frac{2k_B T \gamma}{k^2 \tau} \quad \text{for } \tau \gg \frac{\gamma}{k} \quad (3.58)$$

Let us now again look at the measured force as given by eq. 3.38:

$$F = k\zeta(\ddot{x} - \ddot{x}_0)$$

First, as before we determine \ddot{x}_0 at rest. For simplicity, let us again assume $\ddot{x}_0 = 0$, giving us $F = k\zeta\ddot{x}$ and

$$\ddot{x} = \frac{x}{\zeta} \quad (3.59)$$

Since the AV depends linearly on the PSD (if we ignore any components of f) and the PSD – as seen before – incorporates any pre-factors squared, we then get for the measured AV

$$\check{\sigma}_A^2(\tau) = \frac{2k_B T \gamma}{\zeta^2 k^2 \tau} \left(1 + \frac{2\gamma}{k\tau} e^{-\frac{k\tau}{\gamma}} - \frac{\gamma}{2k\tau} e^{-\frac{2k\tau}{\gamma}} - \frac{3\gamma}{2k\tau} \right) \quad (3.60)$$

For long measuring times $\tau \gg \gamma/k$, we get

$$\check{\sigma}_A^2(\tau) = \frac{2k_B T \gamma}{\zeta^2 k^2 \tau} \quad (3.61)$$

which allows us to calibrate the product $k\zeta$. Just as with PSD, we need high frequencies / low measuring times to get separate values for k and ζ .

Apart from the use for calibration, we can also use Allan variance analysis to characterise the noise and drift behaviour of our system. For more intuitive results, I use the Allan deviation $\sigma_A = \sqrt{\sigma_A^2}$ here. With the calibrated product $k\zeta$ we can easily convert the Allan deviation from arbitrary units to forces in Newton. The resulting values can be understood as an analogue to the standard deviation typical for this measurement system in the relevant time regime τ .

It should be noted that in the case for longer times, the Allan variance in terms of force becomes independent of the trap stiffness, as eq. 3.58 then becomes

$$\sigma_{A,force}^2(\tau) = \frac{2k_B T \gamma}{\tau} \quad \text{for } \tau \gg \frac{\gamma}{k} \quad (3.62)$$

4. Theory of Nanopore translocation

The theory of the translocation of biological molecules, especially DNA, through nanopores is a highly complex interplay of hydrodynamics, electrokinetics and the entropic behaviour of polymer chains. Notably, free translocation is a non-equilibrium process⁷⁴, further complicating theoretical explanation. Andreas Meyer from the Condensed Matter Theory group in Bielefeld collaborated with our group to describe the theoretical background of both free DNA translocation as well as controlled DNA translocation with optical tweezers. The results are presented in his PhD thesis⁷⁵.

Here, I will only briefly describe the structure, role and entropic behaviour of DNA as well as a simple model for the resistance of nanopores.

4.1. DNA

4.1.1. Structure and role

Deoxyribonucleic acid (DNA) is a macromolecular polymer. The monomers of the DNA are nucleotides, consisting of the sugar 2-deoxyribose with one of the nucleobases adenine (A), guanine (G), cytosine (C), or thymine (T) attached to the 1'-C atom. These *bases* are linked together by phosphate groups, forming phosphodiester bonds.

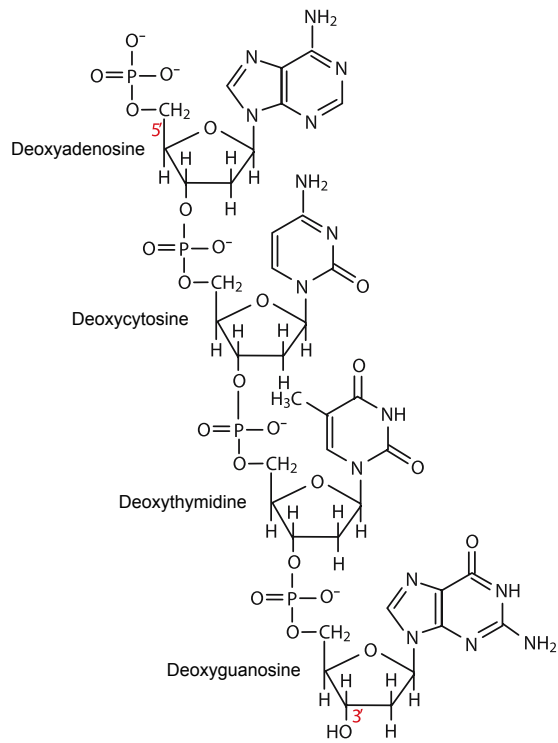
Single stranded DNA (ssDNA) therefore consists of a negatively charged phosphate backbone linking bases. This is illustrated in fig. 4.1a.

Two pairs of anti-parallel strands can form double stranded DNA (dsDNA). In physiological conditions, this forms a right-winded double helix called *B-DNA*. The phosphate backbone is on the outside. On the inside, pairs of bases are linked by hydrogen bonds. Here, A only binds to T with two hydrogen bonds and G only to C with three hydrogen bonds. The strands are therefore complements of each other. This is illustrated in fig. 4.1b

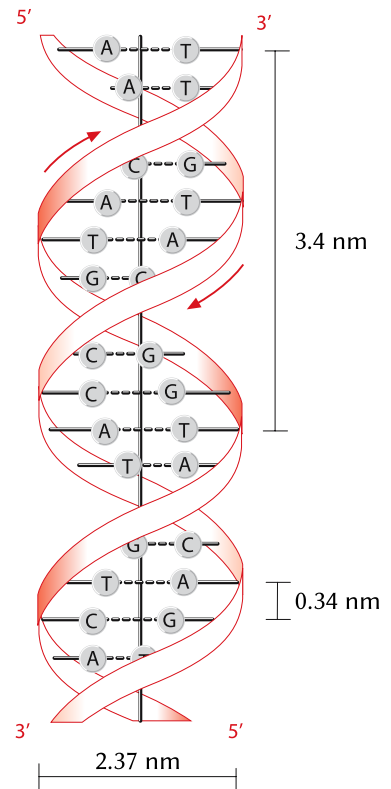
In B-DNA, the distance between neighbouring base pairs is 0.34 nm. Rotation between two pairs is 35.9°. The diameter of the helix is 2.37 nm.

The importance of DNA in biology is due to its role as the carrier of genetic information. The order of bases encodes all genetic information of a living organism. For DNA viruses, in contrast to RNA viruses, DNA also carries their genetic information. Reading out the order

4. Theory of Nanopore translocation



(a) The four bases in a single strand of DNA



(b) Double-helical structure of B-DNA

Fig. 4.1.: Components and structure of DNA, from [76]

of bases in a DNA strand is called *sequencing* of the DNA. Various methods for sequencing DNA have been developed over the years⁷⁷. Most recently, Oxford Nanopore Technologies has introduced a pore-based sequencing device which works by monitoring the electrical current during translocation through a biological nanopore^{78–83}.

4.1.2. Entropic behaviour

dsDNA is best described by the *worm like chain* (WLC) model^{84,85}. We can describe it as a flexible rod, which is characterised by the *persistence length* l_p for which there is no significant curvature. With bending stiffness κ , it is defined as

$$l_p = \frac{\kappa}{k_B T} \quad (4.1)$$

In physiological conditions, for dsDNA $l_p = (53 \pm 2)$ nm.

To describe the typical shape of a polymer molecule, we can use the mean squared end-to-end distance $\langle L^2 \rangle$. In the WLC, for a molecule with *contour length* L_0 , we can calculate

$$\langle L^2 \rangle = \int_0^{L_0} ds \int_0^{L_0} ds' \exp\left(\frac{-|s-s'|}{l_p}\right) = 2l_p L_0 - 2l_p^2 \left(1 - \exp\left(-\frac{L_0}{l_p}\right)\right) \quad (4.2)$$

To stretch a DNA molecule longer than $\langle L^2 \rangle$, we need to apply a force. To stretch it to length x with $x < L_0$, the force can be modelled as⁴⁷:

$$F(x) = \frac{k_B T}{l_p} \left(\frac{1}{4(1-x/L_0)^2} - \frac{1}{4} + \frac{x}{L_0} \right) \quad (4.3)$$

For DNA, the asymptotic force behaviour when approaching L_0 only holds partially. For forces in the range of 65 pN, the double strand instead begins to melt into two parallel single strands. This results in a large elongation without significant force increase. Once the melting has completed and we have two parallel single strands the force rises again asymptotically. Of course, at certain forces either the DNA itself ruptures, or the adhesion of DNA to the anchor, e. g. an optically trapped bead, is severed.

In this thesis, we are working with dsDNA of bacteriophage λ of *E. coli*. It has 48 502 basepairs and therefore a contour length of $L_0 = 16.5$ μm . One end of the DNA is biotinylated, allowing it to bind to streptavidin coated polystyrene beads.

4.2. Electrical resistance of nanopores

For determining the resistance of nanopores, we have to take into account two partial resistances. Assuming a buffer with specific resistance $\rho = 1/\sigma$, which is the reciprocal of the specific conductivity, a cylindrical channel with radius r and length l has a resistance of

$$R_p = \frac{\rho l}{\pi r^2} \quad (4.4)$$

However, here we are working with very small channels, namely nanopores. For these, the resistance to access the pore cannot be neglected. For each side, we have an access resistance of⁸⁶

$$R_{ac} = \frac{\rho}{4r} \quad (4.5)$$

Furthermore, we have to regard further resistivity between electrodes and nanopore. In our setup, the membrane containing the nanopore is placed on one side of a larger micropore (see fig. 6.3). Additionally, we have resistivity by the bulk medium in the channel between nanopore and electrode.

All these resistances act in series and can therefore be added. Let us therefore consider a nanopore of radius r_p in a membrane of thickness l_p at the end of a micropore with radius $r_{\mu p}$ and thickness $l_{\mu p}$. We further assume that one electrode is placed directly at the nanopore. The other electrode is placed after a channel of length l_C with cross section area A_C . Combined, this gives a total resistance of

$$R = R_p^{NP} + 2R_{ac}^{NP} + R_p^{\mu P} + 1R_{ac}^{\mu P} + R^C = \frac{\rho l_p}{\pi r_p^2} + \frac{\rho}{2r_p} + \frac{\rho l_{\mu p}}{\pi r_{\mu p}^2} + \frac{\rho}{4r_{\mu p}} + \frac{\rho l_C}{A_C} \quad (4.6)$$

For ease of future calculations, let us split off the resistances in addition to the pore:

$$R = \frac{\rho l_p}{\pi r_p^2} + \frac{\rho}{2r_p} + R_\xi \quad \text{with} \quad R_\xi = \frac{\rho l_{\mu p}}{\pi r_{\mu p}^2} + \frac{\rho}{4r_{\mu p}} + \frac{\rho l_C}{A_C} \quad (4.7)$$

For a typical setup with a 20 nm thick chip with a 1 μm pore and a 13 mm long channel with cross section $1000 \mu\text{m} \times 60 \mu\text{m}$, the additional resistance is $R_\xi = 742 \times 10^3 \text{ m}^{-1} \rho$. Comparing this to a nanopore with diameter 20 nm in a 0.67 nm thick membrane, we have $R - R_\xi = 52.1 \times 10^6 \text{ m}^{-1}$, which is two orders of magnitude higher.

5. Theory of Cell Elasticity

Cells are the building blocks of life⁸⁷. Whilst this thesis deals only with human cells, the descriptions herein can easily be generalised to at least cover the whole class of *Mammalia*, if not even to all eukaryotic organisms. Below, whenever cells are mentioned, I implicitly assume human cells.

Cells are closed vessels bounded by the cell membrane, a complex phospholipid bilayer wall that contains transmembrane protein channels as well as various other protein and lipid structures. Inside the cell, the cytoplasm contains small organised structures, called organelles. These are surrounded by cytosol, a fluid consisting of approx. 70 % water⁸⁸.

In this chapter, I will briefly describe the biological setup of a cell with emphasis on the cell membrane. I also describe the general concepts of viscoelasticity and introduce viscoelastic models, which can be used for analytical description and approximation of the viscoelastic behaviour of cells.

5.1. Setup of a cell

The typical structure of a cell is shown in fig. 5.1. As stated above, the cell is surrounded by the cell membrane. This membrane is a lipid bilayer mostly made of phospholipid, which are held together mainly by non-covalent interactions⁸⁹. The membrane not only serves to distinguish the inside from the outside of the cell.

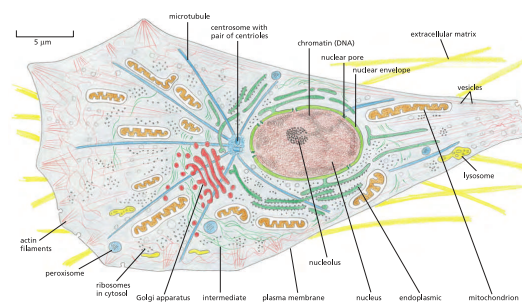


Fig. 5.1.: Structures of a typical cell, from Alberts et al.⁸⁹

5. Theory of Cell Elasticity

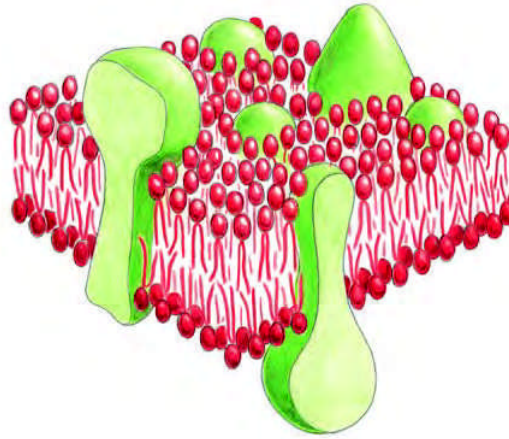


Fig. 5.2.: Structures of the cell membrane, consisting of lipid molecules (red) and protein molecules (green). From Alberts et al.⁸⁹

It also anchors membrane proteins, which in typical cells make up half the mass of the membrane. These proteins provide a wide range of functions and can be anchored in the membrane in various ways. Transmembrane proteins pass through the membrane and allow for specific transport into and out of the cell. Other proteins are placed either inside the cell or outside and are anchored to the membrane either with amphiphilic parts (replacing one layer of the lipid double layer there) or with covalently bound lipid chains. Finally, some membrane proteins do not directly interact with the membrane but instead bind non-covalently to other directly membrane-bound proteins.

Within the cell, the structure is stabilised by a system of filaments called the cytoskeleton. Briefly, the three major types of filaments are Actin filaments responsible for the overall cell shape and movement of the cell, Microtubules which direct intracellular transport and anchor organelles, and Intermediate filaments responsible for mechanical strength.

The remaining volume in the cell is typically occupied half by various organelles and half by the cytosol, which as stated above consists of approx. 70 % water⁸⁸ and 30 % proteins. This high protein concentration also has significant impact on the viscosity of the cytosol, which is typically much higher than that of water^{88,90,91}.

5.2. Viscoelasticity

Most materials exhibit both elastic and viscous properties. Viscoelasticity is the study of these materials with a special interest in solid mechanics⁹². As we have seen, a cell consists of both mainly elastic parts (such as the membrane and the cytoskeleton) and mainly viscous parts (such as the cytoplasm). Therefore, a cell cannot be described in term of purely elastic or purely viscous behaviour. Instead, we need to utilize viscoelastic descriptions.

In three dimensions, the mathematical description of viscoelastic processes can quickly become quite complicated due to the multitude of directions that external strain can apply and cause internal stress.

For simplicity, here we will assume the special 1D uniaxial normal stress case. That means that forces and displacements are only acting along one axis; we will not encounter any shear-forces. Furthermore, we will assume a homogeneous isotropic material. Of course, as we have seen above, a cell is far from homogenous. However, we will use viscoelastic models to incorporate the distinct properties of the various parts of the cell, most importantly of the cell membrane and the intracellular matrix.

5.2.1. Stress and Strain

Normal stress σ is the average tensile force applied on an object divided by the normal (orthogonal) cross-section:

$$\sigma = \frac{F}{A} \quad (5.1)$$

σ is positive if the applied forces are tensile, i. e. they are pointing outside of the object. If the forces are compressing the object, σ is negative. The unit of stress is that of a pressure. The cross-section A is always determined under zero load.

The strain ε of an object is the relative change of length:

$$\varepsilon = \frac{\Delta L}{L_0} = \frac{L - L_0}{L_0} \quad (5.2)$$

As with stress, the strain is positive if the object is elongated and negative if it is shortened.

5.3. Viscoelastic models

A few different models are commonly used to describe the behaviour of viscoelastic materials, which I will describe here.

⁹²The study of primarily fluid viscoelastic materials is commonly called rheology


5. Theory of Cell Elasticity

5.3.1. Purely elastic behaviour (spring)

For purely elastic behaviour, a formula similar to Hooke's Law is used:

$$\sigma = E\varepsilon \quad (5.3)$$

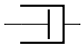
with Young's modulus E ⁹³.

For simplicity, let us call the purely elastic element a *spring*. In model diagrams, we will draw it as .

5.3.2. Purely viscous behaviour (dashpot)

For purely viscous behaviour, stress only occurs during changes of the strain. This is similar to Stoke's law:

$$\sigma = \eta\dot{\varepsilon} \quad (5.4)$$

For simplicity, we will call the purely viscous element a *dashpot* and draw it as .

5.3.3. Series and parallel behaviour

To describe viscoelastic materials, we need to combine the purely elastic and purely viscous behaviour. This can be represented by multiple purely viscous or elastic elements that are connected in series or parallel. Let us name the stress applied to each individual element σ_i and the strain for each element ε_i . Similarly, the elements are described by either E_i (for springs) or η_i (for dashpots).

In a series connection, we have

$$\sigma_s = \sigma_i \forall i \quad \varepsilon_s = \sum_i \varepsilon_i \quad (5.5)$$

Conversely, for a parallel connection we get

$$\sigma_p = \sum_i \sigma_i \quad \varepsilon_p = \varepsilon_i \forall i \quad (5.6)$$

Of course, these relations still hold true if both sides are differentiated with respect to time.

These relations allow us to derive the behaviour of multiple springs or dashpots in series or parallel:

$$E_p = \sum_i E_i \quad E_s = \left(\sum_i \frac{1}{E_i} \right)^{-1} \quad (5.7)$$

$$\eta_p = \sum_i \eta_i \quad \eta_s = \left(\sum_i \frac{1}{\eta_i} \right)^{-1} \quad (5.8)$$

As we can reduce models with purely serial or parallel springs or dashpots to a single spring or dashpot, I will not consider them true multi-element models. It should also be noted that series and parallel connections of viscoelastic elements are commutative: The series connection $(E_1 \circ \eta_1 \circ E_2 \circ \eta_2)$ is the same as $(E_1 \circ E_2 \circ \eta_1 \circ \eta_2)$ and thus as $(E_s \circ \eta_s)$. Likewise, the parallel connection $(E_1 \parallel \eta_1 \parallel E_2 \parallel \eta_2)$ is the same as $(E_1 \parallel E_2 \parallel \eta_1 \parallel \eta_2)$ and thus as $(E_p \parallel \eta_p)$. This of course also holds true with and within sub-parts of a more complex model.

Complex models involving dashpots quickly become difficult to derive using normal means. This is because each dashpot element is in fact a differential equation, from which variables need to be eliminated. Therefore, let us utilise the Laplace transform⁹⁴:

$$\mathcal{L}\{f\}(s) = \bar{f}(s) = \int_0^{\infty} f(t) e^{-st} dt \quad s \in \mathbb{C} \quad (5.9)$$

This transform has the major advantage that differentiation as well as integration are transformed to multiplication and division, respectively. The most important properties that we are exploiting are:

$f(t)$	$\bar{f}(s)$
$af(t) + bg(t)$	$a\bar{f}(s) + b\bar{g}(s)$
$\dot{f}(t)$	$s\bar{f}(s) - f(0)^*$
$c, c \in \mathbb{C}$	c/s

*In the context of Laplace transforms, $f(0)$ refers to $\lim_{x \rightarrow 0^-} f(x)$, that is $f(x)$ if x approaches 0 from the negative side. In the following, we will further assume $f(0) = 0$. As our functions are stress and strain, this corresponds to the completely relaxed starting condition

5.3.4. Multi-element models

The simplest viscoelastic models consist of two elements: a spring and a dashpot. The series configuration is called the *Maxwell model*, whilst the parallel configuration is the *Kelvin-Voigt model*.

5.3.4.1. Maxwell model

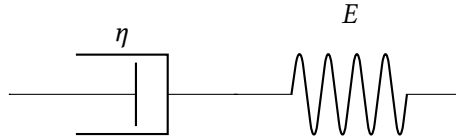


Fig. 5.3.: Maxwell model

The equations governing the Maxwell model (see fig. 5.3) are:

$$\sigma_1 = E\varepsilon_1 \quad (5.10)$$

$$\sigma_2 = \eta\dot{\varepsilon}_2 \quad (5.11)$$

$$\sigma = \sigma_1 = \sigma_2 \quad (5.12)$$

$$\varepsilon = \varepsilon_1 + \varepsilon_2 \quad (5.13)$$

Performing a Laplace transform provides

$$\bar{\sigma}_1 = E\bar{\varepsilon}_1 \quad (5.14)$$

$$\bar{\sigma}_2 = \eta s\bar{\varepsilon}_2 \quad (5.15)$$

$$\bar{\sigma} = \bar{\sigma}_1 = \bar{\sigma}_2 \quad (5.16)$$

$$\bar{\varepsilon} = \bar{\varepsilon}_1 + \bar{\varepsilon}_2 \quad (5.17)$$

which can be solved to

$$\eta s\bar{\varepsilon} = \frac{\eta}{E}s\bar{\sigma} + \bar{\sigma} \quad (5.18)$$

that corresponds to

$$\eta\dot{\varepsilon} = \frac{\eta}{E}\dot{\sigma} + \sigma \quad (5.19)$$

Obviously, applying a constant stress σ to the Maxwell model creates a linearly increasing strain ε . As a direct consequence, the deformation is non-reversible. This *creep* behaviour might be reasonable for liquids but is definitely not correct for solids and solid-like objects.

As the wall of a cell is a fixed lipid membrane, this model does not correctly describe the behaviour of cells.

5.3.4.2. Kelvin-Voigt model

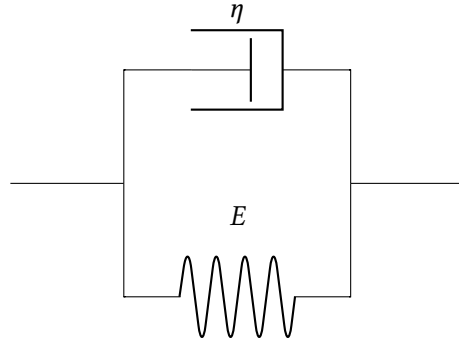


Fig. 5.4.: Kelvin-Voigt model

Similarly to eq. 5.10 to 5.13, the Kelvin-Voigt model (see fig. 5.4) is governed by these equations:

$$\sigma_1 = E\varepsilon_1 \quad (5.20)$$

$$\sigma_2 = \eta\dot{\varepsilon}_2 \quad (5.21)$$

$$\sigma = \sigma_1 + \sigma_2 \quad (5.22)$$

$$\varepsilon = \varepsilon_1 = \varepsilon_2 \quad (5.23)$$

which solves to

$$\sigma = E\varepsilon + \eta\dot{\varepsilon} \quad (5.24)$$

The corresponding creep behaviour is reversible and decays exponentially, which is quite realistic for a solid. However, expanding or compressing the Kelvin-Voigt model (i.e. $\dot{\varepsilon} \neq 0$) leads to sudden stress peaks which are not observed in real materials. Therefore, we need to further expand our model.

5.3.4.3. Zener-Kelvin model

The Zener-Kelvin model is a series connection of a Kelvin-Voigt model with an additional spring (see fig. 5.5). We can therefore use the result for the Kelvin-Voigt model (eq. 5.24) in

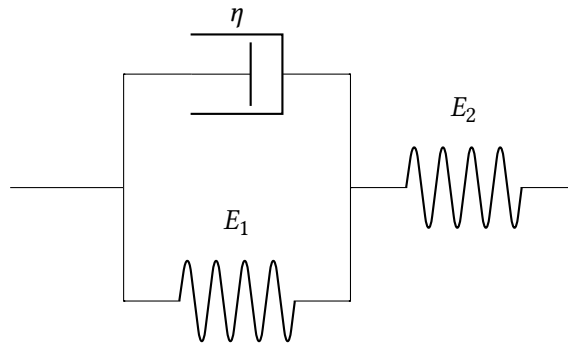


Fig. 5.5.: Zener-Kelvin model

the governing equations:

$$\sigma_1 = E_1 \varepsilon_1 + \eta \dot{\varepsilon}_1 \quad (5.25)$$

$$\sigma_2 = E_2 \varepsilon_2 \quad (5.26)$$

$$\sigma = \sigma_1 = \sigma_2 \quad (5.27)$$

$$\varepsilon = \varepsilon_1 + \varepsilon_2 \quad (5.28)$$

Again utilizing the Laplace transform, we can quite easily solve this to get

$$\sigma + \frac{\eta}{E_1 + E_2} \dot{\sigma} = \frac{E_1 E_2}{E_1 + E_2} \varepsilon + \frac{E_2 \eta}{E_1 + E_2} \dot{\varepsilon} \quad (5.29)$$

As we can see from the differential equation, the issue of the Kelvin-Voigt model regarding $\dot{\varepsilon} \neq 0$ has been addressed by the additional spring E_2 . It is therefore the simplest possible viscoelastic model to sufficiently describe solid-like viscoelastic materials.

5.3.4.4. Generalised model

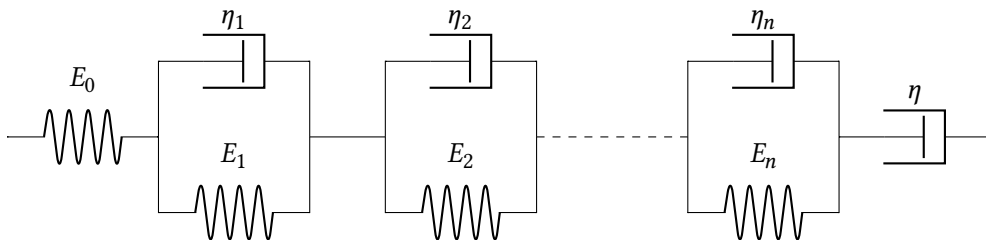


Fig. 5.6.: One possible representation of a generalised model

As an arbitrary number of models are possible and to simplify fitting routines for later, it could be useful to consider a generalised viscoelastic model. We might simply expand the Zener-Kelvin model into a more generalised model as shown in fig. 5.6. However, this is but one possibility.

The general solution to such a model will be a differential equation of arbitrary order (depending on the model). As we are only interested in the behaviour and not in the model representation per se, we can use generalised factors:

$$p_0\sigma + p_1\dot{\sigma} + p_2\ddot{\sigma} + p_3\ddot{\sigma} + \dots = q_0\varepsilon + q_1\dot{\varepsilon} + q_2\ddot{\varepsilon} + q_3\ddot{\varepsilon} + \dots \quad (5.30)$$

We can also write this in the shorthand notation

$$\hat{P}\sigma = \hat{Q}\varepsilon \quad \text{with } \hat{P} = \sum_{i=0}^n p_i \frac{\partial^i}{\partial t^i}, \quad \hat{Q} = \sum_{i=0}^n q_i \frac{\partial^i}{\partial t^i} \quad (5.31)$$

Usually, we also normalise the system by setting $p_0 = 1$. In this case, the units are $[p_i] = \text{s}^i$ and $[q_i] = \text{Pa} \cdot \text{s}^i$.

5.4. Experimental determination of viscoelastic parameters

Once we have selected a viscoelastic model, we need to determine the model parameters experimentally. We cannot use most special apparatus designed to determine the viscoelastic properties as they do not respect the requirements of viable biological samples^{95–97}.

For biological samples, only four ways to determine viscoelastic properties are commonly used. These are the creep recovery test, the stress relaxation test, oscillatory analysis methods involving the complex modulus, and a general method for arbitrary stimuli via numerical solutions to the differential equation.

5.4.1. Creep recovery test

The creep-recovery test analyses the strain behaviour when a constant stress is applied and released. The stress σ_0 is applied at time t_0 and released at t_1 .

The difficulty of this test lies in applying a *constant stress instantaneously*. The instantaneous application of the stress is not strictly necessary as a linear application with well-known loading rate can also be accounted for. However, most methods of applying stress in a microfluidic environment required for viable biological samples rely on force-clamping for this. That means that the apparatus constantly adjusts the applied force / stress to reach the target value via a feedback loop. This inevitably introduces perturbations on the time-scale

5. Theory of Cell Elasticity

of the feedback loop.

Additionally, only observing relaxation behaviour might not give a complete picture of the viscoelastic properties of the observed object. Especially for discerning the validity of different models, relaxation behaviour alone does not provide sufficient data.

5.4.2. Stress relaxation test

Similarly to the creep recovery test, in the stress relaxation test a constant *strain* ε_0 is applied and the stress response is monitored.

As with the creep recovery test, we are only observing relaxation behaviour which might not provide enough data.

5.4.3. Oscillatory analysis

Let us now assume that an oscillatory strain $\varepsilon(t) = \varepsilon_0 e^{i\omega t}$ is applied. Let us further assume that the stress response is also oscillatory, of form $\sigma(t) = \sigma_0 e^{i\omega t + \delta}$, that is phase-shifted by δ . We can now simply express the stress-strain relationship with the complex Young's modulus E^* :

$$\sigma(t) = E^* \varepsilon(t) = \varepsilon_0 E^* e^{i\omega t} \quad (5.32)$$

In fact, a relationship between E^* and the generalised parameters p_i and q_i can be shown⁹⁴ as:

$$E^* = \frac{\sum_{j=0}^n q_j \cdot (i\omega)^j}{\sum_{j=0}^n p_j \cdot (i\omega)^j} \quad (5.33)$$

Obviously, E^* is frequency dependent. Measuring it at multiple frequencies (ideally over a wide range of magnitudes) then allows to recover the constituting parameters p_i and q_i up to whichever order is required to accurately describe the observed system.

It is also interesting to note the complex composition of E^* . Usually, the real and complex components are denoted as the *storage modulus* $E' = \Re(E^*)$ and the *loss modulus* $E'' = \Im(E^*)$ (that is, $E^* = E' + iE''$). If we take a look at the work done on the system during one cycle (which is lost to internal friction and ultimately heat as we return to the exact starting conditions), we get⁹⁴

$$\Delta W = \oint \sigma d\varepsilon = \int_0^{2\pi/\omega} \sigma \dot{\varepsilon} dt = \pi \varepsilon_0^2 E'' \quad (5.34)$$

Whilst oscillatory analysis allows for a detailed analysis of the the viscoelasticity of a sample with quite basic computational demands, it requires strict adherence to the sinusoid oscillation. This is for example the case in AFM measurements in tapping mode^{98,99}. In cases

where this is not possible, such as with our optical tweezers setup, other methods must be used.

5.4.4. General method

A much more general approach to viscoelasticity analysis is to perform a priori arbitrary actions on the sample. Since both stress σ and strain ε are recorded, they can be derived numerically*. This can then be used to fit the parameters either of the governing model chosen, or of the generalised factors p_i and q_i up to the order desired.

By performing a multitude of actions (ideally both with positive and negative stress and/or strain) over a variety of loading rates (ideally over a wide range of magnitudes as with the oscillatory analysis), a solid base for parameter fitting can be obtained.

However, a few practical issues arise. First, the derivatives of σ and ε are not independent, which should be respected in a fit. Additionally, the data has to be derived numerically, which can be done using central finite differences with coefficients given e. g. by Fornberg [100]. Even for completely noise-free data, this is usually not practical beyond the first few orders, limiting the order of the generalised model that can be used. For more noise-intensive data, either smoothing of the data prior to differentiation can be performed or a higher order of accuracy is used. In both cases, time resolution is invariably lost.

In this thesis, I am using optically trapped particles as handles on a cell. The spacing between the particles and therefore the strain ε is rather well known and only subject to minor noise (due to corrections for the trap stiffness, if we want to correct for that prior to analysis). However, the force and therefore the stress σ are subject to non-negligible noise. Therefore, my approach is different:

I calculate ε , $\dot{\varepsilon}$ and σ from the available data. I also limit the model to a first-order differential equation for σ . This implies that I treat ε and $\dot{\varepsilon}$ as independent functions of time that only act as (time-dependent) quasi-constants. Then, I solve the governing differential equation numerically. This numerical solution, let us call it $\hat{\sigma}$, is of course subject to parameters. I am fitting the numerical solution $\hat{\sigma}$ to the measured data set σ , optimising the parameters as usual with the Levenberg-Marquardt least-squares fitting routine^{101,102} included in Gnuplot¹⁰³. Of course, during fitting the numerical solution is performed once per fitting iteration. This process is quite slow but produces better results than achievable by numerically differentiating σ .

The numerical solution of the differential equation can be performed in a few ways. Here,

*I am assuming that there is no practical way to get these derivations experimentally. If, for some specific setup, derivatives are experimentally accessible, they should of course be used and a few of the following limitations might not apply.

5. Theory of Cell Elasticity

I use the Runge-Kutta method^{104,105} *RK4*.

Generally, the *RK4* algorithm for solving the initial value problem $\dot{y} = f(t, y)$ with initial condition $y(t_0) = y_0$ is:

$$t_{n+1} = t_n + h \quad (5.35)$$

$$k_1 = f(t_n, y_n) \quad (5.36)$$

$$k_2 = f(t_n + h/2, y_n + hk_1/2) \quad (5.37)$$

$$k_3 = f(t_n + h/2, y_n + hk_2/2) \quad (5.38)$$

$$k_4 = f(t_n + h, y_n + hk_3) \quad (5.39)$$

$$y_{n+1} = y_n + h/6 (k_1 + 2k_2 + 2k_3 + k_4) \quad (5.40)$$

In our case, we are solving for σ with

$$\dot{\sigma} = \frac{E_1 + E_2}{\eta} \left(\frac{E_1 E_2}{E_1 + E_2} \varepsilon + \frac{E_2 \eta}{E_1 + E_2} \dot{\varepsilon} - \sigma \right) \quad (5.41)$$

for the Zener-Kelvin model, or

$$\dot{\sigma} = \frac{1}{p_1} (q_0 \varepsilon + q_1 \dot{\varepsilon} - p_0 \sigma) \quad (5.42)$$

Part II.

DNA translocation through nanopores in boron nitride and molybdenum disulfide

6. Experimental setup

The experimental setup for this part is based on the setup used for my Bachelor⁵ and Master⁶ thesis. It was also described in multiple papers^{4,51}. Compared to my Master thesis, the polarising beam splitter with the analogue, backscattered light based detector has been removed. Also, the diode-pumped solid state laser lost a lot of power due to ageing and was replaced with a 2 W fibre laser. Most significantly however, the measurement camera was exchanged for a much faster sCMOS camera.

6.1. Optical setup

The setup is based on an Axiovert 100 microscope (Carl Zeiss, Germany) with a 60× water immersion trapping objective (UPL-APO60W/IR, Olympus, Japan).

Until 2018, a diode pumped Nd:YAG laser (LCS-DTL-322-1000¹⁰⁶, Laser 2000, Germany; 1064 nm, 1000 mW, linear polarised TEM₀₀, full divergence angle 1.6 mrad, beam diameter (1.2 ± 0.1) mm) with a long-pass filter and beam expander was used. The telescopic beam-expander increased the diameter of the beam to approx. 9 mm⁵¹, overfilling the back aperture of the objective for tighter focussing (compare to section 3.2.2 and fig. 3.2).

In 2018, I noticed a significantly reduced trapping power and trap stability compared to earlier measurements. Careful analysis revealed a remarkable loss in laser intensity: Setting the desired laser power to 750 mW (typical for our experiments) resulted in a measured laser power (directly behind the long-pass filter, measured with a FieldMate PS10Q, Coherent, USA) of approx. 170 mW. Therefore, I replaced the laser with a Ytterbium doped fibre laser (Faserlasermodule 1060nm 2W Yb-1x33 V1.0, Fibotec Fiberoptics, Germany; 1060 nm, 2 W, non-polarising fibre, collimated output of 9 mm wide beam via 12 mm wide pigtail) with the kind assistance of Dr. Andy Sischka, who constructed an adapter for easy incorporation of the pigtail adapter into the setup. This updated setup is shown in fig. 6.1.

The laser light then passes a central obstruction filter. This is essentially a 1.1 mm wide circular gold layer sputtered on an optical window with a 0.4 mm edge⁵¹. This transforms the TEM₀₀ beam into a TEM₀₁^{*}-like intensity profile for increased axial trapping performance (see section 3.3.3).

6. Experimental setup

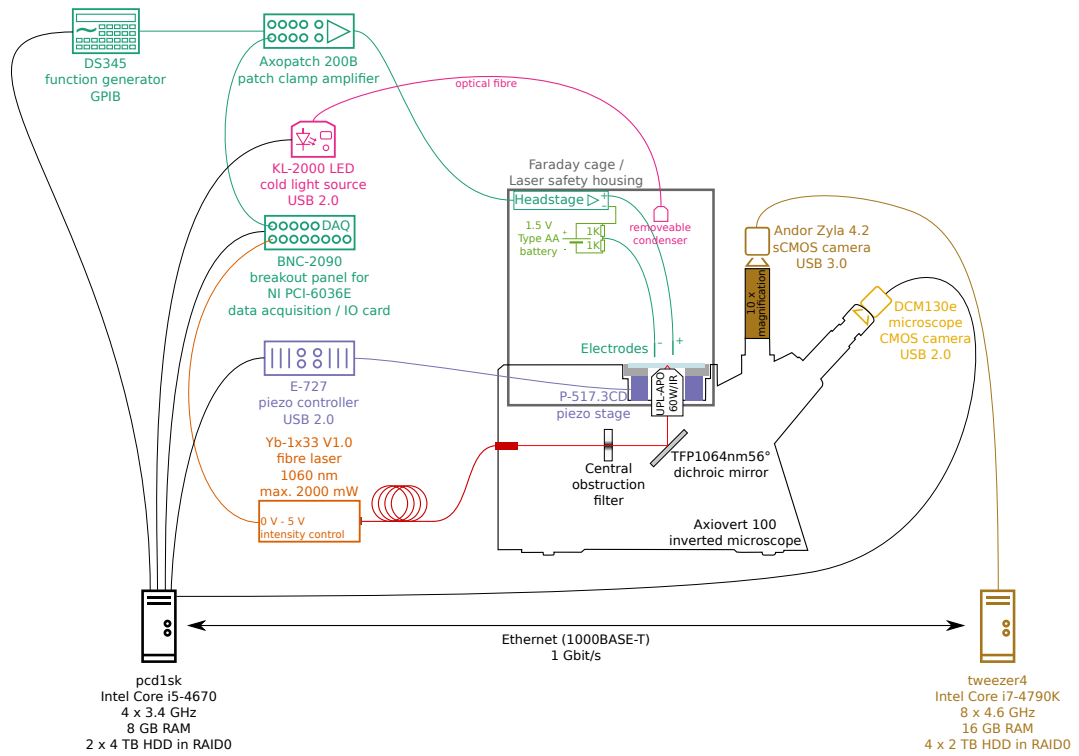


Fig. 6.1.: Schematic setup of the optical tweezers system

It then passes a quarter-wave plate, which is not used in this setup. Then, a dichroic mirror (TFP1064nm56°, Laseroptik, Germany) reflects the trapping light towards to objective, whilst letting the illumination light pass through.

Illumination is performed with a KL-2000 LED cold light source (Schott, Germany; 7×9 W high power LEDs, 1000 lm output at the end of the light guide). The image is projected both on a DCM130 microscope CMOS camera (Hangzhou ScopeTek Opto-Electric Co., Ltd., Hangzhou, Zhejiang, China), which replaces one of the two oculars, as well as through a $10\times$ post-magnification optics onto a water-cooled Zyla 4.2 USB 3.0 sCMOS camera (Andor, Belfast, Northern Ireland; $2048 \text{ px} \times 2048 \text{ px}$, 16 bit depth, 72 % QE, $0.04 \text{ e px}^{-1} \text{ s}^{-1}$ dark current, 1.6 e rms read noise).

The sCMOS (scientific Complementary Metal–Oxide–Semiconductor) sensor in the camera is essentially halved. Each sCMOS pixel converts the incoming light into a voltage (in contrast to simply collecting charges as in a CCD sensor). During readout, each column in the upper half of the chip is read-out with two AD-converters, one for high-gain and one for reduced noise, which are combined into a single value¹⁰⁷. Read-out of the pixels in each column is performed sequentially, with the pixels closer to the edge being read out first¹⁰⁷. Of course,

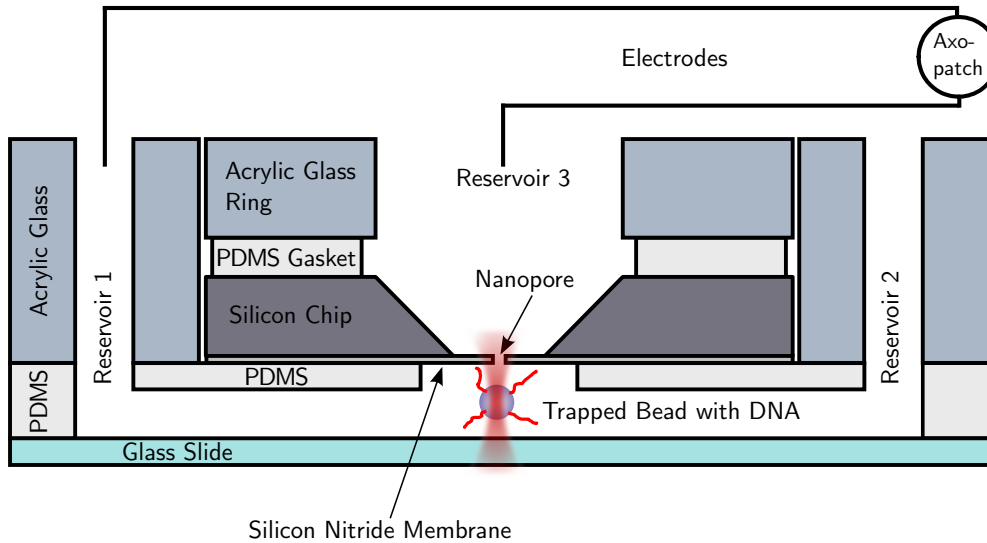


Fig. 6.2.: Overview of the sample chamber layout for nanopore experiments. The nanopore separates the top reservoir from the bottom channel, which is accessible by two reservoirs. Via electrodes, a transmembrane voltage can be applied with the Axo-patch which also measures the transmembrane current. In the channel immediately below the nanopore, beads with attached DNA are trapped to perform translocation experiments.

only the columns in the region of interest are read out, and within each column only those rows that are in the region of interest. The complete read-out hardware is replicated in the lower half of the chip, which is therefore read-out simultaneously¹⁰⁷. By vertically centring the region of interest on the sensor higher frame rates can be achieved, since each half only has to read half of the image.

The sample chamber is mounted on a P-517.3CD piezo stage (Physik Instrumente, Karlsruhe, Germany; closed loop travel range $100\ \mu\text{m} \times 100\ \mu\text{m} \times 20\ \mu\text{m}$, $1\ \text{nm}$ x/y resolution, $0.1\ \text{nm}$ z resolution) controlled by a E-727 controller (also Physik Instrumente, Karlsruhe, Germany). The piezo stage has a central aperture for the objective.

6.2. Microfluidic setup

The microfluidic setup of the sample chamber is illustrated in fig. 6.2 and fig. 6.3. For preparation, glass cover slips #1 (approx. $150\ \mu\text{m}$ thickness, size $24\ \text{mm} \times 60\ \text{mm}$) are cleaned. Microscope slides ($75\ \text{mm} \times 26\ \text{mm}$) are cleaned as well and silanised by placing them in a desiccator together with a few drops of (*Tridecafluoro-1,1,2,2-tetrahydrooctyl*)trichlorosilane (see fig. 6.4) for approx. 30 minutes. Both cover slips and silanised microscope slides are then spincoated

6. Experimental setup

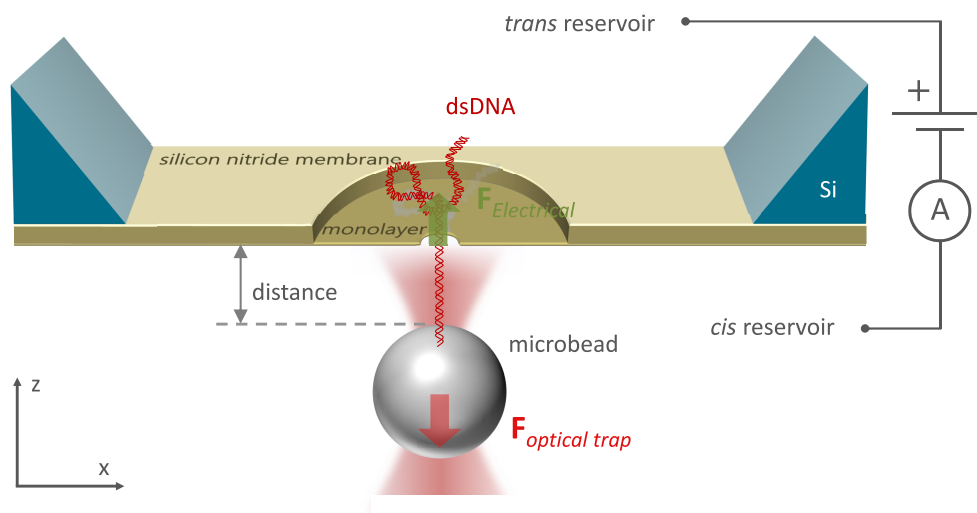


Fig. 6.3.: Detail view of the setup with a nanopore in a monolayer membrane. The monolayer membrane covers a larger hole in the silicon nitride membrane on top of a silicon chip. In the lower, *cis* reservoir, the microbead is optically trapped and attached to the (ds)DNA. The applied transmembrane voltage induces an electrical force acting on the DNA, threading it through the nanopore and pulling on the bead. This pull is counteracted by the force of the optical trap.

with approx. 40 μm thick PDMS (*poly(dimethylsiloxane)*), which is created by mixing SYLGARD 184 silicone elastomer and primer (Dow Chemical Company, Midland, Michigan, USA) in 10:1 ratio*. They are then cured in a drying oven for two hours at 85 $^{\circ}\text{C}$.

The cover slip forms the base of the microfluidic flow cell. With a scalpel, a 26 mm \times 1 mm strip is cut out of the PDMS coating and removed with tweezers. This channel forms the *cis* reservoir. From the microscope slide, a rectangle of PDMS is cut out (and not yet removed) that completely covers the channel. In the middle of that rectangle, a 1.5 mm hole is punched out. For hydrophilisation, both the cover slip with the PDMS channel and the microscope slide with the hole in the PDMS are treated in oxygen plasma for 30 s. The plasma is created

*Whenever PDMS is mentioned in this thesis without annotation, this component is used

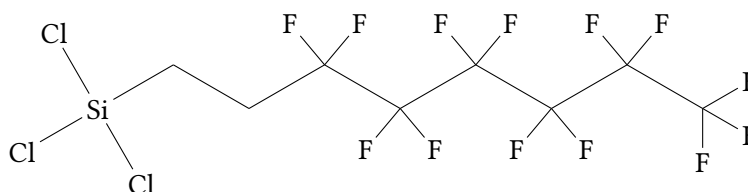


Fig. 6.4.: Chemical structure of (Tridecafluoro-1,1,2,2-tetrahydrooctyl)trichlorosilane

in a vacuum chamber initially flooded with nitrogen atmosphere, which is first reduced to 8×10^{-3} mbar with a vacuum pump and afterwards flooded with 0.1 mbar oxygen with the vacuum pump still running. In this continuous oxygen flow a plasma is ignited by applying an alternating voltage of 20 kV to 45 kV at 500 kHz.

The rectangle is then carefully lifted from the microscope slide with two pairs of tweezers and placed on the cover slip in such a way that the channel is completely covered, the hole is over the middle of the channel, and the side of the PDMS that was previously touching the silanised glass is now in contact with the PDMS on the cover slip. This provides a tight seal and positions the PDMS hole beneath the membrane and nanopore illustrated in fig. 6.2.

Finally, two 3.0 mm holes are punched through both layers of PDMS at the ends of the channel to fabricate reservoirs 1 and 2, as illustrated in fig. 6.2. Placing a large buffer droplet on the centre hole completely fills the channel due to capillary forces. This is shown in fig. 6.5a.

To prevent capillary forces from ripping the nanopore membrane apart, all further steps should be performed completely immersed in the buffer solution used for later experiments. For illustration purposes, the photos in fig. 6.5 were taken outside of the water.

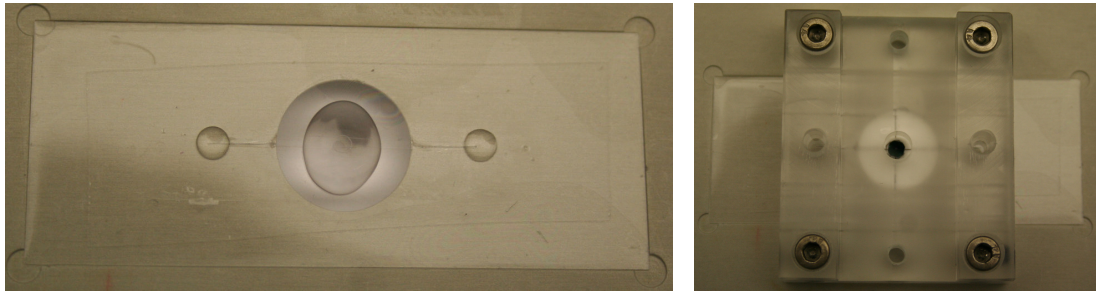
An alignment helper, sample holder and the channel are placed under buffer solution. Any air bubbles trapped in holes or on the surface are manually removed and the channel is placed in the sample holder baseplate.

The chip with the membrane is prepared as described in the next chapter. As a base chip, we use TEM sized (octagonal chips fitting into a 3 mm diameter circle) 200 μm thick silicon chips with a 50 $\mu\text{m} \times 50 \mu\text{m}$ silicon nitride membrane (Silson, Southam, Warwickshire, United Kingdom). Thickness of the membrane varied between 20 nm to 500 nm, as different batches with different parameters were used. Chips were partially provided with a pre-drilled micropore or the micropore was milled in-house with helium ion microscopy (ORION Plus helium ion microscope, Zeiss, Germany) or gallium ion microscopy (Helios NanoLab 600 DualBeam, Thermo Scientific, Hillsboro, Oregon, USA).

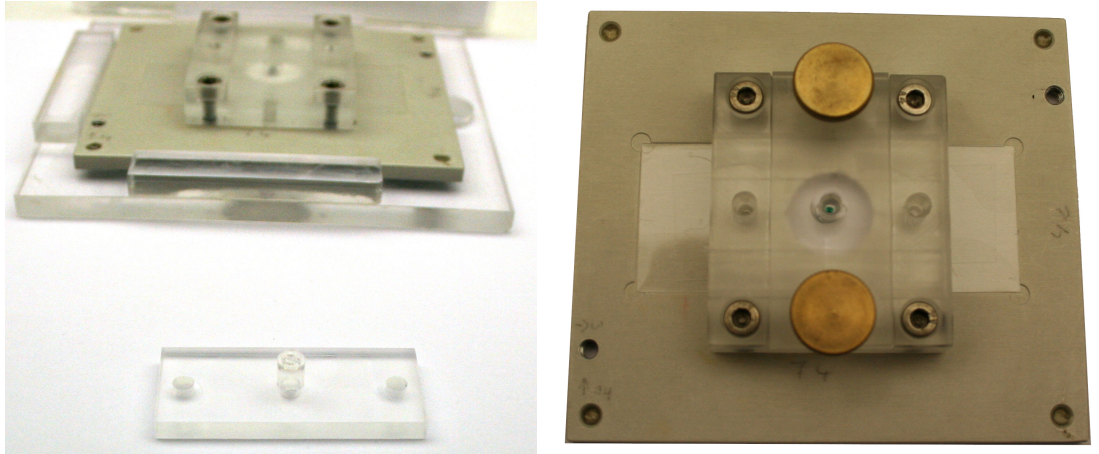
The chip containing the membrane is placed in 50 % ethanol for 30 minutes for hydrophilisation and to ensure that no air bubbles are trapped at the chip. This is also visually controlled. For ease of handling, I designed a small rectangular basin with a central channel that allows the chip to be placed over it, only supported by its edges. This way, the membrane is floating free. The channel, filled with the 50 % ethanol solution is then also placed under buffer solution. Then, the chip is carefully placed over the central hole in the cover of the *cis* channel.

Afterwards, the sample chamber is assembled by first attaching the sample holder base to the baseplate with four screws (fig. 6.5b). Then, an annular gasket is punched out of approx.

6. Experimental setup



(a) Channel filled with buffer medium placed in the baseplate (b) Channel with chip, baseplate, and sample holder base



(c) Background: The alignment helper holding the baseplate with sample holder base. Foreground: The sample holder top. (d) Completed sample ready for experiments

Fig. 6.5.: Photos of the microfluidic setup

0.6 mm thick PDMS (inner diameter 1.5 mm, outer diameter 3.0 mm). It is placed on top of the chip, making sure not to introduce air bubbles. Alternatively, it can be placed on the opening of the sample holder top, as shown in fig. 6.5c. However, when working completely immersed in buffer solution, the gasket tends to detach from the top. Therefore, it is easier to place it directly on the chip which is not moved afterwards. Finally, the sample holder top is added and screwed in place (fig. 6.5d). The PDMS on both sides of the silicon chip creates a tight seal, separating the *cis* reservoir below the chip (accessible with the two side reservoirs 1 and 2) and the *trans* reservoir above (accessible with reservoir 3).

6.3. Software

The setup is controlled by a software that I wrote in LabVIEW (National Instruments, Austin, Texas, USA) 2015 SP1. Unfortunately, there is no native support for the measurement camera in LabVIEW. However, Andor supplied their own DLL based LabVIEW driver and VIs. One of the limits of the driver is that only one frame can be requested from the camera at once. Since the camera is set up to deliver 1555 fps at a resolution of $512 \text{ px} \times 128 \text{ px}$, this means 1555 image transfers per second via the USB 3.0 interface. Whilst the bandwidth is more than sufficient (we use 204 MB s^{-1} , USB 3.0 realistically supports¹⁰⁸ 400 MB s^{-1}), the number of individual requests puts a strain on the USB subsystem of the operating system (Windows 7 Enterprise, Microsoft Corporation, Redmond, WA, USA).

In early experiments, I found that the strain on the USB subsystem is too great as e. g. the piezo controller also communicates this way. Also, whilst performing edge detection, the user interface is not very responsive. As a solution, I split the software into two parts that run on two dedicated PCs which communicate via a dedicated, private 1000BASE-T/IEEE 802.3ab¹⁰⁹ (Gigabit Ethernet over copper) network.

The detail camera is now attached to a separate, relatively powerful PC (tweezer4, Intel Core i7-4790K with four cores (eight threads) overclocked to 4.6 GHz, 16 GB DDR3-1600 memory). This PC gets the individual frames from the camera, saves them to a local hard disk array (since ordinary Gigabit Ethernet only supports transfer up to 125 MB s^{-1} , array is four 2 TB hard drives in RAID-0 mode), and performs live edge detection at a rate of 20 fps. The results of the edge detection as well as the corresponding image are then transferred over to a second, less powerful PC (pcd1sk). This PC controls all other devices (piezo stage, lighting, overview camera, Axopatch, function generator), records their respective data, and presents the user interface.

Additionally, a user-defined region of the overview image can be analysed in an autofocus-like fashion. Within that region, a straight line is searched and its strength measured. If the line is in focus (i. e. the camera is focused on the chip containing the membrane), that strength is maximal. Therefore, for calibration the z axis of the piezo stage is moved its full range (with the manual focus set in such a way that during this movement we will pass the focus) and the edge strength is recorded. Then, for the portion that is below the membrane, the function $f(z) = \frac{a}{z^c - b}$ is fitted to the strength profile and the maximum value z_{max} is stored. Afterwards, by computing the edge strength s the distance from the membrane can be approximated as

$$D = \left(\frac{a}{s} + b \right)^{\frac{1}{c}} - z_{\text{max}} \quad (6.1)$$

6. *Experimental setup*

Data is at first stored in a binary format for higher speed. Notably, video data is saved exactly as delivered from the cameras, including the metadata for the Andor Zyla camera. After the experiment, this video data is repacked into a more compact format: Each single frame is compressed lossless (PNG (portable network graphic) for the overview stream, TIFF with ZIP compression for the detail stream). To prevent a filesystem slowdown, as in the raw data 15 s are saved into one file with a separate index file that contains the timestamps and locations within the files of each individual frame.

For final analysis of the data, I developed a separate analysis tool. Here, the raw data can be read, a batch edge detection with higher quality can be performed and the forces can be calibrated. Finally, the results can be saved into a regular text file.

7. Monolayer membrane and nanopore preparation

As shown in fig. 6.3 the microfluidic setup contains a silicon chip with a silicon nitride membrane. This membrane contains a large hole that is covered by the monolayer membrane, which in turn contains the nanopore.

For experiments, there are therefore three crucial steps that need to be performed beforehand. First, the monolayer membrane needs to be manufactured. Then, the membrane has to be transferred to the chip intact. Finally, a nanopore has to be milled in the monolayer membrane.

In my Master thesis⁶ I have evaluated multiple materials regarding their suitability as a base material for ultra thin solid state membranes: Silicon nitride, graphene, carbon nanomembranes, molybdenum disulphide, molybdenum diselenide, and tungsten diselenide. To briefly summarise: Silicon nitride is quite thick. Graphene allows for atomically thin membranes but is not suitable for use with optical tweezers. Carbon nanomembranes are either too thick or do not provide a closed membrane. On the other hand, transition metal dichalcogenides are very interesting as they allow for easy manufacturing of thin and stable membranes. Molybdenum disulphide is the most prominent representative of this group of materials as it is readily available and offers a few peculiar and useful properties, as we will see below. It is therefore used in this thesis as well.

The slight disadvantage of molybdenum disulphide is the thickness of three atoms per layer. Graphene with only one atom per layer is one of the thinnest possible materials but not suitable here. However, there are graphene analogue materials available. One of them is α boron nitride, which I am investigating in this thesis as well.

This chapter will introduce these two materials and present the used techniques to create and identify monolayer membranes. In the section for molybdenum disulphide, I will also describe in depth the possible methods to transfer the membranes and mill nanopores in them.

7.1. Boron nitride

Boron nitride (BN) is a material isoelectronic to carbon¹¹⁰. Therefore, like carbon, it crystallises in two main forms: The diamond-analogue β boron nitride, and the graphite-analogue α boron nitride or hexagonal boron nitride. Here, I am only interested in the latter form.

7.1.1. Material properties

The crystal structure of α -BN is quite similar to graphite. The unit cell is $a = 2.504 \text{ \AA}$, $c = 6.6612 \text{ \AA}$ ^{111,112}, compared to $a = (2.464 \pm 0.002) \text{ \AA}$, $c = (6.711 \pm 0.004) \text{ \AA}$ for graphite^{112,113}. Similar to graphene, which is single-layer graphite¹¹⁴, single-layer boron nitride can also be prepared with the well-known mechanical exfoliation / cleavage method pioneered by Novoselov, Geim, et al.¹¹⁵. For graphene as well as for single-layer boron nitride, the layer thickness is usually considered as the interlayer distance, which is $c/2 = 3.33 \text{ \AA}$ for boron nitride and $c/2 = 3.35 \text{ \AA}$ for graphene.

Graphene is a semiconductor with zero band-gap, giving it its special electronic and optical properties. Polystyrene particles that are trapped in an optical tweezer start to rapidly melt or disintegrate when brought in the immediate vicinity of free-standing graphene⁶. Since this behaviour is only occurring for graphene membranes, I am strongly assuming that the effect is caused by this special zero-band-gap structure.

In stark contrast, boron nitride is an insulator both in bulk¹¹⁶ and as a single layer¹¹⁷ with a band gap commonly reported between 4 eV to 6 eV.

7.1.2. Exfoliation

Preparation of few and single-layer flakes is performed by mechanical exfoliation. This method was pioneered by the group of Geim and Novoselov in 2004 for graphene¹¹⁵, which was awarded with a Nobel Prize in Physics in 2010.



Fig. 7.1.: Photo of the hBN bulk material source. The bottle is approx. 1 cm diameter

The method is quite straightforward. Multi-layered flakes are peeled from a highly ordered crystal source, which are then reduced in thickness by repeated peeling. The peeling is performed mechanically with adhesive tape.

In this work, I used Nitto tape (SPV 224P, Nitto Denko, Osaka, Japan). The boron nitride bulk material source (Manchester Nanomaterials, Manchester, United Kingdom) are small crystals approx. $1 \text{ mm} \times 1 \text{ mm} \times 0.1 \text{ mm}$. Due to their size, it was not possible to just peel a single flake from the crystal and reuse it afterwards. Instead, Adhesive tape is fixed to the table surface with

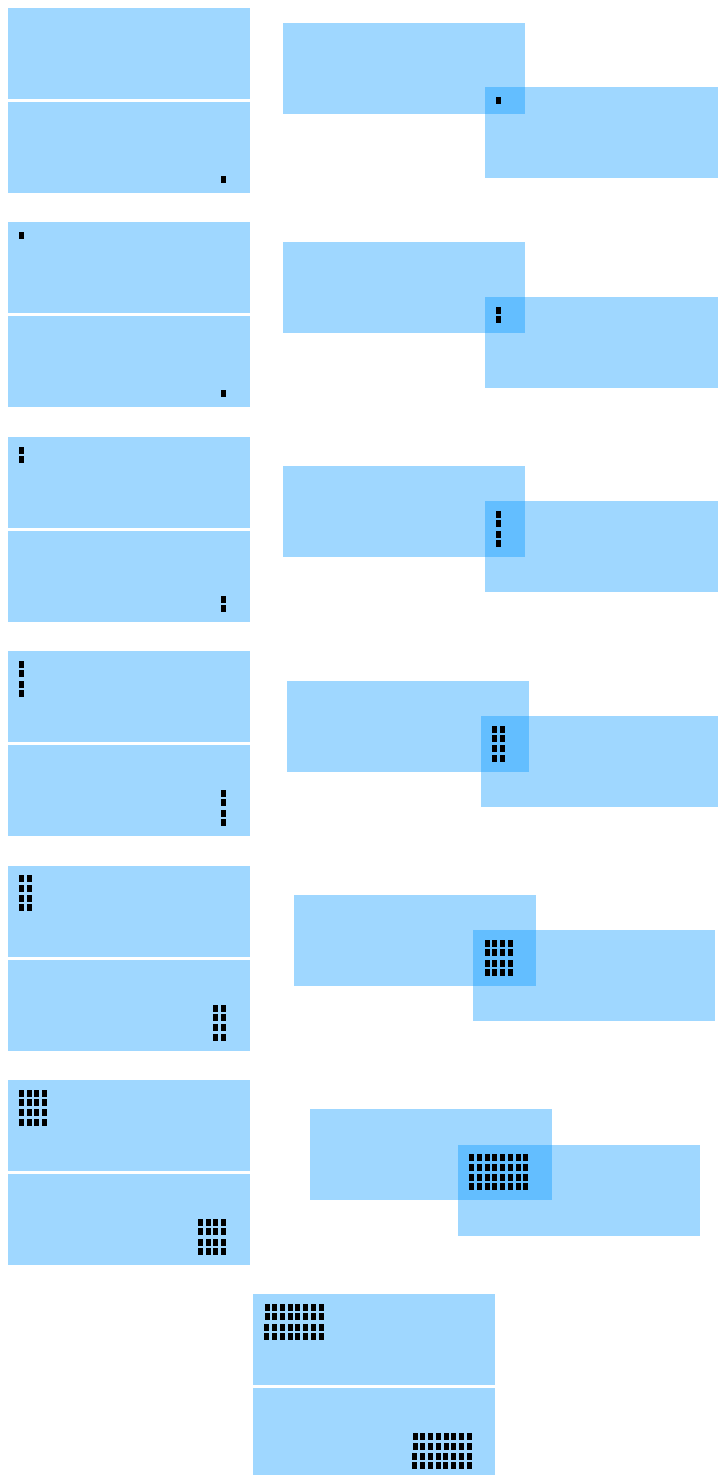


Fig. 7.2.: Illustration of the hBN master tape preparation process. Starting from a single crystal on adhesive tape, we create two tapes with a large area of flakes.

7. Monolayer membrane and nanopore preparation

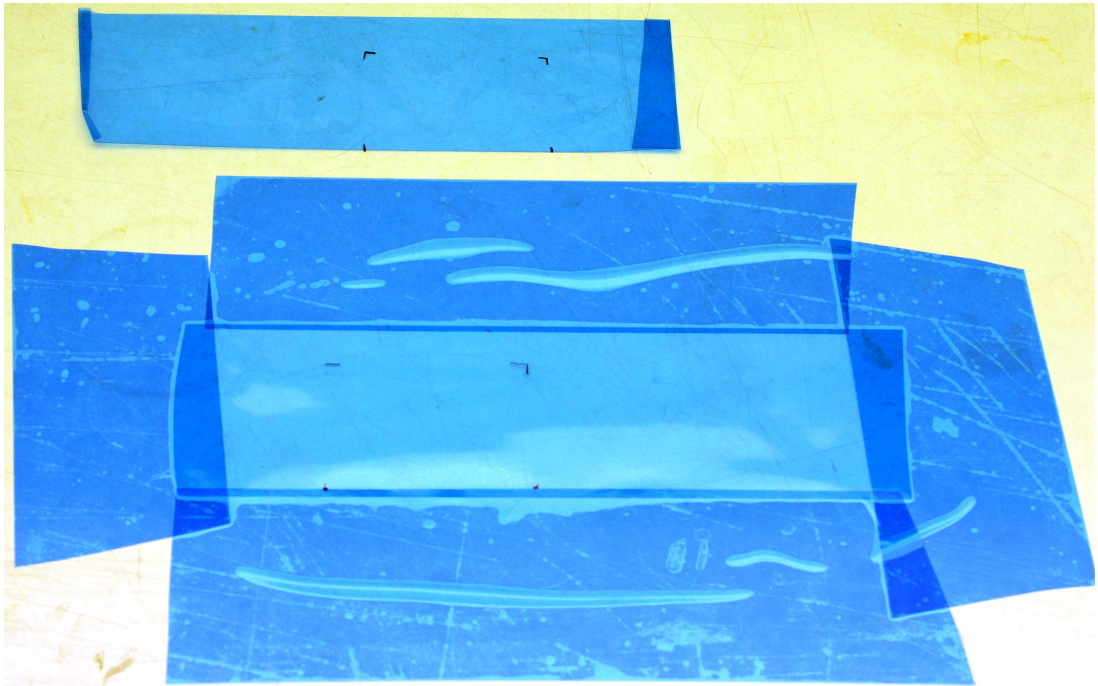


Fig. 7.3.: Photo of the hBN master tapes. The area containing flakes is marked with black brackets. Reflections of the flakes can be seen near the lower edge of the bottom master tape.

the adhesive side up. Then, the crystal is placed on the tape. A second tape is placed with its adhesive side on that crystal and peeled off again. This process is repeated with a slight offset in position, producing two flakes on each tape. This is further repeated until a single column of flakes has been formed, and then further to yield an area full of flakes. This process is illustrated in fig. 7.2. These master tapes with approx. 32 by 32 flakes each can then be used as a master for transfer onto a substrate. A pair of master tapes is shown in fig. 7.3

7.1.3. Transfer to substrate

For identification of usable few-layer and monolayer flakes, the material needs to be transferred from the master tape to a substrate. This transfer is performed by simply pressing the adhesive tape to the substrate and removing it after a few seconds. Essentially, this creates a further cleaving step.

As a substrate I have used a few different materials and material combinations in order to get the best results for transfer and monolayer identification. I have used a silicon wafer with a 90 nm silicon oxide layer, PDMS and PMMA (poly(methyl methacrylate)).

7.1.4. Monolayer identification

Identification of monolayer flakes on a silicon wafer with a uniform silicon oxide is quite straightforward. In such a structure, the white illumination is reflected on both the silicon oxide surface as well as the silicon oxide / silicon interface. The resulting white light interference essentially gives a highly thickness-sensitive colour response. When a thin layer is now added to the silicon oxide surface, the optical path length changes which also changes the colour of the reflected light. This provides a simple method for phase contrast microscopy¹¹⁸. The viability of this method for boron nitride has been shown in literature¹¹⁹.

However, for the pursued DNA translocation experiments, we require a free-standing monolayer membrane. As described before in section 6.2, we want to place the monolayer over a hole in a free-standing silicon nitride membrane on a silicon chip. Therefore, another transfer step is required. For this transfer, which will be described in detail in the next subsection, it would be advantageous to identify the monolayer on a material suitable for soft lithography, such as PDMS or PMMA.

Accordingly, I have also transferred flakes from the master tape onto various forms of PDMS: Pure, unmodified PDMS cast into petri dishes and cut into approx. 10 mm × 10 mm × 2 mm large chunks, silanised PDMS, PDMS that has been plasma-oxidised for 30 s, PDMS spin-coated on a cover slip, and PDMS spincoated on the silicon / silicon oxide wafer. Additionally, flakes were transferred onto PMMA.

7. Monolayer membrane and nanopore preparation

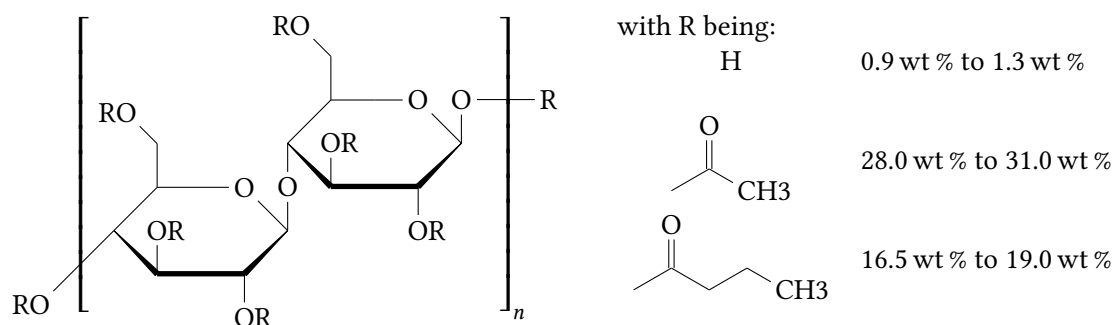


Fig. 7.4.: Chemical structure of the used cellulose acetate butyrate

Identification of potential monolayer flakes for these substrates was performed optically in an Olympus BX51 microscope (Olympus, Tokyo, Japan), which offers both transmission and reflection microscopy modes. Images were acquired to a PC with a EOS 600D (Canon, Tokyo, Japan) DSLR.

For verification of layer thickness, identified potential monolayer flakes were transferred to a freshly cleaved Mica surface and imaged in atomic force microscopy (AFM) measurements. These were performed with a Multimode 8 AFM (Bruker, Billerica, Massachusetts, USA) in tapping mode with Tap300Al-G probes (BudgetSensors, Innovative Solutions Bulgaria, Sofia, Bulgaria).

7.1.5. Transfer to membrane

In my previous works⁶, transfer of flakes to the silicon nitride membrane on a chip from a silicon wafer was performed by first coating the wafer in a cellulose polymer (3 % w/v cellulose acetate butyrate ($M_n \approx 65\,000$, structure shown in fig. 7.4; Sigma Aldrich, St. Louis, Missouri, USA) in ethyl acetate). Then, a small rectangle was cut into the polymer and it was transferred onto a water surface by wedging transfer¹²⁰. The target chip is placed under water, the polymer mechanically trapped on the surface of the water, and the chip slowly raised until contact between the polymer containing the monolayer flake and the chip containing the small hole in the silicon nitride membrane is established. After drying for 24 hours, the polymer is then removed by washing in ethyl acetate.

However, the method can still leave residues of the cellulose polymer on the chip. These residues can bond to the DNA in a translocation experiment, preventing successful translocations. Additionally, this method involves capillary forces acting on the monolayer during coating, wedging transfer, and when contacting the destination chip. These forces could also potentially introduce defects into the monolayer.

Therefore, I used a dry transfer method based on viscoelastic stamping^{121,122}, which is

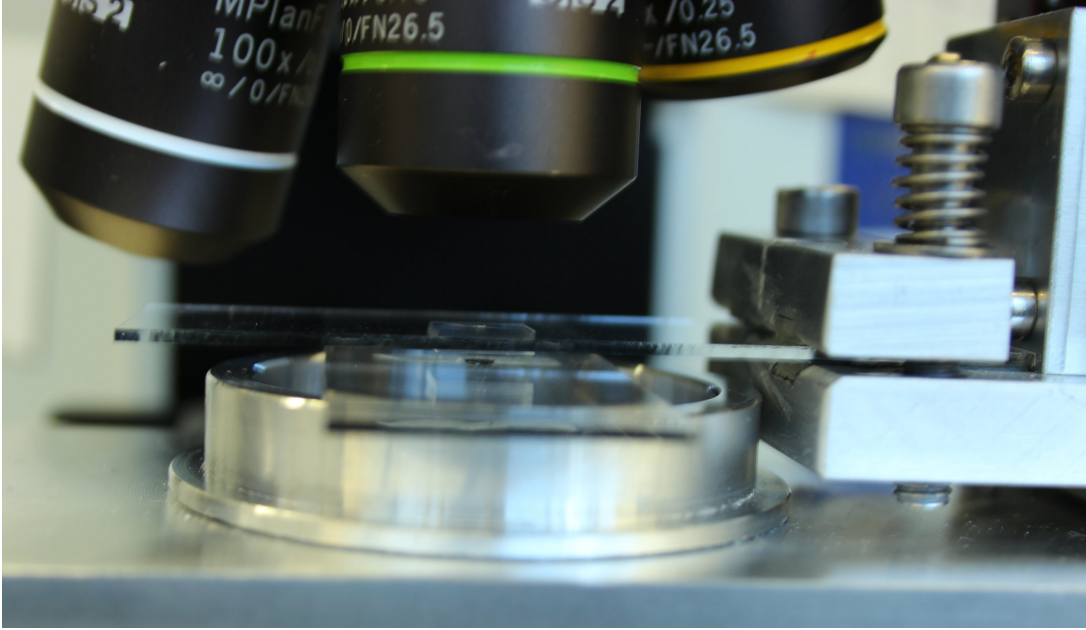


Fig. 7.5.: Setup for dry transfer method. The chip is fixated with double-sided tape on a glass slide, which is in turn fixated on the transfer apparatus. The stamp containing the monolayer flakes is adhered to another glass slide, which is mounted in a 3-axis micromanipulator. The setup is placed on a microscope to facilitate the alignment between stamp and target chip

illustrated in fig. 7.5. The PDMS or PMMA stamp containing the flakes is aligned under a microscope (here, I used the same Olympus BX51 microscope used for monolayer identification) over the target chip with two axis of the micromanipulator. Then, the stamp is lowered whilst alignment is continually checked and adjusted until contact has been established. This can be seen easily in the microscope. Then, the stamp is very slowly peeled off from the chip. Typically, the contact interface should move laterally with a speed of approx. $2\ \mu\text{m}\ \text{min}^{-1}$ during peeling.

7.2. Molybdenum disulphide

Molybdenum disulphide (MoS_2) like α -BN assumes a hexagonal structure like graphite. However, the monolayer consists in fact of three individual layers: In the hexagonal honeycomb, there is alternately a boron atom in the central layer, or there are two sulphur atoms, one each in the top and bottom layer.

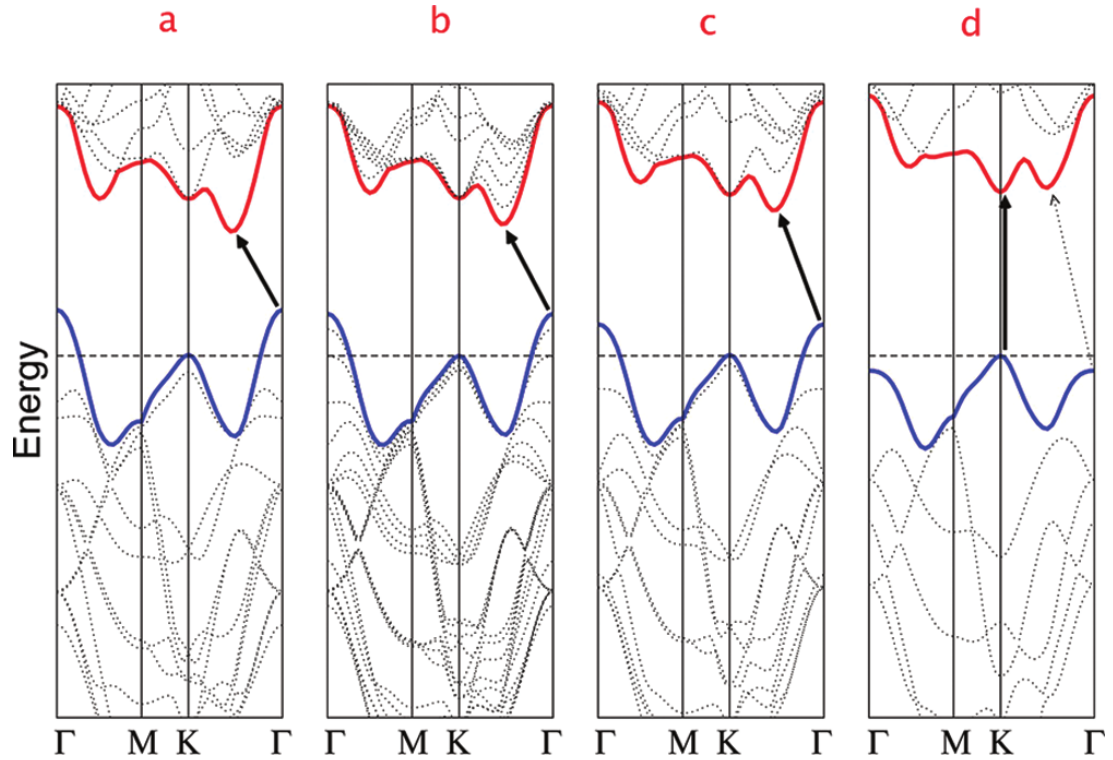


Fig. 7.6.: Calculated band structure from Splendiani et al.¹²⁷. a) bulk MoS₂ b) quadrilayer MoS₂ c) bilayer MoS₂ d) monolayer MoS₂. With thinner layers, the indirect band gap becomes larger. Eventually for the monolayer the barely changed direct excitonic transition at the K point becomes the transition with the lowest energy.

7.2.1. Material properties

The hexagonal unit cell of the crystal structure of MoS₂ is $a = 3.16 \text{ \AA}$, $c = 12.3 \text{ \AA}$ ^{123–126}. As with graphene and boron nitride, a single layer can be cleaved mechanically. As we expect from the three-layer sandwich structure, the thickness $c/2 = 6.15 \text{ \AA}$ is quite large compared to graphene and boron nitride.

Molybdenum disulphide is a semiconductor with a peculiar band gap behaviour. In bulk, molybdenum disulphide exhibits an indirect band gap of 1.29 eV ¹²⁸. However, the band gap gradually increases with decreased thickness. For the single layer material, the band gap finally becomes direct with a magnitude of 1.9 eV ^{127–129}. Notably, this leads to an increase of the photoluminescence intensity of single layer MoS₂ by three orders of magnitude compared to the double layer^{127,128}. The behaviour is illustrated in fig. 7.6 for bulk, quadrilayer, bilayer and monolayer MoS₂.

7.2.2. Exfoliation

Preparation was performed by mechanical exfoliation as well. In contrast to boron nitride, the source crystal of molybdenum disulphide (hq graphene, Groningen, The Netherlands) is large enough (approx. 10 mm × 10 mm × 3 mm) to directly peel the first flake from the bulk crystal. Then, the Nitto tape is folded back on itself and pulled apart 6-8 times.

7.2.3. Transfer to substrate

The exfoliated flakes were transferred with a final cleaving step onto a silicon wafer with a 90 nm silicon oxide layer as well as small (10 mm × 10 mm × 2 mm) pieces of unmodified PDMS. Due to the insights gained in the experiments with boron nitride, only unmodified PDMS was used for molybdenum disulphide.

7.2.4. Monolayer identification

For the initial experiments with a silicon wafer as substrate, monolayers were identified by colour contrast as described for boron nitride. Due to both the increased layer thickness and lower material transparency, identification in this way is quite straightforward. However, this method does not provide definite verification that a certain flake is indeed a monolayer and not a double layer.

For flakes on PDMS substrate, identification of *potential* monolayer flakes was done optically as well. These were marked and verified in a fluorescence microscopy setup (microscope: Axiovert 200, Zeiss, Germany; mercury lamp: HB050, Zeiss, Germany; objective: LD Achromplan 20x/0,40, Zeiss, Germany). Filters were chosen to detect the vastly increased photoluminescence of single-layer MoS₂: excitation filter: bandpass 540 nm to 552 nm, dichroic mirror: 560 nm, emission filter: longpass 620 nm.

This two-step approach of first identifying potential monolayers which are then verified was chosen due to the overall still quite low photoluminescence efficiency. Meaningful signals can only be obtained for high magnifications (40× or higher) and long exposure times (5 s per frame). Scanning a complete substrate with this method is therefore not feasible.

7.2.5. Transfer to membrane

The identified monolayers were transferred to the silicon nitride membrane on the destination chip by wet transfer (for silicon wafer substrates) as well as dry transfer (for PDMS substrates) as described for boron nitride.

7.2.6. Nanopore milling

For the milling of the nanopore, different methods can be used. On the one hand, accelerated particle based scanning microscopes are the de facto standard method for nanopore milling^{130–136}. They can offer intricate control over nanopore size, shape, and position, as well as allow imaging of the membrane and resulting pore.

On the other hand, the electrochemical breakdown method^{137–140} can be integrated into the normal experimental process and apparatus without requiring additional labour-intensive steps and expensive equipment. This method can potentially offer more control over the size of very small nanopores and has been proven to work with molybdenum disulphide monolayer membranes¹⁴⁰.

In this thesis, I am evaluating both helium ion and transmission electron microscopy (HIM & TEM). In addition to these accelerated particle based scanning microscopy techniques, I am also evaluating electrochemical breakdown as an alternative.

7.2.6.1. Helium Ion Microscopy

In previous works, I have used helium ion microscopy for both the milling of the micropores in the silicon nitride membranes as well as for the milling of nanopores. In this work, I partially use chips which already have a micrometer sized hole. For other chips, helium ion microscopy or gallium ion microscopy is used to mill this micropore. Additionally, some nanopores were milled with the helium ion microscope.

Here, I use an ORION Plus helium ion microscope (Zeiss, Germany) with activated electron flood gun to prevent surface charging of the chips during microscopy.

For nanopore milling, typical parameters are 25 kV acceleration voltage and a current of 0.5 pA to 1.0 pA. During milling, the beam is held at the target location for less than two minutes. In preparation, focussing and testing should be done on the silicon nitride membrane and not on the monolayer membrane to avoid unintended damage by the high momentum of the ions (13.7 MeV c^{-1}).

7.2.6.2. Transmission Electron Microscopy

The tendency of the helium ion microscope to damage monolayer membranes calls for another particle scanning microscopy technique.

Here, we use a JEM-2200FS field emission transmission electron microscope (JEOL, Tokyo, Japan), which can be operated with an acceleration voltage of 80 kV and 200 kV. This provides momentums of 0.3 MeV c^{-1} and 0.5 MeV c^{-1} .

Similarly to the operation of the helium ion microscope, for milling of the nanopores the beam is focussed on a single spot for a very short amount of time, typically just one second. However, imaging of the resulting pore is possible without introducing additional damage.

7.2.6.3. Electrochemical breakdown

Molybdenum disulphide is known to exhibit electrochemical behaviour such as catalytic hydrogen generation from water¹⁴¹. This can be exploited to perform electrochemical nanopore formation. When a critical voltage of at least 800 mV is applied¹⁴⁰, a nanopore starts to form from a single atom vacancy or other defect, where available. This nanopore expands as long as the applied voltage remains above the critical threshold.

As we have seen in the theoretical description of a nanopore, we can determine its size (radius r_p) by analysing the electrical resistance R :

$$R = \frac{\rho l_p}{\pi r_p^2} + \frac{\rho}{2r_p} + R_\xi \quad (7.1)$$

Here, we are already applying a voltage. Assuming the zero-point is correctly set for both voltage and current, we can estimate the resistivity by measuring the current. This in turn provides an estimate for the nanopore radius

$$r_p = \left(\frac{\rho}{4(R - R_\xi)} + \sqrt{\left(\frac{\rho}{4(R - R_\xi)} \right)^2 + \frac{\rho l_p}{\pi(R - R_\xi)}} \right) \quad (7.2)$$

with the (often negligible) contact and access resistance R_ξ , buffer solution resistivity ρ , and nanopore length $l_p = 0.67$ nm for a monolayer MoS₂ membrane.

8. Results

8.1. High-speed force detection

As a first step, let us analyse the performance of the new high-speed force detection. To this end I have optically trapped a $3.05\ \mu\text{m}$ polystyrene bead in an otherwise empty flow chamber with a chip to provide a comparable lighting situation to translocation experiments.

To achieve a frame rate of 1555 fps, the region of interest is restricted to $512\ \text{px} \times 128\ \text{px}$. A typical $3.05\ \mu\text{m}$ bead has a radius in the range of 128 px, therefore the top and bottom quarter of the bead are cut off from the image, as illustrated in fig. 8.1.

As the corner frequency is proportional to the trap stiffness, which in turn should be proportional to the laser power, a first test was performed with the laser power reduced to 250 mW. The resulting Allan deviation is shown in fig. 8.2. Due to the lower corner frequency, the non-linear area has moved towards larger times τ , which enables us to not only fit the total conversion factor ζk , but to instead fit both ζ and k individually, which also allows us to determine the maximum trapping force at which we expect a linear response, which is $0.5 R k$ (with bead radius R) as shown in fig. 3.9. Here, we get $\zeta_z = (5.76 \pm 0.08)\ \mu\text{m}$ and $k_z = (19.5 \pm 0.4)\ \mu\text{m}$.

For x and y , results for the respective Allan deviations are also shown in fig. 8.2. For an ideal system, we would expect those to overlap. In fact, as we cut off the top and bottom edge of the particle, detection accuracy in the y direction is severely limited. This is also clearly

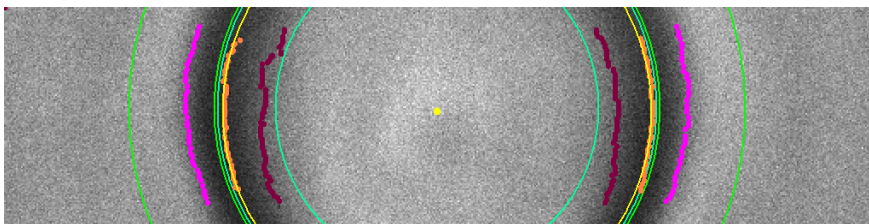


Fig. 8.1.: Detail view of an optically trapped $3.05\ \mu\text{m}$ bead with a region of interest restricted to $512\ \text{px} \times 128\ \text{px}$. Found edges and resulting circle as well as the detection regions of interest are embedded analogue to fig. 3.10

8. Results

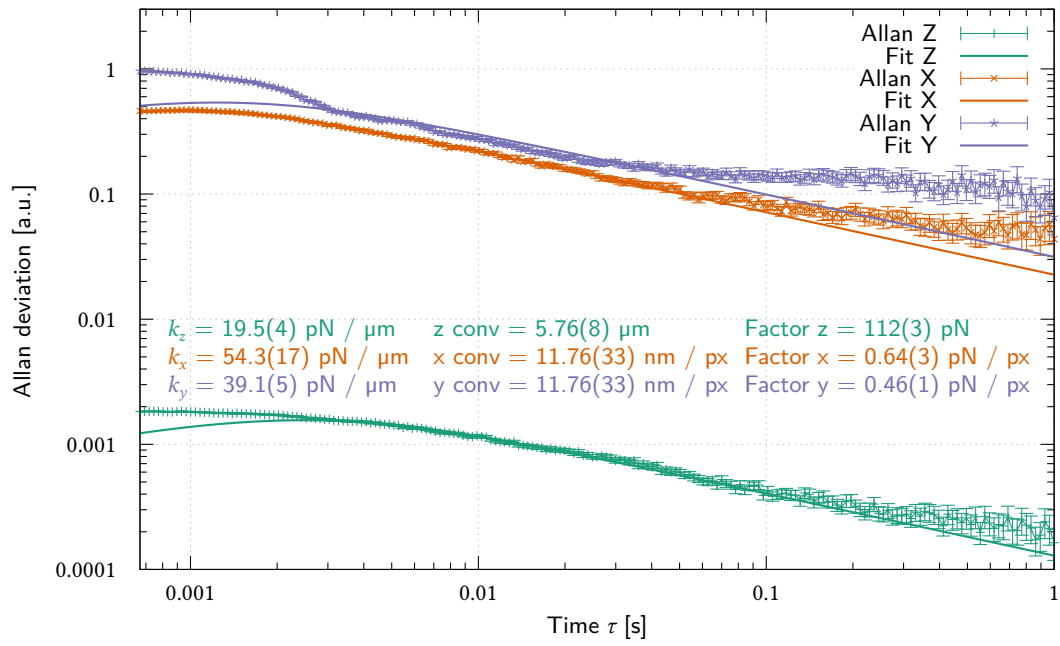


Fig. 8.2.: Allan deviation analysis of a 3.05 μm bead trapped at 250 mW

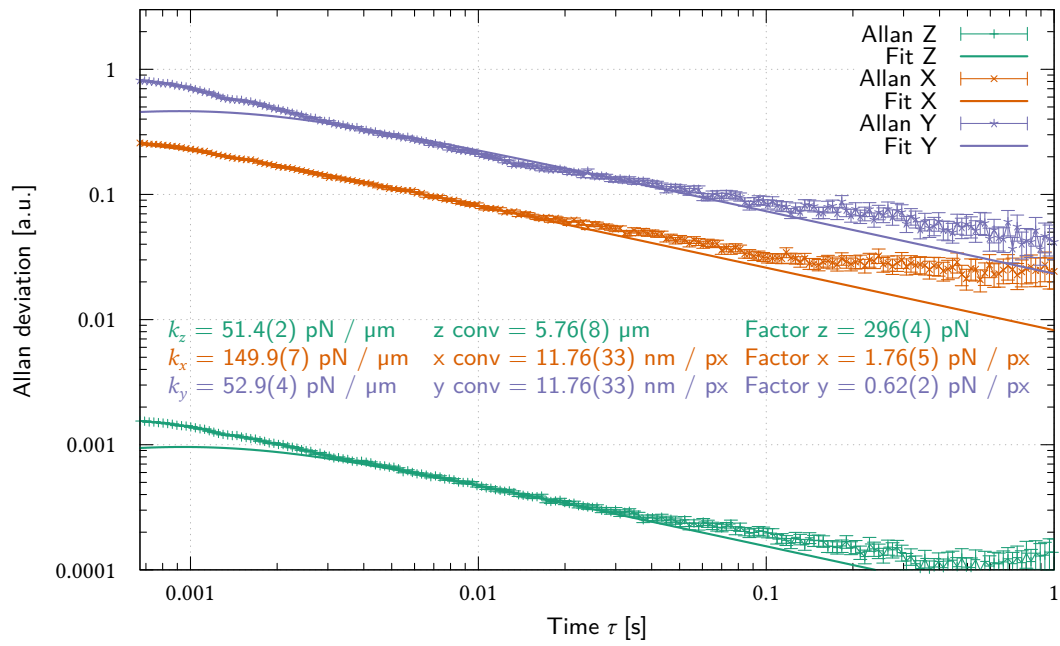


Fig. 8.3.: Allan deviation analysis of a 3.05 μm bead trapped at 750 mW

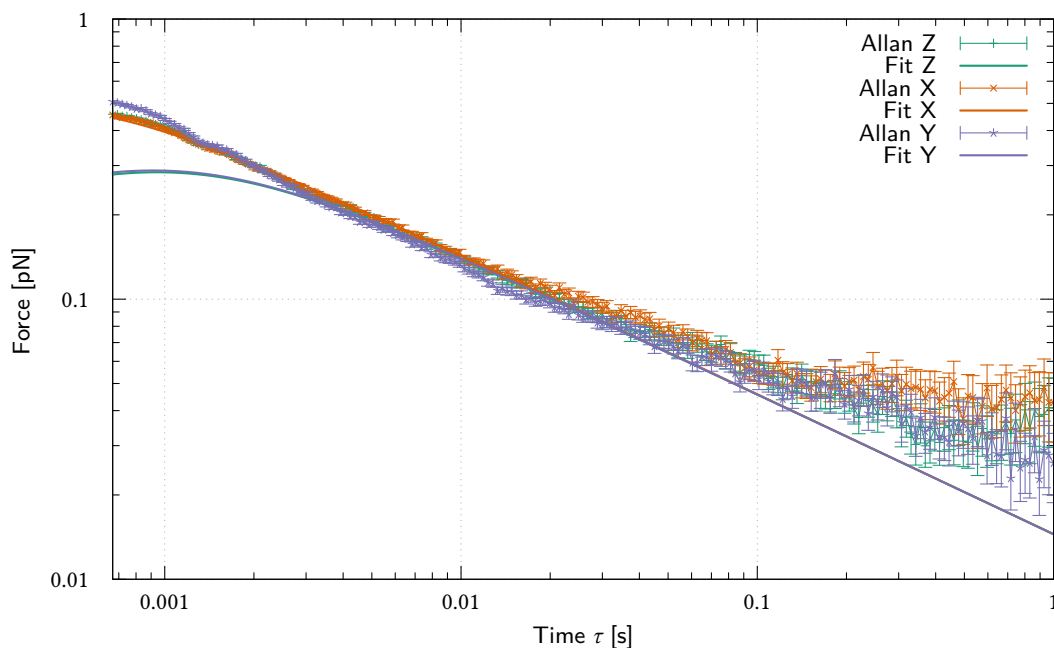


Fig. 8.4.: Allan deviation analysis at 750 mW converted to forces

visible from the Allan variance, as it is significantly higher across all timescales τ for the y axis compared to the x axis and does only barely conform to the theoretical shape. These are clear signs that detection noise is a dominant and limiting factor in force detection in the y axis in this setup, as expected.

However, in x axis we are able to individually determine the conversion factor $\zeta_{xy} = (11.76 \pm 0.33) \text{ nm px}^{-1}$ * as well as the trap stiffness $k_x = (54.3 \pm 1.7) \text{ pN } \mu\text{m}^{-1}$. As expected, trapping is more stable (higher trap stiffness) in the lateral plane than along the axial direction.

As we can see, we have some deviations of the measured Allan variance from the theoretical model. For the z axis, both noticeable deviations for small times $\tau < 3 \text{ ms}$ as well as a smaller deviation for large times $\tau > 0.4 \text{ s}$ are observed. For the x axis, we only see deviations for larger times $\tau > 0.1 \text{ s}$. The deviations for the large time scales can be easily understood as drift. The deviations for short time scales characterise the detection noise. Since we don't experience deviations for the x axis, our system is limited not by detection noise but rather by the physical limitations due to Brownian motion. For the z axis however, detection noise limits the accuracy of our results. As we can see by the different force factors, the detection

*It should be noted that for normal microscopy, this would be a massive oversampling as the resolution is limited by diffraction to approximately half the wavelength, so at best 200 nm or 17 px

8. Results

of axial forces is two to three orders of magnitude more sensitive than the detection of radial forces, explaining these differences between the axes.

In experiments, we are typically using a laser power of 750 mW. Repeating the test with the same particle with this increased laser power yields Allan deviations as shown in fig. 8.3. As the corner frequency is higher, we are reusing the conversion factors ζ from above and only fitting the spring constants k . For the z axis, we get a stiffness of $k_z = (51.4 \pm 0.2) \text{ pN } \mu\text{m}^{-1}$ and for the x axis a value of $k_x = (149.9 \pm 0.7) \text{ pN } \mu\text{m}^{-1}$. Compared to the values for 250 mW, this is a (2.63 ± 0.06) -fold increase for k_z and a (2.76 ± 0.09) -fold increase for k_x .

From the laser power increase, we would expect a 3-fold increase of both values. However, laser power is controlled by an analogue 0 V to 10 V signal. The look-up table for the relation between control input and laser power was provided as a graph from the supplier and might not be accurate at the specific operating conditions during the experiment. The agreement between the increases for k_x and k_z with regards to their respective errors also points towards a laser power increase by only a factor of 2.7 ± 0.1 .

Furthermore, this agreement serves as a verification that the high-speed video-based force detection as well as force calibration by Allan variance analysis is indeed working as intended.

Finally, taking our calibration results, we can easily convert the Allan variance from arbitrary units of displacement to forces. As shown in fig. 8.4 in the case of 750 mW laser power, we have a maximum Allan deviation for both x and z axes of below 0.5 pN.

8.2. Boron nitride

The results shown in this thesis are the first results for boron nitride in our workgroup. As we already have some expertise with molybdenum disulphide from previous works⁶, the goal is to achieve free-standing single-layer boron nitride membranes. As we are only interested in membrane thickness and single layer molybdenum disulphide membranes are comparable to double-layer boron nitride membranes, only single-layer boron nitride is an improvement to previous results.

8.2.1. Silicon wafer substrate

As already described before, due to white light interference thin films can be easily identified on silicon wafers with a silicon oxide layer. Here, a 90 nm thin oxide layer is used. Fig. 8.5 shows boron nitride flakes of varying thickness that have been exfoliated onto such a wafer. A small bulk flake can be seen at the left edge of the image (yellow area). Furthermore, some large areas of few-layer (in the range of a dozen layers) are visible. Additionally, some very thin, light blue areas are visible which are possibly monolayers. The colouring is comparable

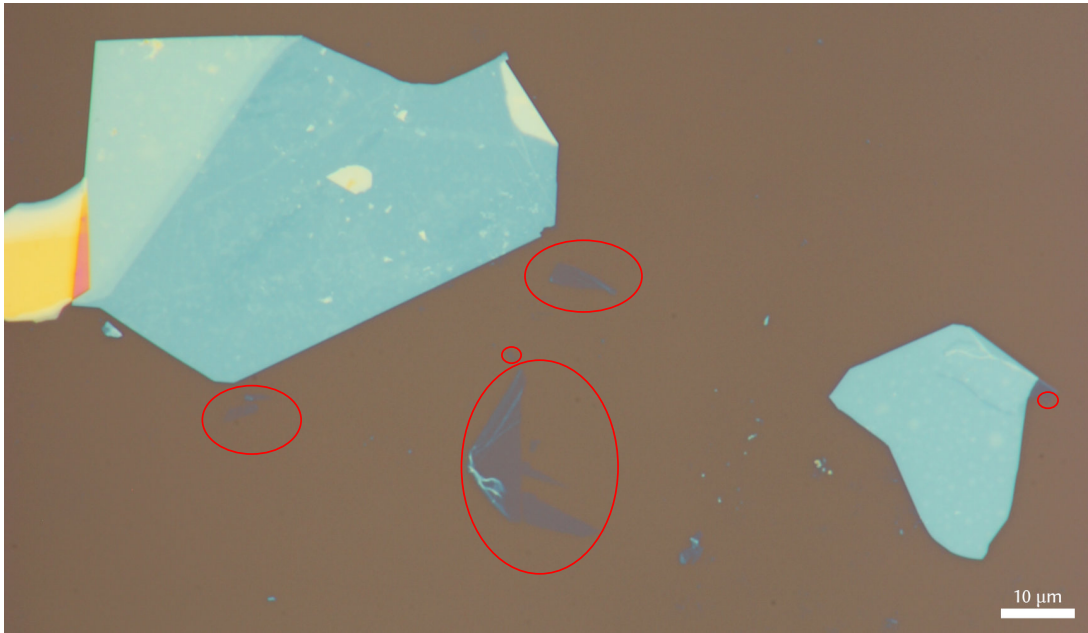


Fig. 8.5.: Potential monolayers of boron nitride (light blue areas marked with red circles) on a silicon + silicon oxide wafer

to graphene monolayers, although they appear more faint as graphene monolayers have a high absorbance of 2.3 % of all visible light¹⁴². This is also in accordance with literature¹¹⁹.

As we wish to transfer the membrane to the chip via soft lithography, we need to first transfer it to a material suitable for soft lithography, such as PDMS. I have tried to transfer these potential monolayers to cured PDMS, cured silanised PDMS, and cured plasmaoxidised PDMS. In all cases, no transfer of the material from the silicon wafer to the PDMS occurred.

Coating the chip with uncured PDMS which was then cured for two hours at 85 °C as usual lead to a transfer of the potential monolayer to the PDMS. However, these flakes could not be stamped viscoelastically to the target chip, in contrast to material directly exfoliated on the PDMS after curing.

Spincoating PDMS directly onto the wafer (9900 rpm for 600 s) followed by curing yields a PDMS layer of at least 3 μm, judged by the interference pattern of the PDMS layer on the chip. This thickness is in agreement with literature values¹⁴³. Exfoliating boron nitride onto that PDMS layer does not produce interference-based colour changes to monolayers, thus not providing any advantage to using pure PDMS without wafer.

Whilst thinning the PDMS layer even further by longer spin coating time and by diluting the (uncured) PDMS in a solvent^{143,144}, both results (i.e. better visibility due to white-light

8. Results

interference) and practicability with regards to the transfer from the spincoated wafer onto the chip remain questionable. Therefore, this was not pursued further.

8.2.2. PDMS substrate

Direct exfoliation on PDMS as a substrate allows for easy transfer via soft lithography to the target chip. According to our expectations the transfer is as straightforward as it is for molybdenum disulphide shown in my earlier works⁶. This is also in agreement with literature¹²¹.

However, the reliable identification of monolayers is very challenging. Unlike monolayer graphene, we do not encounter a significant contrast of few-layer boron nitride on PDMS. I have tested visibility on silanised PDMS, plasmaoxygenated PDMS, and PDMS spincoated on a coverslip, as well as PDMS in front of a white and black background. No change in contrast or visibility of few-layer boron nitride was detected.

Additionally, I tested the visibility on PDMS blackened with carbon black pigment which was originally used in our group for UV fluorescence experiments¹⁴⁵. As the individual pigment particles become visible in high magnifications, visibility was noticeably worse.

To test the thickness of the thinnest flakes that I could notice, I transferred one such flake to Mica via soft lithography. This sample was then imaged with atomic force microscopy (Multi-mode IIIa, Bruker, Billerica, Massachusetts, USA; Tap300AL-G cantilever; tapping mode). The resulting microscopy image (mirrored to correspond to the AFM image) and AFM image are shown in fig. 8.6. Reflection microscopy was used due to better contrast compared to transmission microscopy. The flake has a thickness of more than 1 nm at its thinnest part. As this flake was representative for the thinnest flakes found in a dozen exfoliations on PDMS, we can conclude that either monolayer flakes are not exfoliated onto PDMS, or that monolayer flakes are not visible on PDMS.

8.2.3. PMMA substrate

Exfoliation on PMMA yields more flakes compared to PDMS. However, visibility was comparable and no thinner flakes than the one shown in fig. 8.6 were found. Also, a stamping transfer from the PMMA to the final chip was not possible.

8.3. Molybdenum disulphide

As we could not achieve free-standing single-layer boron nitride membranes, we will now focus on monolayer molybdenum disulphide. With the insights gained for boron nitride, we

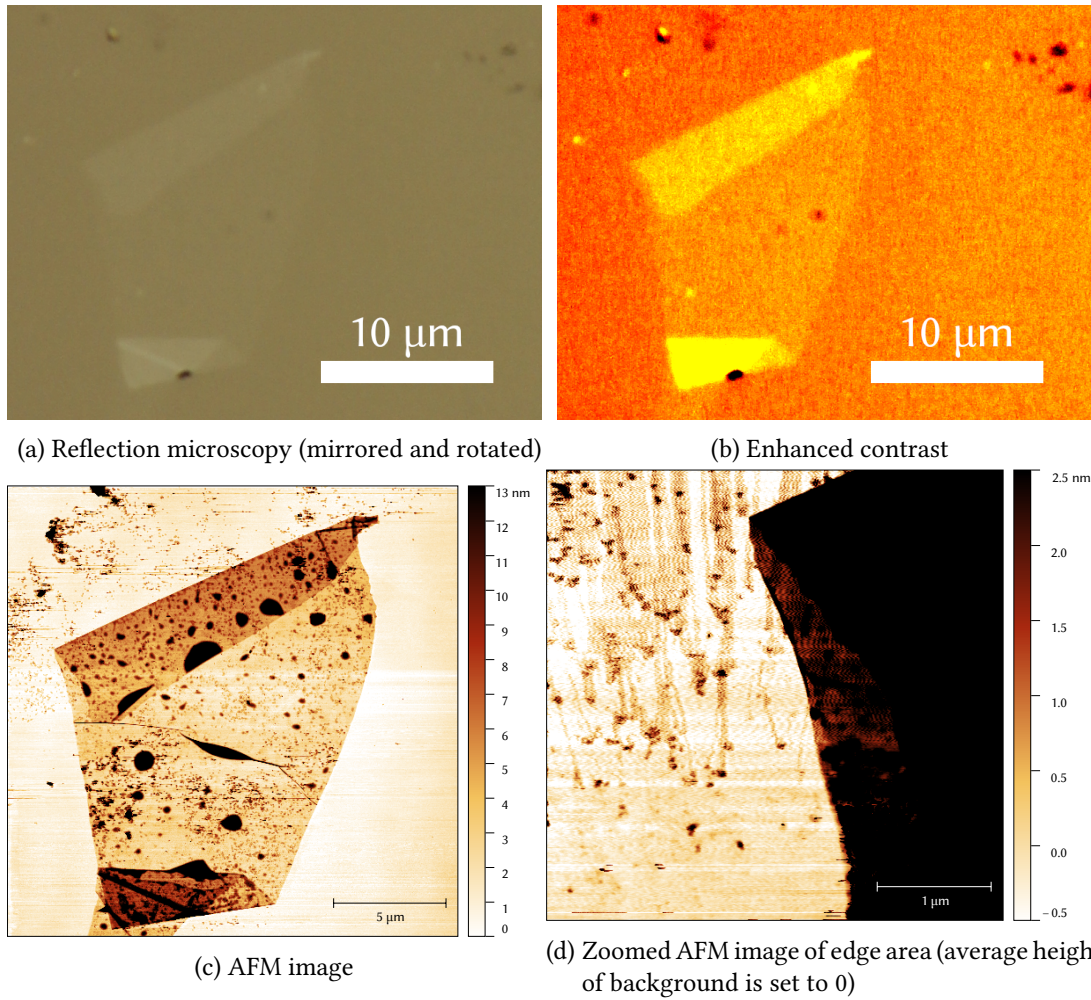


Fig. 8.6.: Microscopy and AFM images of the thinnest boron nitride flake found on PDMS

8. Results

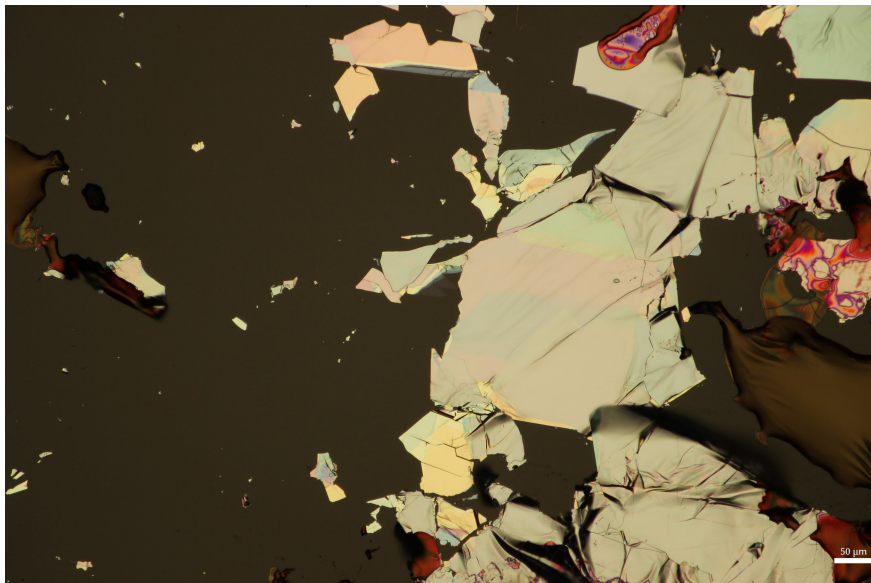


Fig. 8.7.: Reflection microscopy image of PDMS with exfoliated MoS₂. The four red dots used to mark the location are visible at the edge of the image. Scalebar is 50 μm

will only use unmodified PDMS as a substrate here.

8.3.1. Identification of monolayer flakes on PDMS

After exfoliation onto PDMS, typically two to three potential monolayer flakes with a size in the range of 10 μm × 10 μm were found with optical microscopy in reflection microscopy mode, typically next to thicker regions of bulk material (see fig. 8.7).

A typical monolayer flake is shown in fig. 8.8, which is a magnification of fig. 8.7. The flake is shown in reflection microscopy, transmission microscopy, and fluorescence / photo-

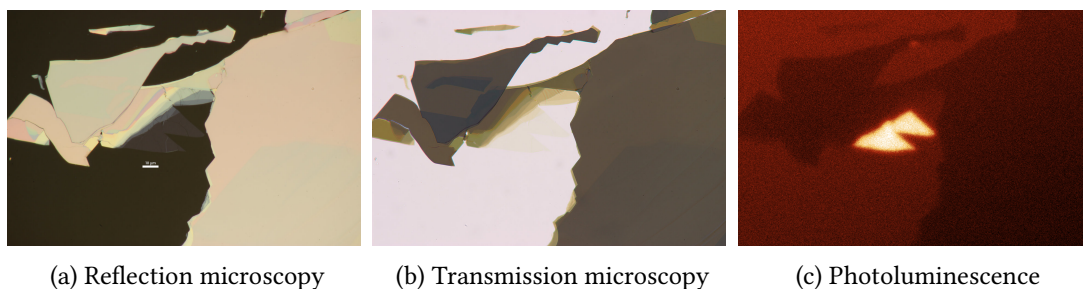


Fig. 8.8.: Reflection microscopy, transmission microscopy and photoluminescence images of a MoS₂ monolayer. All images show the same area. Scalebar is 10 μm.

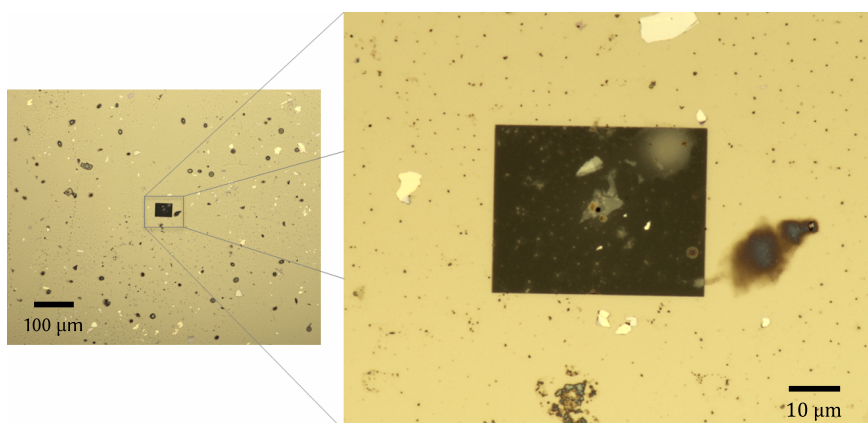


Fig. 8.9.: Residue of cellulose polymer on the silicon chip after wedging transfer. Images taken by Dennis Kreft¹⁴⁶

luminescence microscopy. The latter verifies that the two large areas are monolayers. As we can see, bulk material blocks background photoluminescence. We also see a small area of dual-layer molybdenum disulphide, which is visible in the photoluminescence image with reduced intensity.

8.3.2. Wedging transfer

In the beginning of this work, monolayers were exfoliated onto silicon wafers and a wedging transfer with a cellulose polymer was performed. However, in experiments we often encountered DNA sticking to the nanopore immediately after threading the DNA in. We hypothesised that this is caused by residue of the cellulose polymer. Some residue was already visible in optical microscopy, as shown in fig. 8.9.

To further analyse this issue, AFM images were taken by Dennis Kreft for his diploma thesis under my supervision, as shown in fig. 8.10. Here, we show the phase image which is selective to different surface materials. Obviously, there are multiple sub-micrometer sized residues on this small area of chip. Notably, the residue was not only found on the chip but also on top of a single-layer molybdenum disulphide flake.

We can therefore conclude that residue of the used cellulose polymer remain throughout the chip. Even keeping the chip in ethyl acetate for multiple days with a magnetic stirrer and cleaning the surface of the ethyl acetate with a water aspirator prior to removing the chip could not completely remove the residue.

Therefore, we switched to a dry transfer by viscoelastic stamping.

8. Results

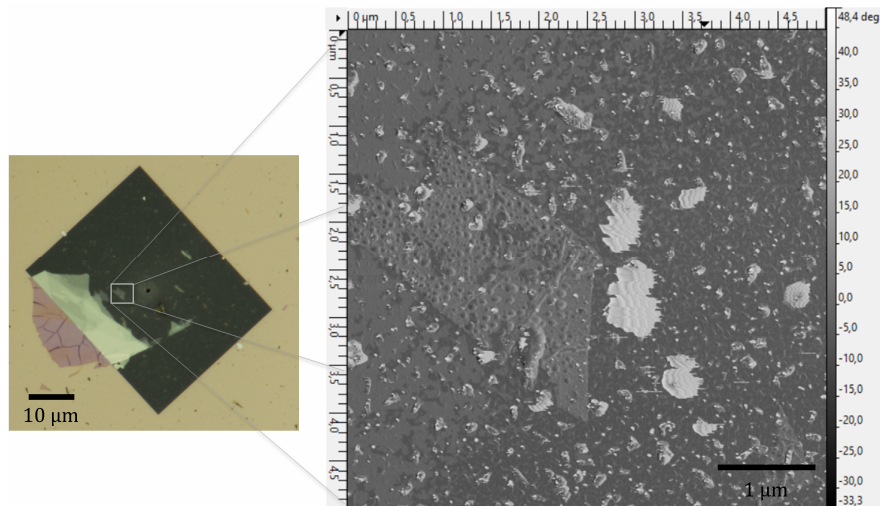


Fig. 8.10.: AFM phase image of the surface of the chip next to the free-standing membrane. A small flake of single-layer MoS₂ with a few air bubbles between flake and chip can be seen as well as various sub-micrometer sized residues. Images taken by Dennis Kreft¹⁴⁶

8.3.3. Transfer by viscoelastic stamping

The viscoelastic transfer proved to be a reliable, high-yield and easy to use alternative to wedging transfer. In my experiments with chips which were milled by the manufacturer by gallium ion microscopy, I achieved a success rate of 100 % for transfers, not counting a few chips where the monolayer was misaligned. In some cases, the transfer was not immediately successful with a stamp-chip contact time of a few minutes, i. e. the material was not transferred to the chip. In these cases, re-contacting chip and PDMS stamp with higher force and keeping the contact for at least half an hour always led to a successful transfer.

In his Master thesis¹⁴⁷ under my supervision, Julian Cremer noticed a reduced yield by approx. 25 % when using chips milled by helium ion microscopy compared to gallium ion microscopy. We are assuming that the milling procedure influences the surface charge of the chip, thus resulting in different yield.

8.3.4. Nanopore milling

8.3.4.1. Electrochemical breakdown

Nanopore milling by electrochemical breakdown occurs at applied voltages of at least 800 mV according to literature¹⁴⁰. I was unable to monitor nanopore formation with voltages up to

1000 mV, the maximum voltage that can be applied with the used Axopatch patch clamp amplifier¹⁴⁸. Therefore, a 1.5 V type AA battery was used in conjunction with two resistors to add approx. 750 mV voltage, as illustrated in fig. 6.1. This way, the applied voltage range was shifted from -1000 mV to 1000 mV to -250 mV to 1750 mV.

Of course, the maximum current measurable with the system remains unchanged by this procedure at 20 nA¹⁴⁸. For the maximum voltage of 1750 mV this would correspond to a resistance of 87.5 M Ω . Assuming we want to manufacture a nanopore with a diameter of 5 nm, we can use eq. 7.1 to determine the minimum resistivity of the buffer solution as 0.37 Ω m (which is 26.8 mS cm^{-1}). Extrapolating conductivity data from literature¹⁴⁹ gives a maximum KCl concentration of 208 mM. Conversely, for a 20 nm nanopore we get a maximum concentration of 44 mM.

It should be noted that in literature, to achieve breakdown at 800 mV a 1 M KCl buffer solution was used. With the above limits, the maximum nanopore diameter we could measure with this buffer concentration at 800 mV would be 1.8 nm. At 1750 mV this reduces further to 1.0 nm.

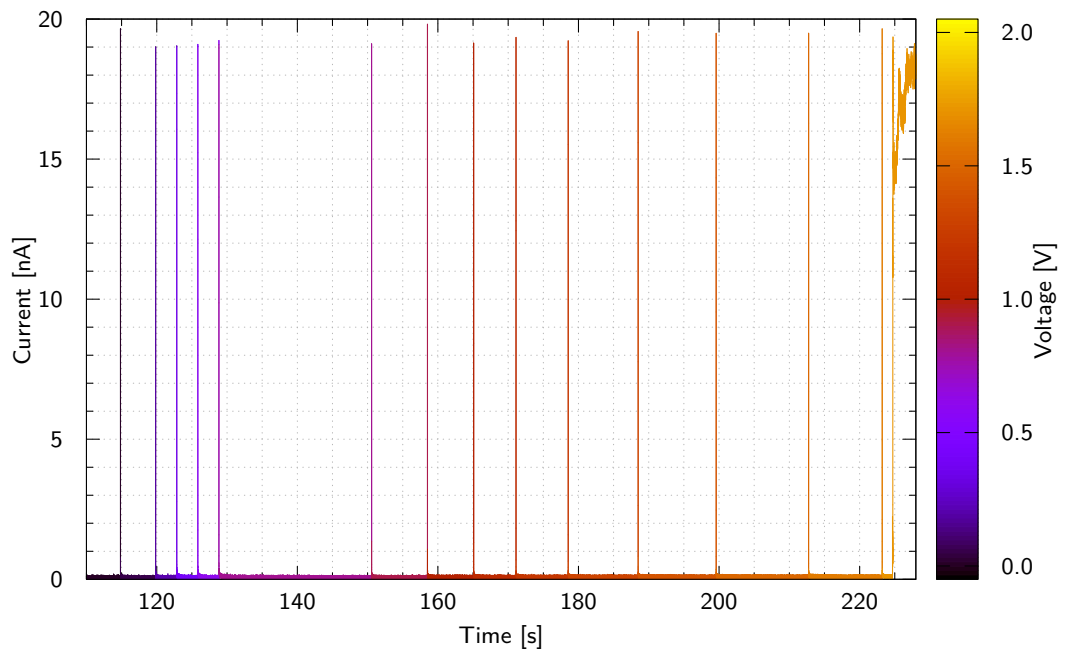
8.3.4.1.1. Sudden pore formation A sudden pore formation at 1.7 V is shown in fig. 8.11. Here, we use 200 mM buffer solution. The data shown in fig. 8.11b is calculated based on the unfiltered 100 kHz signal from the patch clamp amplifier. As we can see, pore formation occurs in discrete steps. The initial formation of a 0.4 nm pore takes only 60 μ s as measured with this setup. The major step from less than 1 nm to approx. 3.9 nm takes 180 μ s. Afterwards, we see a gradual reduction in pore size followed by a two-step increase from 3.4 nm via 3.9 nm to 4.3 nm. The first step takes 120 μ s, the second step is more gradual, taking 250 μ s.

Of course, the pore sizes determined here are based on just individual measurements of voltage and current. To get a definite and accurate pore size, after milling a voltage-current curve is recorded to fit the final resistance. This gives us a value of (91.38 ± 0.04) M Ω , corresponding to a pore diameter of (4.97 ± 0.01) nm.

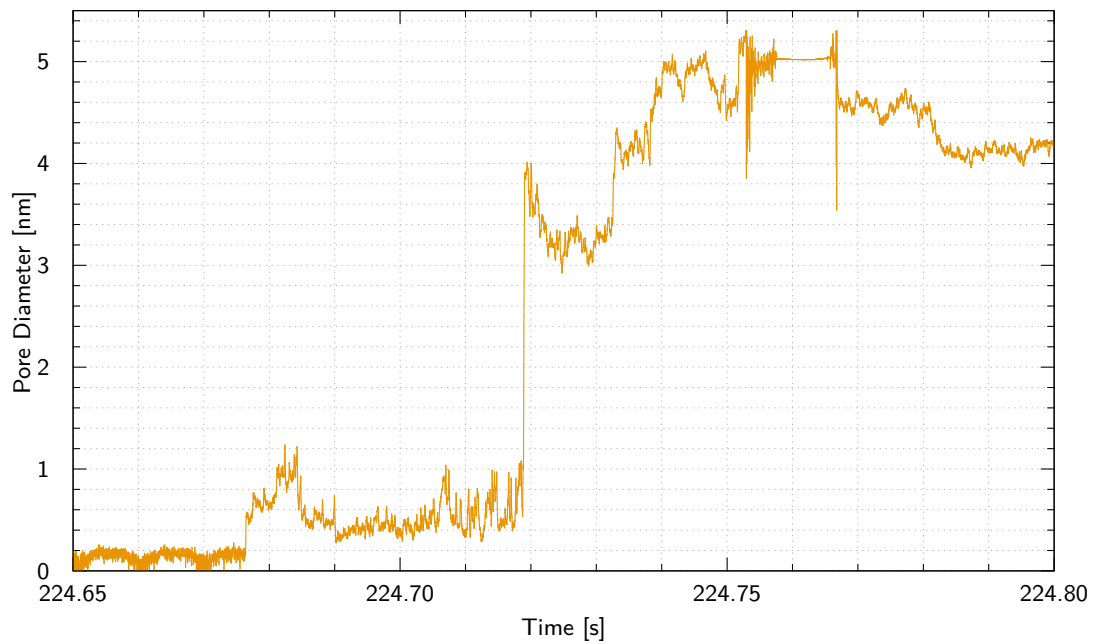
8.3.4.1.2. Gradual pore formation In contrast, a gradual pore formation is shown in fig. 8.12. This formation already occurred at 1.0 V, which might be an explanation for the difference in pore formation and widening behaviour. Ultimately, a pore of (5.1 ± 0.2) nm was formed.

It should be noted that even with averaging of the raw 100 kHz signal down to 1 kHz, the noise in the current signal is still too high to be able to see individual steps of pore formation. This is caused on the one hand by the flow cell design, which is not optimised for low-noise current measurements but instead for suitability for optical tweezers experiments. On the

8. Results



(a) Overview graph of current



(b) Detail graph showing calculated pore diameter

Fig. 8.11.: Sudden pore formation of a 5 nm diameter pore in 200 mM buffer solution. The voltage is increased in steps to 0.0 V, 0.1 V, 0.2 V, 0.4 V, 0.6 V, 0.8 V, 0.9 V, 1.0 V, 1.1 V, 1.2 V, 1.3 V, 1.4 V, 1.5 V, 1.6 V, and 1.7 V

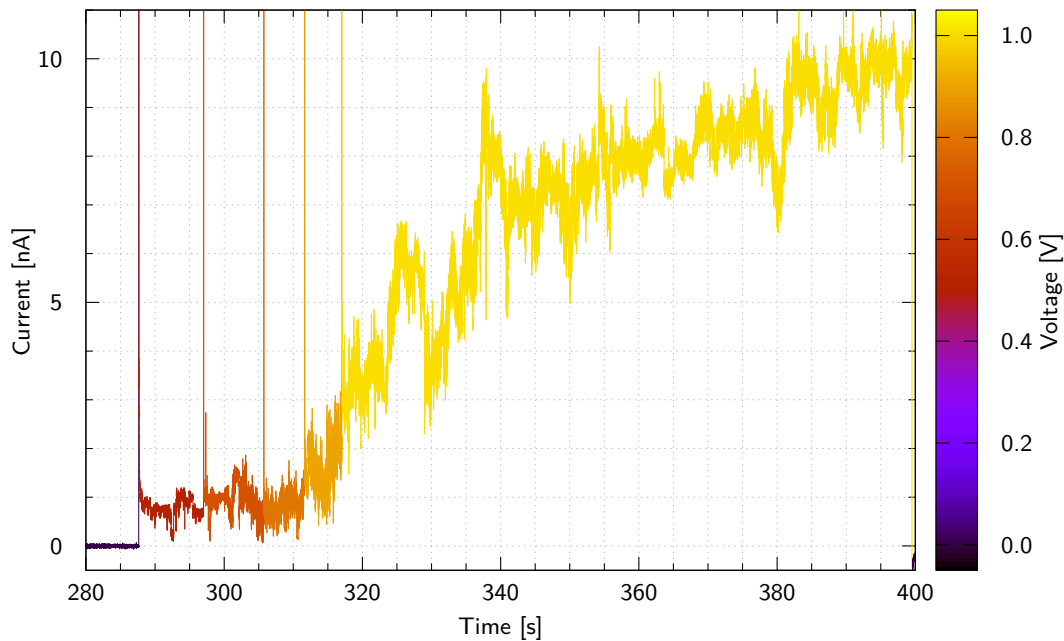


Fig. 8.12.: Gradual formation of a 5 nm diameter pore in 200 mM buffer solution. Voltage was increased in steps to 0 V, 0.5 V, 0.7 V, 0.8 V, 0.9 V, and 1.0 V

other hand, the used patch clamp amplifier is not of sufficient quality to allow the detection of individual steps in pore formation. However, this was not the goal of this work. The step by step opening has been shown for example by Feng et al.¹⁴⁰.

8.3.4.1.3. Capacitive effects due to insufficient wetting In this work, insufficient wetting proved to be a major complication. Not only does the electrochemical breakdown require both sides of the chip to be wetted completely. DNA translocation experiments of course also depend on a completely wetted chip.

Fig. 8.13 shows a current curve of a chip scheduled for electrochemical breakdown. Obviously, especially for large voltages we can see a significant exponential decay in the current signal. This is due to insufficient wetting of the chip. The introduced thin air layer acts as a parallel-plate capacitor, which forms an RC circuit.

This can be used as an indicator whether complete wetting of a chip was achieved. Overall wetting was greatly improved by the introduction of the 30 minutes hydrophilisation in 50 % ethanol in the preparation process.

8. Results

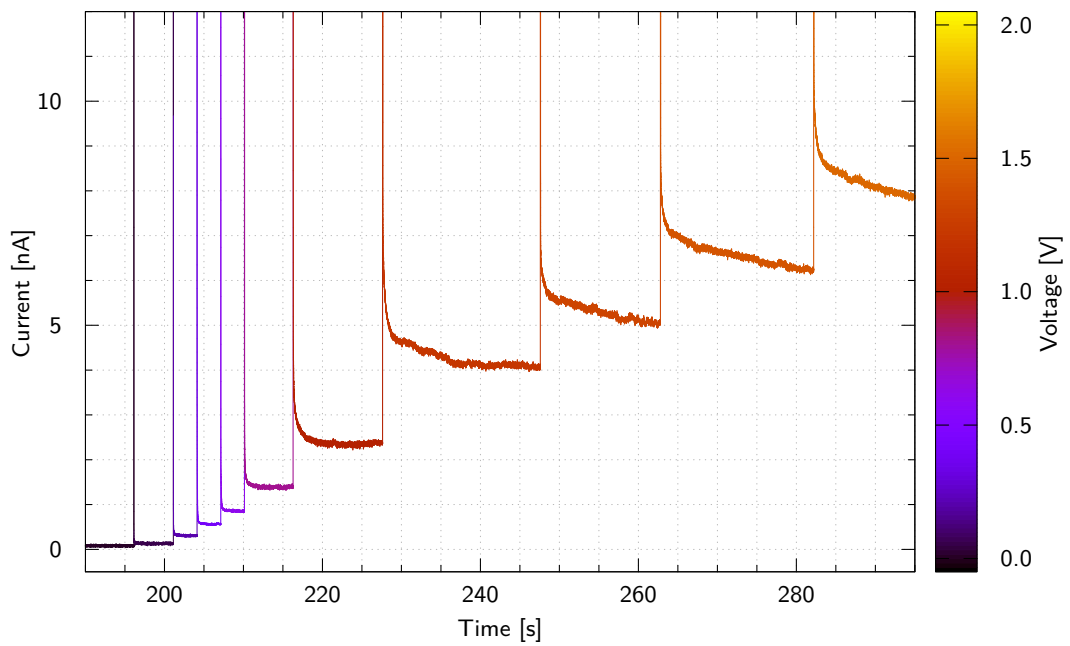


Fig. 8.13.: Current curve of a chip in 200 mM buffer solution showing large exponential decay after voltage changes

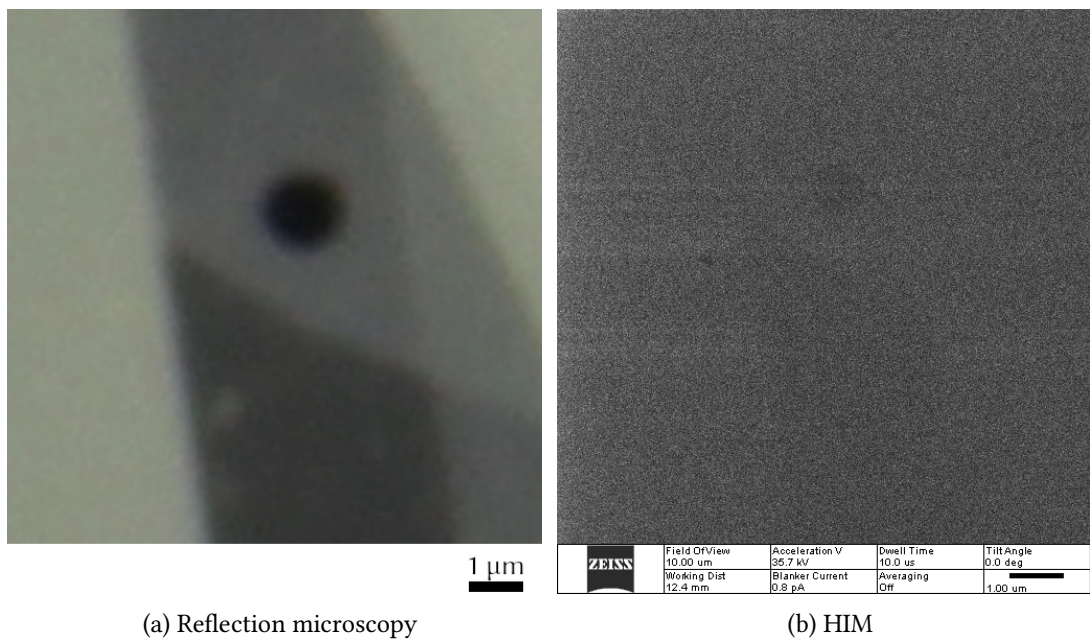


Fig. 8.14.: Reflection microscopy and HIM images of a chip with a 1 μm pore covered by a MoS₂ double layer. The reflection microscopy image has been rotated, cropped and mirrored to show the same region in the same orientation as the HIM image

8.3.4.2. Helium Ion Microscopy

Helium Ion Microscopy suffers from poor contrast in conjunction with thin materials. Fig. 8.14 illustrates this poor contrast at a double-layer MoS₂ membrane covering a 1 μm hole. Milled nanopores are not visible in the Helium Ion Microscope due to a number of reasons: First, the limited contrast makes it very hard to see such a pore. Second, lateral drift of the field of view in the Helium Ion Microscope is not uncommon. As we require a large zoom to see the small nanopores (typical nanopore size when milled with the HIM is in the range of 50 nm) and the nanopore is milled centred on the micropore, no guiding features are available to allow lateral drift compensation. Finally, the high momentum of the helium ions makes microscopy on these thin dimensions quite abrasive. Prolonged imaging inevitably results in a ruptured membrane.

Throughout my work as well as the works of students Dennis Kreft and Julian Cremer under my supervision, approximately one third of the chips milled in Helium Ion microscopy were found to have a ruptured monolayer membrane when the resistance was measured in the optical tweezers setup. This ruptured membrane was characterised as a calculated nanopore size close to the micropore size.

8.3.4.3. Transmission Electron Microscopy

Experiments with Transmission Electron Microscopy were performed by Julian Cremer during his Master thesis¹⁴⁷ in cooperation with Dr. Inga Ennen from the group *Thin Films and Physics of Nanostructures*. When using 200 kV acceleration voltage, the monolayer membrane was destroyed in most cases. However, reducing the acceleration voltage to 80 kV led to a yield of 100 % for all 16 pores milled.

Fig. 8.15 shows a nanopore after milling. In the residue-free areas, the hexagonal structure of MoS₂ is clearly visible. Obviously, this structure is missing in the nanopore. Julian Cremer was able to use Raman spectroscopy and AFM to determine the residue to be PDMS with a thickness of approx. 0.5 nm. As the residue has limited mobility on the surface, we can assume it to be not crosslinked PDMS oligomers or even monomers. The amount of residue also increases with increased pressure during viscoelastic transfer, which further supports this hypothesis. More thorough mixing of the PDMS components also reduced the amount of residue.

In addition to milling the nanopores, TEM can also be used to measure the resulting pore. In his master thesis, Julian Cremer found agreement between the nanopore size determined with TEM and the nanopore size calculated based on the resistance for all pores within the margin of error of both methods (0.5 nm for TEM, 2 nm for resistance based size determina-

8. Results

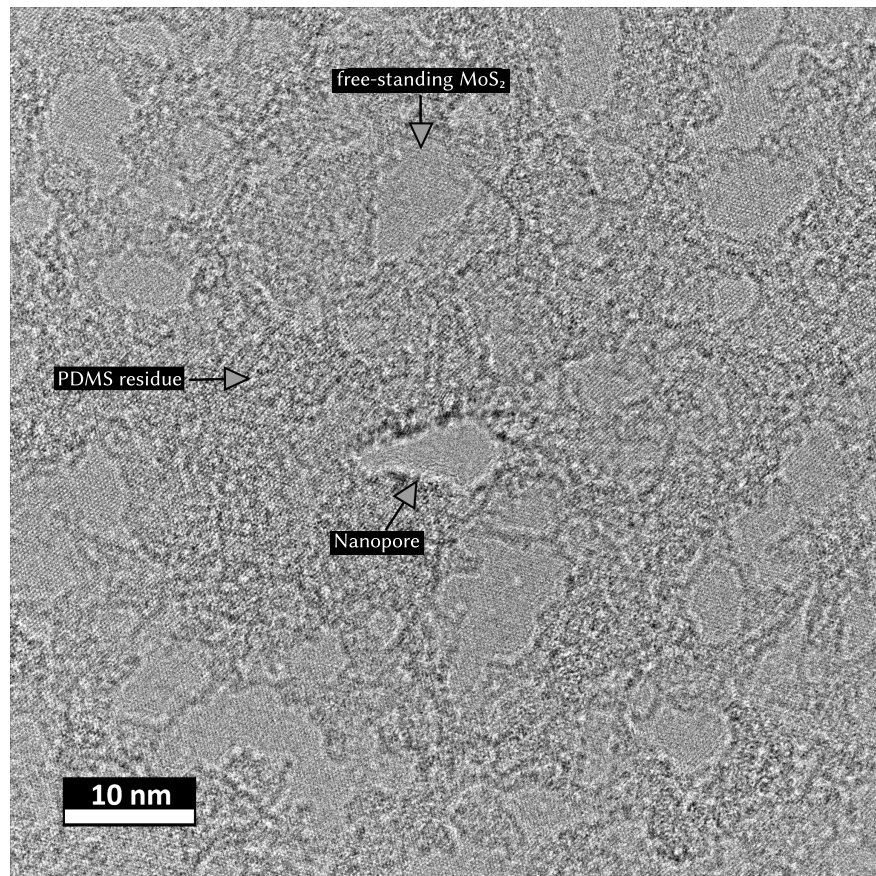


Fig. 8.15.: Free-standing MoS₂ membrane with PDMS residue and nanopore (centre)¹⁴⁷

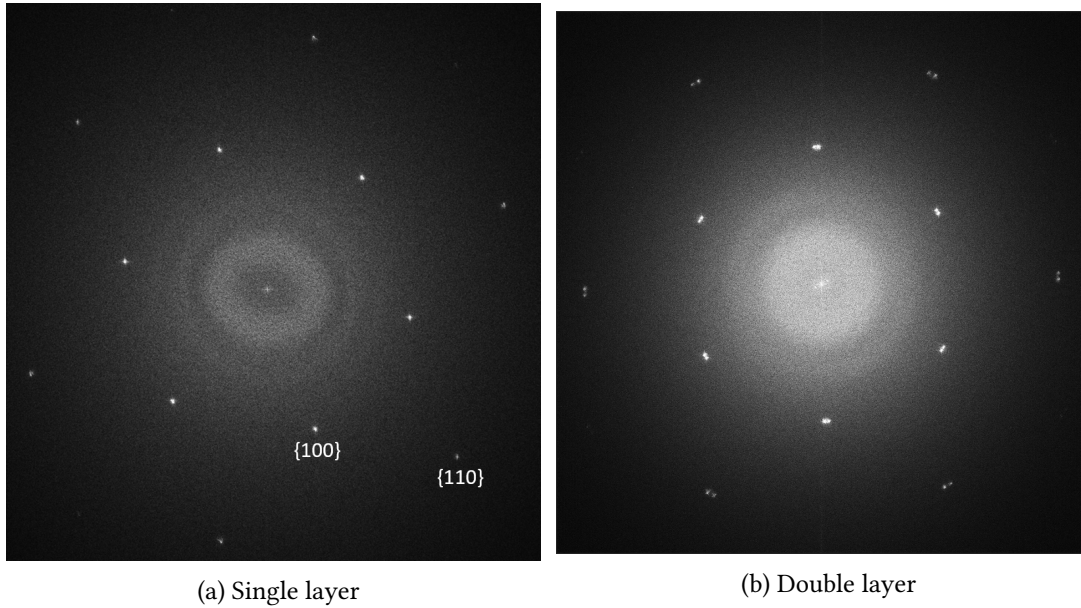


Fig. 8.16.: FFT of the TEM images of a MoS₂ monolayer and a double layer¹⁴⁷

tion).

Furthermore, as we are able to resolve individual atoms with TEM, we can use fourier transformation to verify the crystal structure. Fig. 8.16 shows the fourier transforms of a single layer and a double layer of MoS₂, exhibiting the hexagonal structure. Obviously, the double layer presents double peaks at the hexagonal structure, compared to the single peaks for the monolayer. For the marked spots {100} and {110} we get distances of $d_{100} = 2.6 \text{ \AA}$ and $d_{110} = 1.5 \text{ \AA}$.

We can use the relation

$$d_{hkl} = \frac{a}{\sqrt{\frac{4}{3}(h^2 + k^2 + hk) + \frac{a^2}{c^2}l^2}} \quad (8.1)$$

to convert these two values back to the lattice constant $a = 3.0 \text{ \AA}$ for both values. Taking the obvious astigmatism of the FFT into account, this is in good agreement with the literature value $a = 3.16 \text{ \AA}$ ¹²³⁻¹²⁶.

8.3.5. DNA translocation with optical tweezers

In this thesis, unfortunately only a few successful DNA translocation experiments with optical tweezers could be performed. Apart from the difficulties during manufacturing of the chip containing nanopores in monolayer membranes, two main issues presented themselves.

8. Results

First, to facilitate threading of the DNA into the nanopore, we need to bring the bead close to the pore. This risks accidentally hitting either the monolayer membrane or the neighbouring silicon nitride membrane with the bead. If that happens, in most cases the bead either sticks to the membrane, blocking further experiments, or the membrane is ruptured.

This issue is exacerbated by the fact that the PDMS is a viscoelastic material under pressure by the chip clamped on top and under intense illumination, leading to localised heating. In my experiments, I repeatedly contacted the membrane at a piezo position where just a few minutes prior no contact occurred. To explain this seeming drift in z position, I used edge detection in the overview camera image to get ad-hoc autofocus-like data. This was used to analyse both the edge of the flow channel at the bottom of the flow cell and the edge of the membrane on the chip at the top of the flow cell.

The bottom of the flow cell remained in position relative to the focal plane of the objective. However, the chip did move $(5.4 \pm 0.2) \mu\text{m}$ closer to the bottom in $(132.5 \pm 1.5) \text{s}$, which corresponds to an average velocity of $(41 \pm 2) \text{nm s}^{-1}$ or $(2.46 \pm 0.10) \mu\text{m min}^{-1}$. Of course, this velocity decreases over time, as the PDMS cannot contract infinitely. In my tests, turning on the illumination at least 30 minutes before experimentation greatly reduced further chip drift. Additionally, as a consequence of the discovery of this drifting behaviour, I implemented the continuous monitoring of the real distance between focal point (and therefore trapped bead, with an offset) and chip by autofocus calculation.

The second issue relates to questionable quality of the used λ -phage DNA. It was prepared throughout this thesis as well as earlier works by Helene Schellenberg according to accepted and unchanged protocol. Nevertheless, towards the end of the thesis no controlled DNA translocation experiments were successful. Furthermore, free DNA translocation experiments described in the next section showed a very low translocation rate, compared to earlier free DNA translocation experiments on silicon nitride nanopores. Finally, Dennis Kreft's independent experiments on stretching DNA with another optical tweezers setup also failed inexplicably at the same time.

As neither the preparation protocol, nor experimental protocols or the storage of prepared DNA changed, I was assuming that the issue stemmed from old ingredients. However, even after gradually replacing each ingredient with new ones, the issues still persisted.

Recently, a potential third issue has been described by James Wilson and Aleksei Aksimentiev¹⁵⁰. They discovered that for very small nanopores (in the range of 5 nm diameter) in 2D materials the capture rate of DNA into the nanopore depends highly non-linear on the applied transmembrane voltage. At certain higher voltages, the water in the buffer solution is polarised and subject to strong dielectrophoretic forces. This leads to the build-up of pressure in the nanopore and its immediate vicinity, which repels DNA and prevents it from entering

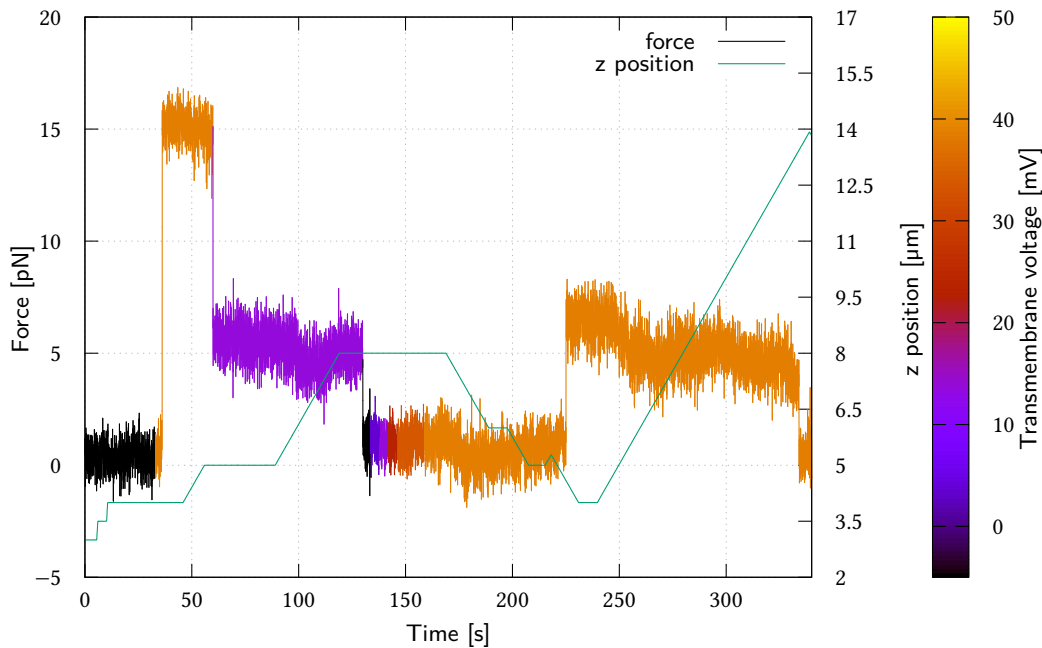


Fig. 8.17.: Overview of a DNA translocation through a (41 ± 8) nm nanopore in a monolayer. The applied transmembrane voltage is colour-coded in the force signal. The teal line (right y axis) shows the distance between bead and membrane. The buffer concentration was 20 mM

the nanopore.

Regardless of these issues, a few DNA translocation experiments were successful, which I show below.

8.3.5.1. 41 nm HIM-milled pore in monolayer

A complete translocation experiment in a (41 ± 8) nm pore (as determined by pore resistance) in a monolayer membrane is shown in fig. 8.17. This experiment was performed together with Dennis Kreft¹⁴⁶. First, we apply a transmembrane voltage with the bead in the immediate vicinity of the nanopore. This leads to the threading in of two separate DNA strands 20 ms apart from each other (see fig. 8.18a). Thanks to the data rate of 1555 Hz, we can resolve both events.

We then directly move away from the membrane, before reducing the transmembrane voltage. We then move a bit further away to measure a voltage-force curve. However, we accidentally apply a negative voltage due to incorrect voltage offset calibration. This leads to the immediate threading out of the DNA strands (see fig. 8.19a).

8. Results

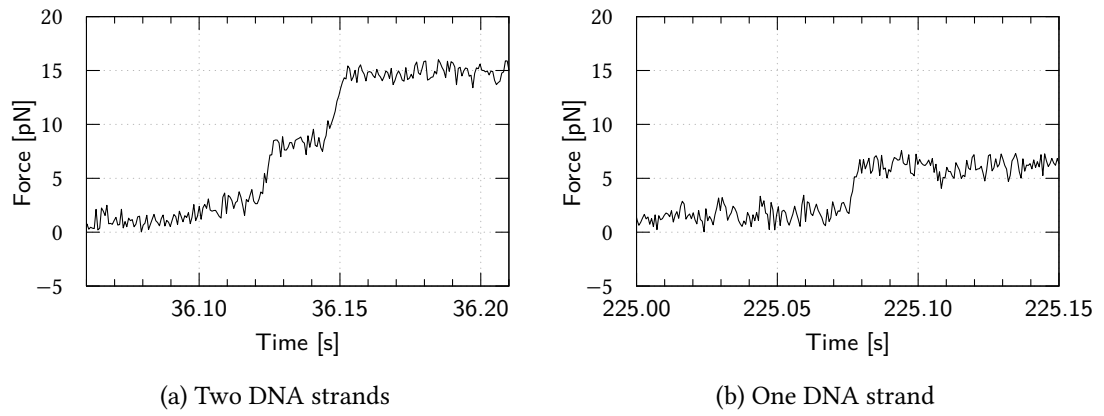


Fig. 8.18.: Threading in of two DNA strands in a short time vs. threading in of just one DNA strand

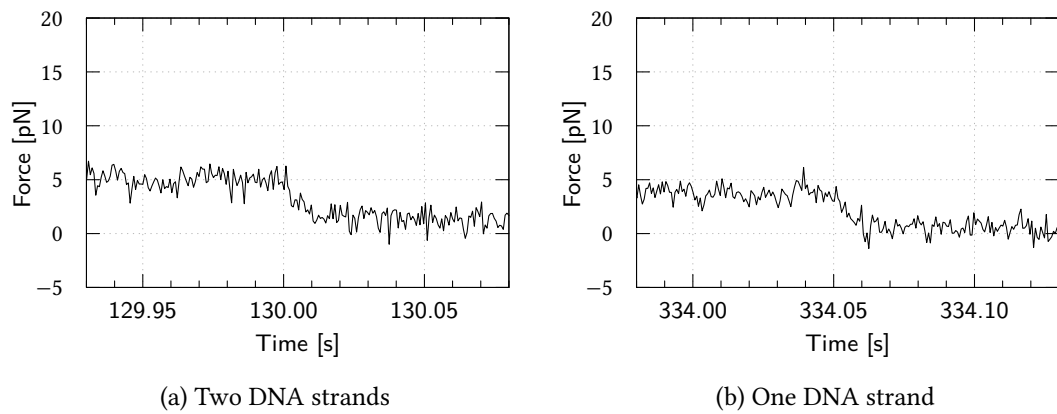


Fig. 8.19.: Threading out of two DNA strands in a short time vs. threading out of just one DNA strand

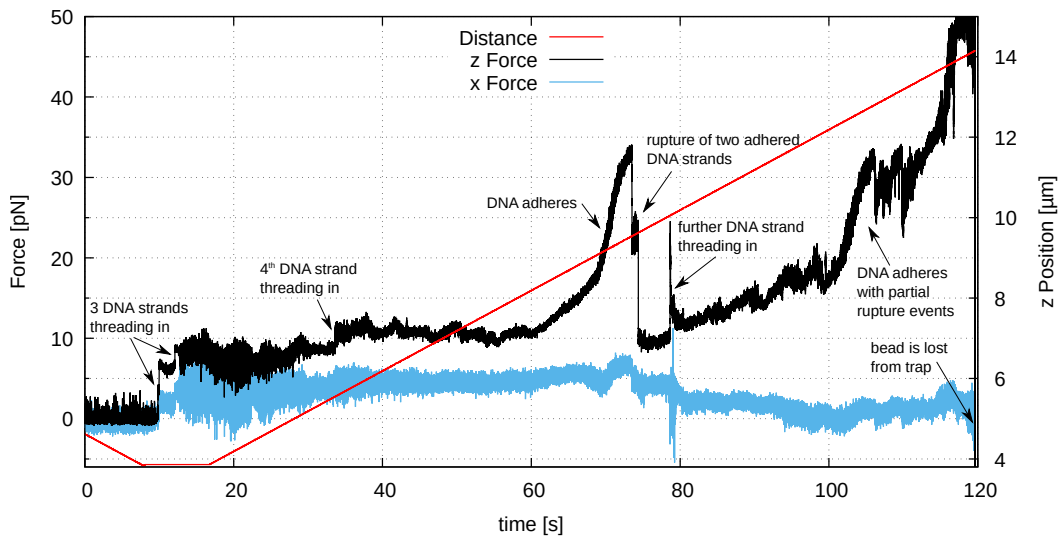


Fig. 8.20.: Translocation of DNA strands through a 200 nm nanopore in a monolayer. The DNA adheres to the membrane at various points. Ultimately, the bead is pulled out of the optical trap. Applied transmembrane voltage 70 mV, buffer concentration 100 mM

Reapplying the positive transmembrane voltage and approaching the membrane again leads to another threading in event, this time with only one DNA strand (see fig. 8.18b). Moving the bead away from the membrane leads to a near-constant force signal, until the DNA is threaded out of the nanopore after 10 μm (see fig. 8.19b).

8.3.5.2. 160 nm HIM-milled pore in monolayer

Fig. 8.20 shows the translocation of DNA strands through a (160 ± 10) nm (as determined by pore resistance) nanopore in monolayer MoS_2 . Throughout the measurement, a transmembrane voltage of 70 mV was applied. The buffer concentration was 100 mM.

Here, we see four distinct threading-in events. Due to the larger pore size, the individual forces for each DNA are lower, compared to the previous measurement. Starting at the 60 s mark, at least two DNA strands are adhering to the membrane. Eventually, the two strands rupture in sequence. Interestingly, we then get another threading-in event even though we have already increased the distance to the membrane by 6 μm . Finally, the remaining DNA continues to adhere to the membrane as partial rupture events are encountered. After moving 10 μm from the starting position, the bead is ultimately lost from the trap as the forces became too large.

8. Results

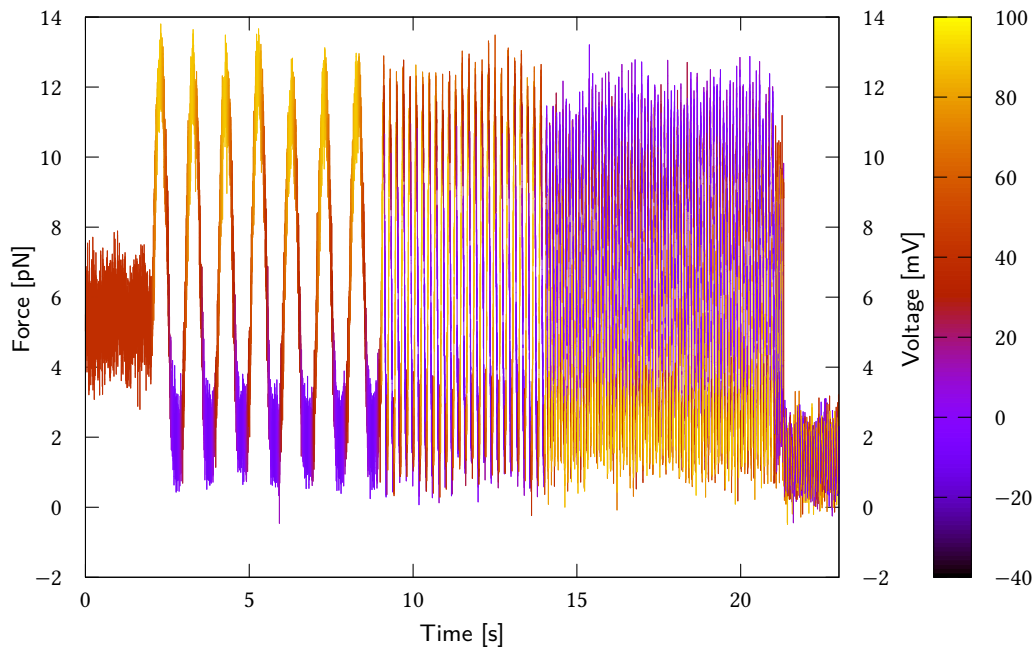


Fig. 8.21.: DNA strand inside the $1\ \mu\text{m}$ hole in the silicon nitride membrane with applied AC voltage (100 mV peak to peak, DC offset 39.3 mV, giving a voltage range of $-10.7\ \text{mV}$ to $89.3\ \text{mV}$) of 1 Hz, 5 Hz, 10 Hz, and 20 Hz. The monolayer membrane is defect. Distance between bead and membrane is approx. $4\ \mu\text{m}$. Buffer concentration 20 mM. Measurement performed by Dennis Kreft¹⁴⁶.

It should be noted that the bead was lost at a measured force of approx. 48 pN. Looking back at fig. 3.9a, we have said that linearity can be assumed for displacements up to $0.5 R$. Comparing the maximum force to the force at this displacement, we get that the maximum force is 2.36 times higher. Consequently, we can only assume force linearity up to 20 pN here. The apparent kink in the z force graph at the first adhesion (at around 70 s) can be explained this way.

8.3.5.3. Translocation with applied AC voltage

Fig. 8.21 shows the force behaviour of a DNA strand with applied AC voltage. The preparation of the chip and the measurement were performed by Dennis Kreft¹⁴⁶ for his diploma thesis under my supervision. Unfortunately, analysis of the UI curve for this chip gives a calculated nanopore diameter of 818 nm ($R = (4.439 \pm 0.001)\ \text{M}\Omega$, $\rho \approx 3.62\ \Omega\ \text{m}$). We can therefore assume the membrane not to be intact, as the micropore is in the range of $1\ \mu\text{m}$. During the measurement shown here, the bead was approx. $4\ \mu\text{m}$ away from the membrane.

The applied AC voltage is 100 mV peak to peak. Unfortunately, due to incorrect voltage

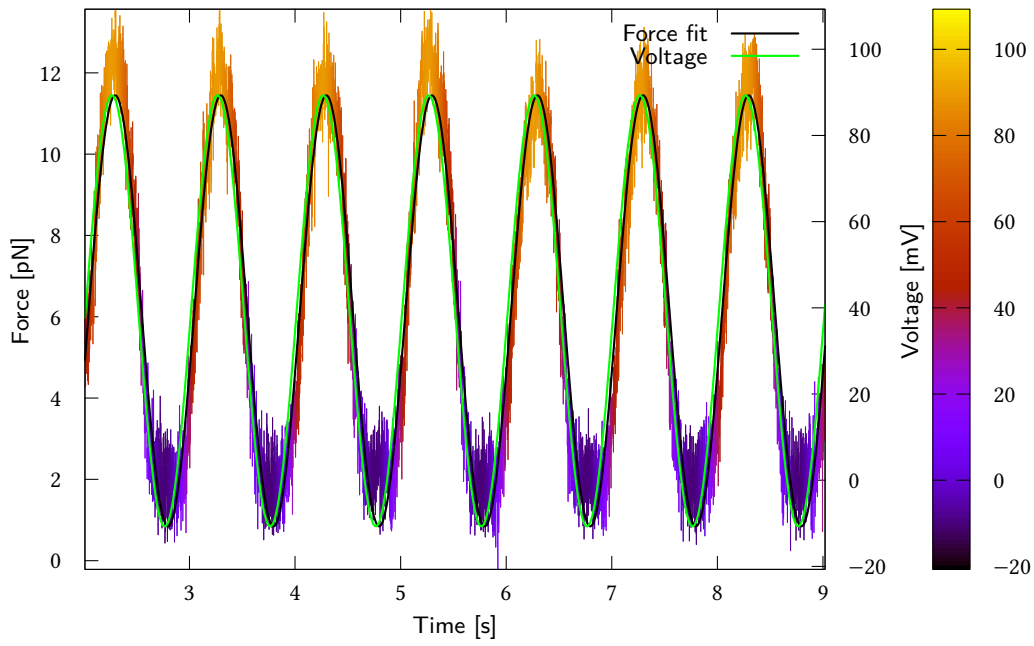


Fig. 8.22.: Detailed force graph at 1 Hz with colour-coded voltage. Sinusoid fit is shown in black, voltage is also shown in green (right y axis)

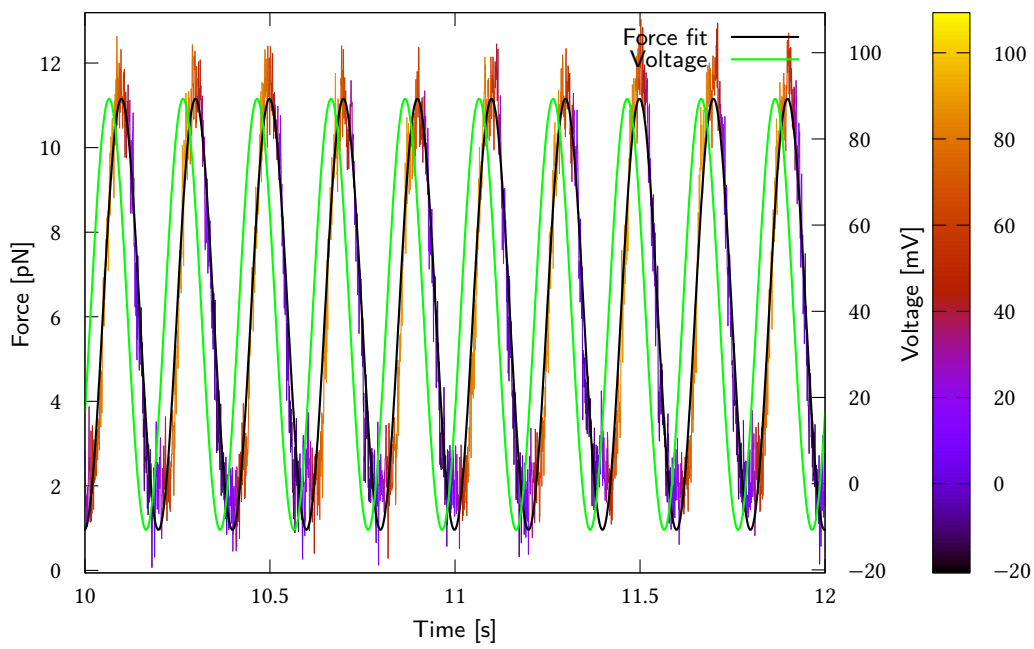


Fig. 8.23.: Detailed force graph at 5 Hz.

8. Results

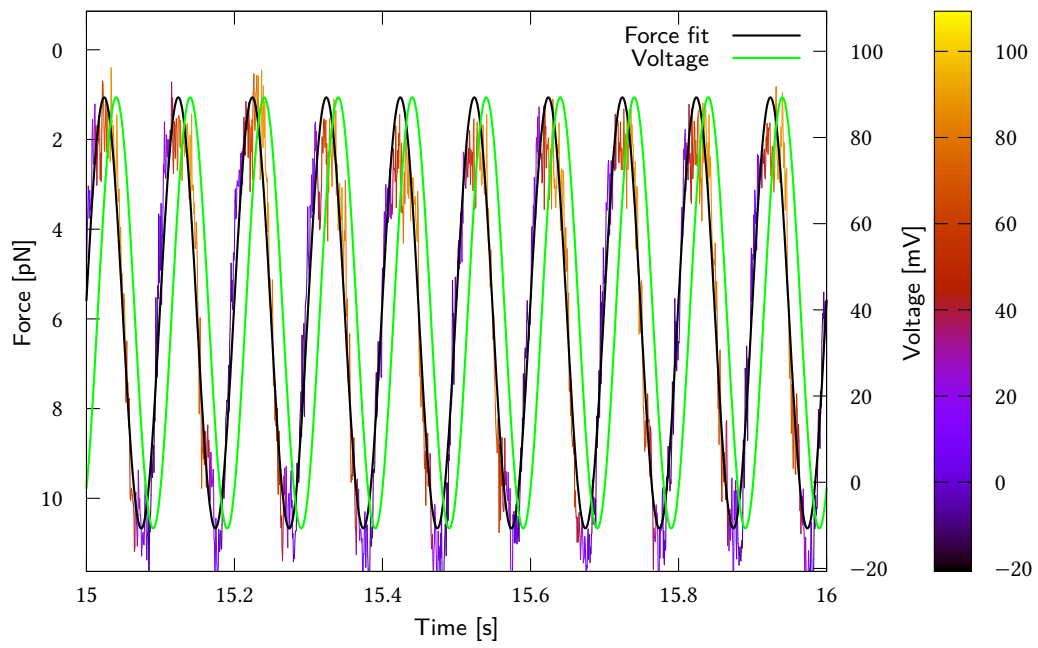


Fig. 8.24.: Detailed force graph at 10 Hz.

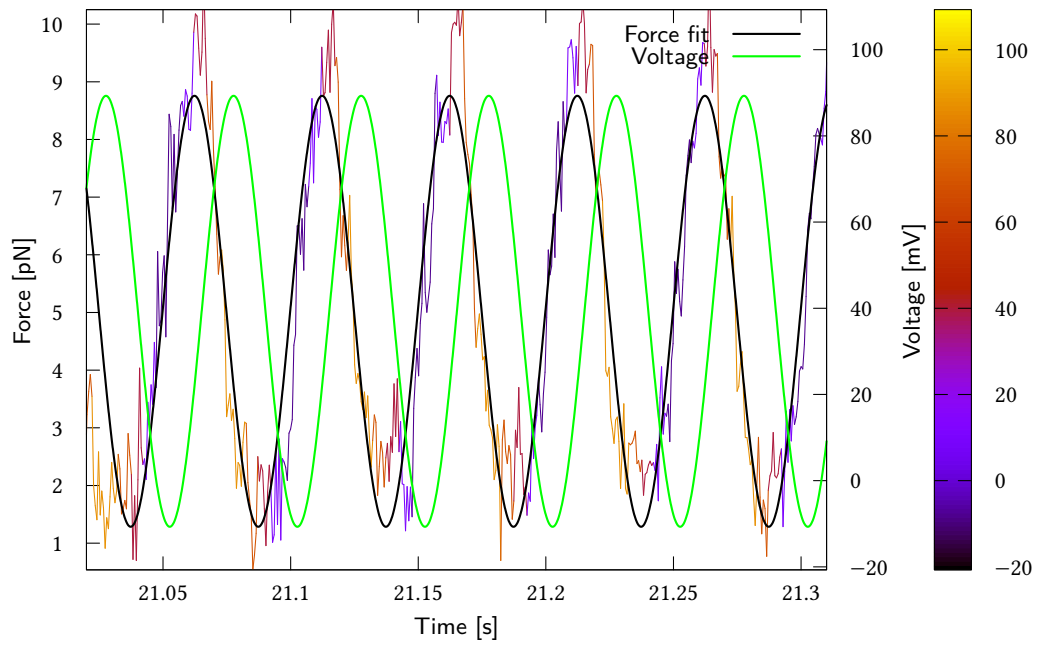


Fig. 8.25.: Detailed force graph at 20 Hz.

f	$\phi_I - \phi_U$	$\phi_F - \phi_U$	Force amplitude
1 Hz	-0.059	-0.197	(5.30 ± 0.01) pN
5 Hz	-0.372	-1.047	(5.10 ± 0.01) pN
10 Hz	-0.954	-2.130	(4.80 ± 0.01) pN
20 Hz	-2.420	-4.358	(3.74 ± 0.01) pN

Table 8.1.: Resulting frequency-dependent phase-shifts for current and force as well as force amplitudes

offset calibration, the DC offset was only 39.3 mV instead of the intended 75 mV. Therefore, the resulting transmembrane voltage was a sinusoid voltage from -10.7 mV to 89.3 mV. We start with a frequency of 1 Hz, which is then increased via 5 Hz and 10 Hz to 20 Hz. Figures 8.22–8.25 show the detailed behaviour for each frequency.

As we apply sinusoid voltage, we expect both current and force values to also have a sinusoid shape. As this is the case, we can determine amplitude and phase shift by fitting the general function $f(t) = A \sin(2\pi f \cdot t + \phi) + C$. Of course, we are not interested in the absolute phase ϕ but instead in the phase shift between voltage and current or force.

The phase shifts, as well as the force amplitudes, are shown in table 8.1. Noticeably, the phase shift of the current becomes less than $-\pi/2$ at 20 Hz, which cannot be explained by a simple RC circuit.

However, in this setup the generated voltage is not monitored. Therefore, a slight delay in the voltage signal might be possible. Assuming the current phase shift is in the range of zero to $-\pi/2$, the voltage signal delay has to be in the range of 6.8 ms to 9.4 ms. Nevertheless, the phase shift behaviour does not fit to the

$$\Delta\phi = \tan^{-1}(-2\pi fRC) \quad (8.2)$$

relation we expect from a parallel RC circuit for any of the possible voltage delays. To prevent unknown delays in the voltage signal in the future, the setup was changed to also record the voltage alongside the current signal.

We also note the phase shift of the force signal. Counter-intuitively, this phase shift is independent of the current phase shift. We also see that the force amplitude is reduced with increased frequency.

Overall, the force behaviour in this setup is quite peculiar and can only be explained as the interplay between entropic and electrokinetic forces.

Let us take a deeper look into the threading-out behaviour of the DNA, which is shown in

8. Results

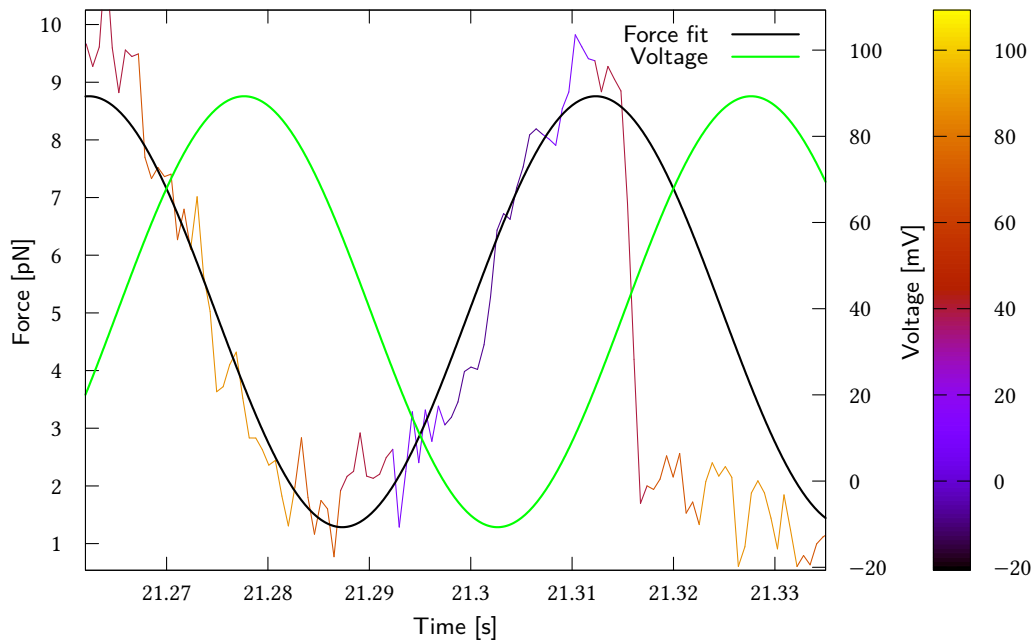


Fig. 8.26.: Detailed force graph of the threading-out behaviour.

fig. 8.26. It takes 2 ms or 3 datapoints. At the point of threading out, the force is just past its maximum and the applied voltage is 37 mV, 12 ms past its minimum. However, the current is negative at this point, at -1.74 nA.

We can therefore conclude that a more in-depth analysis of the AC force behaviour is warranted. Unfortunately, due to the multitude of issues encountered with DNA translocation experiments in general, as described at the beginning of the section, no further experiments were successful.

8.3.6. Free DNA translocation

Due to the low yield of successful controlled DNA translocation experiments and to test the quality of the used DNA, Julian Cremer performed free DNA translocation experiments on nanopores milled in TEM¹⁴⁷. Here, I will only briefly describe the experiments and results.

In free DNA translocation experiments, DNA is introduced in front of the nanopore and a transmembrane voltage is applied. We then monitor the current signal, detecting peaks when the DNA translocates. Due to the sample chamber layout, here the DNA is introduced in the normally *cis* reservoir (Reservoir 3 in fig. 6.2) and a negative voltage is applied, ensuring that the DNA is introduced at the side of the negative electrode.

Fig. 8.27 shows the typical translocation types encountered in free translocation experi-

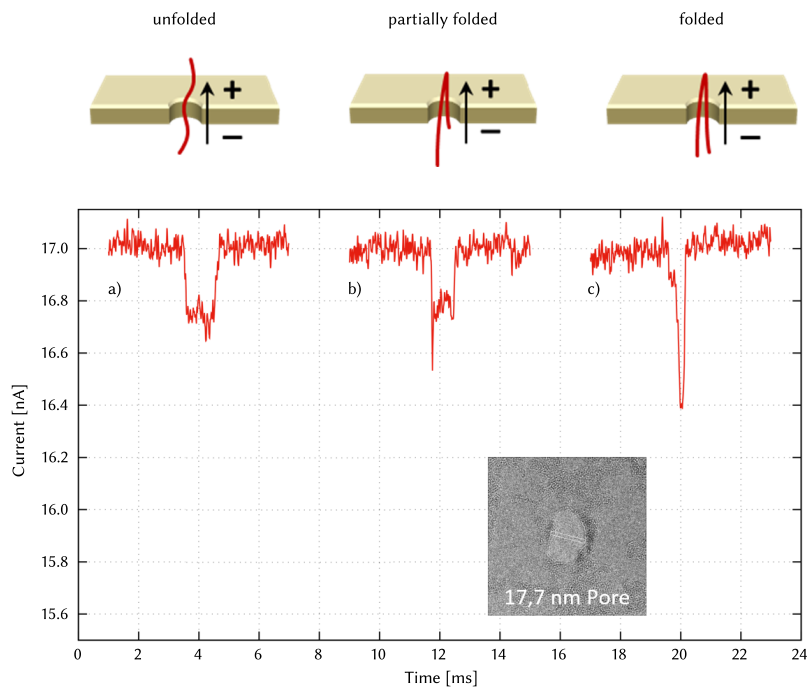


Fig. 8.27.: Different translocation event types encountered with a 17.7 μm MoS₂ monolayer pore. Buffer concentration 1 M. Transmembrane voltage 100 mV. Measurements and graph by Julian Cremer¹⁴⁷

8. Results

ments, based on actual results obtained for a 17.7 nm pore in monolayer MoS₂. However, these events were extremely rare. In a typical 20 min long experiment, 10 to 40 events were recorded. Compared to comparable earlier experiments in our group with silicon nitride nanopores¹⁵¹ as well as comparable reports in literature on graphene^{120,152} and molybdenum disulphide^{153,154} nanopores, this event rate is at least three orders of magnitude below the expected rate.

This, in conjunction with the issues faced by Dennis Kreft in his experiments with the same DNA strongly indicate that there are indeed some deeper issues with the used DNA. Investigations into the cause and exact nature of these issues are still ongoing.

9. Conclusions and Outlook

In this work, I have upgraded the existing optical tweezers setup for high-speed video-based force detection, working reliably at a frame rate of 1555 fps. This upgraded data rate enables in-depth studies on the forces acting on DNA translocating nanopores. It enables the distinction of multi-DNA thread-ins from single DNA thread-ins not just by force magnitude, but by individually resolving each thread-in event.

For boron nitride as a potential membrane material we must conclude that it does not seem possible to create free-standing monolayers by viscoelastic stamping transfer. On the one hand we require the stamping transfer for reliable, non-damaging and residue-avoiding transfer of membranes to the chip. On the other hand, the creation of free-standing molybdenum disulphide monolayers with stamping transfer is possible. Therefore, this work focusses on the MoS₂ monolayer membranes.

For molybdenum disulphide, I have successfully introduced photoluminescence as a reliable monolayer verification method. Transfer of the monolayers to the chip via stamping transfer also proved to be an easy and reliable method.

I investigated the milling of nanopores with Helium Ion and Transmission Electron Microscopy as well as by electrochemical breakdown. Whilst the high momentum of helium ions is unsuitable for monolayer membranes, transmission electron microscopy is shown to be a straightforward and suitable method for the milling of nanopores in the 10 nm to 15 nm range.

Electrochemical breakdown as an alternate method of milling very small nanopores in the 5 nm range were also evaluated successfully. Here, a limiting factor is the used patch clamp amplifier. Exchanging this for a unit with a higher maximum current would allow the use of higher concentrated buffer solutions, possibly increasing yield.

In performing controlled DNA translocation experiments, two main issues limited the experimental success. First, the risk of accidentally contacting the monolayer membrane with the trapped bead was increased by the slow drift of the chip towards the microscopy objective and therefore the focal plane. This is caused by the viscoelasticity of PDMS, which we use as a material for our flow cell. With the incorporation of an autofocus-like measurement of the distance between the focal plane (and therefore the bead) and membrane, I could reduce this

9. Conclusions and Outlook

risk.

The second issue is the still ongoing investigation into the quality of the DNA used for experiments. With the low success rates both in my experiments as well as independent experiments by colleagues with the same DNA, as well as comparison of the translocation event rate during free translocation with both earlier works in our group as well as literature, I succinctly showed that poor DNA quality is the most likely explanation for my low yield.

Nevertheless, in this work I show that the controlled translocation of λ -phage DNA through nanopores in monolayer molybdenum disulphide membranes is possible. The high data rate not only enables discrimination of single and multiple DNA thread-in events. It also allows the investigation of DNA behaviour with an applied AC voltage. In this work, I have shown a first glimpse into the peculiar frequency-dependent behaviour of the forces acting on DNA in a nanopore with applied AC voltage.

For future work, the issue of DNA quality must be addressed. The field of solid-state nanopores in 2D material membranes, especially in conjunction with optical tweezers, is still in its early steps. With the preparation protocols presented herein, a high yield of nanopores is possible. Once sufficient DNA quality is ensured, I suggest experiments of the pore size dependence of the translocation force as well as an in-depth study of the AC voltage behaviour of the force.

As this work establishes nearly atomically thin membranes for nanopores, future work should also investigate if these pores can be used for DNA sequencing using the force signal. Whilst the potential for current-based sequencing in MoS₂ nanopores has already been shown¹⁵⁴, the unique possibility of optical tweezers to seek to any position along the DNA could aid in the sequencing of challenging areas of DNA.

Part III.

**Cell elasticity investigation with
Elasto-Tweezers**

10. Experimental setup

10.1. Optical tweezers setup

The optical tweezers setup for Elasto-Tweezers was conceived and manufactured by Dr. Andy Sischka. It is based on an IX50 inverted microscope (Olympus, Tokyo, Japan) with a 60× water immersion objective (UPlanSApo 60x/1.20W, Olympus, Tokyo, Japan). As we want to perform stretching experiments on cells, we require a double-trap optical tweezers setup. We therefore must split the laser into two beams and modify them in such a way that two distinct focal points emerge. The optics required for this all reside in a microscope deck, which is illustrated in fig. 10.1.

The incoming laser light polarisation is first rotated by a $\lambda/2$ plate and then split by a polarising beam splitter. Assuming the incoming light is linearly polarised in such a way that after the $\lambda/2$ plate, it is rotated 45° in relation to the beam splitter, this gives a 50:50 split as discussed in section 3.2.6. One beam passes straight ahead through a shutter.

The other beam passes a system of four lenses (first and fourth lens: LBF254-100-C; second and third lens: LE1234-C; all converging lenses with $f = 100$ mm; Thorlabs, Newton, New Jersey, USA). These lenses are mounted on three linear stages powered by ultrasonic piezo motors (U-521.23 stages controlled by two C-867 controllers, Physik Instrumente, Karlsruhe, Germany). Additionally, this beam also passes through a shutter. Both shutters are configured to be normally closed (NC) and require energy input to stay open.

The first two lenses, mounted on stages moving in x and y direction, slightly tilt the beam when positioned off-center. Of course, as the two lenses are placed directly behind each other, the focal length of this combination can be approximated as half of the focal length of each individual lens[†]. Therefore, the second pair of lenses is placed 100 mm in front of the first pair of lenses. This recreates a parallel beam which is shifted from the centre axis if the two initial lenses are shifted. Additionally, the second pair of lenses is mounted on a stage moving in the z direction (along the beam propagation). It can therefore also create a slightly convergent or divergent beam. In combination with the microscope objective, this allows not

[†]With $M_i(f) = \begin{bmatrix} 1 & 0 \\ -1/f & 1 \end{bmatrix}$, we get $M_i(f)^2 = \begin{bmatrix} 1 & 0 \\ -2/f & 1 \end{bmatrix} = M_i(f/2)$

10. Experimental setup

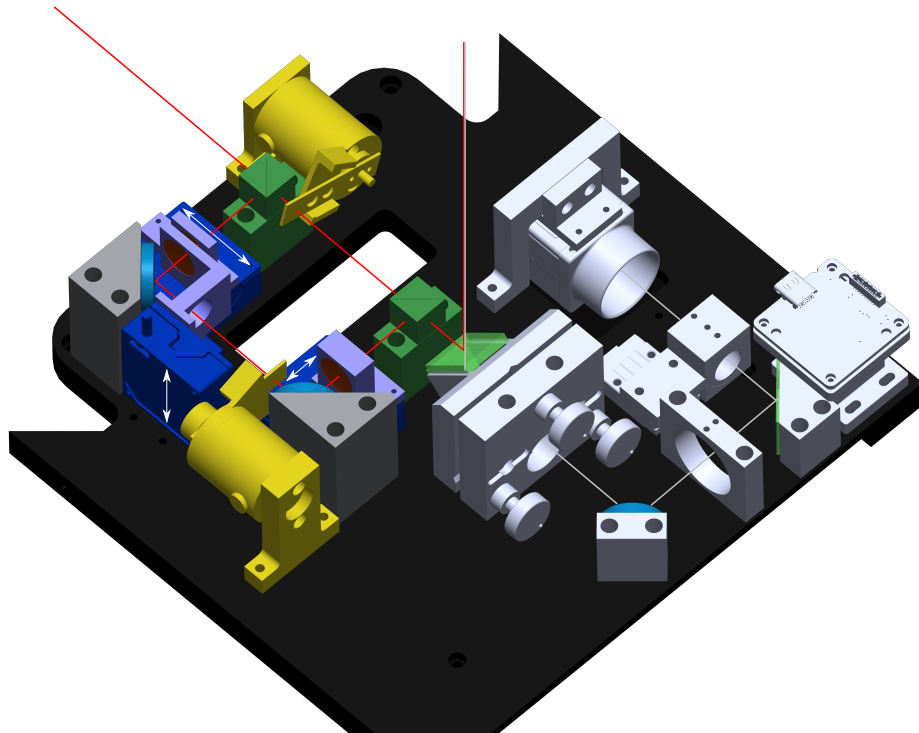


Fig. 10.1.: Optical flow of the laser beams (red) and visible light (grey) in the main microscope deck. Coming from the fibre laser, the beam is split in two by the first polarising beam splitter (green). One of the resulting beams passes through a shutter (yellow) directly into the second polarising beam splitter (green). The other beam passes through two pairs of lenses (red) and a shutter (yellow). In the first pair of lenses, the first lens is mounted (violet mounts) on a linear stage (dark blue, movement direction indicated with white arrows) in x direction. The second lens is mounted on a linear stage in y direction. The second pair of lenses is mounted on a linear stage in z direction. After being merged by the second polarising beam splitter, the laser light gets reflected towards the objective (not shown) by a dichroic mirror (light green).

The visible light passes this dichroic mirror and 80 % gets reflected to the camera system (the remainder goes to the oculars). Again, a mirror (light green) reflects 80 % through a lens onto the detail camera, whilst the remaining 20 % gets passed to the overview camera.

only to shift the beam sideways, but also allows for axial shifts.

The two beams which were split by the first beam splitter are then rejoined by a second beam splitter. They are then projected through the microscope objective via a dichroic mirror.

As a laser source, we initially used the Faserlasermodul 1060nm 2W Yb-1x33 V1.0 which was later used in the nanopore translocation setup. The idea was to tightly wind the fibre to induce an asymmetry into the normally non-polarising fibre. Whilst we were able to obtain polarisation this way, it ultimately proved to be subject to drift (see results section 12.2). Therefore, we replaced this module by a similar module with a PM fibre (Faserlasermodul 1060nm 2W Yb-1x33 PM, Fibotec Fiberoptics, Germany).

In our setup, only one of the two optical traps is moveable, the other is static. To still be able to move both traps independently relative to the microfluidical structures, we also use a three-axis piezo stage similar to the nanopore setup, albeit with a larger movement range (P-527.3CD, Physik Instrumente, Karlsruhe; closed loop travel range $200\ \mu\text{m} \times 200\ \mu\text{m} \times 20\ \mu\text{m}$, 2 nm x/y resolution, 0.1 nm z resolution). For automation, an additional step-motor powered xy-stage is mounted on top (step size: 10 μm , movement range: 20.0 mm \times 19.5 mm).

For force detection and automation, the system is equipped with two cameras. After the dichroic mirror, the visible light passes a 80:20 mirror which reflects the majority of the light towards the cameras, whilst still letting some light pass through to the oculars for study. In the camera path, another 80:20 mirror reflects the majority of the light towards a relatively high-speed CMOS camera (Mako U-029B, USB 3.0, 640 px \times 480 px, 550 fps, 50 % QE; Allied Vision Technologies, Stadtroda, Germany) through a lens for additional magnification. This camera is adjusted to only show the particle trapped in the static trap. An overview camera (UI-3272LE-M, USB 3.1, 2056 px \times 1542 px, 57 fps*; IDS Imaging Development Systems, Obersulm, Germany) sits behind the mirror and collects the remaining light in the camera path. It shows the complete image projected by the objective and is used both for an overview for the experimenter as well as for experiment automation.

10.2. Microfluidics setup

The microfluidics setup consists of the microfluidic chip itself, containing the individual traps and experimental areas, as well as the connections, pumps, switches and reservoirs required to provide beads and cells to the chip and drive them through it in a controlled fashion.

The size of the used beads is a critical parameter for the design of the microfluidics. On the one hand, we want to have beads as large as possible to increase the contact area be-

*The maximum frame rate of 57 fps is only achievable with proprietary drivers and the manufacturer's .NET API, which puts noticeable CPU strain on the system. I therefore opted to use the camera in USB3 Vision compatible mode with only 25 fps which imposes negligible CPU strain

10. Experimental setup

tween beads and cells. On the other hand, smaller particles exhibit an increased trap stiffness compared to larger beads when trapped with constant laser power.

We use beads with a diameter of 15 μm in this work. This size was chosen as it is similar to the size of cells analysed in this work. Therefore, we are maximizing the contact area between cells and beads whilst keeping within the geometric profile necessitated by the cells themselves.

10.2.1. General setup

The general fluid setup is illustrated in fig. 10.2. It consists of three six-port two-position valves. These switches connect the six ports in one of two possible combinations without actuating the connected liquids during the switch. Two primer setups are used to introduce beads and cells to the setup. In the teal configuration, the load is injected manually with a pipette. The injection is performed until the load exits the switch at the port connected to the waste. This ensures that the loop is completely filled. Then, the orange configuration is activated and the carrier can push the load towards the microfluidic chip.

The loop can also be used to block flow by clamping it manually, e. g. with a binder clip. This clamping should only be done in the teal configuration, as this prevents the clamping induced flow from effecting the microfluidics.

After the microfluidic chip, another switch is used. Here, two ports are blocked. This way, only one of the chip outlets is connected to the waste, whilst the other is blocked off.

As a carrier solution, we use Dulbecco's phosphate-buffered saline (DPBS)¹⁵⁵ (Gibco DPBS, Thermo Fisher Scientific, Waltham, Massachusetts, USA) with 1 % w/v Pluronic F-108 (BASF, Ludwigshafen, Germany). The carriers are placed in 15 mL falcon tubes. The flow is controlled via applied pressure with a MFCS-EZ flow control system in conjunction with Fluiwell 1C-15 reservoir caps (Fluigent, Le Kremlin-Bicêtre, France; pressure range 0 mbar to 345 mbar independently settable for both carrier channels).

10.2.2. Microfluidic chip

In this work, our goal is to produce constructs consisting of a cell wedged between two beads to perform cell elasticity measurements. Therefore, we require the microfluidic chip to catch both cells and beads from their respective flows. To be able to reasonably perform automation of the experiment, we want to always trap exactly two beads and one cell reliably in the same position both relative to each other and relative to a predetermined position on the chip. Furthermore, we require a dedicated experimental area that is isolated from the rest of the chip to limit the impact of accidental fluid flow on the experiment.

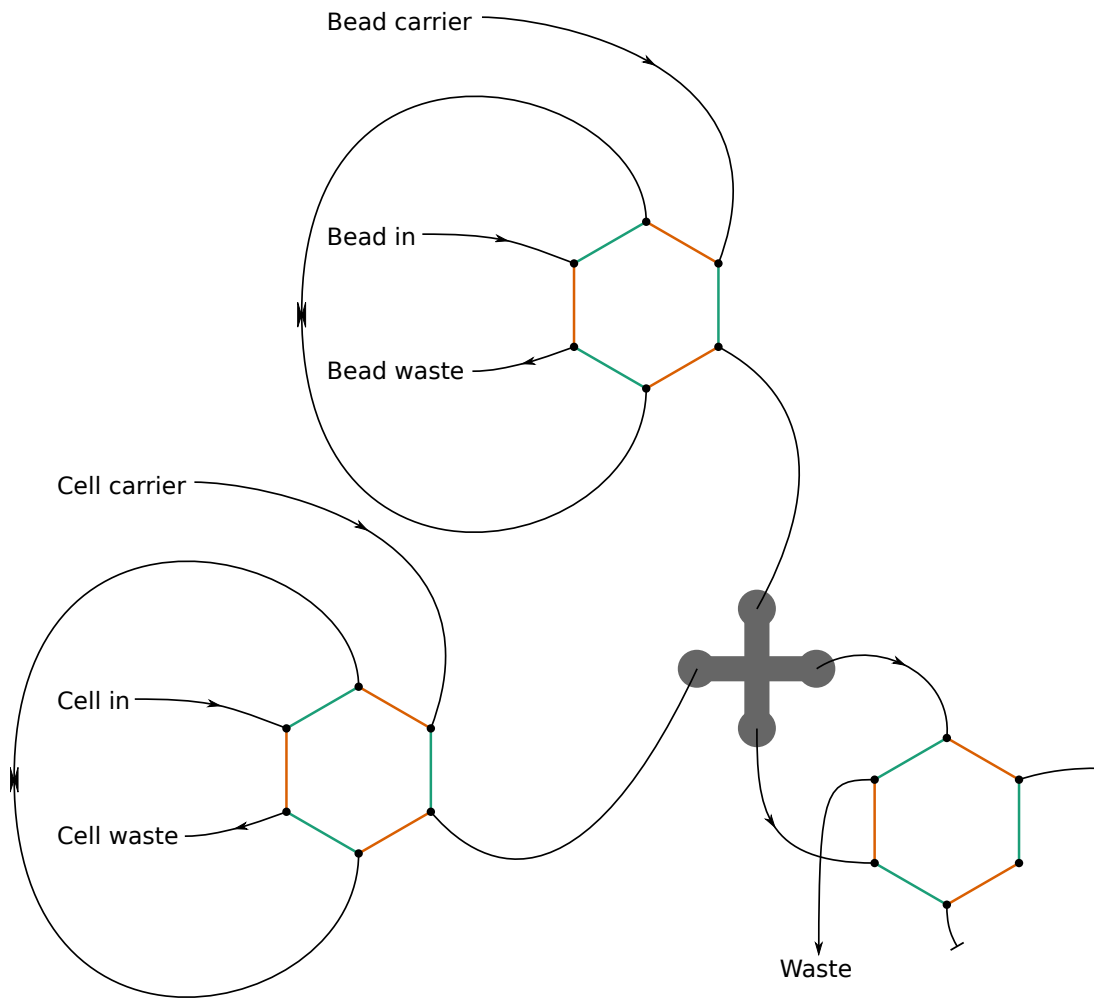


Fig. 10.2.: Illustration of the microfluidics setup. One primer setup each for beads (top) and cells (left) is connected to the microfluidic chip (grey, centre). The outlets of the chip are connected to a switching setup and then to waste. The three six-port two-position valves connect the ports in either the teal or the orange connection.

10. Experimental setup

Additionally, a straight wall of at least 45 μm length should be available in the experimental area as a support against rotation. As optical tweezers cannot apply torque and therefore can't prevent rotation of trapped particles (at least for standard particles and optical tweezers configurations), by leaning the bead-cell-bead complex against a wall we can prevent the formation of a kink during indentation / compression experiments.

Here, we are investigating three different basic cell designs: A design with long corridors and adjacent trapping and experimentation chambers, a simple linear design, and a cross design with separate, orthogonal flows for beads and cells.

The different chip layouts were designed by Bastien Venzac from the University of Twente. Chips in PDMS were manufactured by Bastien as well. Chips in COC were manufactured by Micronit under lead of Elwin Vrouwe.

10.2.2.1. Design 1: Corridors with adjacent trapping chambers

The first microfluidic design is shown in fig. 10.3. Fluid flows from the top to the bottom. First, beads are introduced in one of the inlets at the top. They are divided into the eight long channels (corridors).

As shown in fig. 10.4, small chambers are placed at these corridors in regular intervals. At each chamber, the fluid flow splits into a branch passing through the chamber and a branch bypassing it along the corridor. The length of the bypass is tuned in such a way that the flow resistance along the bypass is higher than through the chamber.

A particle that flows along the corridor will therefore prefer the branch going through the chamber. However, the entry into the chamber along the fluid flow is too small for the particle. It therefore gets trapped in the entry and thereby blocks the bypass, increasing its flow resistance above that of the corridor bypass. Subsequent particles will therefore use the bypass until they encounter the next non-blocked chamber entrance.

Once all chamber entrances are blocked by particles, the flow is briefly reversed. This leads to the particles entering the previous chamber through the backflow entrance. There, they are further trapped by ratchet-like structures that prevent them from exiting the chamber in forward flow.

By performing this loading sequence three times, first with beads, then with cells, and finally again with beads, the components required for elasticity measurements are all placed within the chambers ready for use.

Bastien Venzac evaluated different structures for the trapping chambers themselves, as shown in fig. 10.5.

10.2.2.2. Design 2: Linear design

To improve trapping efficiency and packing density, a simpler linear design was evaluated. The design is illustrated in fig. 10.6 and 10.7. It consists of five areas with five by twenty sets of trapping structures, providing a total of 600 sets per chip.

Each set of trapping structures consists of two traps for beads on one trap for cells. The individual traps consist of a narrowing, 8 μm long path between two barriers. The traps for the beads start with a 15 μm wide opening which constricts to a width of 10 μm . For the cell traps, constrictions down to 3 μm , 5 μm , and 7 μm were evaluated with the opening being 5 μm wider in each case.

Due to the elasticity of the cells, they will pass through the 10 μm constriction of the bead traps when sufficient pressure / flow is applied. For loading the chip, we now first introduce cells until all or most of the cell traps are filled. Then, after flushing with buffer solution, beads are introduced which will be trapped in their respective trapping structures. Afterwards, experiments can be carried out in the free space between the trapping structures.

Obviously, backflow must be avoided at all costs, as this would remove particles from their traps.

10.2.2.3. Design 3: Cross design with integrated experimental areas

The earlier designs either lacked in trapping efficiency (design 1) or had no separate areas for stretching experiments (design 2). This third design takes the general approach for high efficient trapping by placing the traps in the middle of laminar flow carrying the particles to be trapped. By using a cross design with two orthogonal flow directions, dedicated traps for beads and cells are possible. As we require two beads per cell, the bead traps are sized to fit two beads whilst the cell traps only fit a single cell each.

The overview of the design with inlets and outlets is shown in fig. 10.8. A single microfluidic chip contains four layouts, each rotated by 90° in such a way that the two inlets and two outlets are placed at the edge of the chip.

The central structure and the layout of the individual trapping structures are shown in fig. 10.9. Loading of beads and cells is performed sequentially: First, the cell inlet and outlet are closed and beads are introduced. The flow of beads should remain active until most or all trapping structures have two beads trapped. After clearing out any non-trapped beads with buffer solution, the bead inlet and outlet are closed and the cells can be introduced in turn. Again, once the cell traps are filled, we flush with buffer solution.

Due to the trap layout, the trapped beads are not affected by the flow of cells. However, the system is quite sensitive to backflow which must be avoided.

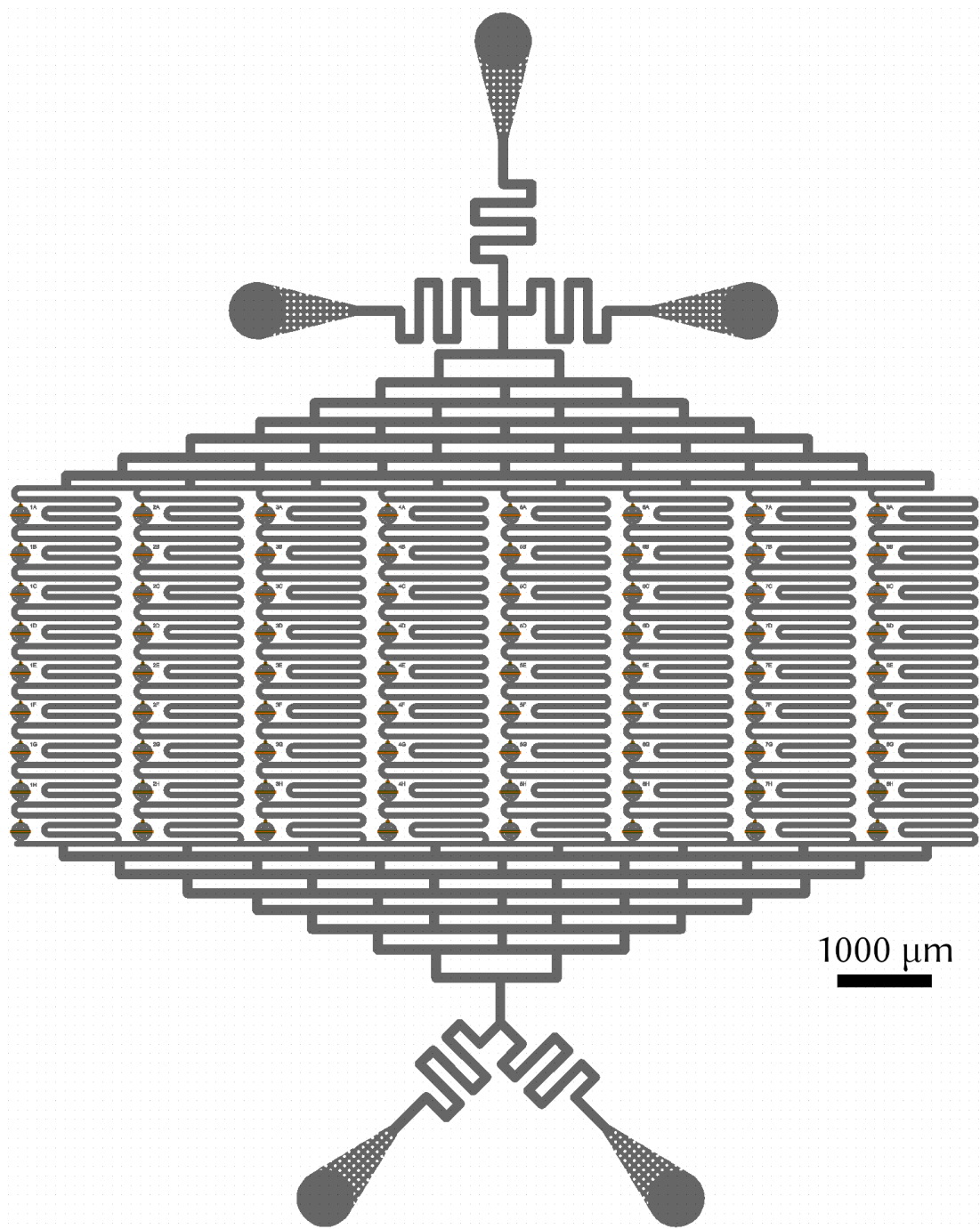


Fig. 10.3.: Overview of design 1.

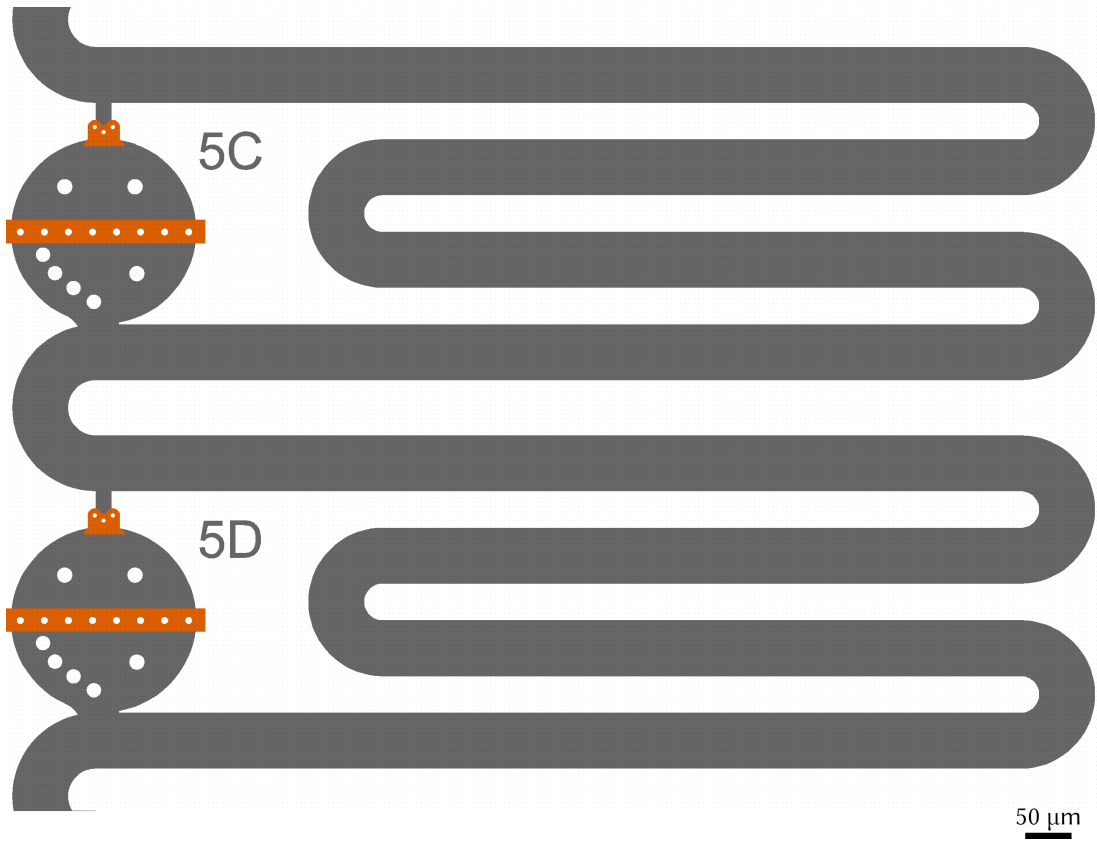


Fig. 10.4.: Detail of design 1.

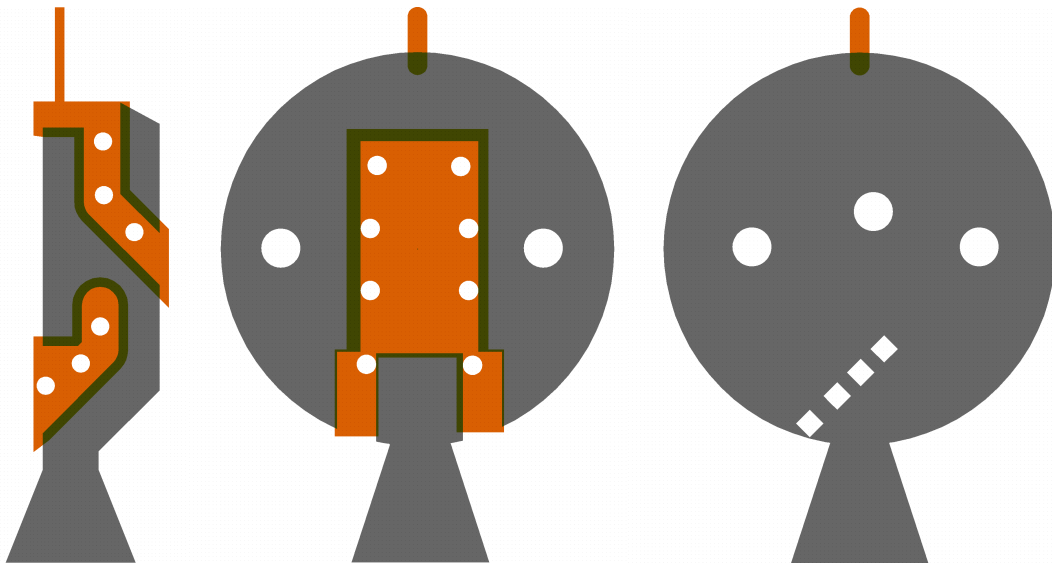


Fig. 10.5.: Different chambers for design 1

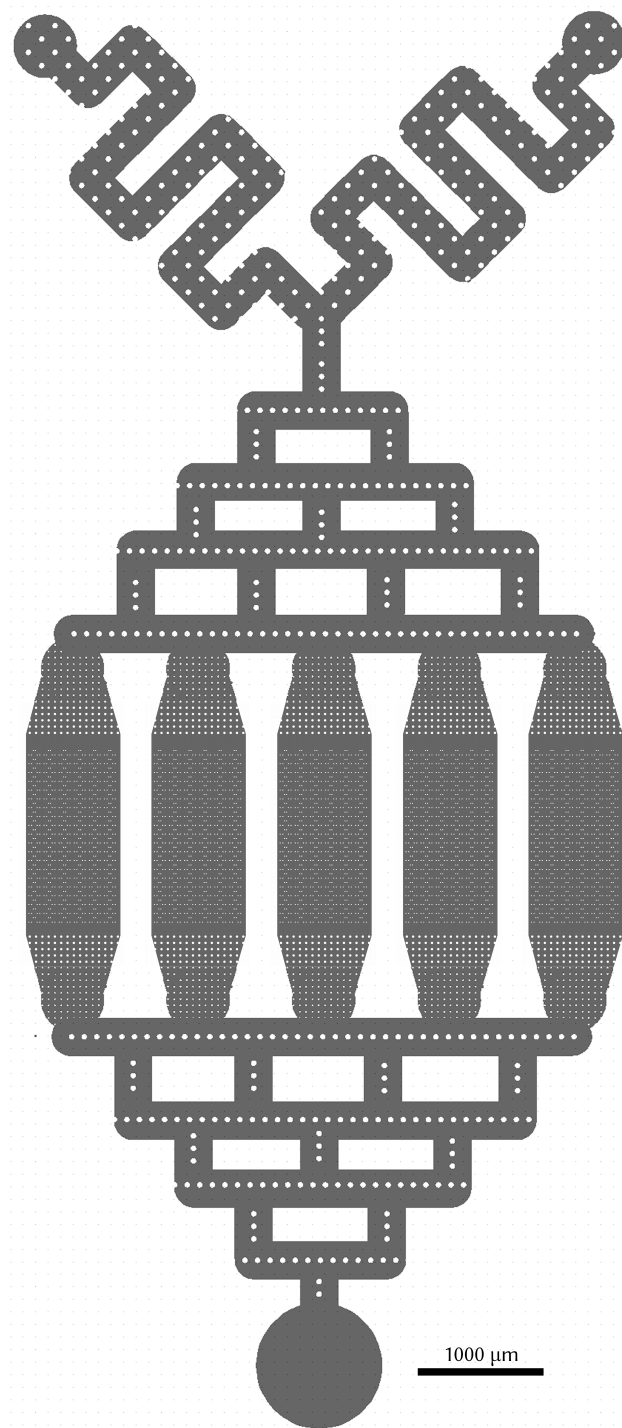


Fig. 10.6.: Overview of design 2.

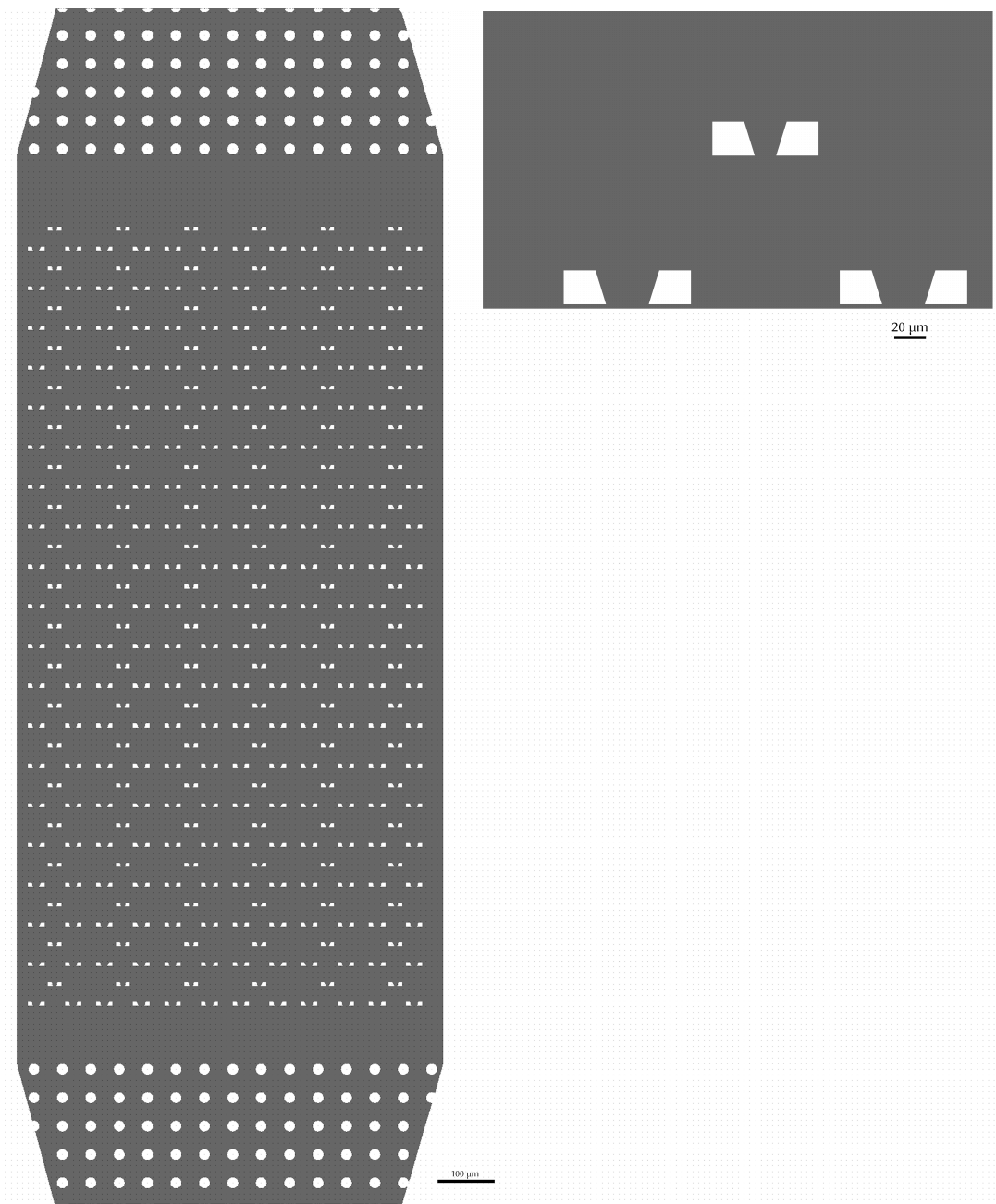


Fig. 10.7.: Detail of design 2.

10. *Experimental setup*

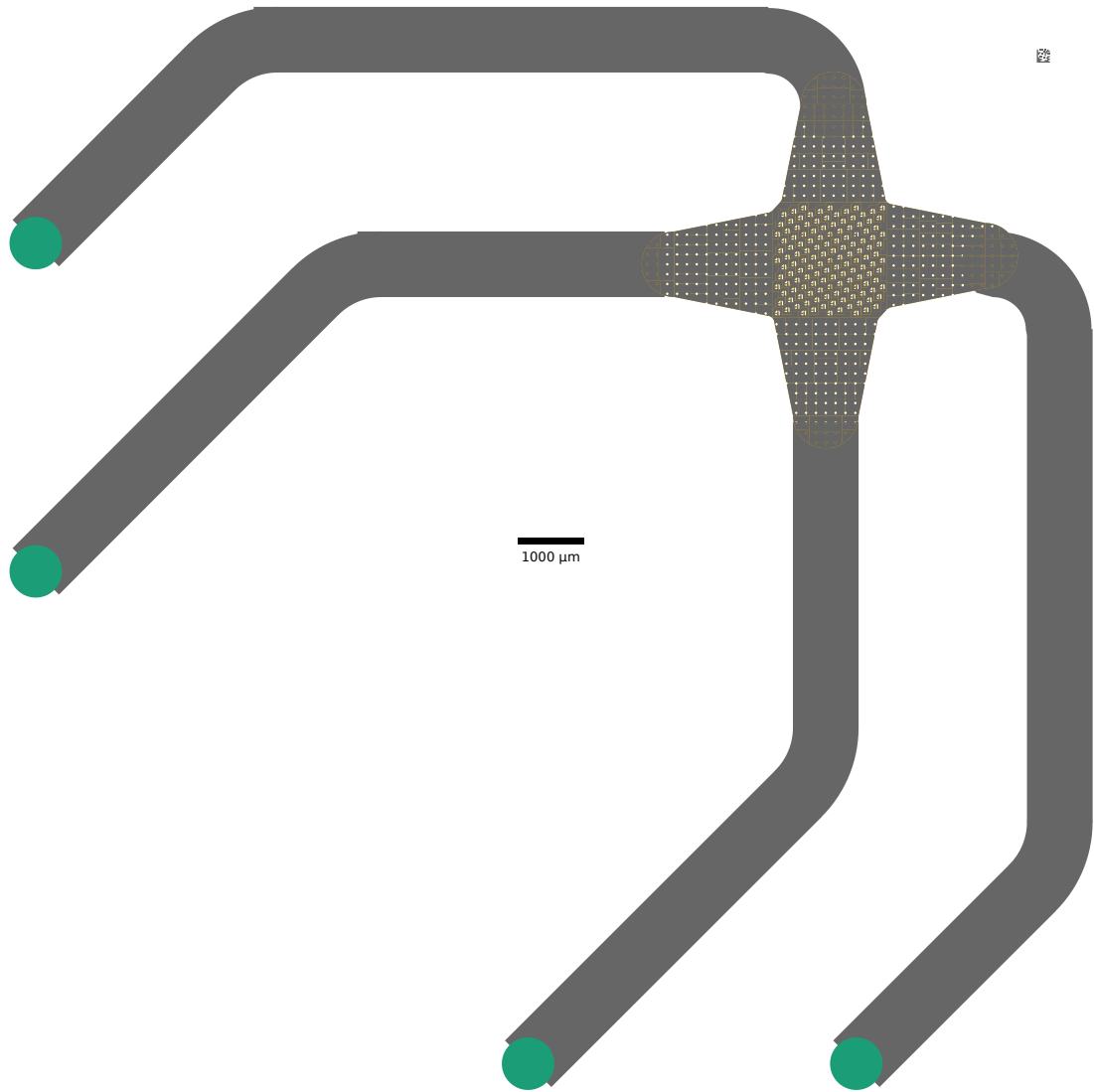


Fig. 10.8.: Overview of design 3. Teal circles are inlets / outlets. Grey areas are 20 μm high, Yellow areas are 5 μm high.

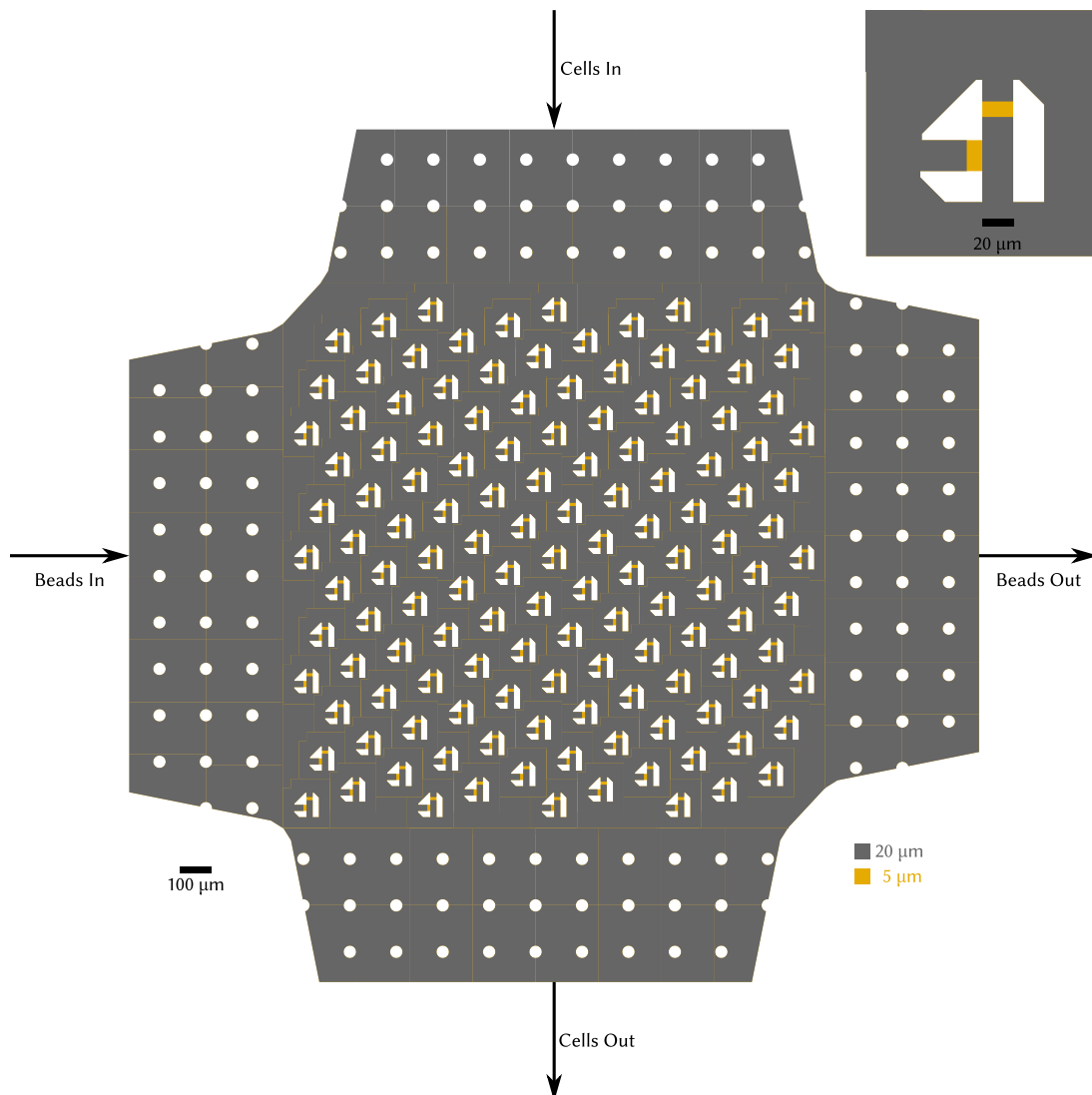


Fig. 10.9.: Detail view of design 3. The central area consists of 135 identical trapping structures shown in the inset at the top right. The channels in each trapping structure are $20\ \mu\text{m}$ wide and $20\ \mu\text{m}$ high with $5\ \mu\text{m}$ high barriers. The barriers separate the trapping structures into a trap for two beads (left), a trap for a single cell (top) and an area for stretching experiments (bottom).

10. Experimental setup

After filling the trapping structures, experiments can be performed. To this end, first a bead is taken from the trap and moved into the experimental area. This is followed by a cell and then another bead. As the optical forces that can be applied to cells are rather small, care must be taken when moving them. In practise, it is typically better to use the cell from the trapping structure below the one where experiments are performed, as this limits the distance that the cells have to travel. This limitation still leaves 120 traps for experiments.

When experiments are finished, the assembled bead-cell-bead complexes are kept in the experimental area. Here, forward flow must be avoided and backflow provides no issues. This can be used to introduce cell viability indicators like trypan blue after the stretching experiments have been performed.

10.2.3. Temperature control

For optimal results with cell experiments, temperature should be controlled at 37 °C. To prevent convective flow due to temperature gradients, the complete microfluidic system should be temperature-controlled to the same value. Therefore, the optical tweezers setup was placed in a 60 cm × 60 cm × 80 cm PMMA box (thickness: 6 mm) for thermal isolation. Heating is provided by a 400 W silicone heater (thermo Flächenheizungsgesellschaft, Rohrbach, Germany) with profile heat sinks and two fans. The heater is controlled by a digital on/off temperature control device (ESM-3710-N; Emko Elektronik, Bursa, Turkey). The Pt100 temperature sensor for control is placed next to the chip. Target temperature is set to 37 °C with the hysteresis set to 2 K. This means that the heating element is switched on when the temperature drops below 35 °C and is switched off once it reaches 37 °C

For testing the system, additional thermocouples are installed. One thermocouple is attached to the microscope objective. A second thermocouple is placed next to the six-port switches.

10.3. Software

The setup is controlled by a software that I wrote in LabVIEW. The particle detection algorithm used is the same as in the nanopore setup. Due to the ever increasing core count of modern processors¹⁵⁶, the software is designed for easily adjustable parallelisation.

The software runs on a single workstation (Precision Tower 5820, Dell Technologies, Round Rock, Texas, USA; Intel Xeon W-2155 10 × 3.3 GHz, 16 GB DDR4-2666 ECC memory, array of four 3 TB hard drives in RAID-0 mode, nVidia GeForce GTX 1050 for use with CUDA¹⁵⁷). This system is capable of performing real-time edge detection at the full frame rate of 550 fps.

However, the system becomes quite unresponsive when performing this detection with highest quality settings.

In this setup, we are interested in radial forces acting on the trapped particles, which can also become quite large, thus leading to large particle deflections from rest position. This poses a challenge to edge detection, as obviously the optimum region of interest for a deflected particle is shifted as well, as described in section 3.4.2. Here, we use the moving average of the last 100 detected particle positions to prevent a single wrong detection to move the region of interest beyond the sensible range.

For live feedback during experimentation, this system is completely sufficient. However, as this work is explorative we still record the raw video footage of both the detail and overview camera similar to the nanopore setup. This data is originally stored in an uncompressed raw format. After experimentation, the video is repacked into files comprising 15 s of either overview or detail camera footage with each frame compressed lossless as a PNG string. In the offline analysis batch edge detection process, a two-pass process is used where a first pass determines the position of the region of interest for the second pass, which in turn is used as the region of interest for the first pass of the next frame. The result of the first pass is sanity-checked and the first pass repeated with the user-defined starting region of interest if necessary.

With the third microfluidic design and using COC chips with known orientation, the system is further able to perform cell elasticity measurements automatically. It can detect the location of trapping structures and evaluate if the required number of cells and beads are available. It then automatically traps beads and cells and moves them into the experimental area. It then performs stretching cycles as defined.

This automation is only available for the final COC chip layout as it requires a predefined orientation of the chip to reliably perform the automated detection of the trapping structure.

11. Experimental protocols

11.1. Cell culture

Cell culture was performed in T25 flasks in an incubator at 37 °C with 5 % CO₂. Culture medium was exchanged three times per week (Monday / Wednesday / Friday or Tuesday / Thursday / Saturday depending on batch). Once per week, passaging down to 10 % is performed during cell culture medium exchange. The remaining 90 % are filled into Eppendorf tubes for use in experiments that or the next day.

Experiments in this work are carried out on HEK-293 cells. This cell line was derived from human embryonic kidney cells by transfection with sheared adenovirus type 5 DNA⁷. The cell line is characterised as being very easy both to grow in culture as well as to transfect. For this reason, it is a widespread used cell line⁸ and serves as a model cell line in this work. For HEK-293 cells, a cell medium of 500 mL DMEM, 50 mL FBS, and 5 mL Amp/Strep is used.

In addition to HEK-293 cells, we also cultured fibroblasts provided by the Heart and Diabetes Center NRW which were sampled from patients both with and without genetic mutations. Cells were provided blinded. Due to the issues encountered in this work, no results were achieved for the fibroblasts. For culture, we use the cell medium for HEK293 cells with added 25 mL 0.5 M HEPES, 5 mL NEAA, and 450 µL β-Mercaptoethanol.

11.2. Manufacture of microfluidic chips

11.2.1. PDMS chips

PDMS chips are manufactured by Bastien Venzac. Silicon wafers are prepared by standard lithography methods. These are then used as a mold. The liquid PDMS is poured onto the wafer and cured. Individual chips are cut out and inlets and outlets are added with a hole puncher. Similarly to the description in section 6.2, the PDMS pieces and glass coverslips are treated in oxygen plasma for hydrophilisation. They are then combined to form a microfluidic chip.

This method follows the established methodology^{10,11,158,159} and is most suitable for microfluidic prototypes.

11. Experimental protocols

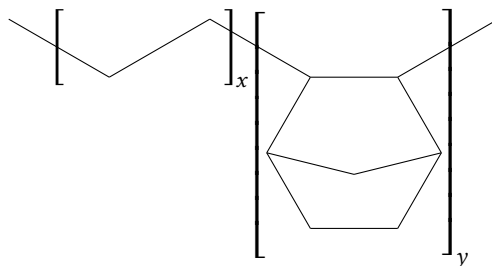


Fig. 11.1.: Chemical structure of cyclic olefin copolymer (COC)

11.2.2. COC chips

Cyclic olefin copolymer (COC, see fig. 11.1 for the chemical structure of the polymer) chips are manufactured by Micronit, who have a wide range of experience in the manufacture and optimisation of COC microfluidics^{160,161}. Structures are created with lithography and micromilling in a silicon wafer. This is then used to create re-useable silicone rubber stamps. These stamps are heated and the structures embossed in COC. The chips are sealed with a 100 μm thick COC foil.

Due to the lithographic production process, design-specific preparation must be performed which is both time and cost intensive. Therefore, only the final microfluidic design, once evaluated positively in PDMS, was used for the production of COC chips.

11.3. Bead surface modifications

Cell elasticity experiments can be performed in two regimes: we can either indent cells to squeeze them, or pull on the cell to stretch them. Whilst squeezing experiments do not put special demand to the interaction between beads and cells, for stretching experiments those do exist.

For optimal stretching experiments, we require a rapid and stable binding between beads and cells. To enable flexibility with regards to the cells analysed, non-specific binding should be sought. However, care must be taken that the beads do not interact with the microfluidic chips, which are made of PDMS or COC.

Here, we are using polystyrene beads, which are standard particles for experiments with optical tweezers^{45,50,68,162} and have been used in the first part of this thesis as well. We use uncoated particles as well as both amino and carboxyl coated particles. The amino coated particles have a functional group density of 0.3 nmol mg^{-1} , which corresponds to a surface density of $4.7 \times 10^5 \mu\text{m}^{-2}$. For the carboxyl coated particles, we get values of 2.5 nmol mg^{-1} and $3.76 \times 10^6 \mu\text{m}^{-2}$. The particle diameter is 15 μm in all cases.

11.4. Declogging of microfluidic switches

The six-port two-position valves used as switches in our microfluidic setup are prone to clogging, especially in conjunction with the used 15 μm beads. Therefore they should be rinsed regularly, preferably after each experiment.

For rinsing, the valve head is disassembled and the switch heads are placed in ethanol and manually rinsed with cotton swabs. After reassembly, we first repeatedly pass ethanol through all 6 possible connections in both directions at high pressure (e. g. with a syringe attached to tubing). This is followed by a rinsing cycle with pure water to prevent ethanol residues.

11.5. Preparation of solutions

As a basic buffer solution, we use PBS with 1 % w/v Pluronic F-108 as described in section 10.2.1. For the bead solution, we mix 50 μL from the stock solution (2.5 % w/v) with 500 μL basic buffer solution. This results in 141×10^3 particles or a concentration of $1286 \mu\text{L}^{-1}$

Cells are prepared by first vortexing the Eppendorf tube for 30 s on level 3 with a Vortex-Genie 2 (Scientific Industries, Bohemia, New York, USA). We then quickly aspirate and dispense 75 μL at the bottom of the tube five times. The sixth aspiration of 75 μL is then dispensed into another tube with 500 μL basic buffer solution and gently stirred with the pipette tip three times. It is then again vortexed for 30 s on level 3. Afterwards, it should be used immediately in the experiment. If there is a delay between preparation and use, the tube should be stored in a water bath at 37 °C and vortexed again for 30 s on power level 3 immediately before use.

11.6. Installation and preparation of microfluidic chip

First, the falcon tubes for the carrier solution are filled with our basic buffer solution and capped with the Fluiwell 1C-15 reservoir caps. Whilst the falcon tube for the beads' carrier solution should be filled completely, the tube for the cells' carrier solution should leave a few mL space for initial filling. Three falcon tubes for the waste lines are taped to the side of the microscope, one each for bead waste, cell waste and waste from the chip (see fig. 10.2).

The chip is visually inspected for any damage and placed in the chip holder with the Micronit logo in the top-right corner and the reservoir openings on the upper side. The tubing is connected according to fig. 11.2, taking care to add the ferrules to prevent leakages.

Taking care that both input switches as well as the output switch are set to the orange position (according to fig. 10.2), a pressure of 1000 mbar is applied to the bead inlet. This quickly fills the chips as well as the bead outlet line and, via backwards filling, the cell inlet

11. Experimental protocols

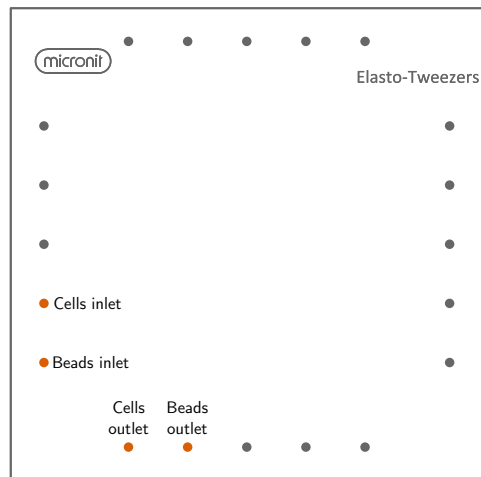


Fig. 11.2.: Schematic of the chip layout showing the Micronit logo, Elasto-Tweezers label and inlets / outlets. Only the four orange inlets / outlets are used.

line. During filling, both inlets should be switched to the teal position for a few seconds intermittently to ensure that no air pockets are trapped there. As soon as the level in the waste reservoir rises, the outlet switch should be set to the teal position. Once it rises again along with the level in the falcon tube for the cells' carrier solution, the pressure is switched off.

For introducing beads into the chip, first the outlet switch is set to the orange position. The cell valve is switched to the teal position. Then, the cell loop is clamped shut and the cell valve switched to the orange position. Then, the bead valve is switched to the teal position. The bead solution is pipetted into the bead inlet at the valve until the bead loop is completely filled and the solution reaches the tubing towards the bead waste. Typically, 100 μL of solution are sufficient for this. Then, the bead valve is switched to the orange position and pressure is applied. For beads, the maximum pressure of 1000 mbar is used.

For introducing cells, the same process is used. First, the outlet switch is set to the teal position. The bead loop is clamped shut and the cells are introduced into the cell loop analogue to the instructions above. The applied pressure should be limited to 300 mbar for fibroblasts. For HEK293 cells, 1000 mbar can be used without damaging the cells.

11.7. Cell viability verification

After experiments, the viability of the tested cells should be verified. Here, I am using trypan blue (0.4 % solution in PBS; GE Healthcare, Chicago, Illinois, USA) to perform the standard dye exclusion test¹⁶³. The trypan blue solution is introduced into the microfluidic chip in a way to prevent the tested cells from moving. For the third design, this means introducing the solution from the cell outlet port.

After incubation for 3 min, the cells are checked for dye stains. Unstained cells have an intact cell membrane and can be considered viable. Stained cells no longer have an intact cell membrane and are therefore considered non-viable. Care must be taken to limit the incubation time to below 5 min as trypan blue itself is cytotoxic and longer incubation will therefore lead to cell death and false results.

Even though the cell viability is only accessed indirectly by determining the intactness of the cell membrane, it is nevertheless an important tool for result selection. Only the results of cells determined to be viable after experimentation should be used for statistical purposes afterwards.

12. Results

12.1. Temperature control

As discussed earlier, we wish to perform experiments at 37 °C and need to avoid convective flows due to temperature gradients. This posed a greater problem than originally anticipated, as I show below.

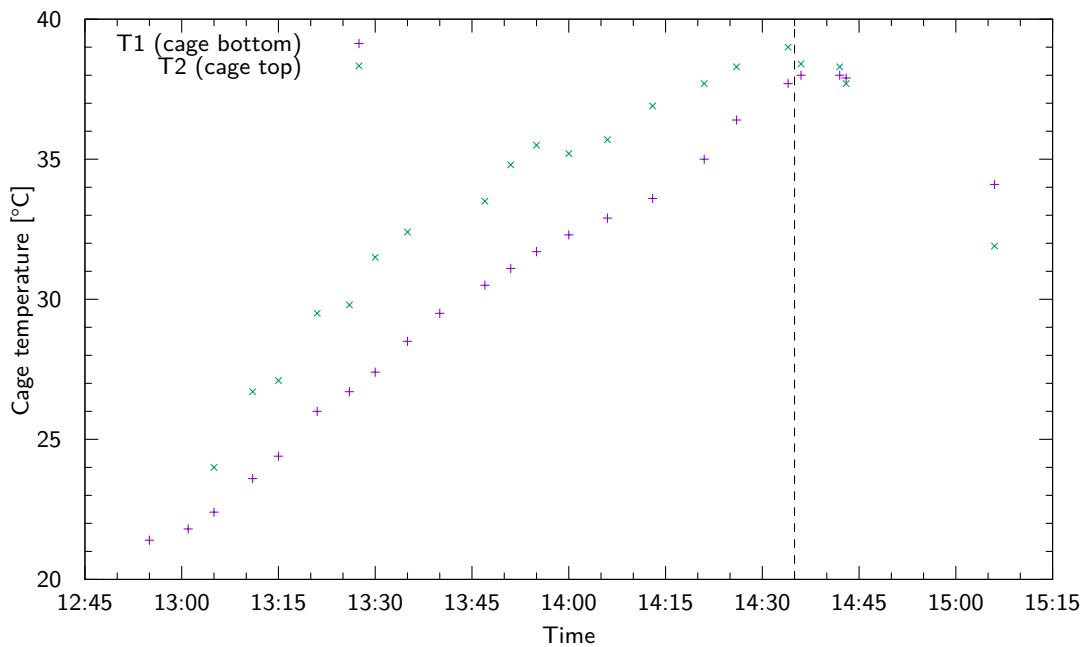


Fig. 12.1.: Temperature behaviour in temperature isolation box. T1: Thermometer / hygrometer on the bottom of the box. T2: Thermocouple two thirds towards to top of the box. Heating element is switched off at 14:35 (dashed line)

As we can see in fig. 12.1, the heating power is sufficient to heat up the box to 37 °C in 1.75 h. However, we can also see that there is a noticeable temperature gradient between the thermometer at the bottom of the box (T1) and a thermocouple that is attached two-thirds of the way up on a side panel of the box.

We further notice that with the temperature controller set to 37 °C, temperatures mea-

12. Results

sured at the valves fluctuate by ± 5 K. In this range, the density of water fluctuates by 1.7 ‰ to 1.9 ‰¹⁶⁴. Assuming the reasonable tubing length of 0.5 m between reservoirs and chip, this results in a liquid movement of up to 1 mm both in forward and backflow. For stable microfluidic trapping, this is of course completely unacceptable.

In fact, even a temperature gradient of just 0.1 K along 0.5 m of tubing results in a fluid shift of 10 μm . Therefore, a simple temperature control is not possible for this setup.

There are two possible solutions to this issue: First, we could significantly reduce tubing length by integrating all valves and switches into the microfluidic chip. For an end product, this is the preferred solution as it not only mitigates temperature gradient issues, but also reduces the amount of liquids, cells, and beads required for experiments. Due to the prototypical nature of this experiment and difficulties in production of microfluidic chips by our partner Micronit, this solution was not possible here.

Therefore, I chose the second solution, which is to forgo temperature control in this way and instead only raise the temperature in the laboratory as far as possible with heating and window insulation. This allowed for approx. 25 °C fluid temperature.

12.2. Polarisation

A constant polarisation is a prerequisite for constant trapping power and therefore constant force conversion factors. To verify that this is fulfilled with the non-polarising fibre laser module with the tightly wound to induce a polarisation, I moved both traps to the same position and trapped one 4.37 μm bead, regularly switching which trap is active. From the resulting data, Allan variance was calculated and automatically fitted to each 1 s block of data.

The resulting time-dependency of the trap stiffness is shown in fig. 12.2. Quite obviously, the trap stiffness is neither identical for the two traps, nor is it constant. Here, the secondary, moveable trap is stronger than the primary trap. A similar evaluation four days prior, after keeping the laser on continuously for six hours, is shown in fig. 12.3. Here, trap stiffness is relatively stable over 12 min.

However, both measurements were performed with the system tuned to equal trap stiffness. As waiting multiple hours for the laser to warm up for a relatively stable polarisation and making sure that the laser power is split 50:50 before each measurement is not feasible, we replaced the laser module with a polarising fibre laser module.

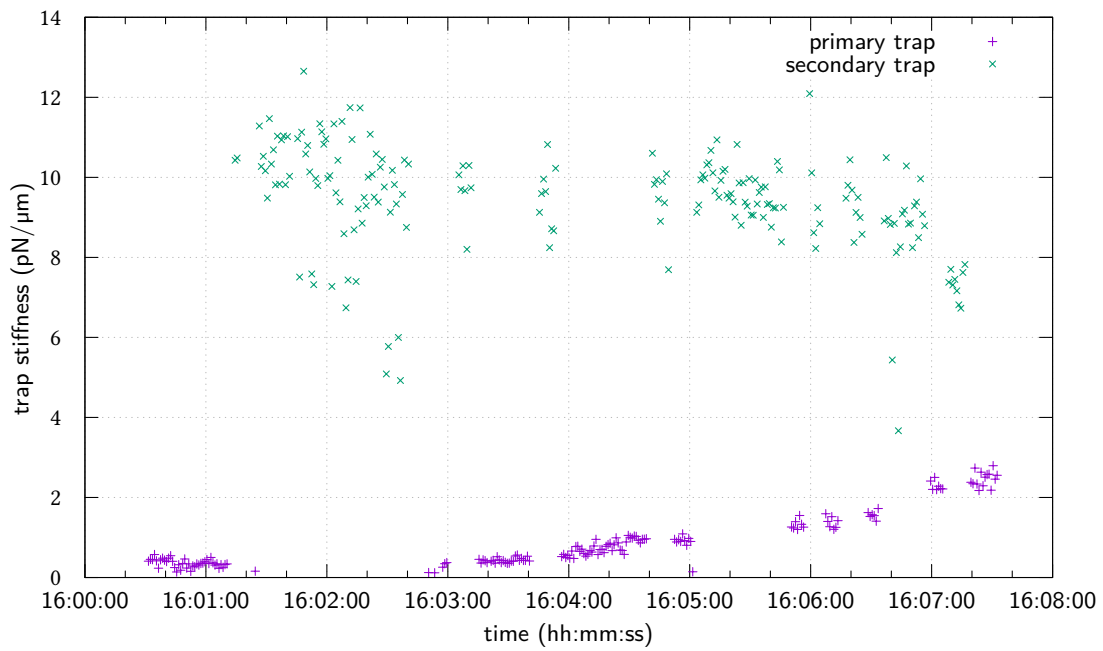


Fig. 12.2.: Time-dependent variation of trap stiffness for primary and secondary trap, trapping the same particle. Laser was turned on at approx. 15:15, 45 min before the start of this measurement.

12. Results

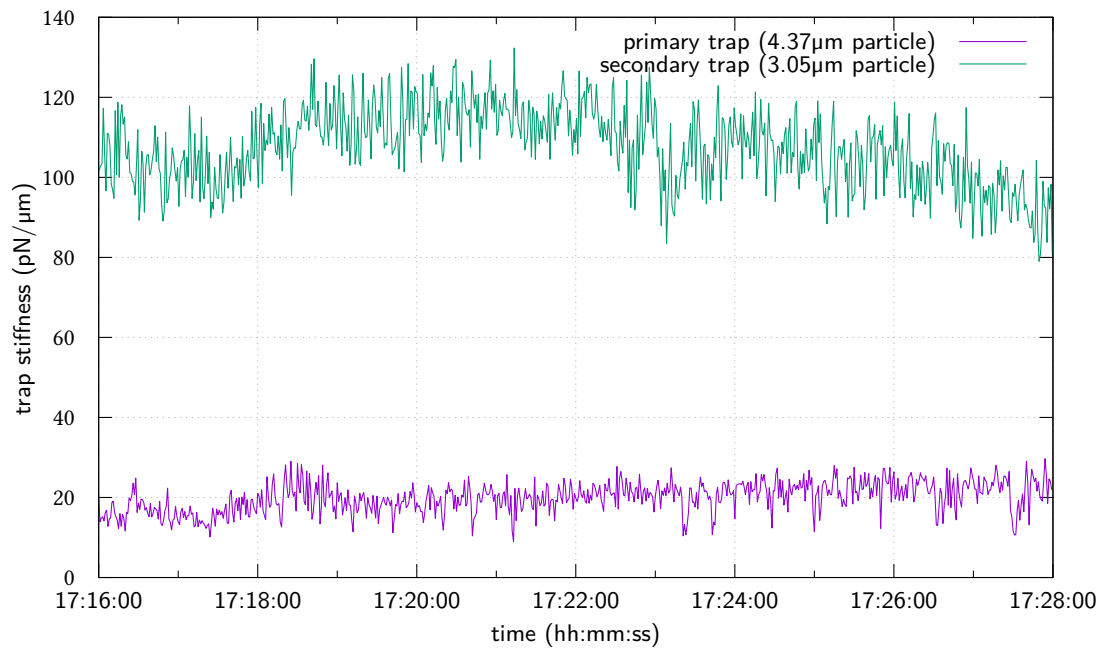


Fig. 12.3.: Time-dependent variation of trap stiffness for primary and secondary trap, trapping different particles simultaneously. Laser was turned on at approx. 11:30, nearly 6 h before the start of this measurement.

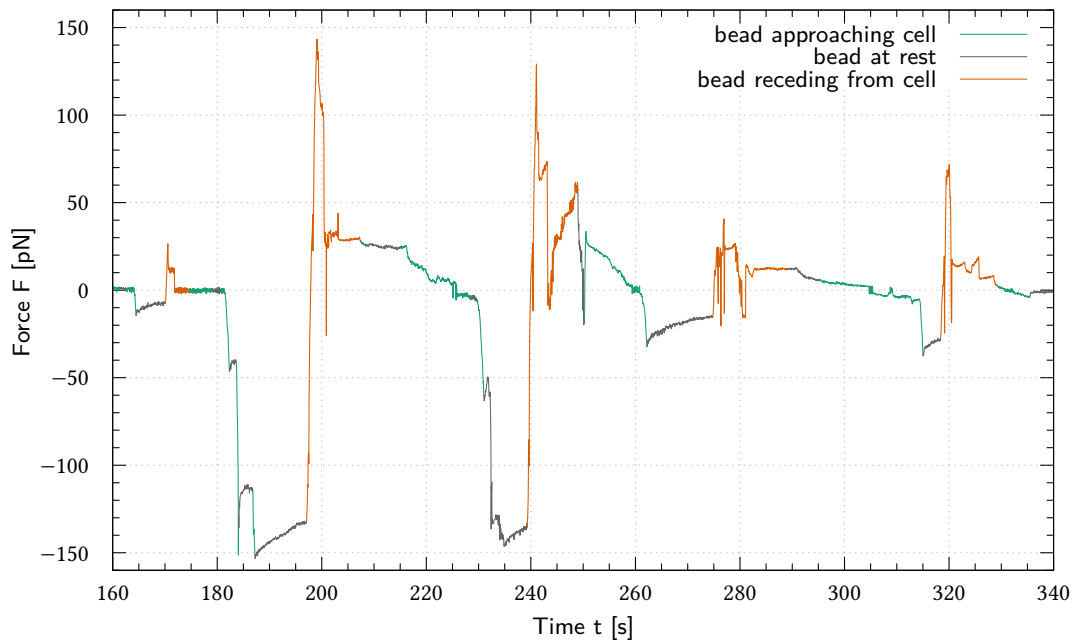


Fig. 12.4.: Measurement of bead-cell rupture forces (positive values) depending on previous adhesion forces (negative values). Bead is trapped in a single-beam optical tweezers setup. Cell is attached to a glass micropipette. Bead velocity during movement is $1 \mu\text{m s}^{-1}$
 Colour coding: Teal: bead is approaching cell, grey: bead is stationary, orange: bead is receding from cell

12.3. Bead surface modifications

12.3.1. Carboxylated beads

In the early stages of the project, I investigated the adhesion between beads in cells in a single beam optical tweezers setup that is usually employed for the investigation of the stretching behaviour of DNA. Here, we partially aspirated a cell with a glass micropipette for immobilisation. A carboxylated 15 μm bead is optically trapped.

For force detection, we record the low-framerate video (25 fps) to an AVI file for later analysis. Using the backscattered light based force detection integrated in the setup does not yield meaningful results due to the immediate vicinity of the cell.

The cell and bead were brought in contact with varying forces for approx. 10 s. Afterwards, we pull on the bead until we see a rupture of the adhesion. The resulting data is shown in fig. 12.4.

From the results, we can observe two conclusions. First, when applying a certain force to a cell-bead complex with carboxylated beads for 10 s, the complex will typically withstand an equal pulling force before rupture.

Second, even after rupture of the primary binding between cell and bead, we still observe a slight and constant pulling force acting on the bead in the range of 10 pN to 30 pN. This force cannot be observed after the first, very slight coupling with only 14 pN applied force, but only after the second, much stronger coupling with up to 153 pN force. This behaviour can be explained by the formation of cell tethers^{165–167}.

Since the surface of the carboxylated beads is charged, beads adhering to the walls of the microfluidic structures as well as beads clogging tubing and valves were a major issue. This could be alleviated partially, but not completely, by using 1 % w/v F108.

12.3.2. Amino coated beads

In addition to carboxylated beads, I also investigated amino coated particles. Results both with regards to adhesion to cells as well as adhesion to microfluidic structures were comparable to carboxylated beads.

12.3.3. Uncoated beads

In contrast to carboxylated beads and amino coated beads, unmodified polystyrene beads did not exhibit immediate adhesion to cells upon contact. However, applying approx. 40 pN force for five minutes reliably leads to a cell-bead adhesion that is stable to up to 150 pN.

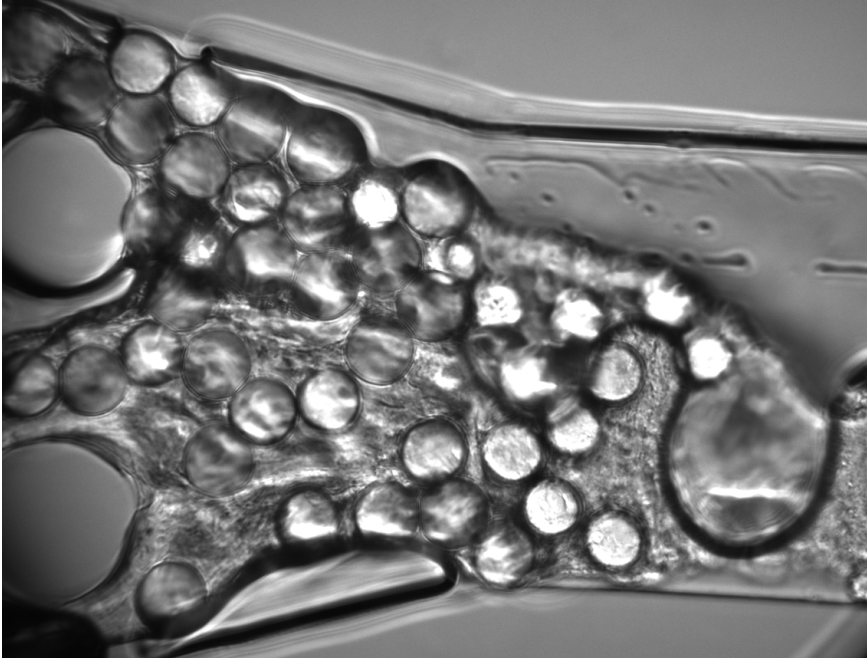


Fig. 12.5.: Example of clogging near the inlet (to the left) of a PDMS chip with design 1

As expected, the adhesion to tubing, valves and the wall of microfluidic channels is also greatly reduced compared to coated particles. By using 1 % F-108 in the carrier solution, this adhesion could be suppressed completely. Conversely, reducing the F-108 concentration to 0.5 % reintroduces adhesion issues.

As this work focusses mostly on the evaluation of microfluidic layouts and experimental protocols, I found uncoated beads to be a suitable tool which is used for most of the work. The great reduction of beads adhering to microfluidic components is well worth the reduced adhesiveness to cells. Indentation experiments can still be performed without adhesion and for stretching experiments, the five minute adhesion period provides a possibility for experiments, albeit at a lower rate.

12.4. Microfluidic design performance

12.4.1. Design 1: Corridors with adjacent trapping chambers

There are three main challenges with the first microfluidic design. First, due to the overall length of the fluid channels in the chip, it exhibits a high fluid resistance. It therefore requires relatively high forces to yield even moderate flow velocities. Additionally, the higher length

of narrow channels provides ample opportunities for clogging.

Clogging however is not a major issue in the long channels. The major clogging issues are instead found directly at the inlets and outlets. As the chips with this design are made out of PDMS, a 0.8 mm hole puncher is used to create the inlets. PEEK tubing is inserted in these holes to provide microfluidic access. Both partial channel collapsing due to integrity loss by hole punching as well as difficulties in height adjustment of the PEEK tubing introduced a large clogging potential near the inlet areas, further restricting the flow towards the microfluidic trapping structures. An example of complete clogging near the inlet is shown in fig. 12.5.

Finally, whilst trapping of beads and cells in the channel entrances during the forward flow was successful in the vast majority of cases, the transfer to the chambers by backflow was not. Here, approximately half of the trapped particles did not enter the chamber and instead bypassed its entrance. Whilst originally, a backflow-preventing gate was intended to be placed between the forward and backflow entrances of each chamber, this could not be implemented in a simple few-layer PDMS chip.

The further exacerbate the issue, trapping in the different ratchet structures within the chamber also provided only mildly successful results. Combined with the aforementioned issues, the overall trapping efficiency was too low to allow for meaningful experimentation.

12.4.2. Design 2: Linear design

In contrast to the first design, the second design limits the amount of narrow channels and provides a much higher density of trapping structures. In fact, the overall trapping performance was acceptable for further experimentation. Whilst the aspect ratio, i. e. the ratio between width and height of channels, was challenging in the narrow openings of the trapping structure, this could easily be solved by using a two-layer design and not only limiting the width but also the height at the trapping structure.

However, the lack of separate areas for stretching measurements introduced a few issues. Primarily, when building the bead-cell-bead constructs, we first trap the first bead and the cell and attach them. Then, we grab this construct only at the bead and try to attach the second bead. However, the bead-cell construct can rotate freely around the bead, as optical tweezers in standard setups cannot apply torque¹⁶⁸. Here, we can use walls in the chip layout to limit rotation. As we don't have narrow channels, this only limits the rotation partially, typically to 180° instead of 360°.

Furthermore, as experiments need to be carried out in the bulk areas, they are not shielded. Residual fluid flows and stray particles can disturb experiments and data gathered therein.

Finally, as we still use the same flow paths for both beads and cells, there still is the pos-

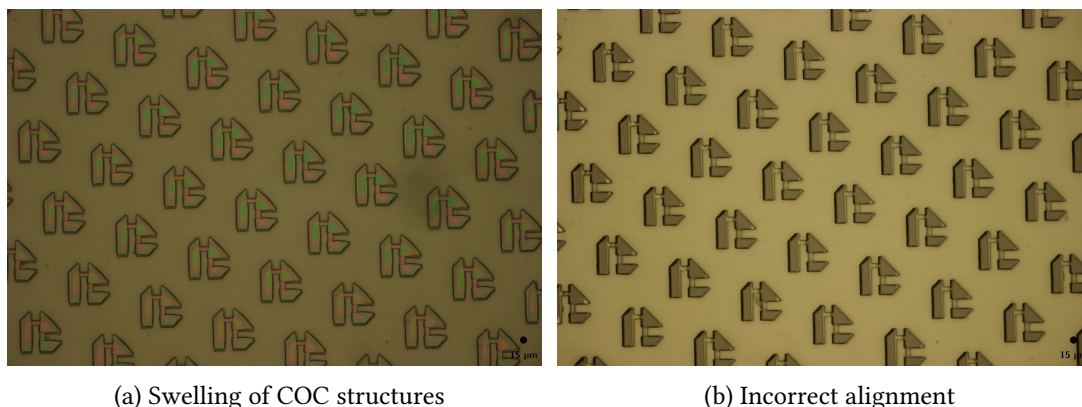


Fig. 12.6.: Different artefacts encountered in COC chips. Both types of artefacts result in smaller trapping structures and experimental channels. The size of a $15\ \mu\text{m}$ particle is shown at the bottom right for scale. The artefacts restricted the structures too much for experimentation, as channel width was around $15\ \mu\text{m}$

sibility of accidental complex formation by residual beads and cells. As these complexes can become arbitrarily large, care must be taken to thoroughly flush all channels between the cells and beads to prevent the formation of complexes large enough to clog the flow.

12.4.3. Design 3: Cross design with integrated experimental areas

The third design combines the advantages of the first two designs. The trapping structures are concentrated in a bulk area and reuse the principle design of the second chip layout. To further improve trapping efficiency, they are staggered. To prevent the premature formation of complexes, cells and beads take different flow paths which only cross in the limited bulk area.

On the other hand, each trapping structure comes with a dedicated experimental area which is only $20\ \mu\text{m}$ wide. This enables the easy formation of complexes with regards to rotation issues whilst still allowing experiments in free-flow, i. e. not attached to any walls. The experimental area is also shielded from bulk flow.

As this last design is the most promising, it was used not only for the creation of PDMS chips but also for COC chips. As the COC manufacturing process at Micronit is not yet matured, yield was as low as 25%. I received chips in two batches: A first batch of 16 chips, only 4 of which had a completely intact seal between the bulk structure and the COC foil. The second batch of 15 chips was completely sealed, however they all either exhibited artefacts as shown in fig. 12.6 or had a height of only $15\ \mu\text{m}$ instead of $20\ \mu\text{m}$. Both issues made all chips of the second batch unsuitable for experimentation.

12.5. Cell elasticity measurements

Due to the issues encountered with the microfluidic performance, unfortunately no measurements of a statistically significant number of cells could be performed. However, I did manage to perform elasticity measurements on HEK-293 cells on six occasions, which are presented in this section.

12.5.1. Cluster of HEK-293 cells and PDMS residue

I obtained first results with a cluster of HEK-293 cells and some PDMS residue in a PDMS chip with the first design. Here, amino coated beads are used, as well as H₂O + F108 as the liquid solution instead of the later used PBS. Cells were injected together with unmodified cell culture medium.

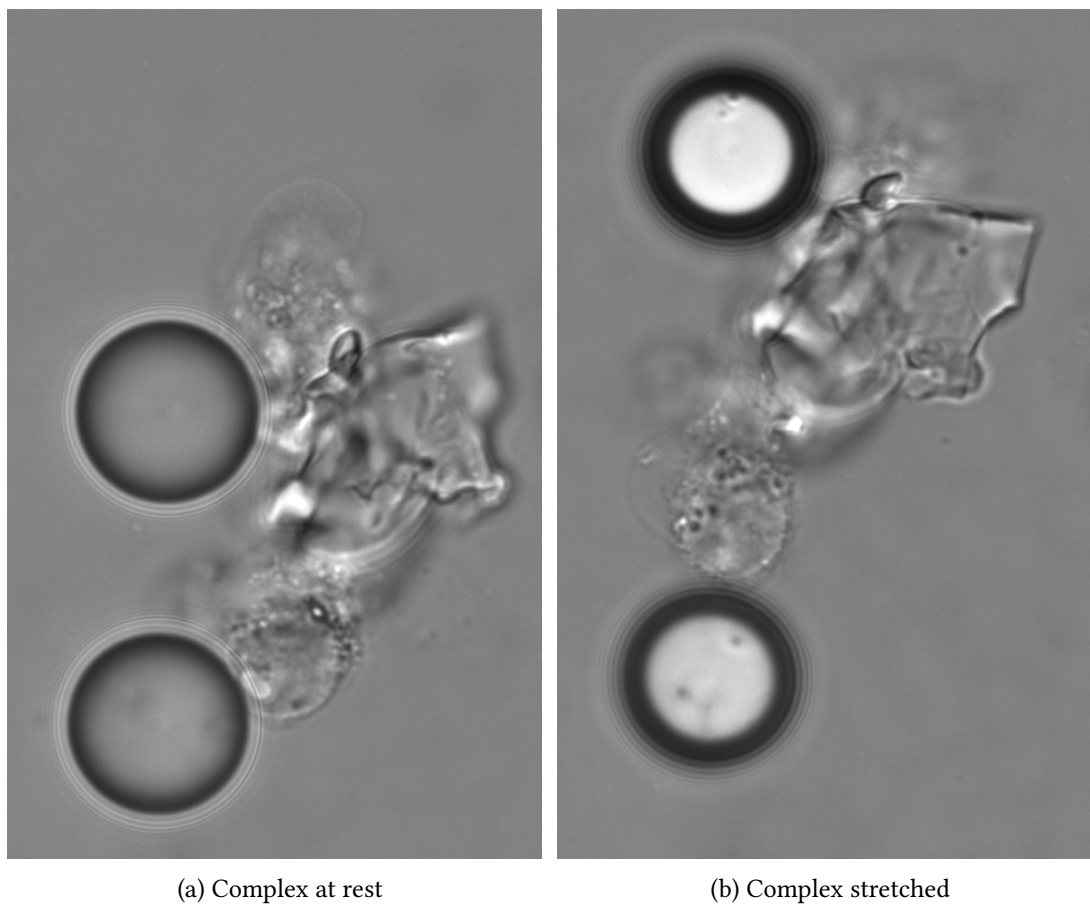


Fig. 12.7.: Cluster of HEK-293 cells with some PDMS residue (large structure near the top bead) relaxed and stretched.

To test the behaviour at different loading rates, the cluster was repeatedly stretched with velocities increasing in $20 \mu\text{m s}^{-1}$ steps from $20 \mu\text{m s}^{-1}$ to $120 \mu\text{m s}^{-1}$. Within each velocity, the force-distance behaviour was comparable.

The resulting behaviour for the different velocities is shown in fig. 12.8. Notably, for slow loading rates ($20 \mu\text{m s}^{-1}$) we see mostly elastic behaviour with negligible hysteresis. For higher loading rates ($60 \mu\text{m s}^{-1}$ and higher) however we do see a noticeable hysteresis between the pulling and retraction. This is a clear indicator of the viscous properties which only emerge at higher loading rates.

For $120 \mu\text{m s}^{-1}$, the highest applied velocity, we can determine the spring constant of elastic behaviour of the complex as $(47 \pm 3) \text{pN } \mu\text{m}^{-1}$. Path integration yields a work of approx. 2.3 aJ that is being performed on the complex per cycle.

12.5.2. Single HEK-293 cell with one static bead

The next results were obtained for a single HEK-293 cell attached to two beads at opposite sides. This corresponds to the desired configuration. The beads are plain, uncoated polystyrene particles and the experiment was performed in a PDMS chip with the third design. However, only one of the beads is trapped optically. The other bead is trapped mechanically. This is illustrated in fig. 12.9.

Here, we use the optically trapped bead to periodically indent the cell with velocities ranging from $10 \mu\text{m s}^{-1}$ to $500 \mu\text{m s}^{-1}$. On pulling back, the cell is also stretched slightly. The resulting stress and strain curves for both extremes are shown in fig. 12.10. Here, we are also fitting the Zener-Kelvin model to our data for the first time.

Overall, we get a very good fit of the data. Notably, for the large loading rate the relaxation behaviour at the large (indentation) strain of -0.72 is not fitted well whereas the relaxation at the (stretching) strain of 0.28 is fitted very good. This is probably a limitation of the rheological model which cannot consider the inhomogeneity of the cell, which in this case of extreme stretching is becoming evident.

Notably for analysis, the size of the cell was shrinking between the first indentations with $10 \mu\text{m s}^{-1}$ and the last indentations with $500 \mu\text{m s}^{-1}$ ten minutes later. In the beginning, cell size was determined to be $(10.8 \pm 0.1) \mu\text{m}$, whereas at the end it was $(9.8 \pm 0.1) \mu\text{m}$. This cell size is the length of the cell along the line between the centres of the two beads.

Fitting parameters at the beginning were $E_1 = 16 \text{ Pa}$, $\eta = 30 \text{ Pa s}$, and $E_2 = 1.9 \text{ Pa}$. In the end, the parameters were $E_1 = 24 \text{ Pa}$, $\eta = 14 \text{ Pa s}$, and $E_2 = 2.4 \text{ Pa}$. Uncertainty for all parameters can only be estimated at 10 %, as manual tuning of the fitting parameters and only selective, iterative fitting was successful.

12. Results

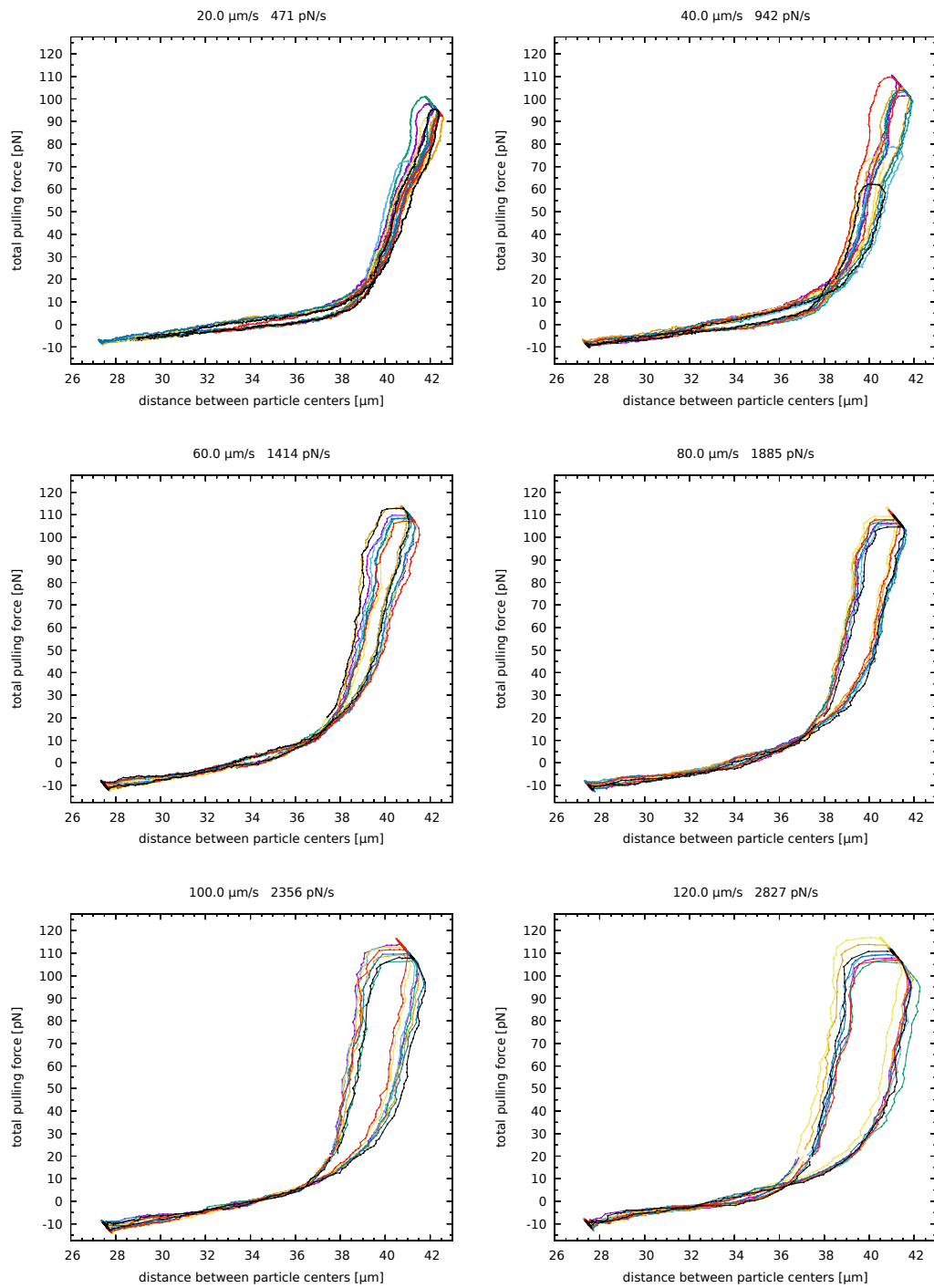


Fig. 12.8.: Force-distance graphs of the complex behaviour at different loading velocities. For each velocity, 8 runs are shown in different colours.

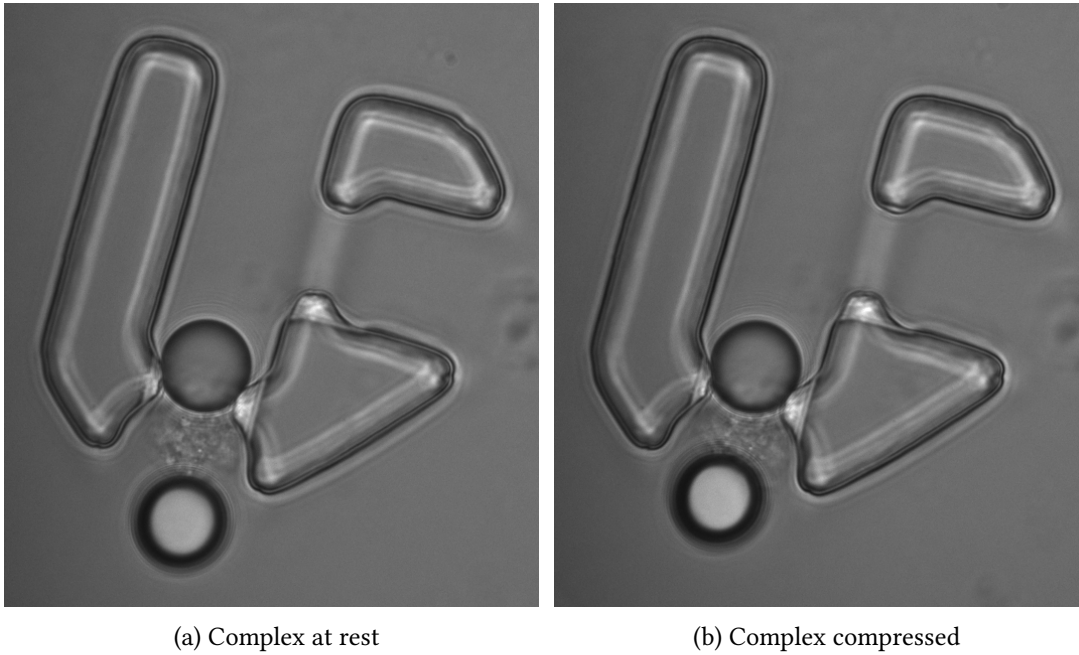


Fig. 12.9.: Bead-cell-bead complex with a single HEK-293 cell. Only the bottom bead is trapped optically. The top bead is mechanically trapped, adhering to the PDMS

In terms of general, model-independent rheological parameters, we can convert these figures to $q_0 = 1.7 \text{ Pa}$, $q_1 = 3.2 \text{ Pa s}$, and $p_1 = 1.7 \text{ s}$ for the beginning with $10 \mu\text{m s}^{-1}$ and $q_0 = 2.2 \text{ Pa}$, $q_1 = 1.3 \text{ Pa s}$, and $p_1 = 0.5 \text{ s}$ for the end with $500 \mu\text{m s}^{-1}$.

The change in cell size during the experiments as well as the significant changes especially of the viscous element (and therefore p_1 and q_1) indicate a structural response of the cell to the external stress.

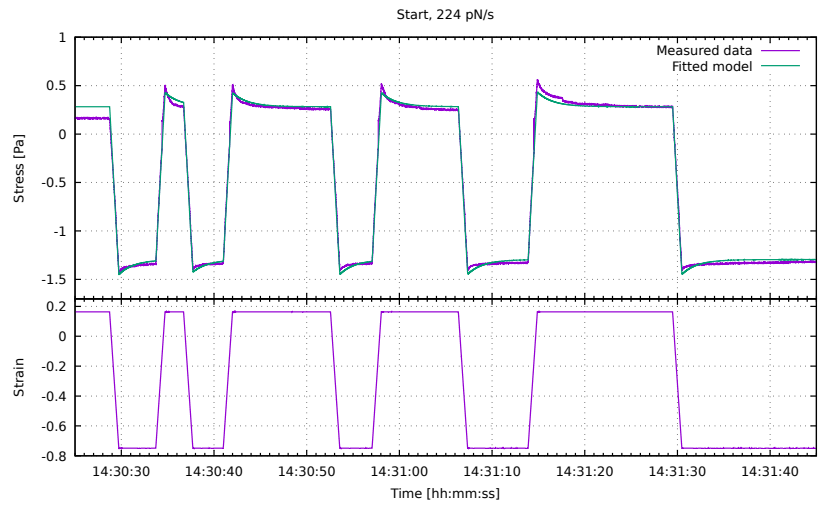
12.5.3. Single HEK-293 cell with two optically trapped beads

Finally, I was also able to perform experiments on a single HEK-293 cell between two optically trapped, plain polystyrene beads. This experiment was also performed in a PDMS chip with the third design.

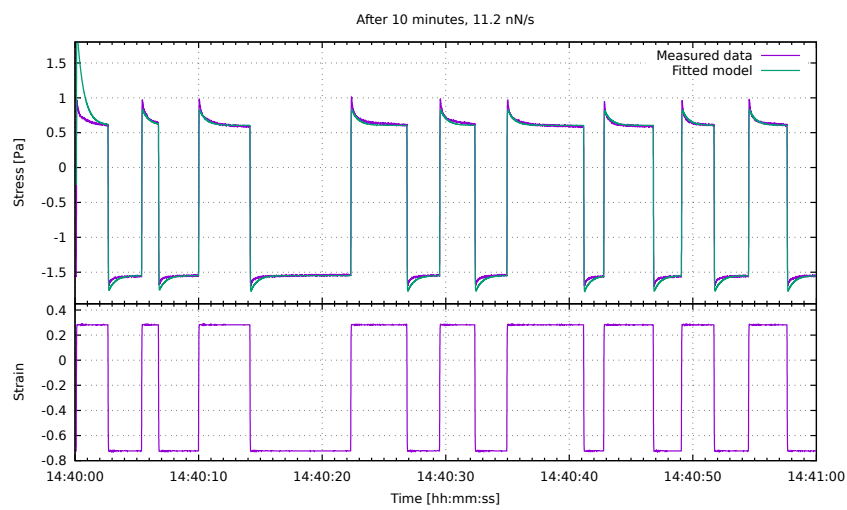
In the experiment, no adhering between the second bead and the cell was achieved. Therefore, in the results shown in fig. 12.12 the strain as well as the fit models for strain were capped to negative values only.

Whilst at first glance the elastic model might seem sufficient, it cannot explain the non-linear stress response to increased strain as shown by the bad match to the stress data in the first three, shallower indentations. In contrast, the viscoelastic Zener-Kelvin model is able to

12. Results



(a) Indentation at $10 \mu\text{m s}^{-1}$ which corresponds to a loading rate of 224 pN s^{-1}



(b) Indentation at $500 \mu\text{m s}^{-1}$ which corresponds to a loading rate of 11.2 nN s^{-1}

Fig. 12.10.: Stress-strain curves of a single HEK-293 cell with one static bead

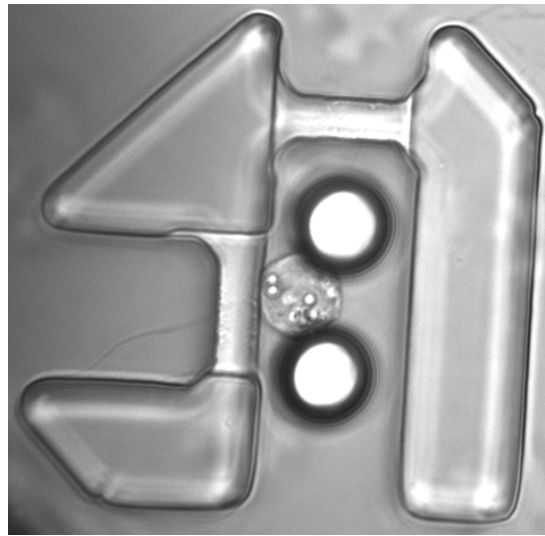


Fig. 12.11.: Bead-cell-bead complex with a single HEK-293 cell. Both beads are optically trapped during experiments

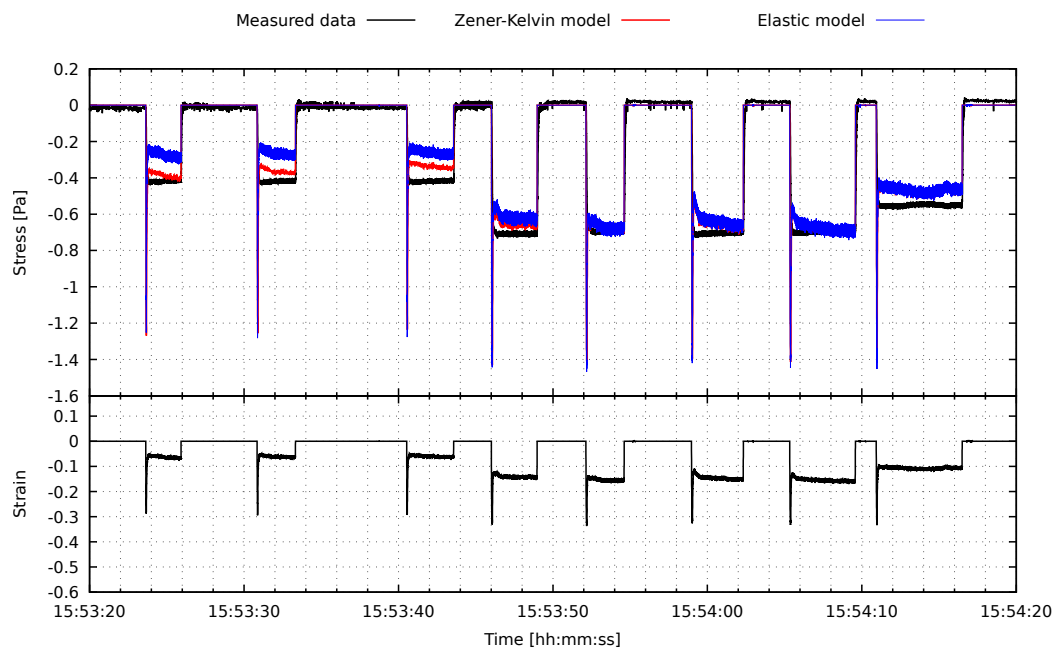


Fig. 12.12.: Stress-strain graph with indentation velocity $100 \mu\text{m s}^{-1}$. Both a fit of the Zener-Kelvin model as well as a purely elastic fit are shown.

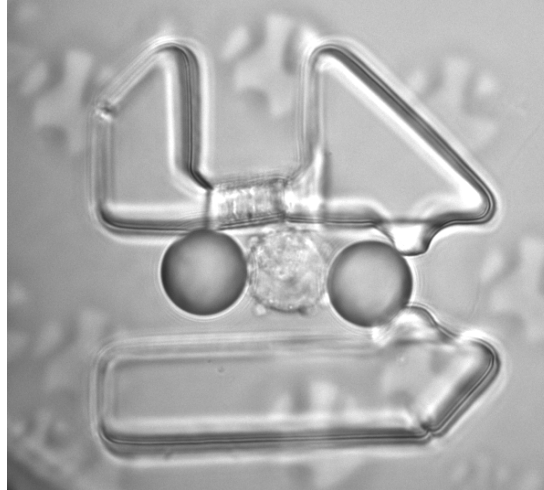


Fig. 12.13.: Bead-cell-bead complex with a single, very stiff HEK-293 cell. Both beads are optically trapped during experiments. The patterns in the background are artefacts from the chip production process which do not affect the experiment.

describe this behaviour.

For the purely elastic model, the fit provides a Young's modulus of $E = (4.35 \pm 0.02)$ Pa. For the Zener-Kelvin model, we get $E_1 = (5.6 \pm 50\,600\,000.0) \times 10^{-6}$ Pa (sic), $E_2 = (4.20 \pm 0.02)$ Pa, and $\eta = (21 \pm 254)$ kPa s. The relative agreement between the pure Young's modulus and the purely elastic component E_2 serves as an additional indicator of sensible results. We can also notice the extremely high errors of the viscous component. This is both due to the complicated fitting of the numerical solution of a differential equation as well as due to the lack of velocity variance in the data.

12.5.4. Very stiff single HEK-293 cell

Fig. 12.13 shows a bead-cell-bead complex with a HEK-293 cell between two plain, uncoated $15\ \mu\text{m}$ beads. The experiment was performed in a PDMS chip with the third design. Both beads are optically trapped.

The resulting stress-strain graph is shown in fig. 12.14. Immediately we can note that the strain is only very minimal in the range -0.04 to 0.02 and rather noisy. To calculate the strain, we take the distance between the two optical traps, subtract one bead diameter and correct for the acting forces with the spring constant of the optical tweezers system. In this measurement, the spring constant was $39.9\ \text{pN}\ \mu\text{m}^{-1}$. As both beads are optically trapped, the effective spring constant of the system is only half that value.

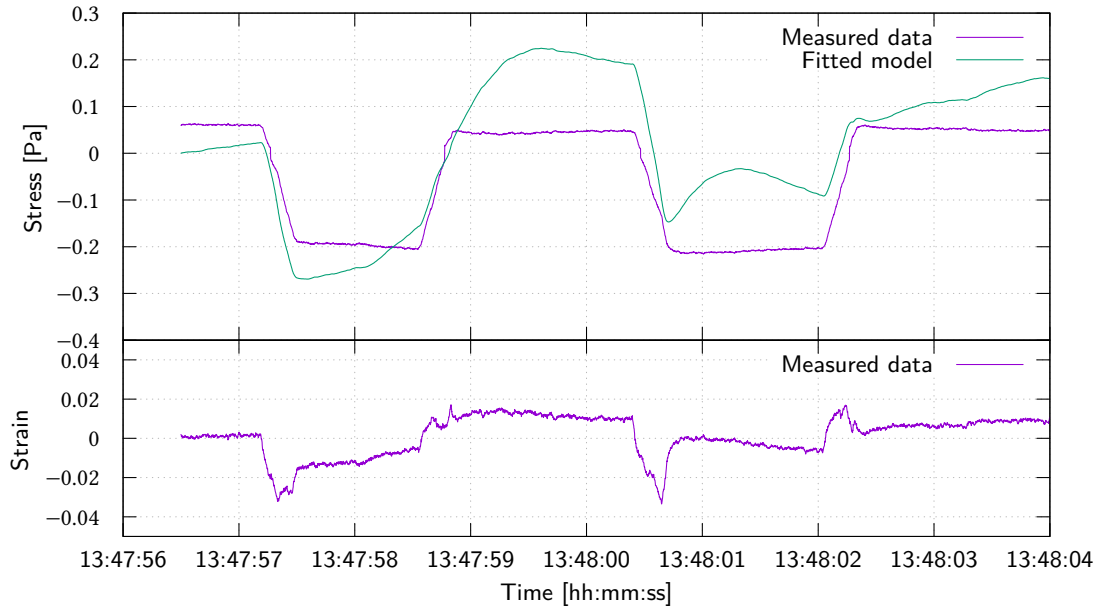


Fig. 12.14.: Stress-strain graph with indentation velocity of $10 \mu\text{m s}^{-1}$. The fitted model cannot adequately explain the measured data

The spring constant of the optical tweezers system acts in series to the viscoelastic model of the cell. If the cell is stiffer than the optical tweezers, the tweezers dominate the system. Correcting for the optical tweezers stiffness then only provides minute strains. As the absolute noise and absolute drift of the optical tweezers system is constant, this will lead to a large relative noise and drift of the resulting, corrected strain.

Here, we see that the two indentations result in approximately the same stress but in two very different strains. In fact, the strain of the second indentation is only half of the strain of the first indentation. This of course is a result of drift and noise, rather than a real measurement result. Consequently, the fit cannot and does not adequately describe the results.

In such a situation the only recourse is to increase the stiffness of the optical tweezers system. This can be done by increasing the laser power, increasing the optical density of the trapped beads, and by decreasing the size of the beads. Only the latter method is practicable with the currently available setup. It should be noted that the increased stiffness of the system with a smaller bead still results in the same maximum trapping power, as the maximum deflection is of course also reduced.

12.6. Cell viability verification

Unfortunately, cell viability verification could not be performed for the cells experimented upon herein. When introducing the trypan blue solution, either the modification of the microfluidic connections itself already introduced sufficient backflow to remove the cells from their locations during experiment, or small air bubbles were introduced accidentally, leading to the same results.

Tests with trypan blue showed that even though we only use black and white cameras in the system, we can nevertheless reliably determine if a cell has been stained or not. As an example, fig. 12.15 shows some cells after incubation with trypan blue. Whilst the blue staining of the background is only visible in direct comparison of the image to one before the introduction of trypan blue, the stained cells are clearly visible and noticeably darker than their unstained counterparts.

Therefore, we are able to reliably identify cells without intact membrane with the trypan blue dye exclusion test in our setup.

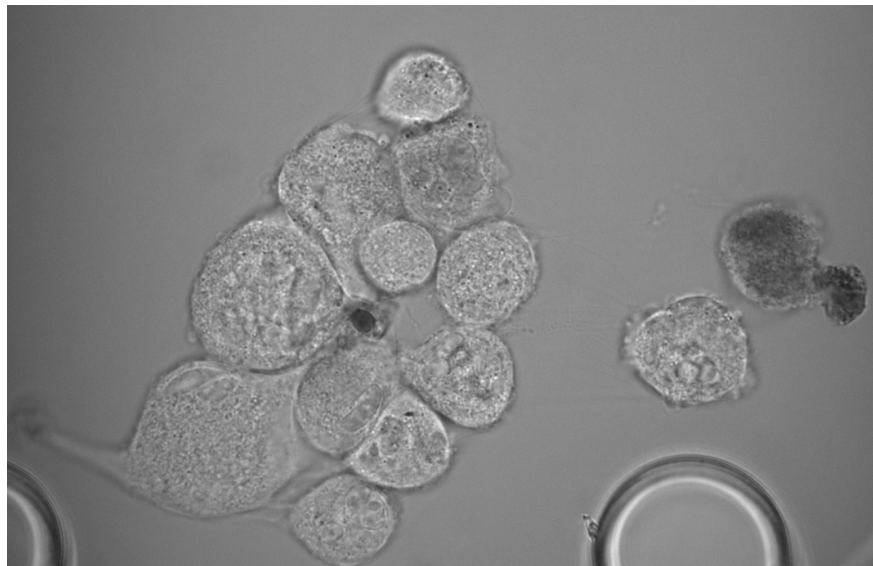


Fig. 12.15.: Image taken with the black and white overview camera of a cluster of cells after incubation with trypan blue. Only the cell in the centre of the cluster as well as the small cluster to the far right are dyed blue.

13. Conclusions and Outlook

In this work, I have shown that the determination of viscoelastic model parameters for the description of cell elasticity behaviour is possible with a dual-beam optical tweezers setup. I have created the software required to control the setup and run stretching experiments both manually and automatically. Further, I have developed an offline analysis program for video-based force detection with higher precision than possible in real-time. I also developed an analysis tool to convert the resulting force data into stress and strain curves for viscoelastic analysis.

Unfortunately, I was not able to perform experiments on a significant amount of cells or on different cell types. Both issues with the microfluidic design and the fabrication of microfluidic chips limited the amount of experiments possible. Therefore, further work is still required.

Regarding the issues with microfluidic, the third design is a promising basis. Currently, the system still requires external pumps, switches and reservoirs which introduce a multitude of possible error sources. For further revisions, I strongly recommend to incorporate as many features as possible into the microfluidic chip to limit external influences. With this miniaturisation, the amount of cells and beads required can also be reduced. Furthermore, this should enable thermostatic control. This is currently not viable due to the long tubing and resulting sensitivity to even minute changes in temperature and therefore fluid density.

Regarding the fabrication of microfluidic chips, a major improvement in yield must be accomplished. Completely cleaning and reusing a chip is neither sensible nor desirable as residues could always remain. Therefore, each experiment requires at least one new chip. As COC is still a rather new material, perhaps alternative materials such as glass should be considered.

A general issue with measuring the elasticity of objects is of course the stiffness of the sensor. Ideally, the stiffness is multiple orders of magnitude higher than the measured object. This way, it can be assumed to be infinitely stiff, greatly simplifying the computational analysis. In this setup, this is not the case. Instead, we have seen that the stiffness of the cells is in the same order of magnitude or sometimes even higher than that of the optical tweezers. Therefore, the use of smaller and optically denser particles should be considered. Whilst the

13. Conclusions and Outlook

refractive index of polystyrene is already high with 1.58, some mineral glasses are available with even higher optical density. In addition, the use of a significantly more powerful laser should be evaluated. Depending on the laser power and its effects on cell viability, it might be sensible to keep the current particle size of 15 μm to prevent the cell from coming into contact with the full-powered laser beam.

Overall, the cell elasticity investigation with dual-beam optical tweezers shows great potential despite its complications. For the analysis of adherent cells, AFM force spectroscopy already provides an ideal tool, especially if used with oscillatory analysis^{98,99}. However, for the analysis of non-adherent cells no other tool provides the combination of time-resolution, time-scale, quality of force measurement and overall versatility than the Elasto-Tweezers setup presented here.

Part IV.

Conclusions, Outlook and Appendix

14. Summary and Outlook

In this thesis, I have demonstrated two optical tweezers setups with high speed video-based force detection. Though similar at first glance, the two setup each serve a specialised experimental niche.

In the field of nanopores experiments, I have introduced new protocols for the reliable preparation of nanopores in free-standing monolayer molybdenum disulphide membranes. With this method, small solid-state nanopores in atomically thin membranes are readily available. I demonstrated that both electrochemical breakdown and transmission electron microscopy are useful for specific size ranges of nanopores. The optical tweezers setup provides low-noise, high-speed detection of axial forces and is tuned for axial trap strength. I established the capabilities of this setup by time resolving the threading of multiple DNA strands into a nanopore in monolayer molybdenum disulphide. Furthermore, the high-speed force detection enables the monitoring of forces acting on DNA in a nanopore with applied AC voltage at various frequencies. As I demonstrated, the peculiar force behaviour during such experiments warrants further investigation.

A prerequisite for further successful research with DNA and nanopores is the establishment of truly reliable procedures for the preparation of DNA in our lab. Unfortunately, all data points towards insufficient quality of DNA as the root cause for the problems experienced in this and other work. Here, I have established a toolbox for experiments ranging from the force behaviour with applied AC transmembrane voltage to the viability of controlled DNA translocation through atomically thin solid-state nanopores for DNA sequencing.

On the other end of the size spectrum, experiments on single cells are also viable with a dedicated optical tweezers setup. In the Elasto-Tweezers setup, the dual-beam optical tweezers allows for controlled manipulation, indentation and stretching of single cells and cell complexes. Here, the high-speed video-based force analysis allows close interaction of trapped beads with neighbouring cells without disturbing the force signal. In this work, I demonstrate the potential of microfluidic design to provide and prepare an environment allowing fully automated cell elasticity experiments. I also show first experiments on cell elasticity, whilst exposing some limitations of both the microfluidic designs as well as the optical tweezers. I am confident that the limitation imposed by the microfluidic design and fabrication can

14. Summary and Outlook

be overcome with further research. The limitations posed by the optical tweezers are of a more fundamental nature, as we are inherently limited by the relative softness of the optical trap compared to the elasticity of cells. Nevertheless, for non-adherent cells Elasto-Tweezers provides a combination of features rivalling other methods.

Further research must concentrate on improving the microfluidic design and fabrication first. The integration of microfluidic valves and reservoirs into the microfluidic chip as well as switching to alternate chip materials such as the well-established glass should be evaluated. Once these limitations have been cleared, statistically significant numbers of model cells as well as healthy and diseased cells can and should be tested with this system to evaluate its performance.

A. User manual for the nanopore setup

A.1. Safety information



Danger: This setup contains a class 4 laser according to DIN EN 60825-1:2001-11 with $P_0 = 2100 \text{ mW}$ at $\lambda = 1060 \text{ nm}$. The setup contains *no safety interlock*. Before opening the front hatch, always make sure that the shutter is closed.

A.2. System overview

A.2.1. Hardware overview

- **Axopatch:** Axon Instruments, Axopatch 200B
Patch clamp amplifier for applying transmembrane voltage and measuring transmembrane current
- **function generator:** Stanford Research Systems, DS345
Function generator controlled by the measurement software (via GPIB), providing the voltage signal for the Axopatch
- **piezo controller:** Physik Instrumente, E-727
Controller of the xyz stage. Controlled by the measurement software via USB
- **laser:** Fibotec Fiberoptics, Faserlasermodule 1060 nm 2 W Yb-1x33 V1.0
Fibre laser module. Power controlled by an applied voltage 0 V to 10 V
- **detail camera:** Andor, Zyla 4.2 USB
Water cooled measurement camera with 10× post-magnification optics
- **LED light:** Schott, KL-2000 LED
Fibre optics illumination, 1000 lm output at fibre
- **overview camera:** ScopeTek, DCM130E
Overview camera placed in ocular holder of microscope

A. User manual for the nanopore setup

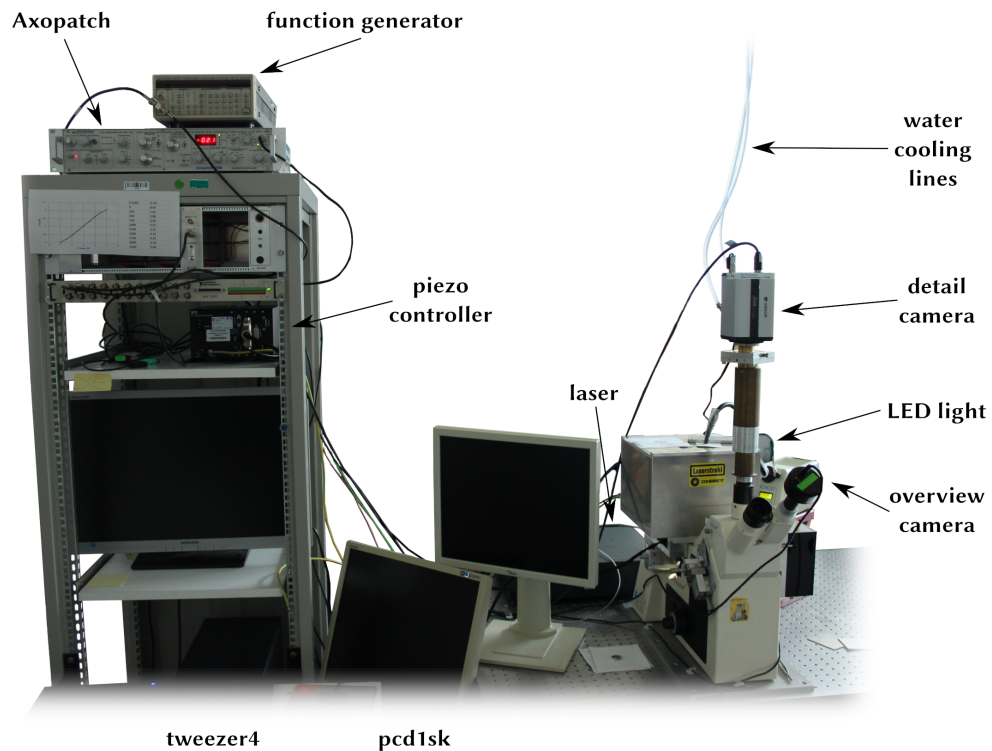


Fig. A.1.: Photo of the experimental setup

A.2.2. Software overview

Before going into detail regarding the individual software components, it is important to note how the software saves measurement data.

Raw video data is stored during measurement in uncompressed raw form, that is into binary files (each for 15 s of data) containing the raw data received by the camera. This data contains the individual frames as well as, for each frame, metadata. This data is stored on a RAID-0 (a volume of multiple hard disks striped together for increased performance and capacity, which loses all data if even a single drive fails). After each experiment, typically during the night this data should be packed and pushed into backup. In packed format, the images are stored in binary files consisting of TIFF files with ZIP compression. Additionally, for each binary file a plain text index file is created. It contains for each frame the timestamp as well as starting position and length (in bytes) within the binary file. Both files must be kept together, as it is very difficult to extract the individual images from the binary files without the index (and impossible to extract the timestamps).

All other data (piezo positions, currents, voltages, etc.) is stored in a binary format containing for each datapoint the timestamp and the value.

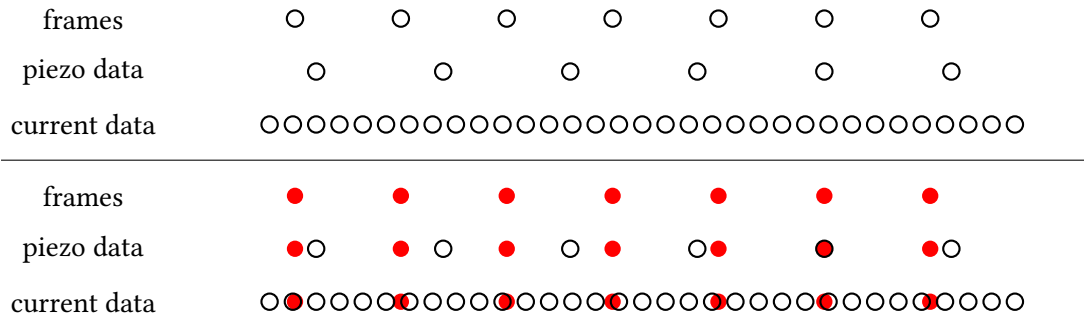


Fig. A.2.: Illustration of the data interpolation process. Top: Video frames, piezo data, and current data all have data points (black circles) at different times. Bottom: If we are primarily interested in data from the video frames, we interpolate the piezo and current data (red circles) at those times where video frames are available.

For analysis, we need to perform the edge detection for each frame, calibrate and zero the resulting bead positions to get displacements / forces and finally align that data with the other data. Since all data has its own timebase (a frame is recorded at a different timestamp than a piezo position), we align by selecting the primary data (typically this would be the force) and then linearly interpolate all remaining data for each timestamp at which primary data is available. This principle is illustrated in fig. A.2 for better understanding.

It should be noted that this interpolation does introduce artefacts into the resulting data. Most notably, noise in the current signal *increases*: We only interpolate the data, even if the data set has a higher rate than the interpolation base. No averaging is performed. In the case that e. g. both force and current signal are important and should be plotted or analysed, I recommend that the current signal is taken as a separate interpolation base.

The software used for measurement is `Andor.vi` and `Tweezer2.vi`, running on `tweezer4` and `pcd1sk`, respectively. `Andor.vi` controls the camera, performs limited real-time edge detection and saves the raw camera feed to the hard disk array. It is usually only started and then runs by itself. `Tweezer2.vi` contains the main user interface and controls all hardware apart from the Andor Zyla camera, saving it as well.

After the experiments `pack.vi` is used on both computers. It is simply started and performs its work without any user interaction, only displaying a progress bar and an estimation of the remaining time. It takes the raw video data, packs it and saves it both to backup storage and to local storage, deleting the raw video data on successful conversion.

For analysis of the data and export into a user-readable format, `offline.vi` is used. This VI also performs batch edge detection on the packed video data.

A.3. Performing experiments

A.3.1. Turning the system on

To turn the system on (the following order is suggested but not necessary):

- turn on PC tweezer4
- turn on PC pcd1sk
- turn on function generator
- turn on Axopatch, making sure that no electrodes are connected
- close shutter, then turn on laser (switch at power outlet left of tweezer4). Danger: Depending on the state of the voltage output AO1, it is possible that this enables the laser with maximum power. Always take appropriate safety measures to prevent direct and indirect exposure to the laser beam.
- turn on detail camera
- activate water cooling (target flow rate: 1 l min^{-1})
- turn on piezo controller
- add immersion water to objective
- place sample chamber
- on pcd1sk connect via remote desktop to tweezer4, placing the remote desktop window in full-screen mode on the lower (centre) screen
- on both PCs load Tweezer2.lvproj
- on pcd1sk open Tweezer2.vi and place it maximised onto the left screen
- on tweezer4 open Andor.vi
- start both VIs within a few seconds of each other (order does not matter)

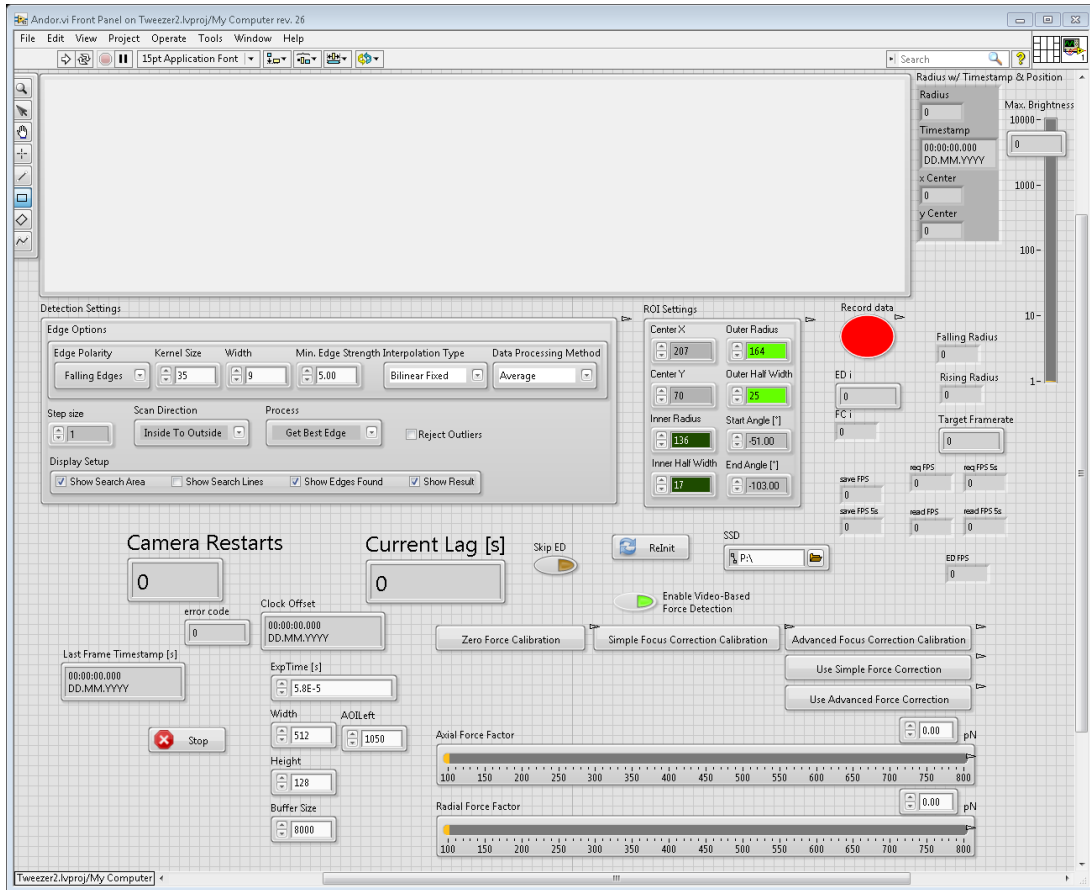


Fig. A.3.: Screenshot of andor.vi

A. User manual for the nanopore setup

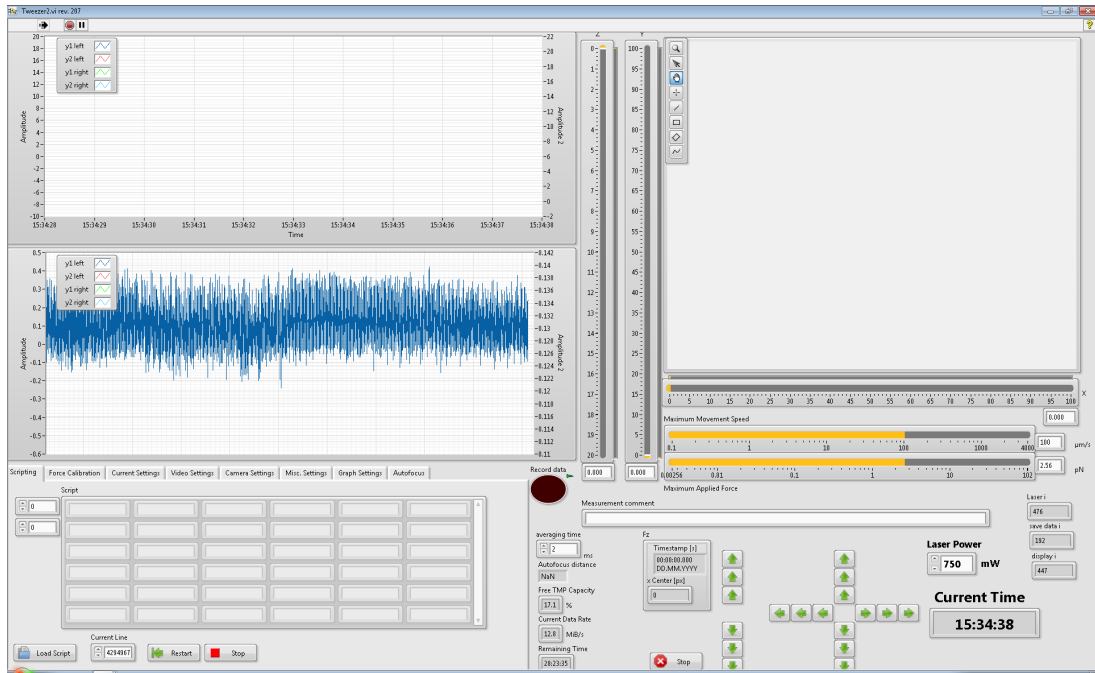


Fig. A.4.: Screenshot of tweezer2.vi with Scripting tab

A.3.2. Controlling andor.vi

The user interface of `andor.vi` is shown in fig. A.3. Apart from starting the VI, no user input is required during experiments. However, the two boldly marked indicators `Camera Restarts` and `Current Lag [s]` should be watched regularly.

Due to issues with the driver for the detail camera it sometimes times out. The software detects such timeouts and restarts the camera, incrementing the `Camera Restarts` indicator. During such a restart, typically between one and two seconds of data is irrevocably lost.

If the software is not able to process the data in a timely fashion, the `Current Lag [s]` indicator increases. It shows the time difference between the acquisition of an individual frame and the finished processing of it. If this lag reaches a value in the range of 1.5 s, the camera restarts as described above.

Sometimes, the restarts due to lag appear quite often, i. e. multiple times per minute. In such a case it is advisable to stop the software, turn off the detail camera, restart `tweezer4` and turn the detail camera on again after roughly a minute. This normally solves the issues.

A.3.3. Controlling tweezer2.vi

tweezer2.vi presents the main user interface for experiments. It should be placed on the left screen and will show the overview video in full-screen mode on the right screen when it runs. At the top left, two graphs show user-selected data for a user-selected time (default: 10 s). In the top right, the detail image is shown with a user-selected overlay showing the results of the edge detection. Below and left of this image, the piezo position in X, Y and Z can be modified. The piezo movement speed and the corresponding Stokes' drag force can also be selected below the image.

Below that, a measurement comment can be entered. It is saved upon exiting the text input field or pressing return with the current timestamp. This way, specific moments during the experiment can be easily annotated. It can of course also be used to identify the experiment or experimental parameters for later use.

Below the measurement comment, a cluster of arrows is visible. The arrows in the cross formation move the piezo in the indicated direction in X and Y, whilst the six arrows to the left of it move the piezo in Z. The distance moved by each button can be selected by the user; the default value is 0.01 μm for the innermost buttons, 0.1 μm for the middle buttons and 1 μm for the outermost buttons.

Also below the measurement comment, the laser power can be set. It should be noted that the power is not reduced back to zero if the program stops – this only happens when pcd1sk is turned off or restarted, or when it is explicitly set back to zero.

The most important setting is the red recording button Record data left of the measurement comment. Raw video data is only saved to disk when this button is activated (bright red). *It is therefore of utmost importance that this button is activated during the experiment as soon as relevant experimental phases are occurring.*

Below the recording button, the averaging time for current measurements can be adjusted. Current and voltage data is acquired with a rate of 100 000 S s^{-1} . This raw data is saved in one file. Additionally, blocks of averaging time (default: 2 ms) length are averaged into a single data point that is saved as U-avg and I-avg channels and displayed in the software.

Further below, the calculated autofocus distance is displayed. This is explained in detail in section A.3.3.8. There is also a display showing the remaining data capacity on pcd1sk as well as the current data rate and remaining time until the disk is full.

Finally, a stop button should be used to stop the program (instead of aborting execution in LabView or quitting LabView altogether) to ensure that all hardware communication is ended gracefully and all data in RAM is saved to disk.

In the bottom left, different tabs can be selected for specific settings and operations. These will be discussed in detail below.

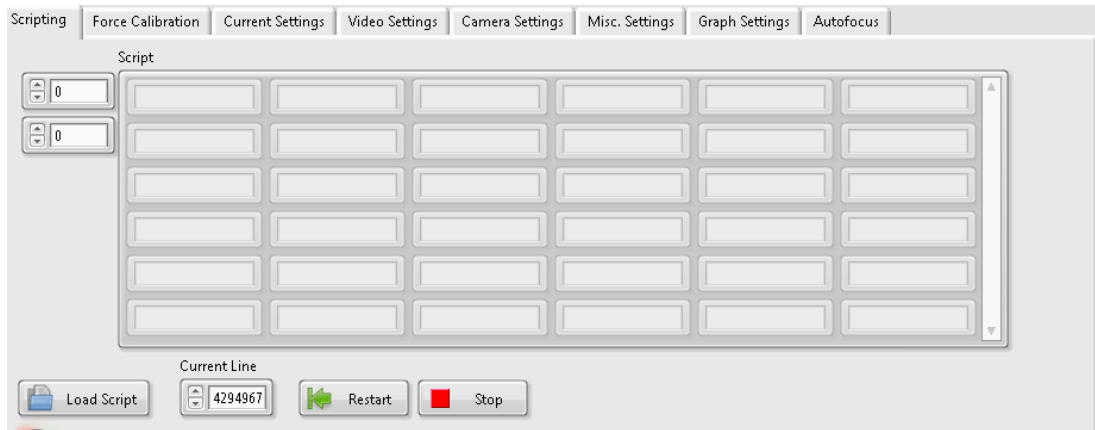


Fig. A.5.: Screenshot of the Scripting tab

A.3.3.1. Scripting

The Scripting tab allows scripting of some of the program features for repetitive or semi-automatable tasks. The large script array contains the script can be modified directly. However, most of the time a script is edited externally with a text editor and then loaded into the software.

The scripting language is based on BASIC. It is line oriented and runs as fast as possible, stopping execution once the current line number exceeds the number of rows in the script array. Script files are expected to be plain text files with tab separation. The first column denotes the line number. It *must* be a strictly increasing number between 0 and 2 147 483 647, inclusive. Gaps in numbering are allowed and in fact encouraged to facilitate later introduction of code passages without having to change all following line numbers. Common practise is to use increments of 10 or 100 in coding, i. e. lines are numbered 10, 20, 30, ... or 100, 200, 300, ...

The second column contains the code instruction. Case is ignored, although all caps is encouraged. The following columns contain the arguments to the code instruction, if any.

Valid code instruction are (in general notation `CMD ARG1 ARG2 ARG3 ARG4`):

- NOOP: no operation
- GOTO int: goes to line ARG1
- SLEEP val: sleeps for ARG1 milliseconds
- SET var val: sets the value of ARG1 to ARG2
- ADD var val: sets the value of ARG1 to (ARG1 + ARG2)

- IFGOTO var cmp val int: if the comparison ARG2 of ARG1 with ARG3 is true, then go to line ARG4 (else continue with the next line)

Where

- int is a positive integer between 0 and 2 147 483 647, inclusive, consisting solely of the digits 0-9. If another character is found, reading stops. If no digit is found, 0 is used.
- var is a valid variable name. Valid variable names are X, Y, Z, V, U, FMAX, BR, VAR0, VAR1, VAR2, VAR3, VAR4, VAR5. Case is ignored, although all caps is encouraged. The variables X, Y, Z, V correspond to the piezo positions in x, y, z, and the piezo speed. Values are as shown in the UI in μm or $\mu\text{m s}^{-1}$. U is the offset voltage. FMAX is the maximum force in pN according to Stokes, thus also setting the piezo speed. BR is the brightness of the illumination, between 0 and 1000. The other five variables do not correspond to a real value and can be used as internal variables.
- val is either a valid variable name or a floating point number. A floating point number consists of the digits 0-9, at most one decimal point (.), at most one letter e or E, and at most two minus signs, one at the beginning and one immediately following an e or E.
- cmp is one of <, >, >=, <=, =, or !=. Comparison is performed floating point save: before comparison values are cast into single-precision floating point numbers and machine epsilons are added or subtracted to the first argument for >/>= or </<=. For equal / non-equal checks, the software tests whether the single-precision value of the first number is within $\pm\epsilon$ of the second number with machine epsilon ϵ .

When loading a script file, the lines are inserted into the script array at the specified line numbers. Empty lines are filled with NOOP.

A.3.3.2. Force Calibration

The Force Calibration tab contains all relevant parameters and routines for force calibration that is used to display the live force data. It is only used for the live data. During offline data analysis, a separate force calibration is used. Therefore, during experiments the force calibration capabilities should only be used to get a rough insight into the forces acting on the trapped particle to perform appropriate actions.

Axial Forces are calculated as

$$F = k \left(\frac{r_0}{r} - 1 \right) \quad (\text{A.1})$$

Radial forces should be calculated as $F = k(x - x_0)$, however the focus was never on radial forces and this calculation is therefore not implemented in the software yet.

A. User manual for the nanopore setup

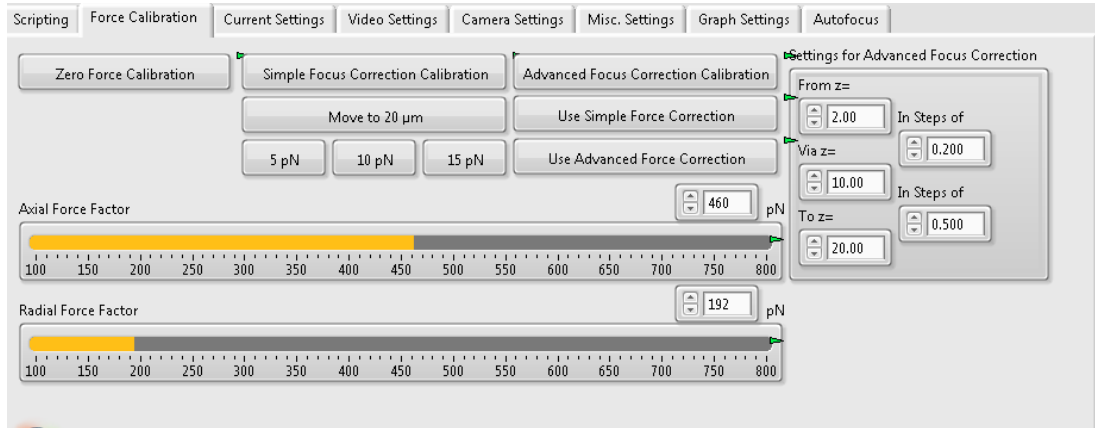


Fig. A.6.: Screenshot of the Force Calibration tab

As a first step for force calibration, the zero force radius r_0 needs to be determined. For this, three different methods are available: The first, basic method simply takes a static value for r_0 . As long as the button Zero Force Calibration is activated, the detected radii are averaged to yield r_0 . In most cases, this is sufficient for a rough glimpse into the force behaviour.

However, the zero force radius r_0 is in fact not constant in most cases. It is instead dependent on the distance between the focal point and the membrane. Therefore, two further, distance dependent calibration modes are available. It should be noted that for these methods, the calibration is based on the z piezo position. Therefore, the focus should be manually set as optimal as possible before calibration. After calibration, focus changes should only be done by using the z piezo axis and not manually.

The simple force correction method calculates $r_0(z)$ as a linear interpolation between to values $r_0(z_1)$ and $r_0(z_2)$. First, at z close to 0 the usual Zero Force Calibration is performed. Then, at large z the Simple Focus Correction Calibration is performed in the same way. The simple force correction method can then be activated with the button Use Simple Force Correction.

A common error is to not move the piezo z axis between the two calibration steps. As both r and z are fluctuating constantly, we will get $z_1 \neq z_2$ but $z_1 \approx z_2$ and $r_0(z_1) \neq r_0(z_2)$ but $r_0(z_1) \approx r_0(z_2)$. Since the noise in r is much greater and non-uniform than the noise in z (and therefore $|r_0(z_2) - r_0(z_1)| \gg |z_2 - z_1|$), this will result in a linear interpolation slope $\frac{\Delta r_0}{\Delta z} \rightarrow \pm\infty$, giving pointless force results.

The advanced force correction methods also works based on linear interpolation, but with multiple sampling points. Activating Advanced Focus Correction Calibration overrides the current script to this:

```

0   SET      V      100
1   SET      VAR2   inc1
2   SET      Z      start
3   SLEEP    100
4   SET      VAR1   1
5   SLEEP    1000
6   SET      VAR1   0
7   IFGOTO   Z      >=   end   99
8   IFGOTO   Z      >=   mid   11
9   ADD      Z      VAR2
10  GOTO     3
11  SET      VAR2   inc2
12  GOTO     9

```

wherein the values `start`, `mid`, `end`, `inc1`, and `inc2` are replaced by the values of the input fields `From z=`, `Via z=`, `To z=`, and the two inputs `In Steps` of. As long as `VAR1` is set to true and `Advances Focus Correction Calibration` is activated, the values of z and r are recorded, averaged and added as a sampling point for later linear interpolation.

As long as the button `Use Advanced Force Correction` is activated, this data is used to calculate r_0 for force calculation.

After having performed the necessary prerequisites for determining r_0 , the axial force factor k needs to be set. For this, the usual method is an iterative one: First, move the piezo z position to a relatively low value and make sure that movement to $z = 20 \mu\text{m}$ is possible. Then, press either the `5 pN`, `10 pN`, or `15 pN` button or set a desired force and corresponding maximum movement speed manually. Then, repeatedly press the button `Move to 20 μm` an even number of times. Whenever this button is active, the set z value is ignored and instead the piezo is moved to $z = 20 \mu\text{m}$. During the movement, watch the z force and adjust the `Axial Force Factor` in such a way that the displayed force (roughly) corresponds to the selected speed / force.

A.3.3.3. Current Settings

The `Current Settings` tab contains the controls for the function generator that controls the voltage applied to the chip by the Axopatch. Communication with the function generator is performed by manufacturer-supplied control VIs. The settings in this tab correspond to the voltage applied to the chip by the Axopatch and are converted appropriately.

The function output of the function generator is connected to the front-switched external

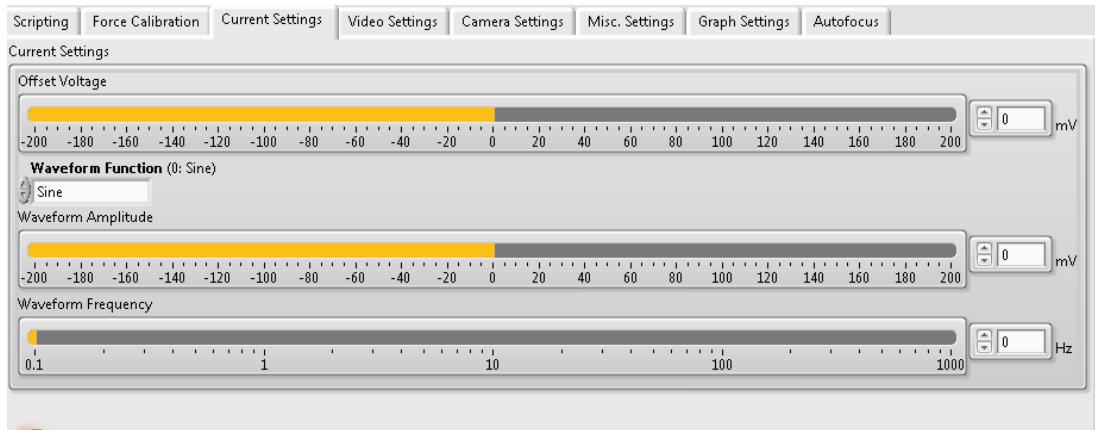


Fig. A.7.: Screenshot of the Current Settings tab

command input of the Axopatch. This input is set to accept a command signal of 20 mV V^{-1} with an input impedance of $10 \text{ k}\Omega$ ¹⁴⁸. However, the function generator output has an impedance of 50Ω ¹⁶⁹. Since the output is terminated into a much higher impedance, the output voltage is doubled¹⁶⁹. Therefore, we internally scale all voltages that the DS345 provides with a factor of 0.025 V mV^{-1} .

The user interface first allows to set an Offset Voltage U_{DC} , a Waveform Amplitude U_{AC} , a Waveform Frequency f and as Waveform Function one of Sine, Square, Triangle, Ramp, and Noise.

As long as U_{AC} is set to 0 V , a constant voltage of U_{DC} is applied. For $U_{\text{AC}} \neq 0 \text{ V}$, the selected function is generated with an amplitude (zero-to-peak) of U_{AC} and frequency f , offset by U_{AC} . It must be ensured that $U_{\text{DC}} + U_{\text{AC}} \leq 200 \text{ mV}$. Also, $f = 0 \text{ Hz}$ at $U_{\text{AC}} \neq 0 \text{ V}$ provides undefined behaviour.

A.3.3.4. Video Settings

The Video Settings tab contains the controls of the video-based force detection as well as the illumination brightness control. For the Illumination Brightness setting to work (which is in per mille of maximum brightness), the LED light needs to be connected to pcd1 sk via USB and be set up in the system as COM3 (this can be done in NI MAX).

The Detection Settings contain the internal settings for edge detection. The default values as shown in the screenshot are tuned for typical experiments on this system. The only parameters that should usually be changed are the checkboxes in Display Setup to select or deselect the edge detection result overlays in the detail image. In case of frequent lags in `andor.vi` that are not resolved by a reboot, setting Step size to a larger value will also

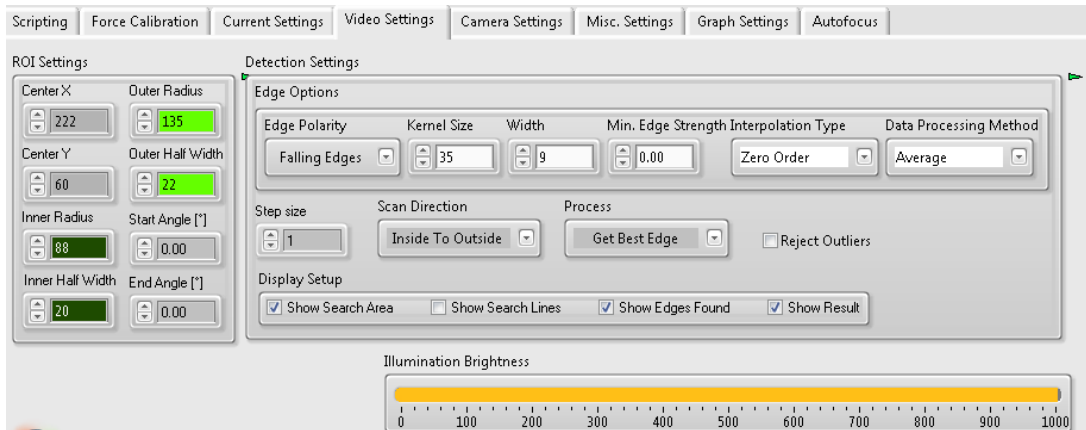


Fig. A.8.: Screenshot of the Video Settings tab

help. Edge detection is performed along radial spokes. This parameter determines the angle (in degrees) between these spokes: 1 corresponds to 360 spokes, 2 to 180 spokes, and so on.

If at any point particles that yield a bright annulus (instead of a dark one) are used, the Scan Direction should be inverted to Outside To Inside.

The ROI Settings select the position of the annular region of interest (ROI) within the frame. Center X and Center Y set the overall position. Inner Radius r_i and Inner Half Width w_i select the radius of the annulus for the inner edge (from bright to dark with default particles): It is from $(r_i - w_i)$ to $(r_i + w_i)$. Analogously, the Outer Radius and Outer Half Width determine the radius of the outer edge (from dark to bright with default particles). Finally, the annulus can be confined between two angles. These are set by the values of Start Angle [°] and End Angle [°]. Those values can be outside the range from 0° to 360° as well for easier configuration. The software automatically takes the entered values modulo 360°. The direction is counter-clockwise, with 0° corresponding to the three o'clock / positive x axis position.

A.3.3.5. Camera Settings

The Camera Settings tab is intentionally left blank. It was not deleted due to the way LabView addresses tab controls.

A.3.3.6. Misc. Settings

The Misc. Settings tab contains a few rarely used settings. First, the parameters for the conversion between piezo speed and force due to Stokes can be selected: The particle size and the fluid viscosity.

A. User manual for the nanopore setup

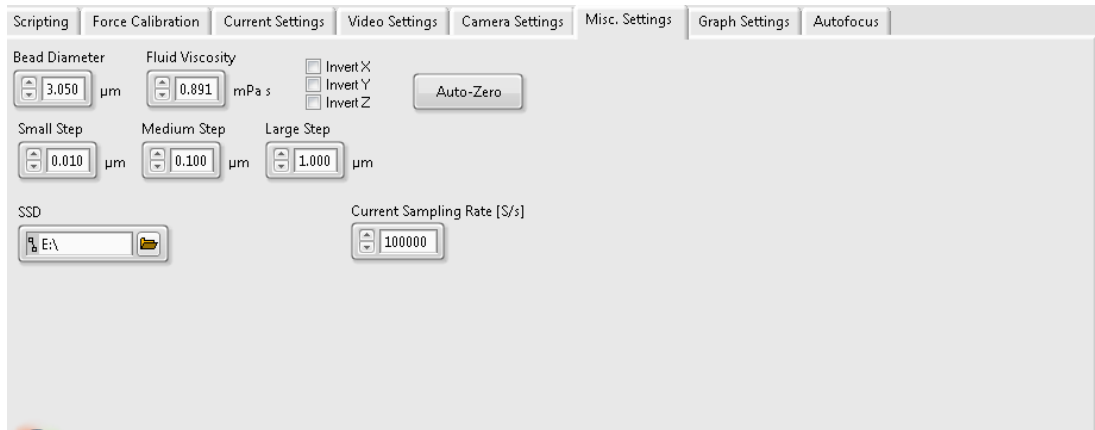


Fig. A.9.: Screenshot of the Misc. Settings tab

The three checkboxes for inverting the piezo axis are currently not used. However, it should be trivial to implement them in the three event cases [1] to [3] of the main event structure, if desired.

The Auto-Zero button performs the AutoZero routine of the piezo controller. The vendor recommends this to be performed once after switching on the controller. Beware that the AutoZero routine might move all three piezo axis along the whole travel range, possibly even exceeding the range available in software by up to 20 %. Therefore, Auto-Zero should only be pressed when there is not sample or the sample is far away from the microscope objective.

The three settings Small Step, Medium Step, and Large Step are the values that the stage moves when of the arrow cluster buttons is pressed, as described earlier.

The SSD input selects the path where all raw data is stored. As with the last parameter, Current Sampling Rate [S/s] that selects the sampling rate of both transmembrane current and voltage, any changes take effect on program restart. For the sampling rate, it should be noted that the hardware limit is $200\,000\text{ S s}^{-1}$ across all channels. Since we record two channels (voltage and current), the default value of $100\,000\text{ S s}^{-1}$ is already the maximum value. Setting higher values does not necessarily result in any directly noticeable error. However, artefacts in the returned data and random misbehaviour are induced if the value is set too high.

A.3.3.7. Graph Settings

The Graph Settings tab should be self-explanatory. Both graphs have the ability to display up to four y values on two axis (two values on the left y axis and two values on the right y

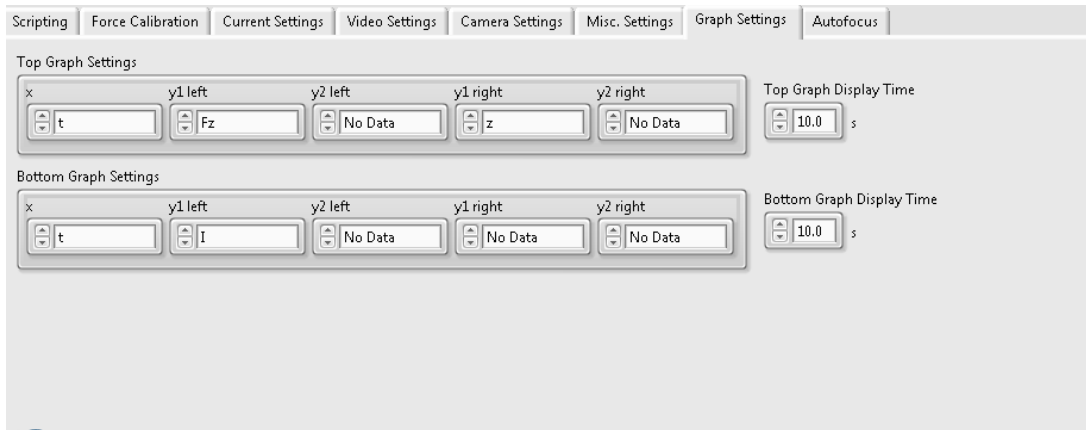


Fig. A.10.: Screenshot of the Graph Settings tab

axis) with an arbitrary x axis. However, x axis values that are not time t are untested and will probably require manual scaling settings.

The data to be displayed is internally cached in fixed-size buffers that hold the last approx. 50 s of data. If more data should be displayed, the buffers' sizes need to be changed in the code. In this case the increased memory usage and processing power for interpolation has to be taken into account.

A.3.3.8. Autofocus

Finally, the Autofocus tab allows for mostly piezo-independent distance detection. In experiments with PDMS channels, they will heat up over time due to illumination. As they heat up, they become more flexible. In typical nanopore experiments with chips tightly held by screwed on caps, this will reduce the overall channel height as the constant force applied to the chip by the holder will further indent the more elastic PDMS. In turn, the reduced channel height will also move the chip closer to the microscope objective. This movement is in the order of multiple micrometer during an experimental run of 15 min. Therefore, to better judge the true distance between the trapped particle and the membrane / chip, Autofocus Calibration can be used.

For autofocus calibration and calculation, the strength of the strongest vertical edge within the given Rectangle is determined. Therefore, after calibration the chip should not be moved in the ver-

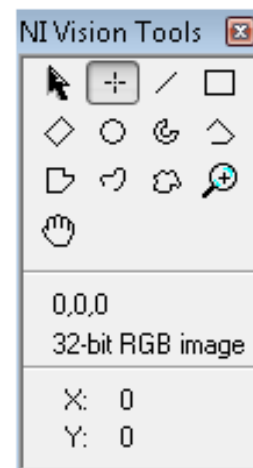


Fig. A.11.: NI Vision Tools palette with point tool selected

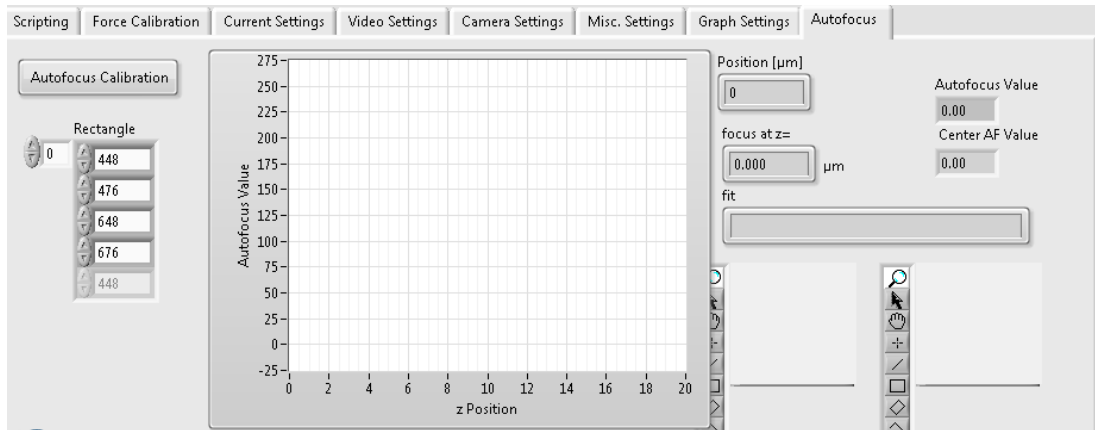


Fig. A.12.: Screenshot of the Autofocus tab

tical direction and only minimally in the horizontal direction so that the same part of the edge is examined. This can easily be prepared by performing the calibration with the laser spot position placed over the nanopore. If movement is required, it is advisable to mark significant positions in the image to be able to later re-move the chip back to its original position. For this, select the point tool in the NI Vision Tools palette (see fig. A.11) and, holding CTRL, click where you want to place a new point within the image. Existing points can be moved by first selecting the top-left cursor tool.

The four components of the Rectangle array are the left, top, right, and bottom position of the rectangular region of interest. This ROI as well as the detected edge points and the resulting edge are all shown in the overview image.

Prior to performing the autofocus calibration, move the piezo to $z = 0 \mu\text{m}$ and make sure that you are beyond the focal point. Set the velocity to a low value such as $v = 1 \mu\text{m s}^{-1}$. Now, pressing Autofocus Calibration will move the piezo to $z = 20 \mu\text{m}$ whilst recording the edge strength as the autofocus value. The piezo should move in such a way that the focal plane and maximum edge strength are reached at approx. $5 \mu\text{m}$. It will continue to move until it has reached $z = 20 \mu\text{m}$ and then automatically deactivate the button. Then, a fit should appear in the graph, with the fit function also shown in the fit text output. Also, the focus at z= output should show a reasonable value.

After calibration, in the main window the Autofocus distance will display the calculated distance between membrane / chip and focus. Note that particles are trapped roughly in the centre of the focus and that therefore one particle radius needs to be subtracted to get the distance between nanopore and particle surface.

A.4. Packing data

During experiments data is only recorded in raw, uncompressed format. To save disk space, the raw video data is compressed afterwards with `pack.vi`. It also copies the data to a user-defined backup location (such as a network volume) if desired.

To start the packing, simply load `pack.vi`, verify and adjust the selected data paths and whether a backup should be taken and the original (uncompressed) files be deleted afterwards, and start the VI. After starting, no user interaction is required. The program automatically searches for all suitable uncompressed measurement data (not just the most recent) and compresses it according to the settings. It also automatically detects which PC it is running on (`pcd1sk` or `tweezer4`) by performing a reverse name lookup of the primary IP address of the PC. It then performs the relevant compression steps.

The parameter `tmp root path` is only used on `tweezer4` and points to the location where the raw video data from the detail camera is stored. `Data root path` is the root path where the compressed data is stored. On `pcd1sk` it is also the path where the raw video data from the overview camera as well as all other raw data is stored. On `tweezer4`, this should point to the mapped network share volume `\\pcd1sk\8tb` – that is for the intended operation, the network share `\\pcd1sk\8tb` must be mapped to the drive letter E.

The `Backup root path` is the location to which all compressed data is copied for backup purposes. It is only used when the `Backup` toggle switch is enabled. Finally, the `Delete original files` toggle switch enables or disables the deletion of the original files after successful compression. Also, if it is disabled the other measurement data sets (for piezo, voltage, and other data) are copied instead of moved to the new location.

The compressed data is stored together with all other required data files in the location `Data root path\YYYY\MM\DD`, where `YYYY`, `MM`, and `DD` are the four-digit year, two-digit month and two-digit day (all with leading zero if required) of the date the experiment was performed. For example, all data belonging to experiments performed on February 28th, 2019 is found in `E:\2019\02\28` and `U:\sknust\backup\2019\02\28` with default settings.

During compression of the detail camera recordings, the program also checks whether a file consists solely of noise by checking if the standard deviation for every single frame is less

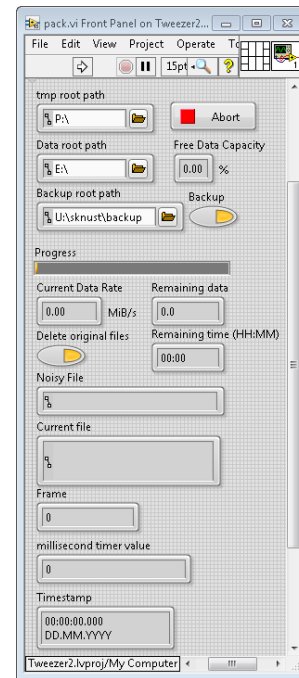


Fig. A.13.: UI of `pack.vi`

A. User manual for the nanopore setup

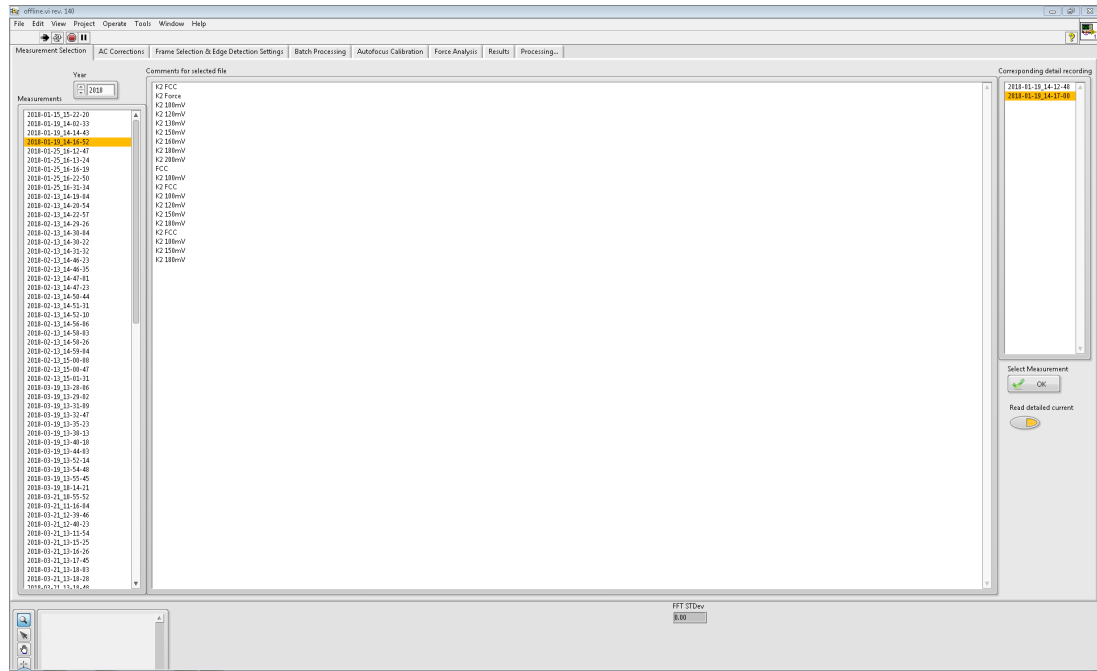


Fig. A.14.: Screenshot of `offline.vi` showing the initial Measurement Selection tab

then 5 (typical frames with a trapped particle have a standard deviation in the range of 30 – 40). If that is the case, the file is deleted.

If the default parameter of one of the values should be changed, simply change the parameter and afterwards, right-click on it and select *Data Operations* ► *Make Current Value Default*. Then, save the VI.

A.5. Analysing data

To get high-resolution force data, the recorded video needs to be analysed. This is done by the program `offline.vi` interactively in a few steps. The program guides the user through these steps in the form of different tabs in the main UI.

A.5.1. Measurement selection

In the first step, the user is prompted to select the measurement to be analysed. First, select the year. Then, from the list of measurements on the left side, select the measurement. The comments for that measurement are then loaded into the central comment display to help identify the correct measurement. Also, on the right side potential corresponding detail recording from the same day are displayed. The correct detail recording has a timestamp

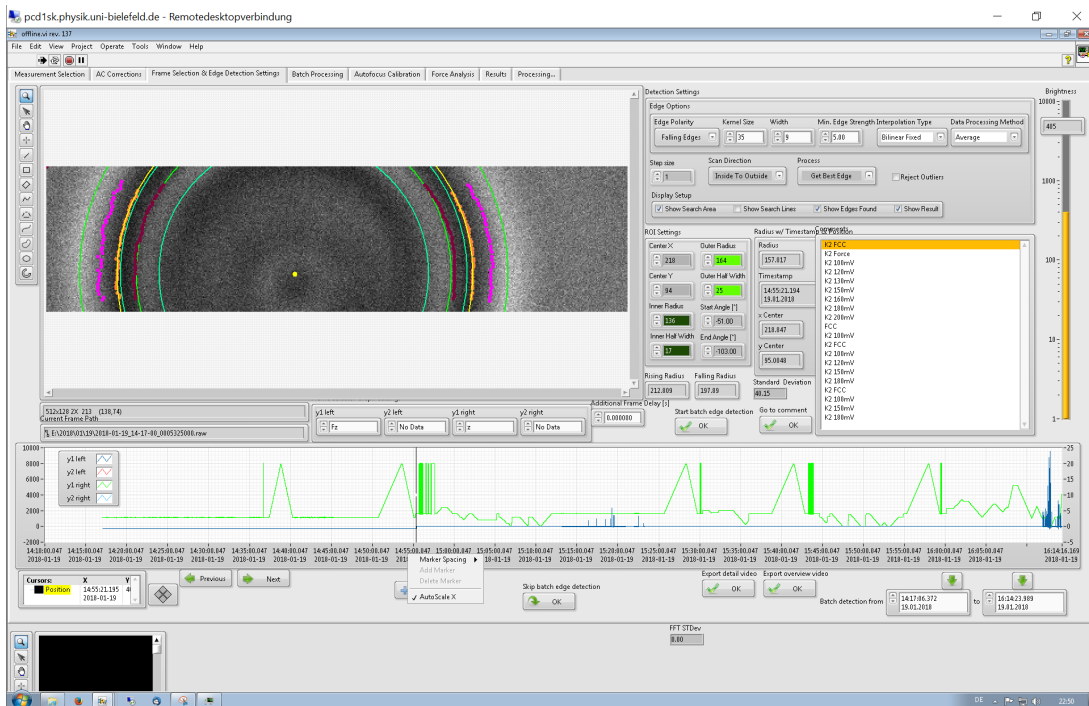


Fig. A.15.: Screenshot of the Frame Selection & Edge Detection Settings tab

very close to the selected measurement. Select it and deselect the Read detailed current switch, as the detailed current is not used in further analysis and only occupies memory. Finally, confirm your choices by clicking the OK button.

Next, a progress bar will show the process of reading the measurement metadata.

A.5.2. Frame Selection & Edge Detection Settings

In the next step, the data recorded during the experiment is shown in a single graph similar to the two graphs in Tweezer4.vi. In the centre of the screen, you can select the data to be displayed in the graph. Also, note that by right-clicking on the x-axis of the graph (or in fact any axis in a LabView VI), you can enable or disable AutoScale. The graph also contains a *cursor*, the black vertical line shown in the screenshot in fig. A.15. If the cursor is not visible, it might be outside the shown data range. In this case, right click on the cursor in the cursor information box (left below the graph) and select Bring to Center. Alternatively, selecting one of the comments and then clicking on the Go to comment button will move the cursor to the timestamp associated with the comment.

The overview and detail image closest to the current cursor position are displayed on the right monitor and in the top left of the program, respectively. For the detail image, edge

A. User manual for the nanopore setup

detection is performed according to the Detection Settings and ROI Settings, with the result being displayed in the image (if selected in Detection Settings) and in Radius w/ Timestamp. Also, the Rising Radius and Falling Radius are displayed, which can be used as a basis for optimising Outer Radius and Inner Radius.

The small + and - buttons can be used to zoom in and out of the graph at the cursor position. They only work as intended if AutoScale is disabled.

For optimal edge detection settings, it is advisable to first zoom into an area with high applied forces. Optimise the settings in such a way that all detected edges lie within the regions of interest both with and without applied force. Also, make sure that the same edges are detected. If the primary edge lies outside the region of interest, an edge for a higher-order Airy disk might be detected unintentionally.

Select the time-region for detection by either moving the cursor to beginning and end and clicking the relevant down-arrow buttons with the cursor at the timestamp to be used. Alternatively, you can also manually enter start and end time in the two fields at the lower right.

After selecting the time range, you can use Export detail video or Export overview video. In both cases, the video is exported as a series of single-frame images (in PNG format for the overview camera, in TIFF format for the detail camera). If required, use third-party tools such as *ffmpeg* to convert the images into a true video format. An exemplary *ffmpeg* command could be `ffmpeg -i overview-%06d.png -c:v h264 -b:v 2000k overview.mp4` or `ffmpeg -i %08d.tiff -c:v h264 -b:v 2000k detail.mp4`. Note that using this method for the detail camera images creates a super slow motion video slowed down by a factor of $1555/25 = 62.2$.

Finally, pressing the Start batch edge detection button initiates the edge detection of the selected time range. In the next screen, the progress is shown with an estimate of the remaining time. Edge detection takes roughly four to five times the length of the selected time range. Therefore, it might be advantageous to only perform the detection on several small intervals instead of one large interval.

A.5.3. Autofocus calibration

After performing the edge detection, the program also performs an autofocus calculation using an FFT (fast fourier transform) method. In the Autofocus Calibration tab, you can currently only export that data into a text file for further analysis outside the software.

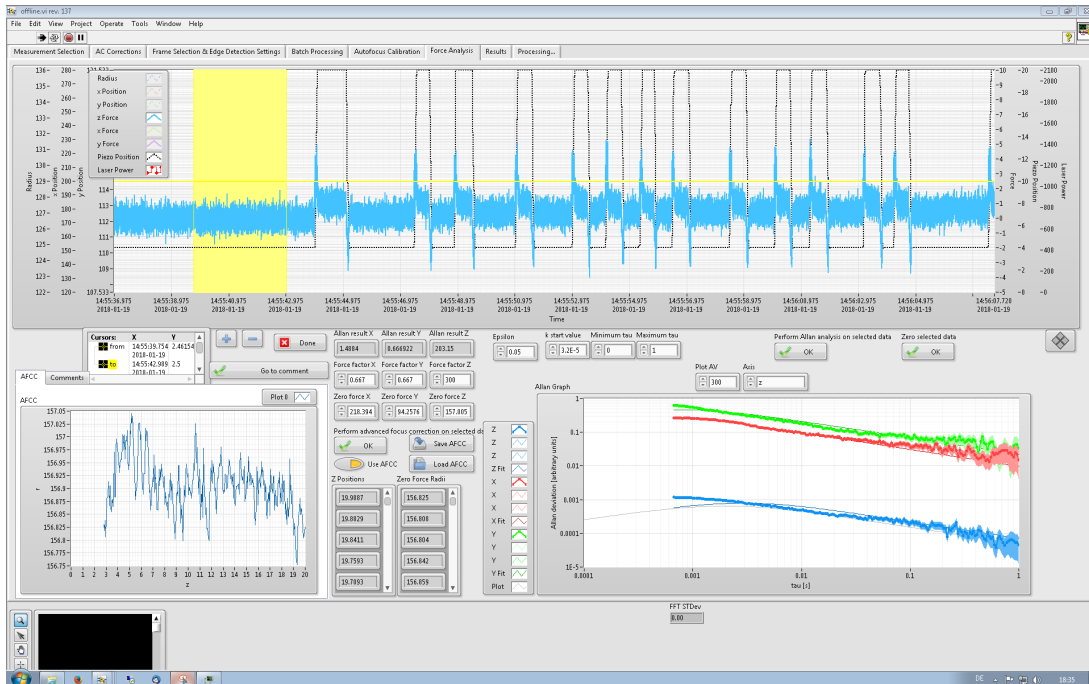


Fig. A.16.: Screenshot of the Force Analysis tab

A.5.4. Force Analysis

The Force Analysis tab presents the results of the batch edge detection. In the top graph, the detected positions and radii are displayed along with the calculated forces. Also, the z piezo axis is shown as well as the laser power. Graphs can be shown, hidden, and customised by right-clicking on the name or icon in the graph legend.

This graph contains two cursors which are used to directly select a time range for multiple operations. As with the frame selection, right-click on a cursor to use Bring to Center if necessary. If both cursors are outside of the shown range, use it on one cursor and move it afterwards in the direction that enlarges the yellow section between the two cursors.

In the bottom left, you can either select a comment and move the currently active (last used or manually selected) cursor to its corresponding timestamp. Alternatively, the state of the advanced focus correction calibration (AFCC) is shown.

The first step in analysis should be to select a time range where the force is zero and then click on the Zero selected data button. This averages the positions and radii within the range and sets the Zero force X, Zero force Y, and Zero force Z input fields to these values. They are then used as zero force positions x_0 and y_0 as well as zero force radius r_0 .

To perform an AFCC, first select a region of rising or declining piezo position, ideally mov-

A. User manual for the nanopore setup

ing slowly through the whole range. Then, click on the Perform advances focus correction on selected data button. The software then builds clusters of data points: The first z position is used as a reference and further positions are compared to it. As long as the deviation is less than `Epsilon` (in μm , default value $0.05 \mu\text{m}$) it belongs to the current cluster. If it deviates more, the current cluster is averaged (in both z and r) if it contains more than 50 valid radii and a new cluster is started, with the current piezo value as a new reference. The results of this analysis is shown in the graph on the left (if visible) and can be saved by clicking Save AFCC. This is especially useful if multiple intervals in the same experiment are analysed. For further intervals, the AFCC can then be loaded by clicking Load AFCC. For both buttons, a file dialogue opens and prompts for a location. That file is also human-readable.

If `Use AFCC` is enabled, the value of `Zero force Z` is ignored. Instead, the zero-force radius r_0 for force calculation is determined by first linearly interpolating the piezo z position for each timestamp and then linearly interpolating the corresponding r_0 from the AFCC data set. Therefore, the AFCC data set must span the complete range of z values encountered during the measurement.

The graph on the bottom right shows the results of an Allan variance analysis. The saturated line with dots is the result and the unsaturated band shows one standard deviation. The thinner line shows the best fit. Additionally, the grey line shows the Allan variance corresponding to the value in `Plot AV` if it is for either x and y , or for z (as selected by `Axis`).

For Allan analysis, a short period (less than 10 s) should be selected. In this period, no forces should be applied. The analysis will then be performed for 200 values of τ logarithmically equidistant between `Minimum tau` or the average distance between subsequent frames, whichever is larger, and `Maximum tau` or half the duration of the selected range, whichever is smaller. For the fit, a starting value for k of `k start value` is used. The results are shown in the graph and, in suitable units (pN px^{-1} for x and y , pN for z), displayed in the three `Allan result` outputs. On purpose the values of the `Force factor` input fields are not overwritten.

Generally, you should perform Allan variance analysis for a few time intervals and always check whether the fit is meaningful. Here, the most important area is in the middle range around $\tau = 0.01$ s. For lower values, noise is an issue. For larger values, drift becomes challenging. Also, always take surface effects into account when performing analysis close to a membrane. Ideally, the results of Allen variance and Stokes' drag calibration give comparable results.

For radial forces, i. e. F_x and F_y , note that the system is much more accurate for horizontal forces F_x . For larger particles, such as the $3.05 \mu\text{m}$ bead used in this manual, the top and bottom of the particle are cropped in the detail camera. Those are however key to determining the vertical position, as the left and right sides of the particle are most important for the

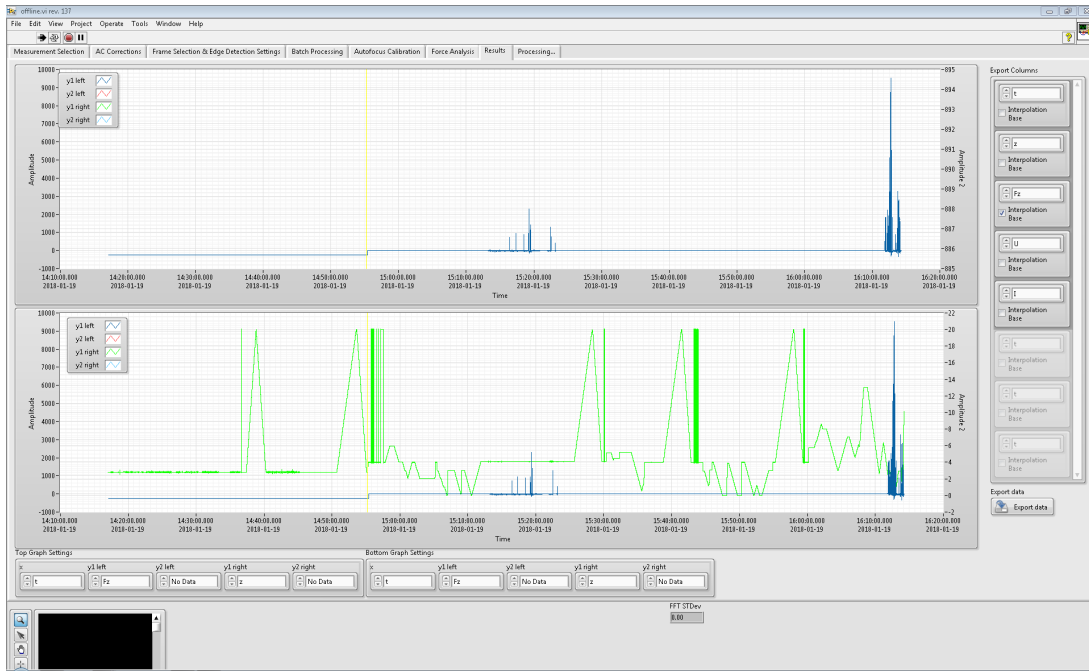


Fig. A.17.: Screenshot of the Results tab

horizontal position.

Finally, when the force calibration was performed, clicking the Done button leads to the final Results tab.

A.5.5. Results

The Results tab once again shows the data in two customisable graphs. It also allows for data export. For this, select the desired output columns in the Export Columns array on the right. As described earlier and illustrated in fig. B.1, one or more interpolation bases need to be selected. This can be done by simply checking the corresponding Interpolation Base checkbox. If multiple interpolation bases are selected, the export will contain data at the timestamps of all interpolation bases, sorted chronologically. That means that a later separation and allocation into the individual interpolation bases is not possible; the exported data is one chronological data set.

If a later separation is required, multiple exports can be performed with different export column configuration. In this case, simply check one interpolation base for the first export and other interpolation base(s) for subsequent export(s).

The data is exported by clicking the Export data button. This prompts the user to specify the desired export file location. The file will be a tab-separated plain-text file. Numbers are

A. User manual for the nanopore setup

output as plain decimal numbers (no E-notation) with six decimal places (e.g. 12345.678901 or 0.000012). Timestamps are formatted according to ISO 8601-1:2019¹⁷⁰ in format [YYYY][“-”][MM][“-”][DD][“T”][HH][“:”][MM][“:”][SS][“.”][sssss], e. g. 2018-01-19T12:34:56.789012.

B. User manual for the Elasto-Tweezers setup

B.1. Safety information



Danger: This setup contains a class 4 laser according to DIN EN 60825-1:2001-11 with $P_0 = 2100$ mW at $\lambda = 1060$ nm. Do not override the safety interlock. Do not open the sides of the microscope deck whilst the laser is operating.

B.2. System overview

B.2.1. Hardware overview

The system is based on an Olympus IX50 inverted microscope and offers a static primary trap as well as a secondary trap that can move in all three dimensions. Both traps offer identical trap stiffness. We use three ultrasonic piezo motor stages (PI U-521.23) to move the lenses for x , y , and z shift of the laser beam and therefore the secondary trap. They are controlled by a pair of PI C-867 controllers (one for x and y , one for z). To move both traps in relation to the microfluidic flow cell, the base plate is mounted on a combination of a stepper-motor xy -stage and a xyz piezo stage. The stepper motors are controlled by a Ionovation control board. The piezo stage is controlled by a PI P-527.3CD unit.

The PI controllers are connected via Ethernet. They are connected to a dedicated network card in the PC (IPv4 address: 10.0.0.1) via a switch. The Ionovation controlled is connected to the PC via USB and identifies as a HID¹⁷¹ device (device ID 0483:574E).

Illumination, laser power and shutters are controlled by a separate Ionovation control board, which also connects to the PC via USB and identifies as a HID device (device ID 0483:5750).

The detail camera (Allied Vision Technologies Mako U-029B) and the overview camera (IDS Imaging Development Systems UI-3272LE-M) connect to the PC via USB 3.0 and USB 3.1, respectively.

B. User manual for the Elasto-Tweezers setup

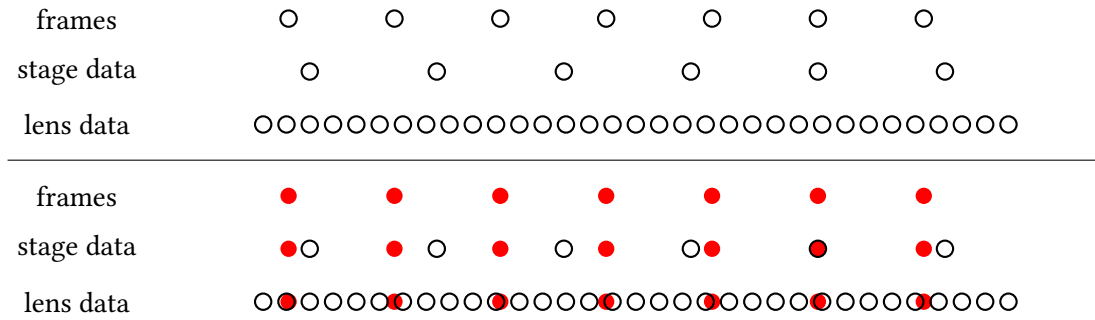


Fig. B.1.: Illustration of the data interpolation process. Top: Video frames, data from the piezo xyz-stage, and data for the position of the lenses all have data points (black circles) at different times. Bottom: If we are primarily interested in data from the video frames, we interpolate the piezo and lens data (red circles) at those times where video frames are available.

B.2.2. Software overview

Before going into detail regarding the individual software components, it is important to note how the software saves measurement data.

Raw video data is stored during measurement in uncompressed raw form, that is into binary files (each for 15 s of data) containing the raw data received by the camera. This data is stored on a RAID-0 (a volume of multiple hard disks striped together for increased performance and capacity, which loses all data if even a single drive fails). After each experiment, typically during the night this data should be packed and pushed into backup. In packed format, the images are stored in binary files consisting of PNG files. Additionally, for each binary file a plain text index file is created. It contains for each frame the timestamp as well as starting position and length (in bytes) within the binary file. Both files must be kept together, as it is very difficult to extract the individual images from the binary files without the index (and impossible to extract the timestamps).

All other data (piezo positions, shutter status, ...) is stored in a binary format containing for each datapoint the timestamp and the value.

For analysis, we need to perform the edge detection for each frame, calibrate and zero the resulting bead positions to get displacements / forces and finally align that data with the other data. Since all data has its own timebase (a frame is recorded at a different timestamp than a piezo position), we align by selection the primary data (typically this would be the force) and then linearly interpolate all remaining data for each timestamp at which primary data is available. This principle is illustrated in fig. B.1 for better understanding.

The software used for measurement is `ET.vi`. On startup, it will open `overview.vi` on the

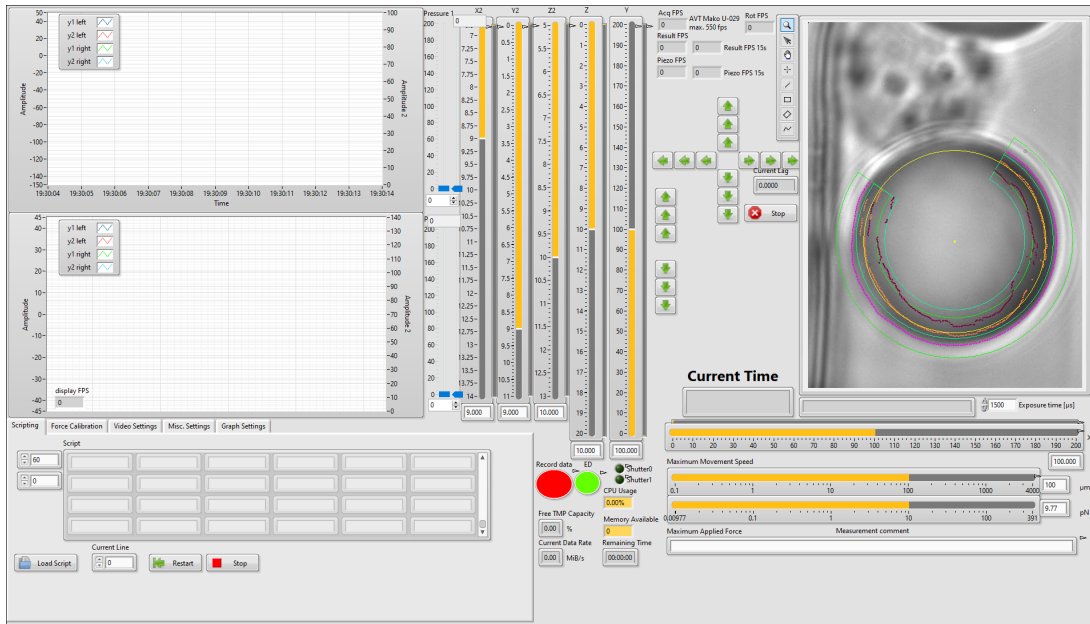


Fig. B.2.: Screenshot of ET.vi with Scripting tab

secondary monitor.

After the experiments pack.vi is used. It is simply started and performs its work without any user interaction, only displaying a progress bar and an estimation of the remaining time. It takes the raw video data, packs it and saves it both to backup storage and to local storage, deleting the raw video data on successful conversion.

For analysis of the data and export into a user-readable format, offline.vi is used. This also performs an offline edge detection for higher accuracy.

Finally, analysis-flexible.vi can be used to calculate stress and strain from force data exported with offline.vi.

B.3. Performing experiments

B.3.1. Turning the system on

To turn the system on, make sure that all three piezo controllers are switched on. They should run for at least one minute before starting ET.vi. Also power on the laser and the two Ionovation controllers before starting the software.

B.3.2. Controlling ET.vi

ET.vi in conjunction with overview.vi presents the main user interface for experiments. At the top left of ET.vi, two graphs show user-selected data for a user-selected time (default: 10 s). In the top right, the detail image is shown with a user-selected overlay showing the results of the edge detection. Below and left of this image, the position of the piezo stage can be modified with the sliders X, Y, and Z. Similarly, the piezos controlling the secondary trap can be controlled with X2, Y2, and Z2. Units of X, Y, and Z is in μm , units of X2, Y2, and Z2 is in mm. The piezo movement speed and the corresponding Stokes' drag force can also be selected below the image. For the secondary trap, this speed is converted to ensure that the trap position, not the individual piezos, move with the selected velocity.

To ensure that both traps are in the same plane, the value of Z2 should be set to 10.350.

Below that, a measurement comment can be entered. It is saved upon exiting the text input field or pressing return with the current timestamp. This way, specific moments during the experiment can be easily annotated. It can of course also be used to identify the experiment or experimental parameters for later use.

Between the detail image and the slides, there are a few indicators at the top showing the frames per seconds and datapoints per second, averaged over 1 s and 15 s, of the image acquisition (only 1 s averaging), force calculation, and piezo data acquisition.

Below these indicators, a cluster of arrows is visible. The arrows in the cross formation move the piezo stage in the indicated direction in X and Y, whilst the six arrows to the bottom left of it move the piezo stage in Z. The distance moved by each button can be selected by the user; the default value is $0.01 \mu\text{m}$ for the innermost buttons, $0.1 \mu\text{m}$ for the middle buttons and $1 \mu\text{m}$ for the outermost buttons.

Next to the arrows, a stop button should be used to stop the program (instead of aborting execution in LabView or quitting LabView altogether) to ensure that all hardware communication is ended gracefully and all data in RAM is saved to disk. Above, the lag between the timestamp of the last analysed frame and the current time is shown. If this value becomes larger than 0.5 s, an audible alarm "Lag!" is played. In that case, edge detection should be turned off (see below) temporarily and it should be ensured that no background tasks are running, reducing system performance. Reducing the step size in Video Settings can also alleviate the problem. If this does not help, rebooting the computer can be used as a last resort.

The most important setting is the red recording button Record data left of the movement speed selector. Raw video data is only saved to disk when this button is activated (bright red). *It is therefore of utmost importance that this button is activated during the experiment as soon as relevant experimental phases are occurring.*

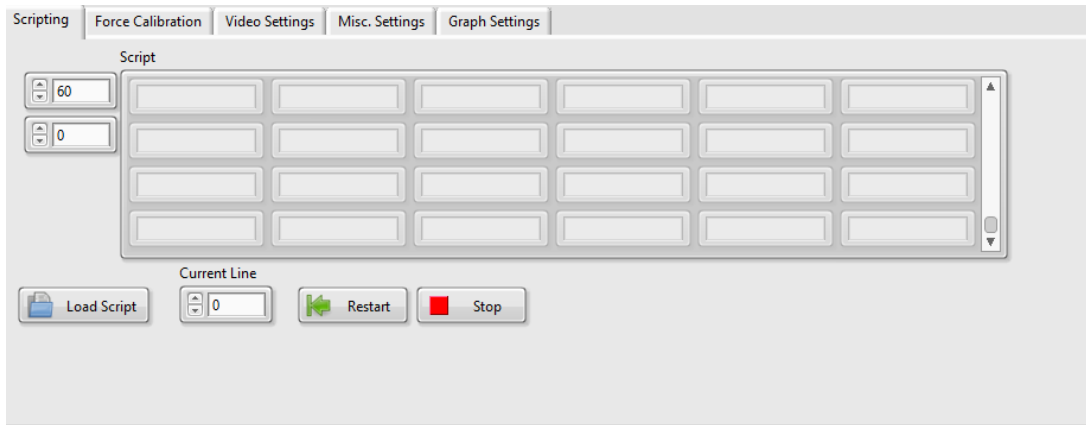


Fig. B.3.: Screenshot of the Scripting tab

Directly next to the recording button, the green button ED controls whether real-time edge detection should be performed. As recording the data puts additional strain on the system, edge detection should be disabled if possible when data is recorded.

Below the recording and edge detection buttons, indicators display current CPU usage, remaining free memory, free storage capacity, current data rate, and the remaining time until the storage is full, assuming the current data rate. When the free memory drops below 2 GB, an audible alarm “Memory!” is played. Reaction should be similar to the lag alarm.

In the bottom left, different tabs can be selected for specific settings and operations. These will be discussed in detail below.

B.3.2.1. Scripting

The Scripting tab allows scripting of some of the program features for repetitive or semi-automatable tasks. The large script array contains the script can be modified directly. However, most of the time a script is edited externally with a text editor and then loaded into the software.

The scripting language is based on BASIC. It is line oriented and runs as fast as possible, stopping execution once the current line number exceeds the number of rows in the script array. Script files are expected to be plain text files with tab separation. The first column denotes the line number. It *must* be a strictly increasing number between 0 and 2 147 483 647, inclusive. Gaps in numbering are allowed and in fact encouraged to facilitate later introduction of code passages without having to change all following line numbers. Common practise is to use increments of 10 or 100 in coding, i. e. lines are numbered 10, 20, 30, ... or 100, 200, 300, ...

B. User manual for the Elasto-Tweezers setup

The second column contains the code instruction. Case is ignored, although all caps is encouraged. The following columns contain the arguments to the code instruction, if any.

Valid code instruction are (in general notation `CMD ARG1 ARG2 ARG3 ARG4`):

- `NOOP`: no operation
- `GOTO int`: goes to line ARG1
- `SLEEP val`: sleeps for ARG1 milliseconds
- `SET var val`: sets the value of ARG1 to ARG2
- `ADD var val`: sets the value of ARG1 to (ARG1 + ARG2)
- `IFGOTO var cmp val int`: if the comparison ARG2 of ARG1 with ARG3 is true, then go to line ARG4 (else continue with the next line)

Where

- `int` is a positive integer between 0 and 2 147 483 647, inclusive, consisting solely of the digits 0-9. If another character is found, reading stops. If no digit is found, 0 is used.
- `var` is a valid variable name. Valid variable names are X, Y, Z, X2, Y2, Z2, V, FMAX, BR, SX, SY, VAR0, VAR1, VAR2, VAR3, VAR4, VAR5. Case is ignored, although all caps is encouraged. The variables X, Y, Z, X2, Y2, Z2, V correspond to the piezo positions and the piezo speed. Values are as shown in the UI. FMAX is the maximum force in pN according to Stokes, thus also setting the piezo speed. BR is the brightness of the illumination, between 0 and 4095 (inclusive). SX and SY are the position values of the stepper motor stage. The other five variables do not correspond to a real value and can be used as internal variables.
- `val` is either a valid variable name or a floating point number. A floating point number consists of the digits 0-9, at most one decimal point (`.`), at most one letter `e` or `E`, and at most two minus signs, one at the beginning and one immediately following an `e` or `E`.
- `cmp` is one of `<`, `>`, `>=`, `<=`, `=`, or `!=`. Comparison is performed floating point safe: before comparison values are cast into single-precision floating point numbers and machine epsilons are added or subtracted to the first argument for `>/>=` or `</<=`. For equal / non-equal checks, the software tests whether the single-precision value of the first number is within $\pm\epsilon$ of the second number with machine epsilon ϵ .

When loading a script file, the lines are inserted into the script array at the specified line numbers. Empty lines are filled with `NOOP`.

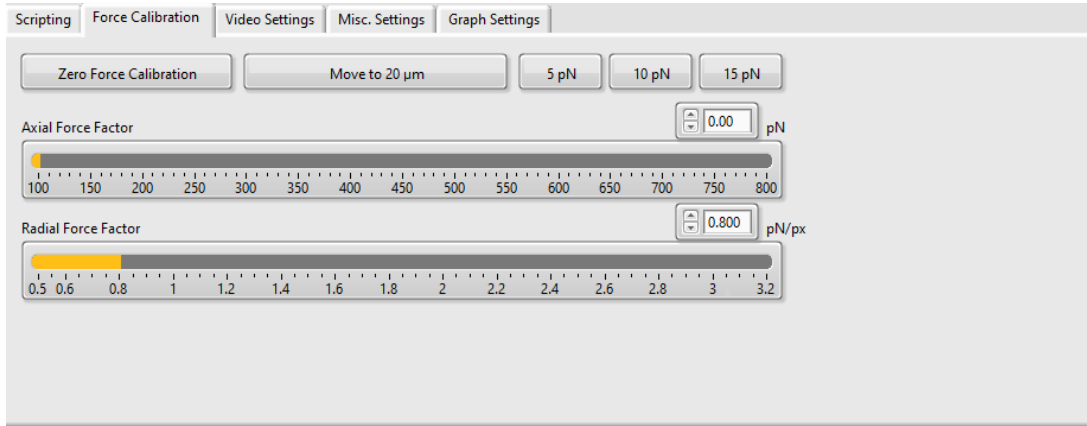


Fig. B.4.: Screenshot of the Force Calibration tab

B.3.2.2. Force Calibration

The Force Calibration tab contains all relevant parameters and routines for force calibration that is used to display the live force data. It is only used for the live data. During offline data analysis, a separate force calibration is used. Therefore, during experiments the force calibration capabilities should only be used to get a rough insight into the forces acting on the trapped particle to perform appropriate actions.

Axial Forces are calculated as

$$F = k \left(\frac{r_0}{r} - 1 \right) \quad (\text{B.1})$$

although the setup is currently not able to perform axial force detection, as the detail camera is in focus. For reliable video-based axial force detection, the detail camera needs to be defocussed, which leads to changes in apparent radius during axial displacement.

Radial forces are calculated as $F = k(x - x_0)$.

As a first step for force calibration, the zero force needs to be calibrated. To this end, press the Zero Force Calibration button whilst a bead is trapped in the primary trap and not subject to forces. Wait a few seconds, then press the button again. As long as the button is active, the detected positions and radii of the bead are collected and averaged.

Then, we can calibrate the Radial Force Factor. Press either the 5 pN, 10 pN, or 15 pN button or set a desired force and corresponding maximum movement speed manually. Then, move the piezo stage in any direction, preferably keeping the trapped particle away from other objects and in the centre of microfluidic structures. In the graphs, a force signal is shown, which should correspond to the selected force. If it does not correspond to the target force, simply change the force factor appropriately.

The maximum movement speeds applies to all piezo axis independently. Therefore, if the

B. User manual for the Elasto-Tweezers setup

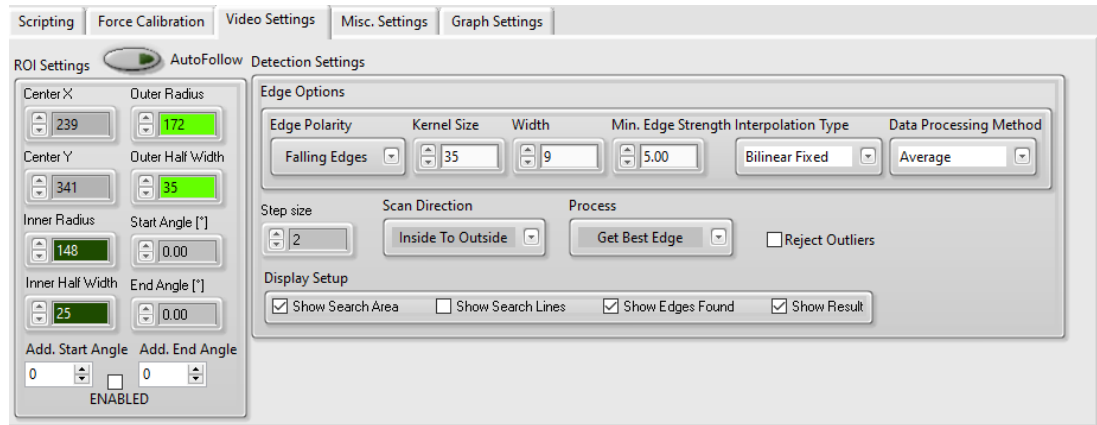


Fig. B.5.: Screenshot of the Video Settings tab

piezo stage is moved in both x and y, equal forces in x and y are encountered and the total force (which is not calculated or displayed in this software) is $\sqrt{2}$ times the desired force.

This calibration procedure does not take correction due to close walls into account. If required, the correction factor can be taken in consideration when comparing the measured force with the desired force F – the measured force should be βF with correction factor β .

Alternatively, instead of calibrating the radial force factor, a static factor can be used and is typically sufficient for real-time monitoring purposes. For full laser power and $15\ \mu\text{m}$ polystyrene particles, a force factor of $1.0\ \text{pN px}^{-1}$ should provide reasonable results.

B.3.2.3. Video Settings

The Video Settings tab contains the controls of the video-based force detection.

The Detection Settings contain the internal settings for edge detection. The default values as shown in the screenshot are tuned for typical experiments on this system. The only parameters that should usually be changed are the checkboxes in Display Setup to select or deselect the edge detection result overlays in the detail image. In case of frequent lags that are not resolved by a reboot, setting Step size to a larger value will also help. Edge detection is performed along radial spokes. This parameter determines the angle (in degrees) between these spokes: 1 corresponds to 360 spokes, 2 to 180 spokes, and so on.

If at any point particles that yield a bright annulus (instead of a dark one) are used, the Scan Direction should be inverted to Outside To Inside.

The ROI Settings select the position of the annular region of interest (ROI) within the frame. Center X and Center Y set the overall position. Inner Radius r_i and Inner Half Width w_i select the radius of the annulus for the inner edge (from bright to dark with default

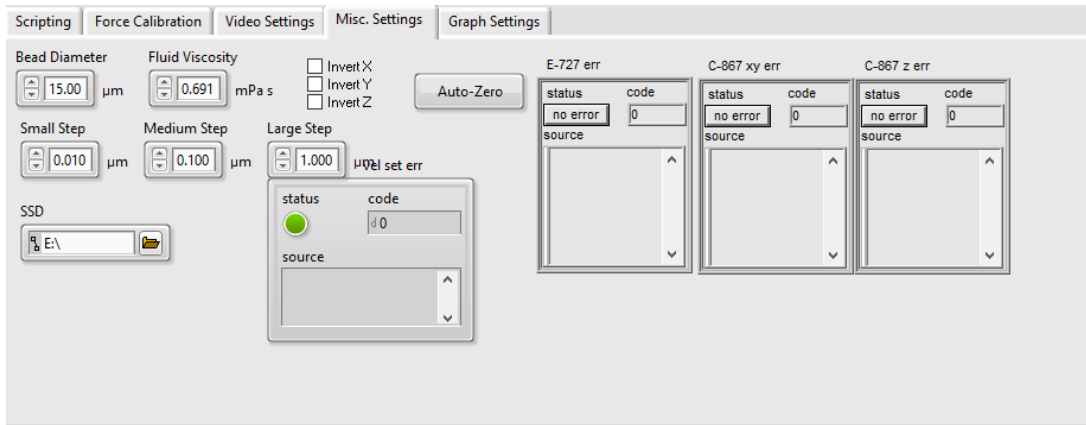


Fig. B.6.: Screenshot of the Misc. Settings tab

particles): It is from $(r_i - w_i)$ to $(r_i + w_i)$. Analogously, the Outer Radius and Outer Half Width determine the radius of the outer edge (from dark to bright with default particles). Finally, the annulus can be confined between two angles. These are set by the values of Start Angle [$^\circ$] and End Angle [$^\circ$]. Those values can be outside the range from 0° to 360° as well for easier configuration. The software automatically takes the entered values modulo 360° . The direction is counter-clockwise, with 0° corresponding to the three o'clock / positive x axis position. This feature should be used to exclude parts of the bead in contact with a cell. If detection should be performed in two disjunct angular regions, the Add. Start Angle and Add. End Angle can be set to a second angular region. Checking the ENABLED checkbox will perform edge detection in both regions.

To facilitate force detection even with large radial forces and therefore large radial displacements, the software contains an AutoFollow feature. It should be enabled once a particle has been trapped. It will then update the Center X and Center Y values every 100 frames to the average of the last 100 detected particle positions. This works reasonably well for typical force ramps. If however a sudden large force spike occurs, this algorithm might not be able to keep up. In this case, the ROI will typically centre to $(0, 0)$. AutoFollow should then be disabled and the ROI manually centred correctly, before re-enabling AutoFollow.

B.3.2.4. Misc. Settings

The Misc. Settings tab contains a few rarely used settings. First, the parameters for the conversion between piezo speed and force due to Stokes can be selected: The particle size and the fluid viscosity. Default values are $15.0 \mu\text{m}$ and the viscosity of water at 37°C .

The three checkboxes for inverting the piezo axis invert the direction of the piezo stage

B. User manual for the Elasto-Tweezers setup

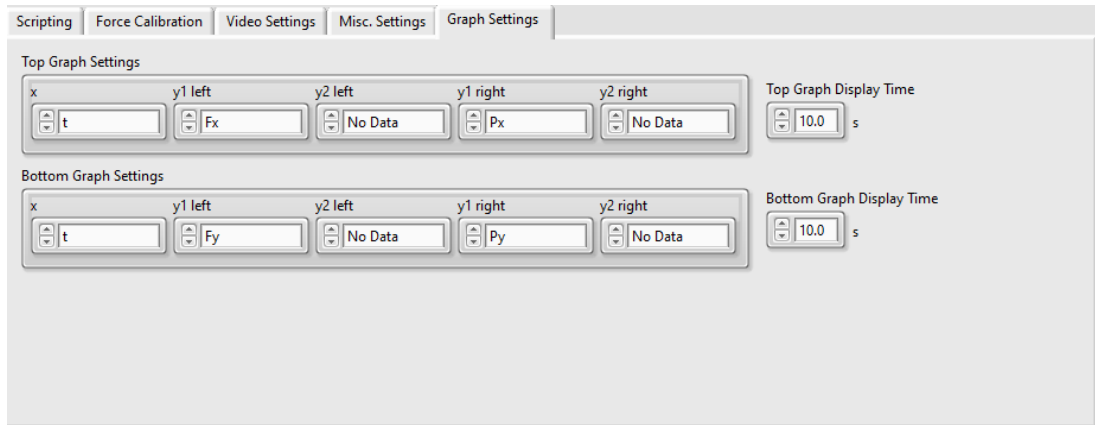


Fig. B.7.: Screenshot of the Graph Settings tab

when clicking the arrows between detail image and slides.

The Auto-Zero button performs the AutoZero routine for all three piezo controllers. The vendor recommends this to be performed once after switching on the controller. Beware that the AutoZero routine might move all three piezo axis along the whole travel range, in the case of the piezo stage possibly even exceeding the range available in software by up to 20 %. Therefore, Auto-Zero should only be used when the laser shutters are closed.

The three settings Small Step, Medium Step, and Large Step are the values that the stage moves when of the arrow cluster buttons is pressed, as described earlier.

The SSD input selects the path where all raw data is stored. Any changes take effect on program restart. The name of the input stems from the historic background. Due to size limitations in SSDs, it points to a RAID-0 array of hard disks. However, any storage can be used as long as it supports sustained write rates of 250 MB s^{-1} .

B.3.2.5. Graph Settings

The Graph Settings tab should be self-explanatory. Both graphs have the ability to display up to four y values on two axis (two values on the left y axis and two values on the right y axis) with an arbitrary x axis. However, x axis values that are not time t are untested and will probably require manual scaling settings.

The data to be displayed is internally cached in fixed-size buffers that hold the last approx. 12 s of data. If more data should be displayed, the buffers' sizes need to be changed in the code. In this case the increased memory usage and processing power for interpolation has to be taken into account.

B.3.3. Controlling overview.vi

The overview software offers a user-friendly point-and-click approach to trapping and manipulating objects. The window is dominated by the camera feed of the overview camera. Superimposed are two green circles, showing the positions of the optical traps. In the screenshot shown in fig. B.8, the bottom trap is the static trap and the top trap is the mobile, secondary trap.

Below the overview image, a slider controlling the Camera Exposure of the overview camera and a numerical control for the LED Brightness. The slider works on an exponential scale. Numerical control of the brightness is possible in a range from 0 to 4095. Illumination begins at 800. Typically, experiments are conducted at a brightness level of 1200 to prevent overexposure of the detail camera footage.

B.3.3.1. Moving the optical traps

The overview image also shows a green and a yellow rectangle. The green rectangle indicates the possible positions of the secondary trap. It always remains static with regards to the video frame. To move the secondary trap, middle click at the desired position. The trap will move towards the target position, which is indicated by a blinking green circle. Movement towards destination is not in a straight line. Instead, x and y axis move independently and with the same velocity to their respective target values, resulting in a movement that is at first diagonal and then approximately horizontal or vertical (as seen by the slight angle of the green rectangle the camera is slightly rotated with regards to the coordinate system of the secondary trap).

The yellow rectangle shows the possible positions of the primary trap with regards to the flow chip. Holding the Shift key and middle clicking on a target destination moves the piezo stage in such a way that the primary trap (which stays static in relation to the camera image) ends up in the indicated position. The new position of the yellow rectangle is blinking during movement.

This way of motion moves both the primary and the secondary trap in relation to the flow cell, whilst keeping the relative orientation between the two traps static. For only moving the primary trap, holding the Shift and Control key whilst middle clicking will move the secondary trap in the opposite direction. That way, only the primary trap moves in relation to the flow cell whilst the secondary trap remains static in relation to the flow cell.

B. User manual for the Elasto-Tweezers setup



Fig. B.8.: Screenshot of overview.vi

B.3.3.2. Controlling the power of the optical traps

The power of the laser is controlled by the Laser Power control. It accepts values between 0 and 4095 (inclusive) and relationship between this value and laser power is approximately linear.

The primary and secondary trap can be turned on and off individually with shutters. These are controlled by the button Shutter 0 (for the primary trap) and Shutter 1 (for the secondary trap). Indicators next to the buttons show the current status. In the case of severe system stress, there might be a delay of a few seconds between toggling the switch, the action of the shutter, and the feedback by the indicator. The mechanical switching of the shutter status can however be heard as a *click* sound and can be seen as a slight disturbance (in the range of a few nanometre) in the position signals of the piezo stage, due to induced vibrations.

To transfer a trapped particle between the two traps, only the trap currently holding the particle should be active. After moving secondary trap to the position of the primary trap, clicking on the Toggle button toggles both shutters simultaneously, ensuring safe transfer of the particle between the traps.

In contrast, manual transfer cannot toggle both shutters at the same time. Disabling the current trap preliminarily can loose the particle if net flow is occurring. Enabling the inactive trap prematurely risks catapulting the particle out of the traps if their focal plane are not exactly identical.

B.3.3.3. Controlling the stepper motor stage

On the first run of the program after a power off, the position sensors of the stepper motor stage need to be initialised. To this end, press the Init Motors button. Both axis are equipped with a centre switch, which toggles at the zero position. Using the current switch status, the system determines the direction towards centre and moves the axis until the switch toggles. It then moves the axis slowly in the other direction until the switch toggles again, setting the zero position.

The controls Pos1 Set and Pos2 Set as well as the scripting variables SX and SY can be used to control the stage position. The units are steps, where one step equals 10 μm . Movement range for the x axis is -1050 to 950 , the range for the y axis is -1400 to 550 . This corresponds to a useable area of $20.0 \text{ mm} \times 19.5 \text{ mm}$.

B.3.3.4. Measurement automation

The software offers a simple routine for measurement automation. When clicking the Start measurement button, first the trapping structure is searched in the image. To this end, the



Fig. B.9.: Illustration of the measurement automation workflow. First, the trapping structure is search with the reference image (inset). The resulting position is annotated in orange. Then, in to top red rectangle, two beads are searched (blue). The bottom rectangle is checked for the presence of a cell. The left bead is then moved into the trapping structure along the dark blue path, followed by the cell along the green path and the right bead along the light blue path.

system searches for edges in the camera feed that form a geometric pattern similar to the edges in the reference image (shown in the inset in fig. B.9). This position is highlighted in the image.

Depending on the position of the structure, the system moves the piezo stage to ensure that all positions required for experiments can be reached by the optical traps. Based on the structure position, it then checks for the existence of two circular edges in the bead trapping portion of the structure and notes their position. It also checks the cell trapping part of the trapping structure below the current one (the offset is known from the chip geometry). Here, the system calculates the standard deviation of the image. If the standard deviation is larger than 25, a cell is assumed to be trapped here. The analysis of the standard deviation is used as a more reliable indicator of the existence of a cell compared to edge detection, due to the lower contrast of cells compared to beads.

Then, the bead-cell-bead cluster is set up in the experimental area of the trapping structure. The leftmost bead, then the cell, and then the rightmost bead are moved along predetermined paths. This movement is performed with the secondary trap. At the end, the then bottom bead is switched over to the primary trap and the secondary trap is placed on the top bead and activated.

Finally, a series of indentation experiments is performed. For each of the velocities $1 \mu\text{m s}^{-1}$, $10 \mu\text{m s}^{-1}$, $100 \mu\text{m s}^{-1}$, and $1000 \mu\text{m s}^{-1}$, the complex is compressed and stretched three times. For $1 \mu\text{m s}^{-1}$ the wait between indentations and stretches is 250 ms. For the other velocities, it is 500 ms.

To facilitate quick switching between trapping structures, selecting a new entry in the Go to drop-down menu will move to the named position with the stepper motor stage. The naming scheme is illustrated in fig. B.10.

B.3.4. Resolving common issues

The most common issue occurs when starting the program and the initialisation of one of the cameras fails. In this case, stop the program, unplug the two cameras from the PC, wait ten seconds, plug them back in and restart the software. This typically fixes all issues, probably arising from an inconsistent firmware state in one of the cameras.

As the software puts extreme strain on the input/output capabilities of the operating system, even slight background tasks such as Antivirus software or Windows Update can inhibit performance. In case of lag, rapid increase of memory usage or unresponsiveness, the PC should be restarted if possible.

B. User manual for the Elasto-Tweezers setup

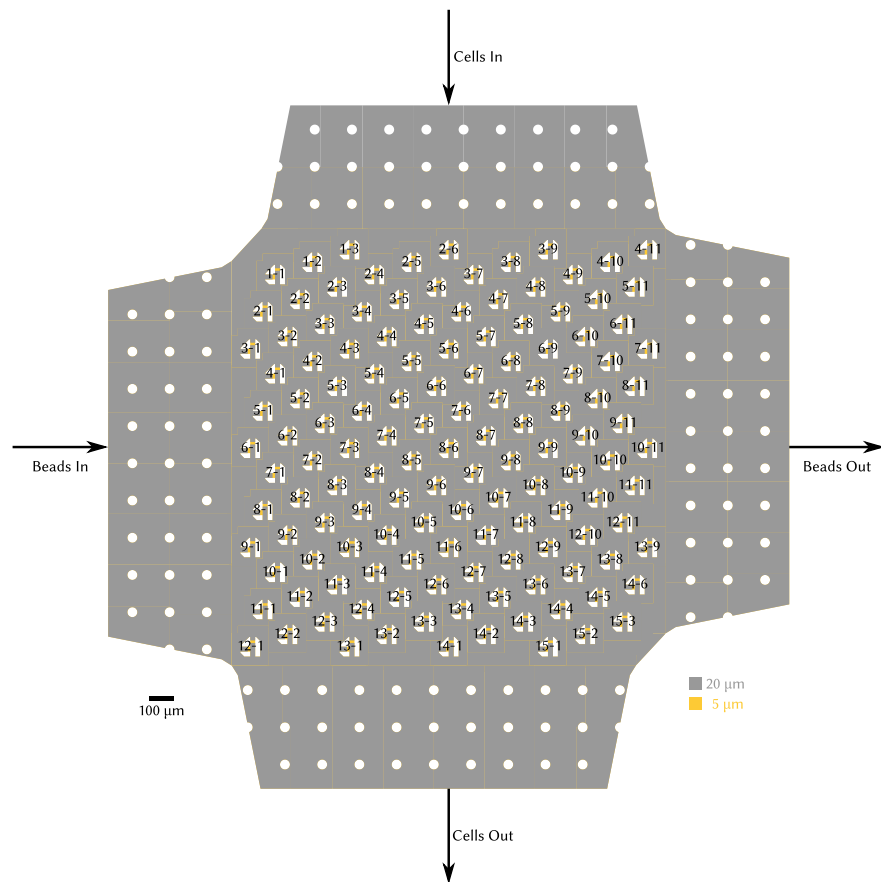


Fig. B.10.: Naming scheme of the trapping structures on the Micronit microfluidic chip

B.4. Packing data

During experiments data is only recorded in raw, uncompressed format. To save disk space, the raw video data is compressed afterwards with `pack.vi`. It also copies the data to a user-defined backup location (such as a network volume) if desired.

To start the packing, simply load `pack.vi`, verify and adjust the selected data paths and whether a backup should be taken and the original (uncompressed) files be deleted afterwards, and start the VI. After starting, no user interaction is required. The program automatically searches for all suitable uncompressed measurement data (not just the most recent) and compresses it according to the settings.

The parameter `tmp root path` points to the location where the raw data is stored. `Data root path` is the root path where the compressed data is stored. The `Backup root path` is the location to which all compressed data is copied for backup purposes. It is only used when the `Backup` toggle switch is enabled. Finally, the `Delete original files` toggle switch enables or disables the deletion of the original files after successful compression. Also, if it is disabled the other measurement data sets (for piezo, voltage, and other data) are copied instead of moved to the new location.

The compressed data is stored together with all other required data files in the location `Data root path\YYYY\MM\DD`, where `YYYY`, `MM`, and `DD` are the four-digit year, two-digit month and two-digit day (all with leading zero if required) of the date the experiment was performed. For example, all data belonging to experiments performed on February 28th, 2019 is found in `E:\2019\02\28` and `X:\2019\02\28` with default settings.

If the default parameter of one of the values should be changed, simply change the parameter and afterwards, right-click on it and select *Data Operations* ► *Make Current Value Default*. Then, save the VI.

B.5. Force analysis

To get high-resolution force data, the recorded video needs to be analysed. This is done by the program `offline.vi` interactively in a few steps. The program guides the user through these steps in the form of different tabs in the main UI.

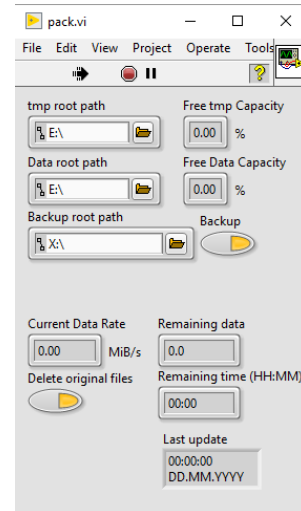


Fig. B.11.: UI of `pack.vi`

B. User manual for the Elasto-Tweezers setup

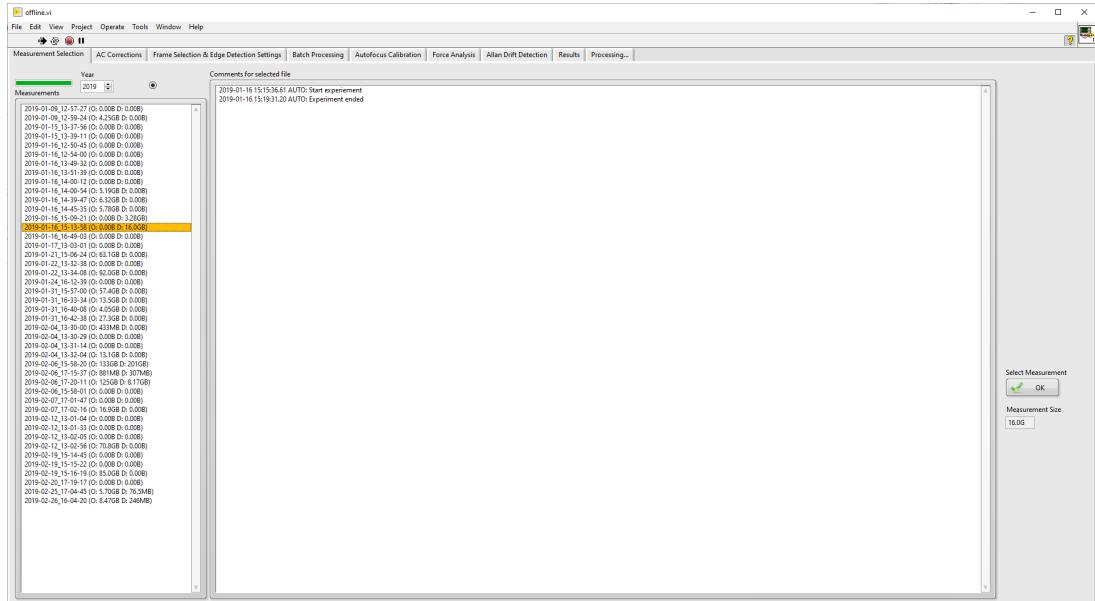


Fig. B.12.: Screenshot of `offline.vi` showing the initial Measurement Selection tab

B.5.1. Measurement selection

In the first step, the user is prompted to select the measurement to be analysed. First, select the year and wait for the program to load the measurement list. Whilst loading, the green bar will fit up. Once loading has finished, the dot next to the year selector will start blinking. Then, from the list of measurements on the left side, select the measurement. As an aid in measurement selection, the size of the overview (O) and detail (D) video footage for each measurement is shown after the timestamp. The comments for that measurement are then loaded into the central comment display to further help identify the correct measurement. Finally, confirm your choices by clicking the OK button.

Next, a progress bar will show the process of reading the measurement metadata.

B.5.2. Frame Selection & Edge Detection Settings

In the next step, the data recorded during the experiment is shown in a single graph similar to the two graphs in `ET.vi`. In the centre of the screen, you can select the data to be displayed in the graph. Also, note that by right-clicking on the x -axis of the graph (or in fact any axis in a LabView VI), you can enable or disable `AutoScale`. The graph also contains a *cursor*, the black vertical line shown in the screenshot in fig. B.13. If the cursor is not visible, it might be outside the shown data range. In this case, right click on the cursor in the cursor information box (left below the graph) and select `Bring to Center`. Alternatively, selecting

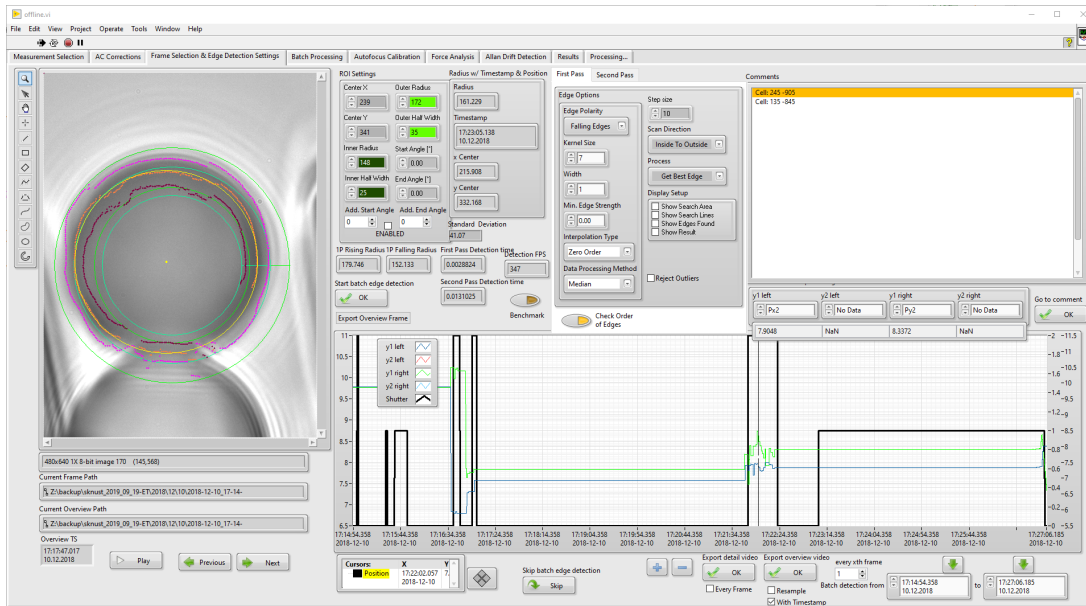


Fig. B.13.: Screenshot of the Frame Selection & Edge Detection Settings tab

one of the comments and then clicking on the Go to comment button will move the cursor to the timestamp associated with the comment. The value of the variables at the cursor position is also shown directly below the variable selection.

The overview and detail image closest to the current cursor position are displayed in a separate screen and in the top left of the program, respectively. For the detail image, edge detection is performed according to the Detection Settings and ROI Settings, with the result being displayed in the image (if selected in Detection Settings) and in Radius w/ Timestamp. Also, the Rising Radius and Falling Radius are displayed, which can be used as a basis for optimising Outer Radius and Inner Radius. Here, a two-pass edge detection is performed. The first pass according to the options in the First Pass tab serves to refine the ROI for the second, more detailed and accurate pass. Here, the starting ROI of the first pass is taken from the ROI Settings.

During batch edge detection, the result of each frame will be used as the starting point of the ROI of the first pass for the next frame. The ROI selected in this screen are only used for the first frame and in case of nonsensical results for a frame, which can occur if the particle is temporarily lost or is subject to sudden displacement changes from one frame to the next.

Therefore, the initial ROI parameters should be set to the *normal* state of the trapped bead during the analysed timeframe. Typically, this is a zero force state.

The small + and - buttons can be used to zoom in and out of the graph at the cursor position. They only work as intended if AutoScale is disabled.

B. User manual for the Elasto-Tweezers setup

Select the time-region for detection by either moving the cursor to beginning and end and clicking the relevant down-arrow buttons with the cursor at the timestamp to be used. Alternatively, you can also manually enter start and end time in the two fields at the lower right.

After selecting the time range, you can use `Export detail video` or `Export overview video`. In both cases, the video is exported as a series of single-frame images (in PNG format). For the detail video, edge detection is also performed and the forces are calculated according to the values in the `Force Analysis` tab. Therefore, typically first a complete analysis is performed and the values are then reused to export the detail video footage. If `Every Frame` is selected, every frame of the detail video will be exported, otherwise only the frames that correspond to overview frames are exported. The `Resample` checkbox controls if the overview frames should be scaled down to 50 %.

If required, use third-party tools such as `ffmpeg` to convert the images into a true video format. An exemplary `ffmpeg` command could be `ffmpeg -i %06d.png -c:v h264 -b:v 2000k video.mp4`. Note that using this method for the detail camera images creates a super slow motion video slowed down by a factor of $550/25 = 22$, if `Every Frame` is selected.

Finally, pressing the `Start batch edge detection` button initiates the edge detection of the selected time range. In the next screen, the progress is shown with an estimate of the remaining time. Edge detection takes roughly twice the length of the selected time range. Therefore, it might be advantageous to only perform the detection on several small intervals instead of one large interval.

B.5.3. Force Analysis

The `Force Analysis` tab presents the results of the batch edge detection. In the top graph, the detected positions and radii are displayed along with the calculated forces. Also, the piezo axis selected by `Piezo Pos. Axis` is shown. Graphs can be shown, hidden, and customised by right-clicking on the name or icon in the graph legend.

This graph contains two cursors which are used to directly select a time range for multiple operations. As with the frame selection, right-click on a cursor to use `Bring to Center` if necessary. If both cursors are outside of the shown range, use it on one cursor and move it afterwards in the direction that enlarges the yellow section between the two cursors.

In the bottom left, you can select a comment and move the currently active (last used or manually selected) cursor to its corresponding timestamp.

The first step in analysis should be to select a time range where the force is zero and then click on the `Zero selected data` button. This averages the positions and radii within the range and sets the `Zero force X`, `Zero force Y`, and `Zero force Z` input fields to these

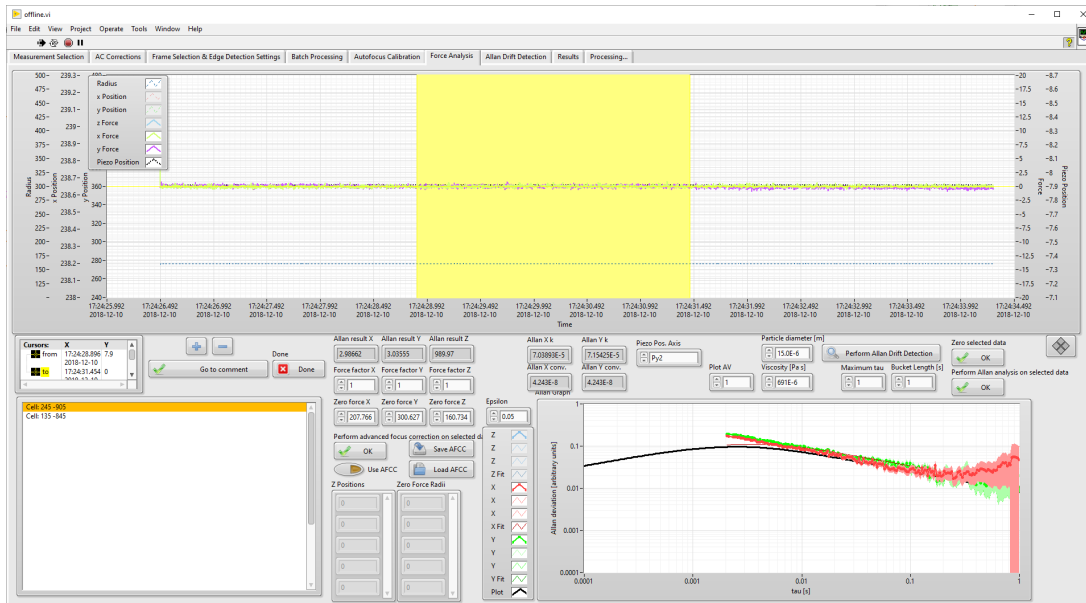


Fig. B.14.: Screenshot of the Force Analysis tab

values. They are then used as zero force positions x_0 and y_0 as well as zero force radius r_0 .

Advanced focus correction calibration (AFCC) is implemented in the software but not used in this setup, as it is only relevant for axial forces. Briefly, to perform an AFCC, first select a region of rising or declining piezo position, ideally moving slowly through the whole range. Then, click on the Perform advances focus correction on selected data button. The software then builds clusters of data points: The first z position is used as a reference and further positions are compared to it. As long as the deviation is less then Epsilon (in μm , default value $0.05 \mu\text{m}$) it belongs to the current cluster. If it deviates more, the current cluster is averaged (in both z and r) if it contains more then 50 valid radii and a new cluster is started, with the current piezo value as a new reference. The results of this analysis is shown in the graph on the left (if visible) and can be saved by clicking Save AFCC. This is especially useful if multiple intervals in the same experiment are analysed. For further intervals, the AFCC can then be loaded by clicking Load AFCC. For both buttons, a file dialogue opens and prompts for a location. That file is also human-readable.

If Use AFCC is enabled, the value of Zero force Z is ignored. Instead, the zero-force radius r_0 for force calculation is determined by first linearly interpolating the piezo z position for each timestamp and then linearly interpolating the corresponding r_0 from the AFCC data set. Therefore, the AFCC data set must span the complete range of z values encountered during the measurement.

The graph on the bottom right shows the results of an Allan variance analysis. The sat-

urated line with dots is the result and the unsaturated band shows one standard deviation. The thinner line shows the best fit. Additionally, the black line shows the Allan variance corresponding to the value in `Plot AV` for x and y axis.

For Allan analysis, a short period (less than 10 s) should be selected. In this period, no forces should be applied. The analysis will then be performed for 200 values of τ logarithmically equidistant between `Minimum tau` or the average distance between subsequent frames, whichever is larger, and `Maximum tau` or half the duration of the selected range, whichever is smaller. For the fit, a starting value for k of `k start value` is used. The results are shown in the graph and, in suitable units (pN px⁻¹ for x and y , pN for z), displayed in the three `Allan result` outputs. On purpose the values of the `Force factor` input fields are not overwritten.

Generally, you should perform Allan variance analysis for a few time intervals and always check whether the fit is meaningful. Here, the most important area is in the middle range around $\tau = 0.01$ s. For lower values, noise is an issue. For larger values, drift becomes challenging. Also, always take surface effects into account when performing analysis close to a membrane. Ideally, the results of Allen variance and Stokes' drag calibration give comparable results.

To analyse fluctuations in trap stiffness, a larger selection can be analysed with `Perform Allan Drift Detection`. This will cut the selected data into buckets configured by `Bucket Length [s]`. For each bucket, Allan deviation is calculated, the fit is performed and displayed and the results are recorded and saved to a selected file. This process is still experimental.

Finally, when the force calibration was performed, clicking the `Done` button leads to the final `Results` tab.

B.5.4. Results

The `Results` tab once again shows the data in two customisable graphs. It also allows for data export. For this, select the desired output columns in the `Export Columns` array on the right. As described earlier and illustrated in fig. B.1, one or more interpolation bases need to be selected. This can be done by simply checking the corresponding `Interpolation Base` checkbox. If multiple interpolation bases are selected, the export will contain data at the timestamps of all interpolation bases, sorted chronologically. That means that a later separation and allocation into the individual interpolation bases is not possible; the exported data is one chronological data set.

If a later separation is required, multiple exports can be performed with different export column configuration. In this case, simply check one interpolation base for the first export and other interpolation base(s) for subsequent export(s).

The data is exported by clicking the `Export data` button. This prompts the user to specify

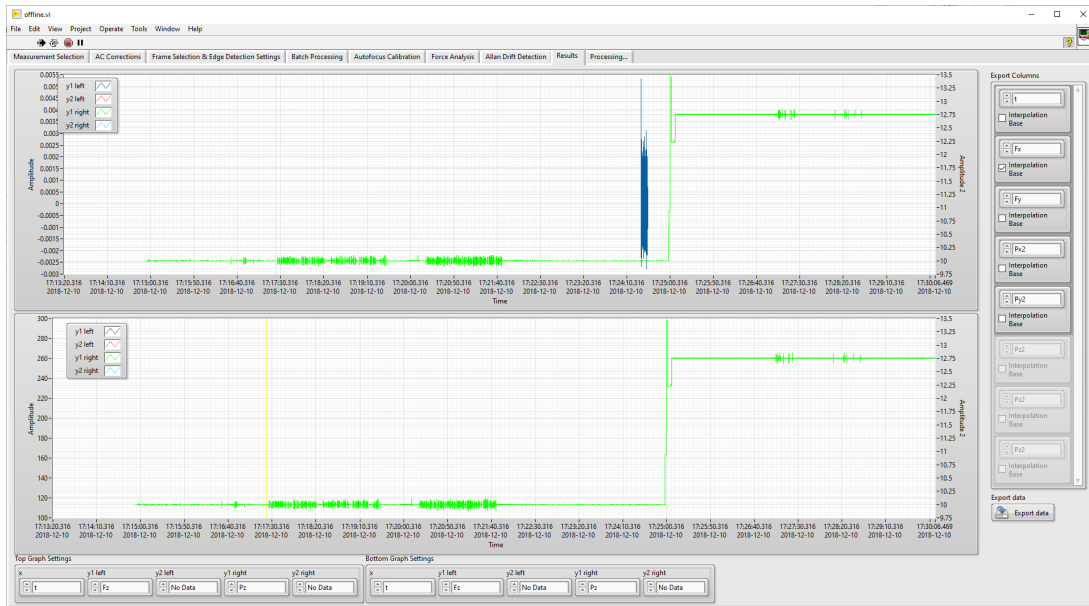


Fig. B.15.: Screenshot of the Results tab

the desired export file location. The file will be a tab-separated plain-text file. Numbers are output as plain decimal numbers (no E-notation) with six decimal places (e.g. 12345.678901 or 0.000012). Timestamps are formatted according to ISO 8601-1:2019¹⁷⁰ in format [YYYY][“-”][MM][“-”][DD][“T”][HH][“:”][MM][“:”][SS][“.”][ssssss], e. g. 2018-01-19T12:34:56.789012.

B.6. Stress / strain analysis

For the analysis of the stress-strain behaviour, `analysis-flexible.vi` can be used to convert force data to stress and strain. When starting the program, the result file to be used is prompted. After selecting the file, the columns should be set up correctly. The column controls expect zero-indexed column numbers for the datetime, x- and y-force, piezo positions for the secondary trap, and the piezo movement velocity. In the screenshot in fig. B.16, the file has the datetime in the 1st column, followed by the positions of the secondary trap piezos, the forces in x and y, and the velocity.

The software crops the data for analysis to the time range selected at the top left corner. The Autoscale button sets the range to the complete datafile. The Deleted data points control can be used to correct for timing offsets between piezo and force, which should not be necessary in normal operation. Positive values remove that amount of data points from the piezo data, shifting it forward. Negative values add data points in the beginning, shifting

B. User manual for the Elasto-Tweezers setup



Fig. B.16.: Screenshot of the analysis-flexible.vi user interface

the data backwards.

To account for experiments without bead-cell adhesion, the strain can be cropped to only negative values. By checking the checkbox allow positive Strain, this cropping is deactivated.

The PX2 Null Position and PY2 Null Position are the piezo positions where the secondary and the primary trap overlap. They should not require adjustment.

The particle diameter is used in the correction of drag force as well as in the calculation of strain. The cell diameter plays a crucial role in strain calculation and must be tuned carefully to ensure that zero strain is set correctly. Typically, this is done on first contact between bead and cell and should be checked at later times to account for cell size or conformation changes.

In the View raw data tab, the unmodified force data is shown as well as the distance between the bead centres without correction for trap stiffness. If required, force offsets can be set up. Furthermore, as the total force $\sqrt{F_x^2 + F_y^2}$ requires a sign, the force component determining it can be selected at Axis for sign. Furthermore, we can select the force and distance to be used for stress and strain calculation. This should always be set to F corr and d corr, respectively.

The View corrected data tab shows the distance data corrected for trap stiffness accord-

ing to the force and conversion factor set in that tab. Furthermore, the force is corrected for Stokes drag according to the selected particle size and the viscosity set in this tab.

The Stress/Strain tab then shows the calculated stress and strain data in two graphs. To assist in the determination of the cell diameter, the Stress/Strain Combined tab shows both curves in a combined graph, enabling fine tuning of the initial contact point.

Once all parameters have been tuned, clicking the button `Finish column selection` prompts for the result file location, which contains the timestamp, stress, numerical derivative of the stress, strain, and the numerical derivative of the strain. This can then be used for model fitting in Gnuplot or other software.

C. Fitting numerical solutions of first-order differential equations with Gnuplot

As described in section 5.4.4, first-order differential equations can be solved with the Runge-Kutta method *RK4*. This is an iterative algorithm for solving initial value problems $\dot{y} = f(t, y)$ with initial condition $y(t_0) = y_0$. Each value $y_{n+1} = y(t_{n+1}) = y(t_0 + (n+1)h)$ with step size h is calculated based only on the previous value y_n . As the fitting routine in Gnuplot evaluates all data points in sequential order, we can implement the numerical solution directly in Gnuplot.

For reference, the *RK4* algorithm is:

$$k_1 = f(t_n, y_n) \tag{C.1}$$

$$k_2 = f(t_n + h/2, y_n + hk_1/2) \tag{C.2}$$

$$k_3 = f(t_n + h/2, y_n + hk_2/2) \tag{C.3}$$

$$k_4 = f(t_n + h, y_n + hk_3) \tag{C.4}$$

$$y_{n+1} = y_n + h/6 (k_1 + 2k_2 + 2k_3 + k_4) \tag{C.5}$$

In our case, we are solving for σ instead of y with $\dot{\sigma} = (q_0\varepsilon + q_1\dot{\varepsilon} - p_0\sigma) / p_1$. Without restrictions we can assume $p_1 = 1$. Of course, ε and $\dot{\varepsilon}$ are also measured and functions of time.

In Gnuplot code, we will then use the relation for $\dot{\sigma}$ as function `f(t, sigma, eps, epsdot)`[†] to express the *RK4* algorithm as a single long function `rk4(t, eps, epsdot)` with parameters t , ε and $\dot{\varepsilon}$:

```
1 f(t, sigma, eps, epsdot) = q0 * eps + q1 * epsdot - p0 * sigma
2
3 h = 1,814e-3
4 firstsigma = 0.0
5 firsteps = 0.0
6 firstepsdot = 0.0
```

[†]We don't require or use the parameter `t` here. However, I chose to keep it for implicit code documentation purposes

C. Fitting numerical solutions of first-order differential equations with Gnuplot

```
7
8 rk4(t, eps, epsdot) = (
9     (t<lastt ? (lastsigma=firstsigma, lasteps=firsteps, lastepsdot=firstepsdot) : 1),
10    (t>lastt+2*h ? (lastsigma=firstsigma, lasteps=firsteps, lastepsdot=firstepsdot) : 1),
11    k1 = f(t-h, lastsigma, lasteps, lastepsdot),
12    k2 = f(t-h/2., lastsigma + h/2.*k1, (eps+lasteps)/2., (epsdot+lastepsdot)/2.),
13    k3 = f(t-h/2., lastsigma + h/2.*k2, (eps+lasteps)/2., (epsdot+lastepsdot)/2.),
14    k4 = f(t, lastsigma + h*k3, eps, epsdot),
15    lastt=t, lasteps = eps, lastepsdot = epsdot,
16    lastsigma = lastsigma + h/6.*(k1 + 2*k2 + 2*k3 + k4)
17 )
```

The first line defines the function to be used in *RK4* as described above. Line 3 sets the interval as the inverse of the data rate, here 551 fps. Lines 4–6 set the initial values for σ , ϵ and $\dot{\epsilon}$ and can be changed if required.

Lines 8–17 define function *rk4* with a few expressions that are executed in sequence. Only the return value of the last expression (line 16) is returned by the function. Line 9 detects if a new fit is performed by checking if the time runs backwards. If so, we reinitialise internal variables. Likewise, line 10 detects if there is a cut in the data to be fitted. This happens routinely if the pause between multiple stretching actions is too long. In this case, the pause should be removed from the data set used for fitting to increase performance.

D. List of figures

2.1.	Correction factor for a particle moving perpendicular to a plane wall	21
2.2.	Correction factor for a particle moving parallel to plane walls	22
2.3.	Simulation of the correction factor for a particle moving parallel to plane walls	23
2.4.	Electric potential near a charged surface	24
3.1.	Focussing of a Gaussian beam by a thin lens	33
3.2.	Profiles of Gaussian beams with different initial beam waists	35
3.3.	Illustration of the mechanisms of photon absorption, spontaneous emission and stimulated emission	36
3.4.	Four level energy diagram for a laser	38
3.5.	Light paths for centred bead in 2D trap	42
3.6.	Light paths for displaced bead in 2D trap	42
3.7.	Light paths for bead in 3D trap	43
3.8.	Beam profiles of TEM_{00} and TEM_{01}^* modes	44
3.9.	Trapping forces for axial and radial displacement	46
3.10.	Still frame of the measurement camera with a trapped polystyrene particle .	49
3.11.	PSD of an optically trapped $3\ \mu\text{m}$ particle	53
3.12.	Measured PSD of an optically trapped $3.05\ \mu\text{m}$ polystyrene particle	55
3.13.	Theoretical Allan Variance of an optically trapped $3\ \mu\text{m}$ particle	57
4.1.	Components and structure of DNA	60
5.1.	Structures of a typical cell	63
5.2.	Structures of the cell membrane	64
5.3.	Maxwell model	68
5.4.	Kelvin-Voigt model	69
5.5.	Zener-Kelvin model	70
5.6.	One possible representation of a generalised model	70
6.1.	Schematic setup of the optical tweezers system	78
6.2.	Overview of the sample chamber layout for nanopore experiments	79

D. List of figures

6.3.	Detail view of a dsDNA translocating through a nanopore	80
6.4.	Chemical structure of Trichlorosilane	80
6.5.	Photos of the microfluidic setup	82
7.1.	Photo of the hBN bulk material source	86
7.2.	hBN master tape preparation process	87
7.3.	Photo of the hBN master tapes	88
7.4.	Chemical structure of the used cellulose acetate butyrate	90
7.5.	Setup for dry transfer method	91
7.6.	Band structure of MoS ₂	92
8.1.	Detail view of an optically trapped 3.05 μm bead at 1555 fps	97
8.2.	Allan deviation analysis of a 3.05 μm bead trapped at 250 mW	98
8.3.	Allan deviation analysis of a 3.05 μm bead trapped at 750 mW	98
8.4.	Allan deviation analysis at 750 mW converted to forces	99
8.5.	Potential monolayers of boron nitride on a silicon + silicon oxide wafer	101
8.6.	Microscopy and AFM images of the thinnest boron nitride flake found on PDMS	103
8.7.	Reflection microscopy image of PDMS with exfoliated MoS ₂	104
8.8.	Reflection microscopy, transmission microscopy and photoluminescence images of a MoS ₂ monolayer	104
8.9.	Residue of cellulose polymer on the silicon chip after wedging transfer	105
8.10.	AFM phase image of the surface of the chip next to the free-standing membrane	106
8.11.	Sudden pore formation of a 5 nm pore	108
8.12.	Gradual formation of a 5 nm pore	109
8.13.	Current curve with insufficient wetting	110
8.14.	Reflection microscopy and HIM images of a chip with a 1 μm pore covered by a MoS ₂ double layer	110
8.15.	Free-standing MoS ₂ membrane with PDMS residue and nanopore	112
8.16.	FFT of the TEM images of monolayer and double layer MoS ₂	113
8.17.	Overview of a DNA translocation through a 41 nm nanopore in a monolayer	115
8.18.	Threading in of two DNA strands in a short time vs. threading in of just one DNA strand	116
8.19.	Threading out of two DNA strands in a short time vs. threading out of just one DNA strand	116
8.20.	Translocation of DNA strands through a 200 nm nanopore in a monolayer	117
8.21.	DNA strand inside the 1 μm hole in the silicon nitride membrane with applied AC voltage	118

8.22. Detailed force graph at 1 Hz	119
8.23. Detailed force graph at 5 Hz.	119
8.24. Detailed force graph at 10 Hz.	120
8.25. Detailed force graph at 20 Hz.	120
8.26. Detailed force graph of the threading-out behaviour.	122
8.27. Translocation event types encountered with a 17.7 μm MoS ₂ monolayer pore	123
10.1. Optical flow of the laser beams in the main microscope deck of Elasto-Tweezers	130
10.2. Illustration of the microfluidics setup	133
10.3. Overview of design 1.	136
10.4. Detail of design 1.	137
10.5. Different chambers for design 1	137
10.6. Overview of design 2.	138
10.7. Detail of design 2.	139
10.8. Overview of design 3	140
10.9. Detail view of design 3	141
11.1. Chemical structure of cyclic olefin copolymer (COC)	146
11.2. Schematic of the chip layout	148
12.1. Temperature behaviour in temperature isolation box	151
12.2. Variation of trap stiffness for primary and secondary trap, trapping the same particle	153
12.3. Variation of trap stiffness for primary and secondary trap, trapping different particles simultaneously	154
12.4. Measurement of bead-cell rupture forces for carboxylated beads	155
12.5. Example of clogging	157
12.6. Artefacts encountered in COC chips	159
12.7. Cluster of HEK-293 cells with PDMS residue	160
12.8. Force-distance graphs of the complex behaviour at different loading velocities	162
12.9. Bead-cell-bead complex with a single HEK-293 cell and one optically trapped bead	163
12.10. Stress-strain curves of a single HEK-293 cell with one static bead	164
12.11. Bead-cell-bead complex with a single HEK-293 cell and two optically trapped beads	165
12.12. Stress-strain curves of a single HEK-293 cell with two optically trapped beads	165
12.13. Bead-cell-bead complex with a single, very stiff HEK-293 cell	166

D. List of figures

12.14. Stress-strain curves of a very stiff cell	167
12.15. Trypan blue staining for cell viability verification	168
A.1. Photo of the experimental setup	176
A.2. Illustration of the interpolation process	177
A.3. Screenshot of <code>andor.vi</code>	179
A.4. Screenshot of <code>tweezer2.vi</code> with Scripting tab	180
A.5. Screenshot of the Scripting tab	182
A.6. Screenshot of the Force Calibration tab	184
A.7. Screenshot of the Current Settings tab	186
A.8. Screenshot of the Video Settings tab	187
A.9. Screenshot of the Misc. Settings tab	188
A.10. Screenshot of the Graph Settings tab	189
A.11. NI Vision Tools palette	189
A.12. Screenshot of the Autofocus tab	190
A.13. UI of <code>pack.vi</code>	191
A.14. Screenshot of <code>offline.vi</code> showing the initial Measurement Selection tab	192
A.15. Screenshot of the Frame Selection & Edge Detection Settings tab . .	193
A.16. Screenshot of the Force Analysis tab	195
A.17. Screenshot of the Results tab	197
B.1. Illustration of the interpolation process	200
B.2. Screenshot of <code>ET.vi</code> with Scripting tab	201
B.3. Screenshot of the Scripting tab	203
B.4. Screenshot of the Force Calibration tab	205
B.5. Screenshot of the Video Settings tab	206
B.6. Screenshot of the Misc. Settings tab	207
B.7. Screenshot of the Graph Settings tab	208
B.8. Screenshot of <code>overview.vi</code>	210
B.9. Illustration of the measurement automation workflow	212
B.10. Naming scheme of the trapping structures on the Micronit microfluidic chip	214
B.11. UI of <code>pack.vi</code>	215
B.12. Screenshot of <code>offline.vi</code> showing the initial Measurement Selection tab	216
B.13. Screenshot of the Frame Selection & Edge Detection Settings tab . .	217
B.14. Screenshot of the Force Analysis tab	219
B.15. Screenshot of the Results tab	221

B.16. Screenshot of the analysis-flexible.vi user interface 222

E. List of publications and conference contributions

Publications

- S. Knust, D. Kreft, R. Hillmann, A. Meyer, M. Viefhues, P. Reimann, D. Anselmetti
Measuring DNA Translocation Forces through MoS₂-Nanopores with Optical Tweezers
Materials Today: Proceedings, **4**, S168-S173 (2017)
- S. Knust, A. Sischka, H. Milting, B. Venzac, S. Le Gac, E. Vrouwe, M. Viefhues, D. Anselmetti, K. Gall
Elasto-Tweezers: A novel platform for high-precision cell elasticity measurements
22nd International Conference on Miniaturized Systems for Chemistry and Life Sciences (μ TAS), November 11–15, 2018, Kaohsiung, Taiwan, 2429-2430 (2018)

Conference contributions

- S. Knust, A. Meyer, P. Reimann, D. Anselmetti
Measuring DNA translocation forces through solid state nanopores with optical tweezers
XVIII Linz Winter Workshop, January 29 – February 1, 2016, Linz, Austria (Talk)
- S. Knust, S. Kißmer, D. Kreft, A. Meyer, P. Reimann, D. Anselmetti
Measuring DNA translocation forces through solid state nanopores with optical tweezers
NMWP Young Academics – Graphen und 2D-Materialien, April 20–21, Siegen, Germany (Talk)
- D. Kreft, S. Knust, D. Anselmetti
Measuring DNA translocation forces through MoS₂ nanopores with optical tweezers
NMWP Young Academics – Graphen und 2D-Materialien, April 20–21, Siegen, Germany (Poster)
- S. Knust, D. Kreft, R. Hillmann, A. Meyer, M. Viefhues, P. Reimann, D. Anselmetti
Measuring DNA Translocation Forces through MoS₂-Nanopores with Optical Tweezers
7th NRW Nano Conference, December 7–8, 2016, Dortmund, Germany (Poster)

E. List of publications and conference contributions

- S. Knust, J. Cremer, D. Kreft, M. Viefhues, D. Anselmetti *Measuring DNA Translocation Forces through Nanopores in MoS₂ Monolayer Membranes with Optical Tweezers* 648. WE-Heraeus-Seminar: Transport Mechanisms in Biological and Synthetic Nanopores and -channels, July 16–21, 2017, Bremen, Germany (Poster)
- S. Knust, A. Sischka, H. Milting, B. Venzac, S. Le Gac, E. Vrouwe, D. Anselmetti *Elasto-Tweezers: A novel platform for high-precision cell elasticity measurements* Spring Meeting of the German Physical Society, March 11–16th, 2018, Berlin, Germany (Poster)
- S. Knust, A. Sischka, H. Milting, B. Venzac, S. Le Gac, E. Vrouwe, M. Viefhues, K. Gall, D. Anselmetti *Elasto-Tweezers: A novel platform for high-precision cell elasticity measurements* NanoBioTech-Montreux, October 29–31, 2018, Montreux, Switzerland (Talk)
- S. Knust, A. Sischka, H. Milting, B. Venzac, S. Le Gac, E. Vrouwe, M. Viefhues, K. Gall, D. Anselmetti *Elasto-Tweezers: A novel platform for high-precision cell elasticity measurements* 8th NRW Nano Conference, November 21–22, 2018, Dortmund, Germany (Talk)

F. Bibliography

- ¹A. Ashkin, “Acceleration and Trapping of Particles by Radiation Pressure”, *Physical Review Letters* **24**, 156–159 (1970).
- ²K. C. Neuman and A. Nagy, “Single-molecule force spectroscopy: optical tweezers, magnetic tweezers and atomic force microscopy.”, *Nature Methods* **5**, 491–505 (2008).
- ³The Royal Swedish Academy of Sciences, *The Nobel Prize in Physics 2018*, Oct. 2018, http://www.nobelprize.org/nobel_prizes/physics/laureates/2018/.
- ⁴S. Knust, A. Spiering, H. Vieker, A. Beyer, A. Götzhäuser, K. Tönsing, A. Sischka, and D. Anselmetti, “Video-based and interference-free axial force detection and analysis for optical tweezers”, *Review of Scientific Instruments* **83**, 103704 (2012).
- ⁵S. Knust, “Video-based and interference-free axial force detection and analysis for optical tweezers”, Bachelor Thesis (Bielefeld University, 2012).
- ⁶S. Knust, “Evaluation of ultra thin solid state membranes and very small nanopores for DNA translocation with optical tweezers”, Master Thesis (Bielefeld University, 2015).
- ⁷F. L. Graham, J. Smiley, W. C. Russell, and R. Nairn, “Characteristics of a human cell line transformed by DNA from human adenovirus type 5”, *Journal of General Virology* **36**, 59–72 (1977).
- ⁸G. Shaw, S. Morse, M. Ararat, and F. L. Graham, “Preferential transformation of human neuronal cells by human adenoviruses and the origin of HEK 293 cells.”, *The FASEB journal : official publication of the Federation of American Societies for Experimental Biology* **16**, 869–871 (2002).
- ⁹G. M. Whitesides, “The origins and the future of microfluidics.”, *Nature* **442**, 368–73 (2006).
- ¹⁰K. Ren, J. Zhou, and H. Wu, “Materials for microfluidic chip fabrication”, *Accounts of Chemical Research* **46**, 2396–2406 (2013).
- ¹¹Y. Song, D. Cheng, and L. Zhao, *Microfluidics: Fundamental, Devices and Applications* (Wiley-VCH Verlag GmbH & Co. KGaA, Weinheim, Germany, Feb. 2018).
- ¹²G. Galilei, *Discorsi e dimostrazioni matematiche, intorno à due nuove scienze* (Lodewijk Elzevir, Leida, 1638).

F. Bibliography

- ¹³D. Janasek, J. Franzke, and A. Manz, “Scaling and the design of miniaturized chemical-analysis systems”, *Nature* **442**, 374–380 (2006).
- ¹⁴T. M. Squires and S. R. Quake, “Microfluidics: Fluid physics at the nanoliter scale”, *Reviews of Modern Physics* **77**, 977 (2005).
- ¹⁵S. Shoji and K. Kawai, “Flow Control Methods and Devices in Micrometer Scale Channels”, in *Microfluidics - technologies and applications* (2011), pp. 1–25.
- ¹⁶B. Abdallah and A. Ros, “Surface coatings for microfluidic-based biomedical devices”, in *Microfluidic devices for biomedical applications* (Elsevier, 2013), pp. 63–99.
- ¹⁷P. Kapitza, “Viscosity of Liquid Helium below the λ -Point”, *Nature* **141**, 74 (1938).
- ¹⁸L. D. Landau and E. M. Lifschitz, *Lehrbuch der theoretischen Physik - Band VI: Hydrodynamik*, edited by W. Weller, 5. Auflage (Verlag Harri Deutsch, Frankfurt am Main, 2007).
- ¹⁹C. L. M. H. Navier, “Sur les lois du mouvement des fluides”, *Mémoires de l’Académie des sciences* **6**, 389 (1827).
- ²⁰G. G. Stokes, “On the Theories of Internal Friction of Fluids in Motion”, *Transactions of the Cambridge Philosophical Society* **8**, 287 (1845).
- ²¹S. P. Sutera and R. Skalak, “The History of Poiseuille’s Law”, *Annual Review of Fluid Mechanics* **25**, 1–20 (1993).
- ²²G. H. L. Hagen, “Ueber die Bewegung des Wassers in engen cylindrischen Röhren”, *Annalen der Physik und Chemie* **122**, 423–442 (1839).
- ²³J. L. M. Poiseuille, “Recherches expérimentales sur le mouvement des liquides dans les tubes de très petit diamètres”, *Comptes Rendus Hebdomadaires des Séances de l’Académie des Sciences* **11**, 961 (1840).
- ²⁴J. L. M. Poiseuille, “Recherches expérimentales sur le mouvement des liquides dans les tubes de très petit diamètres”, *Comptes Rendus Hebdomadaires des Séances de l’Académie des Sciences* **11**, 1041 (1840).
- ²⁵J. Boussinesq, “Mémoire sur l’influence des frottements dans les mouvements réguliers des fluides”, *Journal de Mathématiques pures et appliquées* **13**, 377 (1868).
- ²⁶P. G. Drazin and N. Riley, *The Navier-Stokes Equations: A Classification of Flows and Exact Solutions* (Cambridge University Press, Cambridge, UK, 2006), p. 208.
- ²⁷M. Bahrami, M. M. Yovanovich, and J. R. Culham, “Pressure Drop of Fully-Developed, Laminar Flow in Microchannels of Arbitrary Cross-Section”, *Journal of Fluids Engineering* **128**, 1036 (2006).

- ²⁸G. G. Stokes, “On the Effect of the Internal Friction of Fluids on the Motion of Pendulums”, *Transactions of the Cambridge Philosophical Society* **9**, II–8 (1850).
- ²⁹O. Reynolds, “An Experimental Investigation of the Circumstances which determine whether the Motion of Water shall be Direct or Sinuous, and of the Law of Resistance in Parallel Channels”, *Philosophical Transactions of the Royal Society of London* **174**, 935–982 (1883).
- ³⁰O. Reynolds, “On the Dynamical Theory of Incompressible Viscous Fluids and the Determination of the Criterion”, *Philosophical Transactions of the Royal Society A: Mathematical, Physical and Engineering Sciences* **186**, 123–164 (1895).
- ³¹A. Sommerfeld, “Ein Beitrag zur hydrodynamischen Erklärung der turbulenten Flüssigkeitsbewegungen”, *Atti del IV Congresso Internazionale dei Matematici (Roma, 6-11 Aprile 1908)* **3**, 116–124 (1908).
- ³²B. Lin, *Microfluidics - Technologies and Applications*, edited by B. Lin, Vol. 304, *Topics in Current Chemistry* (Springer Berlin Heidelberg, Berlin, Heidelberg, 2011), p. 344.
- ³³G. K. Batchelor, “Flow due to a moving body at small Reynolds number”, in *An introduction to fluid dynamics*, 2nd ed. (Cambridge University Press, Cambridge, UK, 1967) Chap. 4.9, pp. 229–240.
- ³⁴J. Happel and H. Brenner, *Low Reynolds number hydrodynamics*, 1st paperb, Vol. 1, *Mechanics of fluids and transport processes* (Springer Netherlands, Dordrecht, 1983).
- ³⁵H. Faxén, “Der Widerstand gegen die Bewegung einer starren Kugel in einer zähen Flüssigkeit, die zwischen zwei parallelen ebenen Wänden eingeschlossen ist”, *Annalen der Physik* **373**, 89–119 (1922).
- ³⁶R. Kuhn and S. Hoffstetter-Kuhn, *Capillary Electrophoresis: Principles and Practice* (Springer-Verlag, Berlin, Heidelberg, 1993).
- ³⁷B. J. Kirby, *Micro- and Nanoscale Fluid Mechanics: Transport in Microfluidic Devices* (Cambridge University Press, Cambridge, UK, 2010).
- ³⁸R. Brown, “A brief account of microscopical observations made in the months of June, July and August 1827, on the particles contained in the pollen of plants; and on the general existence of active molecules in organic and inorganic bodies”, *The Edinburgh new philosophical journal* **4**, 358 (1828).
- ³⁹A. Einstein, “Über die von der molekularkinetischen Theorie der Wärme geforderte Bewegung von in ruhenden Flüssigkeiten suspendierten Teilchen”, *Annalen der Physik* **322**, 549–560 (1905).

F. Bibliography

- ⁴⁰P. Langevin, “Sur la théorie du mouvement brownien”, *Comptes rendus hebdomadaires des séances de l’Académie des sciences* **146**, 530 (1908).
- ⁴¹D. S. Lemons and A. Gythiel, “Paul Langevin’s 1908 paper “On the Theory of Brownian Motion” [“Sur la théorie du mouvement brownien,” *C. R. Acad. Sci. (Paris)* 146 , 530–533 (1908)]”, *American Journal of Physics* **65**, 1079–1081 (1997).
- ⁴²W. Sutherland, “A dynamical theory of diffusion for non-electrolytes and the molecular mass of albumin”, *The London, Edinburgh, and Dublin Philosophical Magazine and Journal of Science* **9**, 781–785 (1905).
- ⁴³M. von Smoluchowski, “Zur kinetischen Theorie der Brownschen Molekularbewegung und der Suspensionen”, *Annalen der Physik* **326**, 756–780 (1906).
- ⁴⁴A. Ashkin and J. M. Dziedzic, “Optical Levitation by Radiation Pressure”, *Applied Physics Letters* **19**, 283 (1971).
- ⁴⁵A. Ashkin, J. M. Dziedzic, J. E. Bjorkholm, and S. Chu, “Observation of a single-beam gradient force optical trap for dielectric particles”, *Optics Letters* **11**, 288 (1986).
- ⁴⁶S. M. Block, L. S. Goldstein, and B. J. Schnapp, “Bead movement by single kinesin molecules studied with optical tweezers.”, *Nature* **348**, 348–52 (1990).
- ⁴⁷C. Bustamante, J. Marko, E. Siggia, and S. Smith, “Entropic elasticity of lambda-phage DNA”, *Science* **265**, 1599–1600 (1994).
- ⁴⁸A. Sischka, “Aufbau einer Optischen Pinzette”, Diploma Thesis (Bielefeld University, 2002).
- ⁴⁹A. Sischka, “Kraftspektroskopie und Einzelmoleküldetektion mit der Optischen Pinzette”, Dissertation (Bielefeld University, 2005).
- ⁵⁰A. Sischka, K. Toensing, R. Eckel, S. D. Wilking, N. Sewald, R. Ros, and D. Anselmetti, “Molecular mechanisms and kinetics between DNA and DNA binding ligands.”, *Biophysical Journal* **88**, 404–11 (2005).
- ⁵¹A. Sischka, C. Kleimann, W. Hachmann, M. M. Schafer, I. Seuffert, K. Tönsing, D. Anselmetti, M. M. Schäfer, I. Seuffert, K. Tönsing, and D. Anselmetti, “Single beam optical tweezers setup with backscattered light detection for three-dimensional measurements on DNA and nanopores”, *Review of Scientific Instruments* **79**, 063702 (2008).
- ⁵²J. Eichler and H. J. Eichler, *Laser: Bauformen, Strahlführung, Anwendungen*, 6. Auflage (Springer, 2006).
- ⁵³O. Svelto, *Principles of Lasers* (Springer US, Boston, MA, 2010).
- ⁵⁴W. T. Silfvast, *Laser Fundamentals*, 2nd ed (Cambridge University Press, 2004).

- ⁵⁵B. E. A. Saleh and M. C. Teich, *Grundlagen der Photonik*, 2. ed (Wiley-VCH, 2008), pp. 26–36.
- ⁵⁶D. Meschede, *Optik, Licht und Laser*, 3rd ed. (Vieweg+Teubner, Wiesbaden, Germany, 2008).
- ⁵⁷W. Demtröder, *Experimentalphysik 3*, Springer-Lehrbuch (Springer-Verlag, Berlin/Heidelberg, 2005).
- ⁵⁸F. P. Kapron, D. B. Keck, and R. D. Maurer, “Radiation losses in glass optical waveguides”, *Applied Physics Letters* **17**, 423–425 (1970).
- ⁵⁹S. Bedö, W. Lüthy, and H. P. Weber, “The effective absorption coefficient in double-clad fibres”, *Optics Communications* **99**, 331–335 (1993).
- ⁶⁰M. Kerker, *The scattering of light - and other electromagnetic radiation*, edited by E. M. Loebel (Academic Press, New York, 1969).
- ⁶¹A. Ashkin, “Forces of a single-beam gradient laser trap on a dielectric sphere in the ray optics regime”, *Biophysical Journal* **61**, 569–582 (1992).
- ⁶²W. Denk and W. W. Webb, “Optical measurement of picometer displacements of transparent microscopic objects.”, *Applied optics* **29**, 2382–91 (1990).
- ⁶³U. F. Keyser, J. van der Does, C. Dekker, and N. H. Dekker, “Optical tweezers for force measurements on DNA in nanopores”, *Review of Scientific Instruments* **77**, 105105 (2006).
- ⁶⁴J. Crocker, “Methods of Digital Video Microscopy for Colloidal Studies”, *Journal of Colloid and Interface Science* **179**, 298–310 (1996).
- ⁶⁵G. E. Moore, “Cramming more components onto integrated circuits”, *Electronics* **38**, 114 (1965).
- ⁶⁶R. Courtland, “The Law That’s Not A Law”, *IEEE Spectrum* **52**, 38–57 (2015).
- ⁶⁷A. Zahid, B. Dai, R. Hong, and D. Zhang, “Optical properties study of silicone polymer PDMS substrate surfaces modified by plasma treatment”, *Materials Research Express* **4**, 10.1088/2053-1591/aa8645 (2017).
- ⁶⁸V. Bormuth, A. Jannasch, M. Ander, C. M. van Kats, A. van Blaaderen, J. Howard, and E. Schäffer, “Optical trapping of coated microspheres”, *Optics Express* **16**, 13831 (2008).
- ⁶⁹J. W. Cooley and J. W. Tukey, “An Algorithm for the Machine Calculation of Complex Fourier Series”, *Mathematics of Computation* **19**, 297 (1965).
- ⁷⁰A. Khintchine, “Korrelationstheorie der stationären stochastischen Prozesse”, *Mathematische Annalen* **109**, 604–615 (1934).
- ⁷¹N. Wiener, “Generalized harmonic analysis”, *Acta Mathematica* **55**, 117–258 (1930).

F. Bibliography

- ⁷²B. M. Lansdorp and O. A. Saleh, “Power spectrum and Allan variance methods for calibrating single-molecule video-tracking instruments.”, *Review of Scientific Instruments* **83**, 025115 (2012).
- ⁷³J. A. Barnes, A. R. Chi, L. S. Cutler, D. J. Healey, D. B. Leeson, T. E. McGunigal, J. A. Mullen, W. L. Smith, R. L. Sydnor, R. F. C. Vessot, and G. M. R. Winkler, “Characterization of Frequency Stability”, *IEEE Transactions on Instrumentation and Measurement* **IM-20**, 105–120 (1971).
- ⁷⁴S. C. Vollmer and H. W. De Haan, “Translocation is a nonequilibrium process at all stages: Simulating the capture and translocation of a polymer by a nanopore”, *Journal of Chemical Physics* **145**, 10.1063/1.4964630 (2016).
- ⁷⁵A. J. Meyer, “Elektrokinetische Phänomene in Siliziumnitrid-Nanoporen und ihr Einfluss auf DNS-Translokationen”, Dissertation (Bielefeld University, 2019).
- ⁷⁶P. Christen and R. Jaussi, *Biochemie*, Springer-Lehrbuch (Springer-Verlag, Berlin/Heidelberg, 2005).
- ⁷⁷M. Janitz, ed., *Next-Generation Genome Sequencing* (Wiley-VCH, Weinheim, 2008).
- ⁷⁸A. S. Mikheyev and M. M. Y. Tin, “A first look at the Oxford Nanopore MinION sequencer”, *Molecular Ecology Resources* **14**, 1097–1102 (2014).
- ⁷⁹A. D. Hargreaves and J. F. Mulley, “Assessing the utility of the Oxford Nanopore MinION for snake venom gland cDNA sequencing”, *PeerJ* **3**, e1441 (2015).
- ⁸⁰L. J. Steinbock and A. Radenovic, “The emergence of nanopores in next-generation sequencing”, *Nanotechnology* **26**, 074003 (2015).
- ⁸¹L. M. Petersen, I. W. Martin, W. E. Moschetti, C. M. Kershaw, and G. J. Tsongalis, “Third-generation sequencing in the clinical laboratory: Exploring the advantages and challenges of nanopore sequencing”, *Journal of Clinical Microbiology* **58**, 10.1128/JCM.01315-19 (2020).
- ⁸²N. Kono and K. Arakawa, “Nanopore sequencing: Review of potential applications in functional genomics”, *Development Growth and Differentiation* **61**, 316–326 (2019).
- ⁸³L. Xu and M. Seki, “Recent advances in the detection of base modifications using the Nanopore sequencer”, *Journal of Human Genetics* **65**, 25–33 (2020).
- ⁸⁴J. F. Marko and E. D. Siggia, “Stretching DNA”, *Macromolecules* **28**, 8759–8770 (1995).
- ⁸⁵H. Yamakawa, “Stiff-Chain Macromolecules”, *Annual Review of Physical Chemistry* **35**, 23–47 (1984).

- ⁸⁶J. E. Hall, “Access resistance of a small circular pore”, *The Journal of General Physiology* **66**, 531–532 (1975).
- ⁸⁷P. Mazzarello, “A unifying concept: The history of cell theory”, *Nature Cell Biology* **1**, E13–E15 (1999).
- ⁸⁸K. Luby-Phelps, “Cytoarchitecture and Physical Properties of Cytoplasm: Volume, Viscosity, Diffusion, Intracellular Surface Area”, *International Review of Cytology* **192**, 189–221 (1999).
- ⁸⁹B. Alberts, A. Johnson, J. Lewis, D. Morgan, M. Raff, K. Roberts, and P. Walter, *Molecular Biology of The Cell*, 6th ed., Vol. 16, 1-4 (Garland Science, New York, NY, 2015).
- ⁹⁰H. C. Chang, Y. C. Lin, and C. T. Kuo, “A two-dimensional diffusion model quantifying intracellular transport with independent factors accounting for cytosol viscosity, binding, and steric hindrance”, *Biochemical Engineering Journal* **41**, 217–227 (2008).
- ⁹¹S. Bicknese, N. Periasamy, S. B. Shohet, and A. S. Verkman, “Cytoplasmic viscosity near the cell plasma membrane: measurement by evanescent field frequency-domain microfluorimetry”, *Biophysical Journal* **65**, 1272–1282 (1993).
- ⁹²H. F. Brinson and L. C. Brinson, “Stress and Strain Analysis and Measurement”, in *Polymer engineering science and viscoelasticity* (Springer US, Boston, MA, 2008) Chap. 2, pp. 15–54.
- ⁹³T. Young, “On Passive Strength and Friction”, in *A course of lectures on natural philosophy and the mechanical arts* (London, 1807) Chap. 13.
- ⁹⁴P. Kelly, “Viscoelasticity”, in *Solid mechanics part i: an introduction to solid mechanics*, 2019-08-11 (Auckland, NZ, 2019) Chap. 10, pp. 283–342, http://homepages.engineering.auckland.ac.nz/~pkel015/SolidMechanicsBooks/Part_I/index.html.
- ⁹⁵R. J. Angel, J. M. Jackson, H. J. Reichmann, and S. Speziale, “Elasticity measurements on minerals: A review”, *European Journal of Mineralogy* **21**, 525–550 (2009).
- ⁹⁶C. P. Chen and R. S. Lakes, “Apparatus for Determining the Viscoelastic Properties of Materials Over Ten Decades of Frequency and Time”, *Journal of Rheology* **33**, 1231–1249 (1989).
- ⁹⁷H. F. Brinson and L. C. Brinson, “Characteristics, Applications and Properties of Polymers”, in *Polymer engineering science and viscoelasticity* (Boston, MA, 2008) Chap. 3, pp. 55–97.

F. Bibliography

- ⁹⁸H. Milting, B. Klauke, A. H. Christensen, J. Müsebeck, V. Walhorn, S. Grannemann, T. Münich, T. Šarič, T. B. Rasmussen, H. K. Jensen, J. Mogensen, C. Baecker, E. Romaker, K. T. Laser, E. zu Knyphausen, A. Kassner, J. Gummert, D. P. Judge, S. Connors, K. Hodgkinson, T. L. Young, P. A. Van Der Zwaag, J. P. Van Tintelen, and D. Anselmetti, “The TMEM43 Newfoundland mutation p.S358L causing ARVC-5 was imported from Europe and increases the stiffness of the cell nucleus”, *European Heart Journal* **36**, 872–881 (2015).
- ⁹⁹M. Dieding, “Funktionale Charakterisierung Herzmuskelspezifischer Proteinvarianten”, PhD thesis (2016), p. 115.
- ¹⁰⁰B. Fornberg, “Generation of Finite Difference Formulas on Arbitrarily Spaced Grids”, *Mathematics of Computation* **51**, 699 (1988).
- ¹⁰¹K. Levenberg, “A method for the solution of certain non-linear problems in least squares”, *Quarterly of Applied Mathematics* **2**, 164–168 (1944).
- ¹⁰²D. W. Marquardt, “An Algorithm for Least-Squares Estimation of Nonlinear Parameters”, *Journal of the Society for Industrial and Applied Mathematics* **11**, 431–441 (1963).
- ¹⁰³T. Williams, C. Kelly, and E. al., *Gnuplot 5.0: an interactive plotting program*, 2018, <http://www.gnuplot.info>.
- ¹⁰⁴C. Runge, “Ueber die numerische Auflösung von Differentialgleichungen”, *Mathematische Annalen* **46**, 167–178 (1895).
- ¹⁰⁵W. Kutta, “Beitrag zur näherungsweise Integration totaler Differentialgleichungen”, *Zeitschrift für Mathematik und Physik* **46**, 435 (1901).
- ¹⁰⁶Laser 2000, *Laser und Lichtquellen*, 2011, <http://www.laser2000.de/index.php?id=363099>.
- ¹⁰⁷B. Fowler, C. Liu, S. Mims, J. Balicki, W. Li, H. Do, J. Appelbaum, and P. Vu, “A 5.5Mpixel 100 frames/sec wide dynamic range low noise CMOS image sensor for scientific applications”, *Proc. SPIE* **7536**, 753607–753612 (2010).
- ¹⁰⁸Hawlett-Packard Company, Intel Corporation, Microsoft Corporation, NEC Corporation, ST-NXP Wireless, and Texas Instruments, *Universal Serial Bus 3.0 Specification*, tech. rep. (2008).
- ¹⁰⁹IEEE Standards Association, *IEEE 802.3ab-1999 - IEEE Standard for Information Technology - Telecommunications and information exchange between systems - Local and Metropolitan Area Networks - Part 3: Carrier Sense Multiple Access with Collision Detection (CSMA/CD) Access Method and Physical Layer Specifications - Physical Layer Parameters and Specifications for 1000 Mb/s Operation over 4 pair of Category 5 Balanced Copper Cabling, Type 1000BASE-T* (1999).

- ¹¹⁰A. S. Mukasyan, *Boron Nitride* (Elsevier Inc., 2017), pp. 45–47.
- ¹¹¹R. W. G. Wyckoff, *Crystal structures*, 2nd ed. (Interscience Publ., New York, NY, 1963).
- ¹¹²J. Wang, F. Ma, and M. Sun, “Graphene, hexagonal boron nitride, and their heterostructures: properties and applications”, *RSC Advances* **7**, 16801–16822 (2017).
- ¹¹³P. Trucano and R. Chen, “Structure of graphite by neutron diffraction”, *Nature* **258**, 136–137 (1975).
- ¹¹⁴H. P. Boehm, R. Setton, and E. Stumpp, “Nomenclature and terminology of graphite intercalation compounds (IUPAC Recommendations 1994)”, *Pure and Applied Chemistry* **66**, 1893–1901 (1994).
- ¹¹⁵K. S. Novoselov, A. K. Geim, S. V. Morozov, D. Jiang, Y. Zhang, S. V. Dubonos, I. V. Grigorieva, and A. A. Firsov, “Electric field effect in atomically thin carbon films.”, *Science* **306**, 666–9 (2004).
- ¹¹⁶D. M. Hoffman, G. L. Doll, and P. C. Eklund, “Optical properties of pyrolytic boron nitride in the energy range 0.05–10 eV”, *Physical Review B* **30**, 6051–6056 (1984).
- ¹¹⁷L. H. Li and Y. Chen, “Atomically Thin Boron Nitride: Unique Properties and Applications”, *Advanced Functional Materials* **26**, 2594–2608 (2016).
- ¹¹⁸K. S. Novoselov, D. Jiang, F. Schedin, T. J. Booth, V. V. Khotkevich, S. V. Morozov, and A. K. Geim, “Two-dimensional atomic crystals”, *Proceedings of the National Academy of Sciences of the United States of America* **102**, 10451–10453 (2005).
- ¹¹⁹C. Lee, Q. Li, W. Kalb, X.-Z. Liu, H. Berger, R. W. Carpick, and J. Hone, “Frictional characteristics of atomically thin sheets.”, *Science* **328**, 76–80 (2010).
- ¹²⁰G. F. Schneider, S. W. Kowalczyk, V. E. Calado, G. Pandraud, H. W. Zandbergen, L. M. K. Vandersypen, and C. Dekker, “DNA Translocation through Grapheme Nanopores”, *Nano Letters* **10**, 3163–3167 (2010).
- ¹²¹A. Castellanos-Gomez, M. Buscema, R. Molenaar, V. Singh, L. Janssen, H. S. J. van der Zant, and G. a. Steele, “Deterministic transfer of two-dimensional materials by all-dry viscoelastic stamping”, *2D Materials* **1**, 011002 (2014).
- ¹²²P. J. Zomer, M. H. D. Guimarães, J. C. Brant, N. Tombros, and B. J. van Wees, “Fast pick up technique for high quality heterostructures of bilayer graphene and hexagonal boron nitride”, *Applied Physics Letters* **105**, 013101 (2014).
- ¹²³R. G. Dickinson and L. Pauling, “The Crystal Structure of Molybdenite”, *Journal of the American Chemical Society* **45**, 1466–1471 (1923).

F. Bibliography

- ¹²⁴B. Schönfeld, J. J. Huang, and S. C. Moss, “Anisotropic mean-square displacements (MSD) in single-crystals of 2 H - and 3 R -MoS₂”, *Acta Crystallographica Section B Structural Science* **39**, 404–407 (1983).
- ¹²⁵O. Hassel, “Über die Kristallstruktur des Molybdänglanzes”, *Zeitschrift für Kristallographie - Crystalline Materials* **61**, 3–10 (1924).
- ¹²⁶V. Petkov, S. J. Billinge, P. Larson, S. D. Mahanti, T. Vogt, K. K. Rangan, and M. G. Kanatzidis, “Structure of nanocrystalline materials using atomic pair distribution function analysis: Study of (formula presented)”, *Physical Review B - Condensed Matter and Materials Physics* **65**, 1–4 (2002).
- ¹²⁷A. Splendiani, L. Sun, Y. Zhang, T. Li, J. Kim, C.-y. Chim, G. Galli, and F. Wang, “Emerging Photoluminescence in Monolayer MoS₂”, *Nano Letters* **10**, 1271–1275 (2010).
- ¹²⁸K. F. Mak, C. Lee, J. Hone, J. Shan, and T. F. Heinz, “Atomically thin MoS₂: A new direct-gap semiconductor”, *Physical Review Letters* **105**, 136805 (2010).
- ¹²⁹B. Radisavljevic, A. Radenovic, J. Brivio, V. Giacometti, and A. Kis, “Single-layer MoS₂ transistors”, *Nature Nanotechnology* **6**, 147–150 (2011).
- ¹³⁰J. Li, D. Stein, C. McMullan, D. Branton, M. J. Aziz, and J. a. Golovchenko, “Ion-beam sculpting at nanometre length scales.”, *Nature* **412**, 166–169 (2001).
- ¹³¹A. J. Storm, J. H. Chen, X. S. Ling, H. W. Zandbergen, and C. Dekker, “Fabrication of solid-state nanopores with single-nanometre precision”, *Nature Materials* **2**, 537–540 (2003).
- ¹³²A. R. Hall, S. Van Dorp, S. G. Lemay, and C. Dekker, “Electrophoretic force on a protein-coated dna molecule in a solid-state nanopore”, *Nano Letters* **9**, 4441–4445 (2009).
- ¹³³M. Van Den Hout, I. D. Vilfan, S. Hage, and N. H. Dekker, “Direct force measurements on double-stranded RNA in solid-state nanopores.”, *Nano Letters* **10**, 701–7 (2010).
- ¹³⁴J. Yang, D. C. Ferranti, L. A. Stern, C. A. Sanford, J. Huang, Z. Ren, L. C. Qin, and A. R. Hall, “Rapid and precise scanning helium ion microscope milling of solid-state nanopores for biomolecule detection”, *Nanotechnology* **22**, 10.1088/0957-4484/22/28/285310 (2011).
- ¹³⁵F. Sawafra, A. T. Carlsen, and A. R. Hall, “Membrane thickness dependence of Nanopore formation with a focused helium ion beam”, *Sensors (Switzerland)* **14**, 8150–8161 (2014).
- ¹³⁶I. Yanagi, T. Ishida, K. Fujisaki, and K.-i. Takeda, “Fabrication of 3-nm-thick Si₃N₄ membranes for solid-state nanopores using the poly-Si sacrificial layer process”, *Scientific Reports* **5**, 14656 (2015).
- ¹³⁷K. Briggs, H. Kwok, and V. Tabard-Cossa, “Automated fabrication of 2-nm solid-state nanopores for nucleic acid analysis”, *Small* **10**, 2077–2086 (2014).

- ¹³⁸H. Kwok, K. Briggs, and V. Tabard-Cossa, “Nanopore fabrication by controlled dielectric breakdown”, *PLoS ONE* **9**, 10.1371/journal.pone.0092880 (2014).
- ¹³⁹I. Yanagi, R. Akahori, T. Hatano, and K.-i. Takeda, “Fabricating nanopores with diameters of sub-1 nm to 3 nm using multilevel pulse-voltage injection”, *Scientific Reports* **4**, 5000 (2015).
- ¹⁴⁰J. Feng, K. Liu, M. Graf, M. Lihter, R. D. Bulushev, D. Dumcenco, D. T. L. Alexander, D. Krasnozhan, T. Vuletic, A. Kis, and A. Radenovic, “Electrochemical Reaction in Single Layer MoS₂ : Nanopores Opened Atom by Atom”, *Nano Letters* **15**, 3431–3438 (2015).
- ¹⁴¹H. I. Karunadasa, E. Montalvo, Y. Sun, M. Majda, J. R. Long, and C. J. Chang, “A Molecular MoS₂ Edge Site Mimic for Catalytic Hydrogen Generation”, *Science* **335**, 698–702 (2012).
- ¹⁴²R. R. Nair, P. Blake, A. N. Grigorenko, K. S. Novoselov, T. J. Booth, T. Stauber, N. M. R. Peres, and A. K. Geim, “Fine structure constant defines visual transparency of graphene.”, *Science* **320**, 1308 (2008).
- ¹⁴³J. H. Koschwanetz, R. H. Carlson, and D. R. Meldrum, “Thin PDMS films using long spin times or tert-butyl alcohol as a solvent”, *PLoS ONE* **4**, 2–6 (2009).
- ¹⁴⁴J. Danglad-Flores, S. Eickelmann, and H. Riegler, “Deposition of polymer films by spin casting: A quantitative analysis”, *Chemical Engineering Science* **179**, 257–264 (2018).
- ¹⁴⁵L. Galla, D. Greif, J. Regtmeier, and D. Anselmetti, “Microfluidic carbon-blackened polydimethylsiloxane device with reduced ultra violet background fluorescence for simultaneous two-color ultra violet/visible-laser induced fluorescence detection in single cell analysis”, *Biomicrofluidics* **6**, 10.1063/1.3675608 (2012).
- ¹⁴⁶D. Kreft, “Evaluation von MoS₂-Nanoporen für DNA-Translokationsexperimente mit der Optischen Pinzette”, Diploma Thesis (Bielefeld University, 2016).
- ¹⁴⁷J. Cremer, “Evaluation von MoS₂-Nanoporen für Translokationsexperimente”, Master Thesis (Bielefeld University, 2019).
- ¹⁴⁸Axon Instruments Inc., *Axopatch 200B Patch Clamp Theory and Operation*, tech. rep. 1 (1999), pp. 1–153.
- ¹⁴⁹W. M. Haynes, D. R. Lide, and T. J. Bruno, *CRC Handbook of Chemistry and Physics*, 97th ed. (CRC Press, Boca Raton, FL, USA, 2017).
- ¹⁵⁰J. Wilson and A. Aksimentiev, “Water-Compression Gating of Nanopore Transport”, *Physical Review Letters* **120**, 268101 (2018).
- ¹⁵¹A. Spiering, “Einzelmolekül-Experimente an Nanoporen mit der Optischen Pinzette”, Dissertation (Universität Bielefeld, 2014).

F. Bibliography

- ¹⁵²C. A. Merchant, K. Healy, M. Wanunu, V. Ray, N. Peterman, J. Bartel, M. D. Fischbein, K. Venta, Z. Luo, A. T. C. Johnson, and M. Drndić, “DNA translocation through graphene nanopores”, *Nano Letters* **10**, 2915–2921 (2010).
- ¹⁵³K. Liu, J. Feng, A. Kis, and A. Radenovic, “Atomically thin molybdenum disulfide nanopores with high sensitivity for dna translocation”, *ACS Nano* **8**, 2504–2511 (2014).
- ¹⁵⁴J. Feng, K. Liu, R. D. Bulushev, S. Khlybov, D. Dumcenco, A. Kis, and A. Radenovic, “Identification of single nucleotides in MoS₂ nanopores”, *Nature Nanotechnology* **10**, 1070–1076 (2015).
- ¹⁵⁵R. Dulbecco and M. Vogt, “Plaque Formation and Isolation of Pure Lines with Poliomyelitis Viruses”, *The Journal of Experimental Medicine* **99**, 167–182 (1954).
- ¹⁵⁶M. Ferdman, A. Adileh, O. Kocberber, S. Volos, M. Alisafae, D. Jevdjic, C. Kaynak, A. D. Popescu, A. Ailamaki, and B. Falsafi, “Quantifying the mismatch between emerging scale-out applications and modern processors”, *ACM Transactions on Computer Systems* **30**, 10.1145/2382553.2382557 (2012).
- ¹⁵⁷J. Nickolls, I. Buck, M. Garland, and K. Skadron, “Scalable parallel programming with CUDA”, *Queue* **6**, 40–53 (2008).
- ¹⁵⁸J. C. McDonald and G. M. Whitesides, “Poly(dimethylsiloxane) as a material for fabricating microfluidic devices”, *Accounts of Chemical Research* **35**, 491–499 (2002).
- ¹⁵⁹J. Friend and L. Yeo, “Fabrication of microfluidic devices using polydimethylsiloxane”, *Biomicrofluidics* **4**, 1–5 (2010).
- ¹⁶⁰R. R. Carvalho, S. P. Pujari, E. X. Vrouwe, and H. Zuilhof, “Mild and Selective C-H Activation of COC Microfluidic Channels Allowing Covalent Multifunctional Coatings”, *ACS Applied Materials and Interfaces* **9**, 16644–16650 (2017).
- ¹⁶¹A. Tsopela, S. Meucci, S. Rocchiccioli, G. Pelosi, and M. Brivio, “Lab-on-Chip Prototype for the Detection of Coronary Artery Disease Biomarkers”, *Proceedings* **2**, 390 (2018).
- ¹⁶²S. B. Smith, Y. Cui, and C. Bustamante, “Overstretching B-DNA: The Elastic Response of Individual Double-Stranded and Single-Stranded DNA Molecules”, *Science* **271**, 795–799 (1996).
- ¹⁶³W. Strober, “Trypan Blue Exclusion Test of Cell Viability”, in *Current protocols in immunology* (John Wiley & Sons, Inc., Hoboken, NJ, USA, May 2001), pp. 2–3.
- ¹⁶⁴G. W. C. Kaye and T. H. Laby, *Tables of Physical & Chemical Constants*, 16th Ed. (Kaye & Laby Online Version 1.0, 2005).

- ¹⁶⁵B. Pontes, N. B. Viana, L. T. Salgado, M. Farina, V. M. Neto, and H. M. Nussenzveig, “Cell cytoskeleton and tether extraction”, *Biophysical Journal* **101**, 43–52 (2011).
- ¹⁶⁶J. Helenius, C. P. Heisenberg, H. E. Gaub, and D. J. Muller, “Single-cell force spectroscopy”, *Journal of Cell Science* **121**, 1785–1791 (2008).
- ¹⁶⁷J. Dai and M. P. Sheetz, “Membrane tether formation from blebbing cells”, *Biophysical Journal* **77**, 3363–3370 (1999).
- ¹⁶⁸M. Padgett and R. Bowman, “Tweezers with a twist”, *Nature Photonics* **5**, 343–348 (2011).
- ¹⁶⁹Stanford Research Systems, *Model DS345 Synthesized Function Generator*, tech. rep. (2016).
- ¹⁷⁰International Organization for Standardization, *ISO 8601-1:2019 Date and time – Representations for information interchange – Part 1: Basic rules*, 1st ed. (2019).
- ¹⁷¹USB Implementers’ Forum, *Device Class Definition for Human Interface Devices (HID)*, tech. rep. (2001).

G. Danksagung

Diese Dissertation wäre ohne Unterstützung von Projektpartnern, Kollegen, Freunden und Familie nie zustande gekommen. Ich möchte mich zunächst herzlich bei Prof. Dr. Dario Anselmetti für die Möglichkeit der Promotion in seiner Arbeitsgruppe und die vielfältige Unterstützung bedanken. Mein Dank gilt außerdem Prof. Dr. Thomas Huser für seine Bereitschaft zur Begutachtung der Arbeit.

Diese Arbeit geht an die Grenzen der Leistungsfähigkeit heutiger Computer. Für die umfangreiche technische Unterstützung und Beratung bedanke ich mich Christoph Pelargus ebenso wie für gemeinsame Motorradtouren, Musikempfehlungen und Spieleabende.

Mein Dank für die Betreuung und Unterstützung bei der Strukturierung geht an Dr. Martina Viefhues. Ich konnte von dir viel Nützliches auch für das Leben außerhalb der akademischen Welt lernen, danke!

Ich danke Sabrina Kißmer, Julian Cremer und Dennis Kreft für die tolle Zusammenarbeit bei ihren jeweiligen Abschlussarbeiten und darüber hinaus.

Dr. Roland Hillmann, Dr. Sören Grannemann, Dr. Alexander Beel, Niklas Biere und Marcel Peplonski haben sich mit mir gemeinsam durch unsere jeweiligen Promotionen gekämpft. Vielen Dank für eure Unterstützung. Besonders möchte ich mich bei Roland und Niklas für die Einarbeitung am AFM bedanken.

Dr. Andy Sischka hat meine Bachelor- und Masterarbeit betreut, diese Arbeit Korrektur gelesen, die optischen Pinzetten aufgebaut und war ein verlässlicher Partner bei Elasto-Tweezers. Er stand jederzeit, auch nach seiner Beschäftigung in der Arbeitsgruppe, für Fragen zur Verfügung. Ohne seine Vor- und Mitarbeit wäre diese Arbeit nicht möglich gewesen, vielen Dank!

Natürlich wäre der Elasto-Tweezers-Teil dieser Arbeit ohne die Kooperationspartner nicht möglich gewesen. Ich möchte mich für die intensive Zusammenarbeit bei Dr. Bastien Venzac bedanken. Mein Dank gilt auch Dr. Karsten Gall, Prof. Dr. Hendrik Milting, Astrid Kassner, Prof. Dr. Séverine Le Gac und Dr. Elwin Vrouwe.

Mein Dank gilt außerdem den Unterstützern der ROCKET-Initiative für die finanzielle Unterstützung dieser Arbeit: Die Europäische Union im Rahmen von INTERREG Deutschland Nederland, das niederländische Ministerium für Wirtschaft und Klima, die Provinzen Over-

G. Danksagung

ijssel und Gelderland, das niedersächsische Ministerium für Bundes- und Europaangelegenheiten und Regionale Entwicklung sowie das Ministerium für Wirtschaft, Innovation, Digitalisierung und Energie des Landes Nordrhein-Westfalen.

Ich möchte mich außerdem bei Helene Schellenberg für die Übernahme der Zellkultur und der DNA-Präparation bedanken. Auch dem Rest der Arbeitsgruppe möchte ich herzlich für vielfältige Unterstützung und ein tolles Arbeitsklima danken.

Für die Unterstützung bei theoretischen Problemen danke ich Dr. Andreas Meyer und Thomas Töws. Vielen Dank für die TEM-Messungen an Dr. Inga Ennen und Daniela Ramermann.

Auch außerhalb des akademischen Umfelds möchte ich meinen Dank aussprechen. Danke an Jenny, Sarah, Lia, Luisa, Jonathan, Miriam und Jonas für schöne Spiele-Abende. Danke auch an Armin, Andy, Franzi, Michi, Jonas, Niklas und Jonathan für die schönen Stunden beim Pen-&-Paper-Rollenspiel.

Vielen Dank möchte ich Franziska Neugebauer aussprechen: Fürs Korrektur lesen, für die moralische Unterstützung, für die Motivation und für zwischenzeitlich dringend benötigte Ablenkung durch gemeinsames Grillen.

Ohne die Unterstützung und das Vertrauen meiner Mutter Waltraud Knust wäre diese Arbeit wahrscheinlich nie fertig geworden. Danke für alles!